Characterizing Polarized Illumination in High Numerical Aperture Optical Lithography with Phase Shifting Masks

Gregory Russell McIntyre

Electrical Engineering and Computer Sciences
University of California at Berkeley

Technical Report No. UCB/EECS-2006-52
http://www.eecs.berkeley.edu/Pubs/TechRpts/2006/EECS-2006-52.html

May 12, 2006

Characterizing Polarized Illumination in High Numerical Aperture Optical Lithography with Phase Shifting Masks

by

Gregory Russell McIntyre

B.S. (United States Military Academy at West Point, New York) 1996
M.S. (University of California, Berkeley) 2003

A dissertation submitted in partial satisfaction of the requirements for the degree of

Doctor of Philosophy
in

Engineering - Electrical Engineering
and Computer Sciences

in the

GRADUATE DIVISION

of the

UNIVERSITY OF CALIFORNIA, BERKELEY

Committee in charge:

Professor Andrew R. Neureuther, Chair
Professor Jeffrey Bokor
Professor Robert E. Cole

Spring 2006

Characterizing Polarized Illumination in High Numerical Aperture Optical Lithography with Phase Shifting Masks

Abstract

Characterizing Polarized Illumination in High Numerical Aperture Optical Lithography with Phase Shifting Masks

by

Gregory Russell McIntyre

Doctor of Philosophy in Electrical Engineering

University of California, Berkeley

Professor Andrew R. Neureuther, Chair

The primary objective of this dissertation is to develop the phase shifting mask (PSM) as a precision instrument to characterize effects in optical lithography related to the use of polarized partially coherent illumination. The intent is to provide an *in-situ* characterization technique to add to the lithographer's tool-kit to help enable the stable and repeatable mass production of integrated circuits with feature sizes approaching $1/6^{th}$ the wavelength of light being used.

A series of complex-valued mathematical functions have been derived from basic principles and recent advances in photomask fabrication technology have enabled their implementation with four-phase mask making. When located in the object plane of an imaging system, these test functions serve to engineer a wavefront that interacts with one particular optical effect, creating a measurable signal in the image plane. In most cases, these test patterns leverage proximity effects to create a central image intensity and are theoretically the most sensitive to the desired effect. Five novel classes of test patterns have been developed for *in-situ* characterization. The first two classes, The Linear Phase Grating (LPG) and Linear Phase Ring (LPR), both serve to characterize illumination angular distribution and uniformity by creating signals dependent on illumination angular frequency. The third class consists of the Radial Phase Grating (RPG) and Proximity Effect Polarization Analyzers (PEPA), which each create a polarization-dependent signal

by taking advantage of the image reversal of one polarization component at high numerical aperture (NA). PSM Polarimetry employs a series of these patterns to form a complete polarization characterization of any arbitrary illumination scheme. The fourth and fifth classes employ sub-resolution interferometric reference probes to coherently interact with proximity effect spillover from a surrounding pattern. They measure the effective phase and transmission of the shifted regions of an alternating PSM and projection lens birefringence, respectively.

A secondary objective of this dissertation has been to leverage some of these functions to extend the application of pattern matching software to rapidly identify areas in a circuit design layout that may be vulnerable to polarization and high-NA effects. Additionally, polarization aberrations have been investigated, as they may become important with hyper-NA imaging systems.

Three multi-phase test reticles have been developed for this thesis and have pushed the limits of photomask fabrication. Coupled with a variety of experimental and simulation studies at 193nm wavelength, they have validated the scientific principles of the PSM monitors and have offered unique insight into implementation issues such as electromagnetic (EM) effects and mask making tolerances. Although all five classes are novel theoretical concepts, it is believed that PSM Polarimetry is commercially viable. Despite a 70% loss of sensitivity due to mask making limitations and a 20% loss due to EM effects, it can likely still monitor polarization to within 2%. Experimental results are comparable to the only other known technique, which requires special equipment.

Taken collectively, the five novel classes of PSM monitors offer the lithographer an independent tool-kit to ensure proper tool operation. They also provide circuit designers an understanding of the impact of imaging on layouts. Although they have been developed for optical lithography, their principles are relevant to any image-forming optical system and are likely to find applications in other fields of optics or acoustics.

_____

Professor A. R. Neureuther
Committee Chairman

Dedicated to

Mom, Dad, and Liza – for getting me on my way

and to

Suzanne and Grace – for giving meaning to the journey

ACKNOWLEDGEMENTS

This research would not have been possible without the tremendous help and support from so many people. First, I would like to give a special thanks to my advisor, Professor Andrew Neureuther, for his guidance and support and for opening so many doors in the industry. He is a remarkable source for both the spontaneous and stimulated emission of innovation. Without a doubt, the most inspiring moments of graduate school have been during brainstorming sessions in his office. I would also like to thank Professors Jeff Bokor, Costas Spanos and Robert Cole for being on my dissertation and/or qualifying exam committees. They, in addition to Professors J. Stephen Smith, William Oldham, and David Attwood have all been positive influences during my academic development at Berkeley.

Thanks to the Feature Level Compensation and Control Grant, a U.C. Discovery Project which has provided most of my financial support, I have had more opportunities for collaboration with industry than I could have imagined possible for a graduate student. Accordingly, I am grateful to the following individuals and organizations for the tremendous help I have received during the course of this research: AMD (Jongwook Kye, Harry Levinson, Alden Acheta, Bruno La Fontaine, Adam Pawloski, and Luigi Capodieci), Nikon (Steve Slonaker, K. Fujii, H. Nishinaga, and T. Miyagi), Benchmark Technologies (Patrick Reynolds, Venu Vellanki), Photronics (Bryan Kasprowicz, Marc Cangemi, Ramkumar Karur-Shanmugam, Rand Cottle, Justin Novak, and Mark Smith), Toppan Photomasks (Greg Hughes, Paul Walker, and Susan McDonald), ASML (Mircea Dusa), and Panoramic Technologies (Tom Pistor). I had a particularly valuable experience during an internship with AMD. I would also like to acknowledge SPIE – the International Society for Optical Engineering – as a critical part of my development for creating such a collaborative environment in our industry and for financial support. Additionally, I am grateful for financial support this past year as an Applied Materials Graduate Fellow.

I have also been fortunate to be surrounded by many good friends and colleagues at Berkeley. Many thanks to (in alphabetical order): Jason Cain, Adam Cataldo, Dan

Ceperley, Yunfei Den, Paul Friedberg, Frank Gennari, Scott Hafeman, Juliet Holwill, Michael Lam, Steve Molesa, Wojtek Poppe, Garth Robins, Dan Schonberg, Michael Shumway, Mike Williamson, Lei Yuan, Charlie Zhang, and fellow officers from the EE graduate student association.

I would also like to thank the UC Berkeley Management of Technology program, headed by Professor Andrew Isaacs, for offering unique insight into the world of high-tech entrepreneurship and especially to the Mayfield Fellows Program for a year of invaluable immersion into the workings of Silicon Valley. The most valuable lessons as Mayfield Fellow were likely learned via my fellow fellows: Jeannie Yang, Eri Takahashi, Will Plishker, Ameet Ranadive, Rahul Shah, Sirish Chandrasekaran, and Josh Elman.

Adding to the list of unique experiences has been the opportunity to co-found a startup company, now known as CommandCAD, Inc. I am indebted to my co-founders Frank Gennari, Ya-Chieh Lai and Michael Lam. Additionally, Frank's many useful CAD tools have been key enablers for my own research.

Also, for their cheerful assistance with administrative and grant issues, I would like to thank Ruth Gjerde, Mary Byrnes, Charlotte Jones, Ellen Lenzi, Pat Hernan, Diane Chang and Vivian Kim. I can only wish that throughout life there is someone as helpful as Ruth to always point me in the right direction.

Most importantly, I cannot express my appreciation enough for the five people who are most dear to me. Mom and Dad - your love, support, and encouragement throughout all of the years have given me not only the foundation to succeed, but a deep appreciation for what I have. You've taught me many things, but most importantly to be a student of life. Liza – from the days of teaching me what you learned in school as a kid, you have been more of a big sister than I could have asked for. I must also give credit and thanks to my faithful study companion, Zoë (the dog).

Finally, and certainly most of all, I am especially grateful for the unending love, patience, and dedication of my wife, Suzanne, and newborn daughter, Grace. The two of you make all of this worthwhile. I love you both very much!

TABLE OF CONTENTS

1 Introduction

Given that it took our species over 200,000 years to develop techniques to image anything smaller than what is visible to the naked eye, it is quite remarkable that just in the last few generations, we have learned to not only detect objects on the atomic scale, but to simultaneously engineer billions of useful devices out of them. Leading the charge in these efforts of mass-scale miniaturization has been the semiconductor industry. In the late 1940's when the first semiconductor transistor was first discovered, the world's largest computing machine occupied 1000 square feet and performed just 5000 operations per second[1] [91]. Now, thanks to the unique properties of semiconductor materials and to the Herculean efforts of engineers in manipulating those properties into useful devices, an ordinary computer easily performs over ten billion operations per second while fitting conveniently under one's desk.

Optical lithography quickly became the centerpiece in the mass production of integrated circuits (ICs) soon after Perkin-Elmer and GCA introduced the first projection printing tools in the mid 1970s. Using light to rapidly pattern all of the transistors on a single chip, these first tools had a minimum resolution of nearly 1μm [86]. Since then, advances in resolution capability have not only kept optical lithography the workhorse of the IC manufacturing process, but have been the driving force behind the amazing success of the semiconductor industry. Many predictions have been made over the years as to the demise of optical lithography, typically citing better resolution abilities with

[1] The ENIAC was the world's first electronic digital computer and was developed by Army Ordnance to compute World War II ballistic firing tables.

another technology. However, none of these technologies have lived up to the economic realities required to churn out computer chips at an affordable price with acceptable resolution and within the existing infrastructure. Today's lithography tools can resolve nearly 45nm transistor features and pattern roughly 100 wafers per hour, where each wafer holds on the order of 50 billion transistors.

Advances in lithographic resolution have primarily been the result of two factors: enhanced tool precision and the invention of various imaging strategies. Steady improvements in tool precision have resulted from advancing materials processing technologies, to the more accurate fabrication and assembly of tool components, and the ability to precisely measure optics and tool performance. On the other hand, the invention of various clever imaging 'tricks', which are typically referred to as Resolution Enhancement Techniques (RETs), have periodically shattered conventional wisdom as to the limiting factors of projection printing.

Advancing tool precision and RETs have set optical lithography on the path to image features less than $1/6^{th}$ the wavelength of the light being used by the year 2013. However, as these resolution requirements delve into the nanometer regime, slight imperfections in certain parts of the tool can have devastating consequences for image fidelity and thus device performance. Therefore, the development of precise *in-situ* lithographic characterization and monitoring techniques is critical to maintaining an acceptable rate of resolution improvement and device miniaturization.

The primary goal of this thesis is to investigate and develop various methods to monitor *in-situ* some of the key parameters of optical lithography, particularly the imaging capabilities required by recently developed RETs. This will be done using phase shifting masks as precision 'on-board' instrumentation. The main concepts explored in this thesis are phase shifting masks, proximity effects, high numerical aperture vector effects and the use of polarized off-axis illumination schemes. Additionally, the consequences of some of these manufacturing concepts will be related to the IC design community.

1.1. Dissertation research themes and organization of text

Chapter 2 will provide a basic introduction to the photolithography process and lay the groundwork for concepts relevant to this thesis. An overview of the principles of projection printing will pay particular attention to the advances in imaging techniques and outline the concepts of phase shifting masks, high numerical aperture vector effects, off-axis illumination, proximity effects and polarized illumination. Additionally, a brief overview will be given of various common non-idealities due to realistic imaging conditions, highlighting in greater detail the ones most relevant to this work. The remainder of the text can be subdivided into the three research themes of this dissertation: the phase-shifting mask as precision 'on-board' instrumentation, screening circuit design layouts for vulnerabilities to polarization effects using pattern-matching, and an investigation of polarization aberrations.

1.1.2. Phase-shifting mask (PSM) as a precision instrument for characterizing optical lithography

Clearly, the main effort of this dissertation has been to develop a series of phase shifting mask monitors to characterize various lithographic effects. As mentioned earlier, the ability to monitor lithographic tool performance is critical to the end user to consistently maintain nanometer-scale resolution. However, the end user is typically limited to two access locations in a tool: the wafer and reticle (photomask) stages. Thus, the primary objective of this research has been to develop a series of photomask test patterns that, by creating measurable signals in photoresist, enable characterization of various lithographic effects.

Five novel classes of test mask patterns have been developed for *in-situ* characterization of polarized illumination, phase shift mask performance and projection lens birefringence. The basic strategy has been to leverage knowledge of optical effects and the topography enabled by state-of-the-art, multi-phase photomasks to create patterns that are sensitive to one aspect of projection printing. Each design is believed to be theoretically the most sensitive pattern to the desired effect. To test these concepts, three four-phase industrial-quality test reticles have been designed and fabricated for this thesis. A variety of experimental and simulation studies at 193nm wavelength have

validated the monitor's scientific principles and have helped allow understanding of limitations due to realistic imaging conditions, most notably the electromagnetic interaction with mask topography and mask making limitations. Additionally, although these multi-phase monitors are not standard topographies found in IC manufacturing, they do offer unique insight for the industry into not only the effects of the photomask on imaging, but also to how the photomask interacts with polarization and high-NA vector effects, oblique angles of incidence, partial coherence and proximity effects. Various comparisons of thin and thick mask simulation to experimental data in this thesis reveal the relative effects of limitations such as electromagnetic interaction and mask making imperfections [52][53].

For each PSM monitoring technique, this thesis will

- develop the theoretical concept by deriving the monitors from basic optical principles
- investigate the theoretical sensitivity to the desired effect
- describe the physical image-plane measurement and data reduction techniques
- explore various potential applications and illustrate examples
- examine the relevant limitations due to realistic imaging conditions
- explain methods to either alter the design or calibrate the test reticle to counteract or account for some of these limitations
- comment on the overall assessment and practicality of the technique

The PSM monitors developed in this thesis are:

Illumination Monitors: The first two monitors, the linear phase grating (LPG) and linear phase ring (LPR), both serve to characterize illumination angular distribution and uniformity and will be addressed in Chapters 3 and 4, respectively. The LPG consists of four successive phase-shift regions, etched linearly in a chrome-less mask. This diffracts incident light into only the +1 and higher diffraction orders at an angle determined by the period of the grating. The pupil of the projection lens is then employed as an aperture to clip only a certain portion of the illuminator. The total

intensity of this portion is then recorded in photoresist. Multiple LPGs placed strategically on a mask enable a quick means to compare intensity in various parts of the illuminator. The LPR accomplishes a similar goal, but does so in a different manner. A circular pattern resembling the point spread function, combined with a four-phase linear grating, creates a central image intensity dependent on only one illumination angular frequency. Again, multiple patterns on the mask sample different parts of the illuminator. Although both the LPG and the LPR are likely not sensitive or practical enough to outdo existing techniques in the industry, they offer unique insight into the effects of the photomask and provide a useful background understanding for the development of the polarization monitors in Chapter 5 [54][55].

Polarization Monitors: Polarization has quickly become an important topic in lithography due to the rapid adoption of ultra high numerical aperture (NA) systems. At high-NA, the imaging dependence on the polarization state of the illuminator becomes severe. Thus, tools with polarized illumination are currently entering the marketplace. The PSM Polarimeters described in Chapter 5 take advantage of a typically unwanted side effect of high-NA imaging to create a central image intensity that is dependent on polarization state. By grouping a number of patterns together and adapting theory from the field of imaging polarimetry, proper calibration of the test reticle enables a reasonable polarization measurement, even despite severe mask topography effects and mask making limitations. Experiments from two test reticles that have employed variations of the polarization monitors will be described and compared to rigorous thick-mask simulations which account for high-NA vector effects. Analysis of the unique mask topography sheds light on subtle polarization-dependent electromagnetic proximity effects. It is concluded that this technique is likely capable of monitoring the Stokes parameters to within 0.02 or 0.03 for linear polarization, where the Stokes parameters are a mathematical means to completely characterize polarization. This corresponds to a polarization measurement to within less than 2%. As the illumination requirements of the Stokes parameters for the first or second generation of tools with polarized illumination will likely to be within 0.05, PSM polarimetry offers a potential commercially viable technique. Additionally, to

decrease measurement time, a design modification and double exposure technique is proposed to enable electrical detection of the measurement signal [56][57][58].

Monitors for self-calibration of PSM performance: Chapter 6 describes a class of patterns that are designed to self-test the effective phase and transmission of the shifted regions of a phase shift mask. In other words, they are used to ensure that the phase etch of phase shifted regions are manufactured properly. A sub-resolution interferometric reference probe is employed where the image intensity changes (relative to a nearby isolated probe) due to phase and transmission errors in the surrounding geometry. Due to the orthogonality of phase and transmission, the use of either a 0° or 90° probe segregates these effects. It is concluded that this technique is likely the most sensitive image-plane measurement available for certain feature types, does not require through-focus analysis, and can achieve a sensitivity of over 1 percent of the clear field per degree phase error. This technique is especially well suited for use in an Aerial Image Measurement System (AIMS) [100], offering the mask maker a means to verify the mask is fabricated according to specification [59].

Birefringence Monitors: A technique to characterize the level of birefringence in projection lens systems is briefly introduced in Chapter 8 at the conclusion of the study into polarization aberrations. A series of chromeless gratings of varying height provide interferometric references with programmed levels of phase delay between orthogonal polarization components. Proximity effect spill-over from nearby clearfield locations interacts with this reference and, with the help of polarizers in the backside of the test reticle and at the image plane, provides a signal sensitive to lens birefringence.

It is noted that the monitors derived in this thesis follow in a thread of research initiated by Robins, Neureuther, and Adam to monitor projection lens aberrations [76][78]. There, proximity effect patterns for each Zernike aberration term were derived as the inverse Fourier transform of that particular Zernike polynomial. Combined with a sub-resolution interferometric reference probe in the center of the pattern, they provided

an image-plane signal dependent on the amount of aberration present in the projection lens.

1.1.2. Screening IC layouts for areas vulnerable to polarization and high numerical aperture effects using pattern matching

The development of the polarization monitoring technique of Chapter 5 led to an in-depth understanding of the nature of high-NA and polarization-dependent proximity effects. In Chapter 7, an effort is made to push that knowledge upstream towards the IC design community by extending the application of pattern matching software developed by Gennari [25]. This software was first developed to screen layouts for areas sensitive to projection lens aberrations, where pattern matching identifies areas with a certain degree of similarity to a given input function. This function represents the coherent proximity effects associated with a particular aberration. Chapter 7 extends this pattern matching concept to identify areas in a circuit design layout that are particularly vulnerable to high-NA and polarization vector effects. Simulated examples show that the predictions of this technique are generally accurate to better than 90%, suggesting this is a good technique to quickly screen layouts for areas in need of more attention. Additionally, theory is described to extend this concept to account for off-axis illumination, which has recently been implemented by Holwill [32][60].

1.1.3. Investigation of polarization aberrations

Polarization aberrations, which are potentially important with hyper numerical aperture tools (NA>1), are a complicated phenomena that refer to induced polarization dependent wavefront distortions as light propagates through an imaging system. Various representations of polarization aberrations are described and compared in Chapter 8, to include representations based on the Mueller-matrix, the Jones-matrix, and the Jones matrix decomposed into a Pauli spin matrix basis. Although each has its own advantages and disadvantages, it is concluded that the Jones matrix representation decomposed into a Pauli spin matrix basis offers the most useful format for the lithographer due to its compact notation, physically intuitive interpretation, ability to be implemented into standard imaging equations, and its usefulness as an input into a lithographic simulator. Also, a simple metric for lens polarization quality based on this representation is

proposed [61]. Finally, the phase shift mask birefringence monitoring technique previously discussed is introduced.

1.2. Major contributions of this thesis

The invention, theoretical development and experimental verification of the five novel PSM-based monitors are the most obvious contributions of this thesis. In all cases, the concept of reciprocity is employed to create patterns that maximize proximity effect spill-over to a central location for one particular optical effect. The use of a four-phase progression within the patterns provides a novel means to maximize these proximity effects for only a select illumination angular frequency. Although all five techniques are novel theoretical contributions, PSM polarimetry and the PSM performance monitors of Chapters 5 and 6 are likely sensitive and robust enough to find commercial application in optical lithography. PSM polarimetry can likely monitor polarization to within 2%, meeting the probable specifications for the first generations of tools. Furthermore, it appears to meet a growing need in the industry, as tools with polarized illumination are just entering the marketplace and no commercially available means yet exists to independently verify tool polarization performance. The interferometric-probe monitoring method for PSM performance is likely the most sensitive image-plane technique available for characterizing the effective phase of certain feature sizes and types.

Furthermore, in pushing the limits of photomask engineering, this research has offered unique insight into the capabilities of phase shifting mask technologies by considering the electromagnetic interaction with mask topography that nature dictates – and of the limitations of mankind in fabricating perfect mask geometries. Additionally, the investigation of high-NA proximity effects of Chapters 2, 5, and 7 highlight some subtle differences between the proximity effects of TE and TM polarized light with off-axis illumination.

Additionally, a technique using pattern matching has been shown to successfully identify areas in a circuit design layout that may be particularly vulnerable to polarization and high numerical aperture effects. This pattern matching technique is a potential

addition to the arsenal of tools to help integrate manufacturing knowledge into the design process and to assist in the recent trend within the semiconductor industry of design-for-manufacturability.

Finally, the investigation into polarization aberrations of Chapter 8, which was done in collaboration with researchers at Advanced Micro Devices, has offered the industry an additional – and perhaps a preferred – means to describe a complicated effect that may become important in future tools with hyper numerical aperture (NA>1).

1.3. Anticipated impact of this work

Taken collectively, the five novel classes of phase shift monitors developed as the primary effort of this thesis offer, at a minimum, the lithographer an independent tool-kit to ensure proper tool operation. They also provide circuit designers an understanding of the impact of imaging on various layouts. Although they have been developed for optical lithography, their principles are relevant to any image-forming optical system and are thus likely to find applications in other fields of optics or acoustics. Finally, the special attention that has gone into pushing the limits of photomask manufacturing and the advanced understanding of the impact of proximity effects on imaging may potentially lay the groundwork for future resolution enhancement techniques. Hopefully, this will help make optical projection printing cost-effective for the mass production of integrated circuits with feature sizes less than $1/6^{th}$ the wavelength of light.

2 Imaging and Tool Characterization in Optical Lithography

The purpose of this chapter is to provide a basic introduction to the photolithography process and to lay the groundwork for concepts relevant to this thesis. Section 2.1 steps the reader through the basic operation of optical projection printing, with special emphasis on the role of the illumination. Both scalar and vector theory are addressed. Additionally, a few significant resolution enhancement techniques will be outlined, as they are the underlying reasons for the use of polarization, off-axis illumination schemes and phase shifting masks, the three main concepts investigated in this thesis. Section 2.2 will highlight some of the common non-idealities that arise due to realistic imaging conditions and comment on how they impact imaging. Tool characterization is defined as the attempt to identify and quantify these non-idealities. Although various characterization strategies exist, the use of test reticles is generally the only strategy accessible to the end user of a lithography tool to independently verify the tool is operating to the appropriate specification. The concept of test reticles, where images of specially designed test patterns reveal tool imperfections, an overview of the test reticle market, and a summary of the three test reticles that were designed and fabricated for this thesis are provided in Section 2.2.

2.1. Photolithography operation

A projection printing tool, referred to as a stepper or scanner in photolithography, consists of a complex system of optical elements, often costing in excess of $30 million for a state-of-the art tool. This complex system can be simplified greatly by the diagram in Figure 2-1. In modern tools, a 193nm excimer laser provides a coherent and linearly polarized beam. The illuminator and condenser optics scramble this beam in an optimal

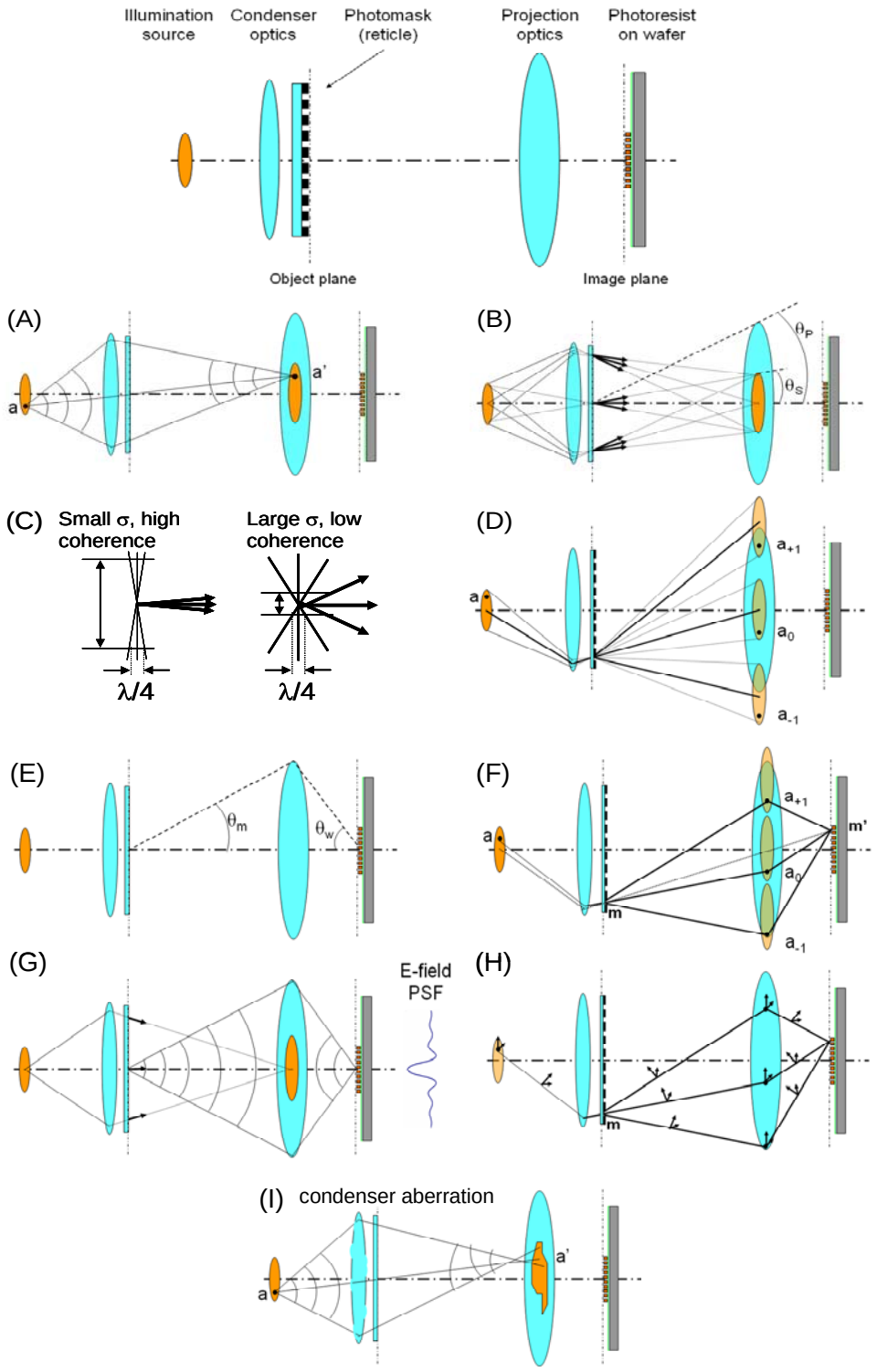

Figure 2-1. The concept of photolithography with Köhler illumination described by various ray paths through the optical system.

way to provide the desired degree of polarization and spatial coherence. The light is then scattered by the reticle (commonly referred to as the photomask) and is captured and redirected by the projection optics, de-magnifying an image of the mask (object plane) onto the wafer (image plane). The image is recorded in photoresist, a chemical substance that, when exposed with a sufficient number of photons, becomes soluble. Subsequent processes are then used to transfer the pattern to an underlying material.

This lithographic process is repeated many times to gradually construct the billions of transistors, capacitors, and interconnects that together form a computer chip, memory device, or other integrated circuit application. Although various lithographic technologies have emerged over the years[1], each with the promise of outdoing optical lithography, optical still remains the workhorse of the industry and will likely remain so until at least 2013. Although other techniques offer better resolution or process latitude, optical lithography enables the massively parallel patterning, and thus the wafer throughput, required by the economics of today's semiconductor manufacturing industry.

2.1.1. Imaging with Kohler illumination system

2.1.1.1. Scalar theory

Optical projection printing systems are typically configured with Köhler illumination [43], as shown in Figure 2-1. The key concept of a Köhler illumination system is to focus an image of the source at the entrance pupil of the projection lens. To illustrate the benefits of doing so, a series of ray paths through the imaging system are shown in Figure 2-1 and are explained below in the context of scalar imaging theory:

A) The condenser optics form an image of the source in the entrance pupil of the projection lens. This image of the source if often referred to as the **pupil-fill** or **source-image**. After manipulation of the incident laser by the illumination optics, the

[1] Some of the major contenders over the years have been x-ray lithography, electron-beam lithography, ion-beam lithography. Although much uncertainty remains, currently the leading contenders that may eventually take optical lithography's place are extreme ultraviolet (EUV) lithography, nano-imprint lithography, or perhaps electron-projection lithography.

source can be considered an incoherent collection of numerous individual point sources, each of which radiates light independently (i.e. they each emit randomly phased wavetrains), but with the same wavelength. Each source point creates a spherical wavefront that is captured by the condenser optics and redirected to the point source's reciprocal location in the source-image.

B) The photomask is located in the exit pupil of the condenser optics.

i) Thus, each source point illuminates the entire mask uniformly and any bright or dark spots within the illuminator are averaged over the reticle. This enables a high degree of **across-field dose uniformity**.

ii) At any mask location, the light from each source point results in a single **plane wave**, directed towards the source point's image in the pupil. This plane wave is said to be of a single **illumination angular frequency** and is on-axis if directed towards the pupil center and off-axis otherwise.

iii) Considering all source points, each mask location is illuminated with the same directional distribution of incoherent plane waves (i.e. the same cone of light), directed towards the center of the projection optics. This enables **stationary imaging**, the ability to image a given pattern the same regardless of its position in the field. This directional distribution of plane waves defines the effective source for that mask location, and is sometimes referred to as the **local value of partial coherence** or simply the **local effective source**. It will be shown later that aberrations in the condenser optics can cause variation of this effective source across the field. For a circular source, the quantity σ is defined as:

$$\sigma = \frac{\mathbf{sin}(\theta_S)}{\mathbf{sin}(\theta_P)} = \frac{\mathrm{NA}_S}{\mathrm{NA}_P} \qquad \text{Eq. 2-1.}$$

C) The spatial extent of the illuminator determines **spatial coherence**. The degree to which the light illuminating two nearby mask locations will be correlated in phase depends on the spatial extent of the illuminator, as described by σ for a circular

source. With a small cone of light (small σ), mask locations separated relatively far apart will be illuminated sufficiently in phase that each may affect the other's image. Conversely, with large σ, this interaction distance is less. The details of this interaction are appropriately described by the **mutual coherence function**, which is related to the inverse Fourier transform of the source distribution and is described further in [29]. Generally, for the purposes of optical lithography

$\sigma < 0.3$	coherent
$0.3 < \sigma < 2.0$	partially coherent
$\sigma > 2.0$	incoherent

Table. 2-1. Partial coherence in optical lithography

It is noted that the illumination and polarization monitors developed in this dissertation depend on coherent interactions between surrounding and center locations within the pattern and hence require a small cone of illumination (small σ, thus a high degree of spatial coherence). Consequently, in some cases a pinhole aperture in the backside of the photomask is employed for both frequency selection and to ensure a high degree of spatial coherence (generally $\sigma \cong 0.1$).

D) Each incident cone of light is diffracted into the pupil at angles depending on the features on the photomask. It is the specifics of the angular spectrum of light captured by the pupil that determines nominal image formation at the wafer. Each scattered plane wave is referred to as a **diffraction order**, seen for source point a in Figure 2-1D to be a_{+1}, a_0 and a_{-1}. As seen in the same figure, some of the diffracted light may not be captured by the pupil for certain small feature sizes, as the pupil serves as a **low-pass frequency filter**. However, the spatial extent of the source can be used as a lever to ensure that more than one diffracted order from some of the source points are collected by the projection lens, thus enabling some modulation from interference on the wafer. In terms of Fourier optics, this ability to produce modulation from frequency components past the coherent cutoff of the system (i.e. periodic features smaller than .5 λ/NA) is described by the **optical transfer function** (OTF), which specifies the relative complex weighting factor applied to each frequency component by the optical system [27].

E) The projection lens forms a demagnified image of the mask onto the wafer. The demagnification of the system (M) is defined as:

$$M = \frac{\sin(\theta_W)}{\sin(\theta_M)} = \frac{\mathrm{NA}_W}{\mathrm{NA}_M} \qquad \text{Eq. 2-2.}$$

M is typically 4 for most modern scanner designs.

F) For each source point, the diffracted orders from any mask location are correlated in phase with each other. The resulting electric field distribution in the image plane (u,v) is then a superposition of the interfering plane waves from the diffracted orders captured by the pupil:

$$E_{Wafer}(u,v,\alpha,\beta) = \frac{1}{\pi}\int_0^{2\pi}\int_0^{1} E_{Diff}(\rho,\varphi,\alpha,\beta) e^{ik[\rho\cos(\varphi)x' + \rho\sin(\varphi)y']} e^{ik\Phi(\rho,\varphi)} \rho d\rho d\varphi \qquad \text{Eq. 2-3.}$$

where $E_{Diff}(\rho,\varphi,\alpha,\beta)$ represents the scalar field in the pupil (radius ρ and angle φ, or Cartesian coordinates ξ and η) diffracted from the photomask for a given illumination source point (Cartesian coordinates α,β). The first exponential represents the lens effect and the second exponential accounts for any scalar aberrations in the projection lens (see Chapter 8 for a more detailed explaination). **The image intensity is then determined as the incoherent sum over all illumination source points**:

$$I_{Wafer}(u,v) = \iint_{source} \left| E_{wafer}(u,v,\alpha,\beta) \right|^2 d\alpha d\beta \qquad \text{Eq. 2-4.}$$

G) The finite size of the projection optics (NA):

i) limits the resolution capability. Considering a single open clear field location as a Huygen's source (i.e. a pinhole) which emits a spherical wavefront that uniformly fills the pupil, the resultant electric field distribution in the image can be found by equation 2-3 and is referred to as the point spread function (PSF). For a circular pupil, the PSF is simply the inverse Fourier transform of the unaberrated pupil and is in the form of the Airy function, shown in Figure 2-1G. The inability of the imaging system to accurately form an image of the pinhole is a direct result of the pupil's inability to capture

high frequency information. This ultimately limits the feature sizes that can be produced by the imaging system. The minimum feature is typically expressed as:

$$l_w = k_1 \frac{\lambda}{NA} \qquad \text{Eq. 2-5.}$$

where λ is the wavelength of light, NA is defined as the numerical aperture on the wafer side ($NA = \sin(\theta_w)$), and k_1 represents all of the other levers that lithographers can manipulate to print smaller features. Resolution enhancement is most simply provided by decreasing λ or by increasing NA. For various reasons, the usable wavelength for the industry is fixed at 193nm[1]. Ways to manipulate k_1 will be discussed in Section 2.1.2.

ii) determines, in conjunction with the mutual coherence function, the extent proximity effects influence imaging. The PSF determines, for a single source point, the magnitude and phase of proximity effect spill-over that occurs from one object location to a nearby location in the image plane. The mutual intensity function, on the other hand, determines how strongly this proximity effect will impact imaging after summation of the images from all source points.

It is noted that many of the monitors developed in this thesis take advantage of proximity effects and a high degree of spatial coherence by creating patterns that maximize coherent proximity-effect spill-over to a single location.

2.1.1.2. Vector theory

The previous section followed scalar diffraction theory, where the electric fields are considered scalar quantities. However, light is not a scalar phenomena, rather the propagating fields always have some sort of directionality at any particular instant in time. This directionality, when averaged over time, determines the polarization

[1] The next viable option is in the extreme ultraviolet (EUV), with a wavelength of around 13nm. However, a host of engineering and economic issues remain to be solved and the viability of EUV is the subject of much debate in the industry.

characteristics of light. Traditionally in lithography, scalar theory has been sufficient for most purposes as the electric field polarization has had little relevance to imaging. However, due to the recent and rapid adoption of high numerical aperture systems, imaging now greatly depends on polarization and thus the true vector nature of light must be considered. Figure 2-2 illustrates how this evolution from low- to high-NA systems introduces a component of electric field oriented normal to the image plane, which is referred to in this thesis as the z-component. This z-component results exclusively from the component oriented radially in the pupil, commonly referred to as the transverse-magnetic (TM) component.

To illustrate how high-NA vector effects can significantly affect imaging (and to lay the groundwork for why polarized illumination is now necessary), Figure 2-3 considers two coherent interfering plane waves from symmetric pupil locations. The resulting three vector components of either propagating wave are:

$$\mathbf{E}_y = \mathbf{E}_{TE}\, e^{-i\vec{k}_0\cdot\vec{r}}\, \hat{\boldsymbol{y}} \qquad \text{Eq. 2-6}$$

$$\mathbf{E}_x = \mathbf{E}_{TM}\, \mathbf{cos}(\theta)\, e^{-i\vec{k}_0\cdot\vec{r}}\, \hat{\boldsymbol{x}} \qquad \text{Eq. 2-7}$$

$$\mathbf{E}_z = -\mathbf{E}_{TM}\, \mathbf{sin}(\theta)\, e^{-i\vec{k}_0\cdot\vec{r}}\, \hat{\boldsymbol{z}} \qquad \text{Eq. 2-8}$$

Equation 2-8 can be expressed as

$$\mathbf{E}_z = -\mathbf{E}_{TM}\, \frac{|k_x|}{|k_0|}\, e^{-i\vec{k}_0\cdot\vec{r}}\, \hat{\boldsymbol{z}} \qquad \text{Eq. 2-9}$$

where k_0 and k_x are the wavevectors in the direction of propagation and in the image plane, respectively, as shown in Figure 2-3. Also,

$$\vec{k}_0 \cdot \vec{r} = k_x x\hat{\boldsymbol{x}} + k_y y\hat{\boldsymbol{y}} + k_z z\hat{\boldsymbol{z}} \qquad \text{Eq. 2-10}$$

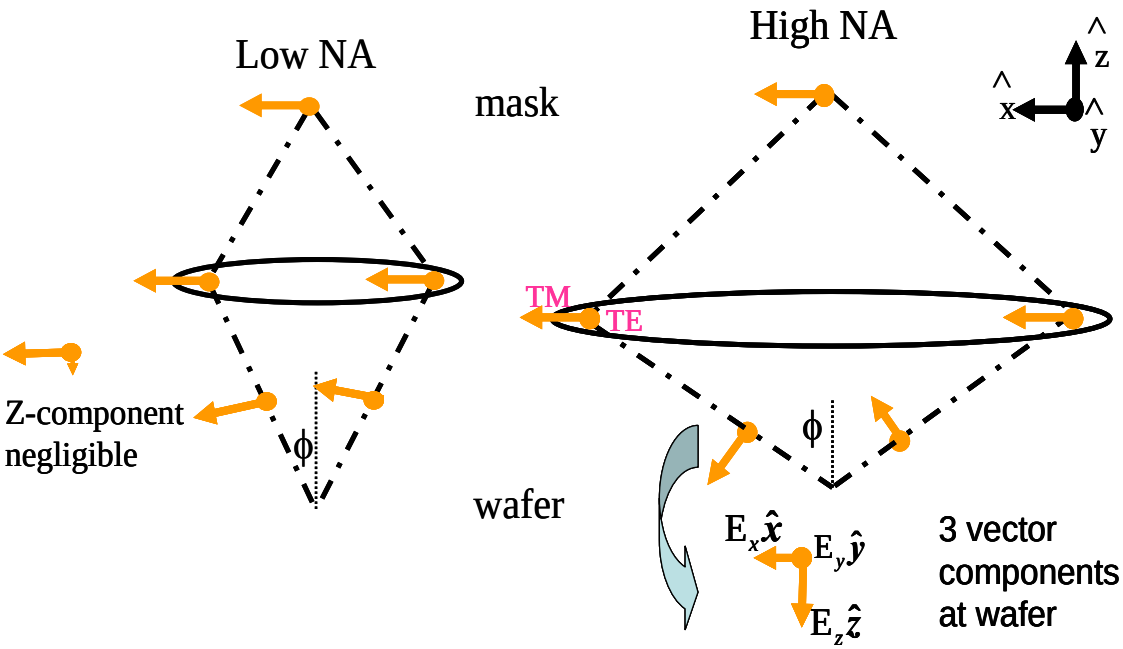

Figure 2-2. High-NA vs. low-NA

Z-component of the electric field in the image is (a) negligible at low-NA and (b) appreciable at high-NA. Thus, analysis of high-NA requires vector theory.

Differentiating equation 2-7:

$$\frac{\delta}{\delta x}\mathbf{E}_x = -ik_x\,\mathbf{E}_{TM}\,\mathbf{cos}(\theta)\,e^{-i\vec{k}_0\cdot\vec{r}} \qquad \text{Eq. 2-11}$$

and expressing the image plane wavevector as:

$$\left|k_x\right| = \frac{-1}{\mathbf{E}_{TM}\,\mathbf{cos}(\theta)}\frac{\delta}{\delta x}\mathbf{E}_x \qquad \text{Eq. 2-12}$$

the z-component of electric field can then be expressed as:

$$\mathbf{E}_z = \frac{1}{\left|k_0\right|\mathbf{cos}(\theta)}\frac{\delta}{\delta x}\mathbf{E}_x\,e^{-i\vec{k}_0\cdot\vec{r}}\,\hat{z} \qquad \text{Eq. 2-13}$$

Thus, the z-component of electric field is proportional to the spatial derivative of the electric field component that is parallel to the TM component in the pupil (the x-direction in this derivation). This relation is a key component in the derivation of the polarization monitors of Chapter 5 and the polarization test functions used for pattern matching in

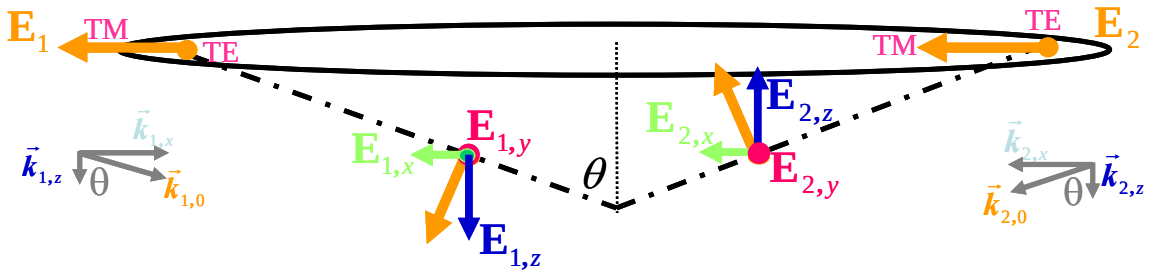

Figure 2-3. High-NA vector effects

Chapter 7. Additionally, the magnitude of this z-component gets larger with increased angle of incidence.

The consequence of this z-component on imaging is evident by considering the interference of the two off-axis plane waves of Figure 2-3. Due to coherent superposition, the one-dimensional field distribution in the image-plane (z = 0) with the electric field oriented parallel to the TE pupil component (y-direction, in this case) is:

$$\mathbf{E}_y(x) = (\mathbf{E}_{1,y} + \mathbf{E}_{2,y})\,\hat{\boldsymbol{y}} \quad = \mathbf{E}_{TE}\left[e^{-i\vec{k}_1\cdot\vec{r}} + e^{-i\vec{k}_2\cdot\vec{r}}\right]\hat{\boldsymbol{y}} \qquad \text{Eq. 2-14}$$

The interfering waves are traveling in this case only in the x- and z-directions, thus $k_y = 0$ and $\vec{k}_1 \cdot \vec{r} = -k_x x$ and $\vec{k}_2 \cdot \vec{r} = k_x x$. Therefore,

$$\mathbf{E}_y(x) = \mathbf{E}_{TE}\left[e^{-ik_x x} + e^{ik_x x}\right]\hat{\boldsymbol{y}} \quad = 2\,\mathbf{E}_{TM}\,\mathbf{cos}(\mathrm{k}_x x)\,\hat{\boldsymbol{y}} \qquad \text{Eq. 2-15}$$

Likewise, the resulting field in the direction parallel to the TM component is:

$$\mathbf{E}_x(x) = (\mathbf{E}_{1,x} + \mathbf{E}_{2,x})\,\hat{\boldsymbol{x}} \;= \mathbf{E}_{TM}\,\mathbf{cos}(\theta)\left[e^{-ik_x x} + e^{ik_x x}\right]\hat{\boldsymbol{x}} \qquad \text{Eq. 2-16}$$
$$= 2\,\mathbf{E}_{TM}\,\mathbf{cos}(\theta)\,\mathbf{cos}(\mathrm{k}_x x)\hat{\boldsymbol{x}}$$

However, combining equations 2-7 and 2-13, the interference pattern oriented in the z-direction is found to be:

$$\mathbf{E}_z(x) = (\mathbf{E}_{1,z} + \mathbf{E}_{2,z})\hat{\boldsymbol{z}} \quad = \frac{-ik_x}{k_0}\mathbf{E}_{TM}\left[e^{-ik_x x} - e^{ik_x x}\right]\hat{\boldsymbol{z}} \qquad \text{Eq. 2-17}$$
$$= -2\,\mathbf{E}_{TM}\,\mathbf{sin}(\theta)\,\mathbf{sin}(k_x x)\hat{\boldsymbol{z}}$$

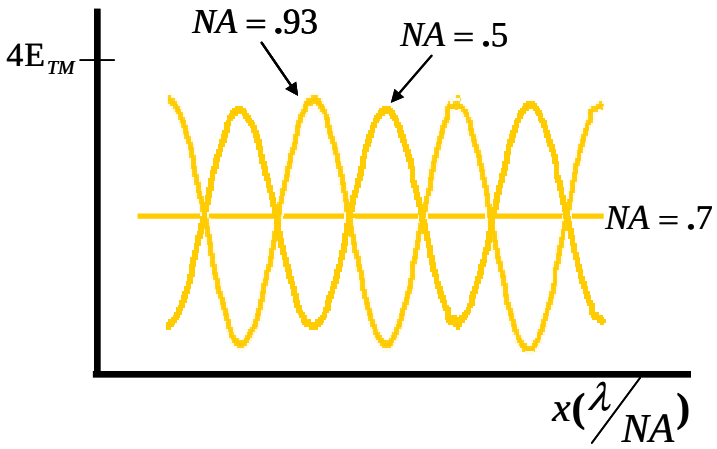

Figure 2-4. Image reversal due to high-NA vector effects

Two-beam interference patterns of equation 2-18 are shown only for the TM pupil components for various NAs.

Considering only the pupil TM component, the resulting intensity distribution in the image plane is then:

$$I(x) = \mathbf{E}_x \cdot \mathbf{E}_x^* + \mathbf{E}_z \cdot \mathbf{E}_z^* \quad = 4\mathbf{E}_{TM}[\cos^2(\theta)\cos^2(k_x x) + \sin^2(\theta)\sin^2(k_x x)] \qquad \text{Eq. 2-18}$$

where * represents the complex conjugate. Using this relation, the aerial image intensity distributions for NAs of 0.5, 0.7 and 0.93 are plotted in Figure 2-4. Due simply to the large angles of incidence of high-NA imaging, a complete reversal of the image may occur! Furthermore, this image reversal only occurs for one polarization component, the TM pupil component. At the very least, the TM component is responsible for degrading image contrast and will thus decrease exposure latitude, the tolerance for dose variation.

Thus, at high-NA, scalar theory breaks down and the true vector nature of light must be considered and it becomes critical to understand how each component impacts the state of polarization as light propagates through the optical system. To account for polarization effects, equation 2-3 can be expressed in vector form as:

$$\begin{bmatrix} E_x \\ E_y \\ E_z \end{bmatrix}_{Wafer} (u,v,a,Pol) = \frac{1}{\pi}\int_0^{2\pi}\int_0^{1} \begin{bmatrix} F_\perp & F_\parallel^{xy} & 0 & 0 & 0 \\ 0 & 0 & F_\perp & F_\parallel^{xy} & 0 \\ 0 & 0 & 0 & 0 & F_\parallel^{z} \end{bmatrix} \begin{bmatrix} P_{x\perp x} & P_{y\perp x} \\ P_{x\parallel x} & P_{y\parallel x} \\ P_{x\perp y} & P_{y\perp y} \\ P_{x\parallel y} & P_{y\parallel y} \\ P_{x\parallel z} & P_{y\parallel x} \end{bmatrix} \begin{bmatrix} J_{xx} & J_{xy} \\ J_{yx} & J_{yy} \end{bmatrix} \begin{bmatrix} E_x \\ E_y \end{bmatrix}_{Diff} e^{ik[\rho\cos(\theta)u+\rho\sin(\theta)v]} \rho d\rho d\theta$$

Source polarization | **Thin film (resist stack) effects** | **High-NA geometric effect** | **Pupil effects** | **Mask diffracted fields** | **Lens effect**

Eq. 2-19.

where all four matrices within the integral can be functions of field position (x,y) and pupil position (ρ,φ). The first three matrices within the integral can be though of as the polarization-specific transfer functions that effectively mondify the frequency content of the lens. They account for the polarization effects of a stratified resist stack, the vector rotation due to large angles of incidence at the image plane, and the polarization aberrations of the projection lens, and will be discussed further in Chapter 8. The fourth matrix represents the diffracted fields, which may also be dependent on the location (a(α,β)) and polarization (pol) of the illumination source point. Similar to equation 2-4, the total image intensity is then:

$$I_{wafer}(u,v) = \int_{source}\int_{pol} \left|\mathbf{E}_{wafer}(u,v,a,pol)\right|^2 dpol\, da \qquad \text{Eq. 2-20.}$$

where the integral over the source reflects the incoherent summation of intensity from orthogonal polarization components [19].

Thus, the final image and its through focus behavior result from a complex interplay of the angular distribution of the source, the source polarization, the scattering off of the photomask, the collection and redirection by the projection lens, and finally the refraction, reflection, and interference effects that occur within the resist stack. The operational principle of imaging with a Kohler illumination system that was discussed in the previous section remains valid. However, as in Figure 2-1H, the propagation of light through the optical system must be considered as a vector quantity in order to account for polarization-specific behavior.

It is noted that the imaging theory discussed in this section has followed the approach typically referred to as Abbe's method [1]. Although this method is conceptually easy to understand, it is from a computational standpoint very inefficient. Various techniques have been developed to more efficiently calculate the image intensity such as Hopkin's method [33] and Sum of Coherent Systems (SOCS) [13]. These are beyond the scope of this thesis, but have been studied extensively in the literature and are commonly employed in the industry to simulate lithographic effects.

2.1.2. Resolution enhancement techniques (RET)

In addition to decreasing wavelength or increasing NA, various methods have been developed to increase resolution and process latitude. A good theoretical discussion of RETs is provided by Wong [92]. Some of the key RETs recently employed by the industry are briefly mentioned here:

A) Phase shift masks (PSM). Equation 2-18 illustrates how the period of modulation on the wafer is related to k_x, the wavevector along the image plane. If $k_x = 0$, no modulation occurs. Thus, the 0^{th} diffraction order from the traditional imaging of a binary photomask with on-axis illumination, as seen in Figure 2-5, provides no modulation. It limits resolution in the image and should be avoided. One means to eliminate the on-axis 0^{th} diffraction order is with an alternating phase shift mask (Alt-PSM), shown in Figure 2-5b [47]. Since light travels faster in air than in glass, etching into the quartz substrate creates a local wavefront advancement and thus a local phase shift of the light that propagates through the shifted region. Etch depth (d) is related to phase shift (Φ) as:

$$\boldsymbol{d} = \frac{\Phi\lambda}{360(\boldsymbol{n}-1)} \qquad \text{Eq. 2-21.}$$

Etching a 180° phase shift in alternate open regions of a periodic grating causes destructive interference of the 0^{th} diffraction order. The resulting 2-beam imaging not only increases the resolution limit, but also increases depth of focus.

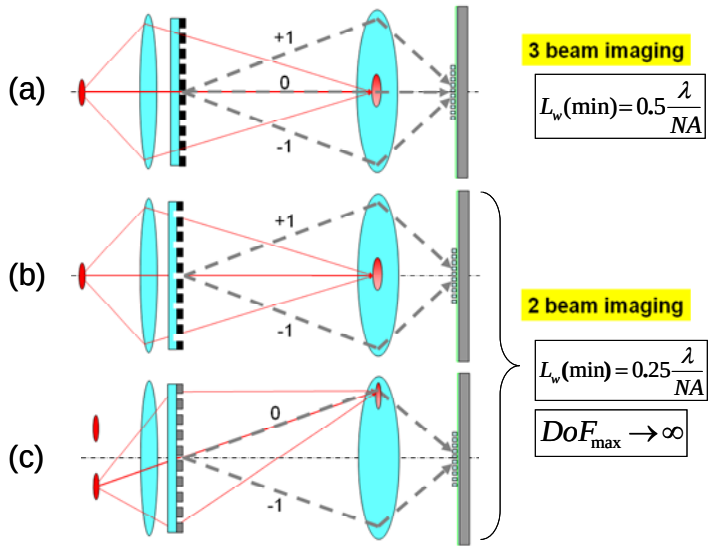

Figure 2-5. Resolution enhancement

Improvements in resolution and depth of focus over (a) traditional 3-beam imaging (on-axis illumination of a binary mask) is possible with 2-beam imaging by employing (b) phase shifting masks or (c) off-axis illumination.

Other phase shifting mask technologies, such as chromeless phase lithography (CPL) [35] and four-phase vortex vias [46] have been explored in the literature.

B) Off-axis illumination (OAI). Another means to eliminate low spatial frequencies in the image plane is to illuminate the mask with off-axis illumination, as shown in Figure 2-5c. The two-beam imaging in this case is provided by the 0^{th} and either the + or – 1^{st} diffraction orders. Thus, compared to the traditional case, pitches can be made twice as small on the mask. However a trade-off exists, as off-axis illuminators designed for one pitch typically have trouble printing others. This often limits the designer with what are termed forbidden pitches. Attenuated phase shift masks (Attn-PSM), in which the dark field consists of a material that provides a 180 degree phase while only transmitting about 6% of the field, are often used to balance the intensity between the two diffraction orders.

C) Immersion lithography. Traditionally, the photoresist and the last lens element of the lithography tool have been separated by air. However, filling this gap with a high index liquid enables light from high angular frequencies to more easily couple into

the photoresist. A simple application of Snell's law ($n_1\sin(\theta_1) = n_2\sin(\theta_2)$) shows the angles of incidence at the resist interface becomes relaxed. Thus, immersion increases the depth of focus – the tolerance allowed for the wafer to move with respect to the image plane. Secondly, immersion enables the creation of lithography tools with ultra-high or hyper (NA>1) numerical aperture. With immersion, the NA is defined as

$$NA = n_l \, \mathbf{sin(}\theta\mathbf{)} \qquad \text{Eq. 2-22.}$$

where n_l is the index of refraction of the liquid. NA can likely exceed 1.3 with water in the next few years and perhaps approach 1.6 or higher with a not-yet-identified high-index liquid or solid.

C) Polarized illumination. As derived in Section 2.1.1.2, the image created by the TM pupil component can be severely affected by high-NA vector effects. Thus, as tools are currently entering the market with NAs greater than 1, polarization has quickly risen towards the top of the lithographer's list of concerns [50][83][2][66][19]. Traditionally, illumination systems employed unpolarized light – where there is no preferential direction of the electric field when averaged over time. However, to accompanying the increases in NA, polarization control is being engineered into the illuminators of the state-of-the-art tools that are now entering the market. Generally, the goal is to use TE polarization and to limit TM light whenever possible and thus improve contrast and exposure latitude. A few examples from industry of polarized

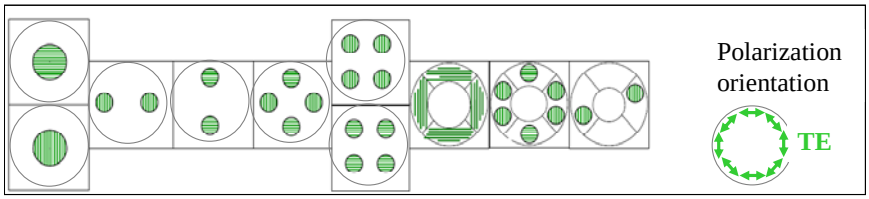

from ASML, Bernhard (Immersion symposium 2005)

Figure 2-6. Examples of various off-axis illumination schemes with polarized light.

off-axis illumination schemes are shown in Figure 2-6. An additional benefit of polarized illumination is the tendency for less line edge roughness due to the improved image log slope that accompanies improved contrast.

D) Optical proximity correction and sub resolution assist features. Optical proximity correction (OPC) fine-tunes the layout to counteract the loss of image fidelity due to proximity effects. Also, sub-resolution assist features (SRAF) are often added to manipulate proximity effects to optimize the diffraction pattern. These, and similar concepts have been described extensively in the literature and are only briefly mentioned here [13][63].

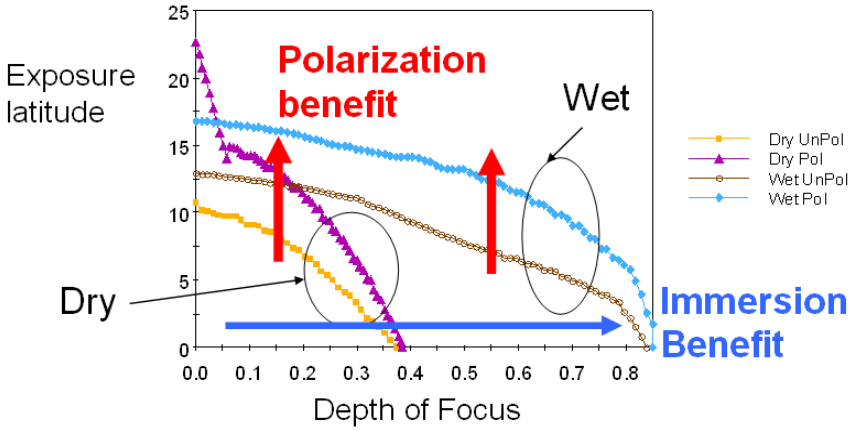

Figure 2-7. The primary benefits of immersion and polarization

Simulation conditions: NA=0.95, Dipole 0.9/0.7, 60nm equal line/space

The use of OAI and PSM technologies have enabled the k_1 factor to approach its theoretical single-exposure limit of 0.25. In addition to enabling the creation of hyper-NA tools, the use of immersion and polarization serve to increase the depth of focus and exposure latitude, respectively. The result, as shown in Figure 2-7, is an enlarged process window. With the help of OPC and SRAF, these RETs are responsible for enabling optical lithography to remain the workhorse of the industry down to the 45nm – and likely the 32nm - technology nodes; perhaps beyond. Considering this final feature size is less than $1/6^{th}$ of the wavelength of the light being used, this is quite an impressive accomplishment!

Component	Imperfection or characteristic	Effect	Impact on imaging	Reference	
Illumination Source	finite bandwidth	imaging with multiple wavelenths	image blur caused by chromatic aberrations (i.e. focus)	[8],[36]	
	intensity imbalance	loss of telecentricity	thru-focus image drift of larger features	[28],[70]	*
	finite min/max size	limits illumination frequencies	limits range of printable pitches	[5]	*
	source bright spots	some frequencies stronger than others	dose non-uniformity among different pitches	[14]	*
	polarization not to specification	loss of image contrast	decreased exposure lattitude	[50],[19]	*
	polarization imbalance	H-V contrast difference	H-V image bias	[50],[19]	*
Condenser optics	condenser aberrations, misalignment	alters local effective source (across mask or from design)	loss of stationary imaging, through-focus issues, etc.	[28]	*
	polarization dependent coatings, birefringence…	polarizaton aberrations	polarization-dependent effective source		*
Photomask	electromagnetic-interaction with 3-D mask topography	transmission imbalance of shifted regions	CD error, image placement error	[34]	*
		effective phase error	through-focus CD and image placement error	[22]	*
		polarization-dependent diffraction	H-V bias, CD error, etc.	[18]	
		incident angle dependent diffraction	variation in behavior of pitches	[72]	
		Mask error enhancment (MEEF)	amplify across mask CD error	[71]	
	mask making errors			[17]	
	feature size error		CD error		*
	phase etch error	no complete destructive interference of 0th order	through-focus CD and image placement error	[22],[87]	*
	side-wall angle	amplify imbalance effect	CD error	[10]	
	alignment error	layer-to-layer misalignment	various issues with device		
	pellicle polarization-dependent transmission	effective source variation for each polarization	H-V bias	[73]	
	Mask blank stress	plate birefringence	field dependent HV bias	[89]	
Projection optics	material or polishing non-uniformities, misalignment	Scalar aberrations	image placement, CD error, through-focus issues, etc.	[7],[78]	
	finite NA	Loss of high-frequency information	inability to perfectly replicate mask pattern		
	polarization dependent coatings, birefringence…	Polarization aberrations	double image with various effects	[79],[88]	*
	roughness	Optical flare	loss of contrast, image slope, exposure latitude, etc.	[45]	
Immersion	bubbles, watermarks, defects, heat gradients, etc	various	various		
Resist	resist and stack thickness or material variations	variation in standing waves, spherical aberration, dose to clear, etc.	across field or wafer CD error		
	polarization-dependant reflection (Fresnel)	TM generally couples better into resist at large angles	loss of constrast with TM, pitch dependance	[20]	
Wafer	wafer drift from focal position, non-planar wafer	Defocus	Image blur, CD error	[93]	
	wafer topography	feature-dependent defocus, reflective knotching, etc.	Across field CD error	[31]	
	large angles of incidence	TE vs. TM behavior	loss of constrast with TM	[20]	

Table 2-2. Common imaging non-idealities and some of their primary effects. The * identifies the effects monitored in this dissertation.

2.2. Characterization of Photolithography

Various imperfections may arise during the manufacturing, maintenance or usage of a lithographic projection printing tool. Depending on the nature of these imperfections, they may have important consequences on imaging and should be closely monitored. This section will introduce in tabular format some of the common imaging non-idealities found in optical lithography, attempting to concisely describe their potential impact on imaging. Three of these non-idealities that are especially relevant to this thesis will be explored in slightly more detail. Next, the concept of test reticles will be described and after a brief discussion of the test reticle market, the general concept of the phase shift mask monitors developed in this dissertation will be introduced.

2.2.1 Common imaging non-idealities

Table 2-2 lists a variety of imperfections that may exist in an imaging tool and comments on their effects and how they may impact imaging. For the interested reader, references for more information are listed for each topic. As they are relevant to this thesis, three of these will be discussed in more detail: condenser lens aberrations and source imbalance, electromagnetic interaction with mask topography, and mask making limitations.

2.2.1.1 Condenser lens aberrations and source imbalance

The illumination pupil-fill, which represents the directional distribution of plane waves incident on the mask, can often deviate from design due to condenser lens aberrations, condenser lens apodization, a misalignment of condenser and projection systems, or from a non-uniform or unbalanced source intensity distribution. An illustration of how condenser aberrations may impact the source-image is shown in Figure 2-1I. The primary effect of an unbalanced source-image is a loss of system telecentricity, thus reducing depth of focus and process latitude. Attempting to monitor this source-image and how it may vary across the field is the subject of Chapters 2 and 3.

The extent that imperfect illumination effects imaging depends not only on the magnitude of illumination error, but also on the size and type of features being printed. Generally, illumination non-uniformity affects large features more so than small features.

As an example, consider a small, sub-resolution feature on the mask. Light incident on the small feature will diffract in all directions and energy will uniformly fill the projection lens. Thus, only the projection lens will determine aerial image placement, which will be centered where the projection lens chief ray meets the wafer (i.e. telecentric). However, if the feature is large, diffraction effects will be less significant and the energy centroid follows a narrow diffraction pattern in the direction of the aberrated condenser ray. Thus the aerial image placement, which is dependent on the intersection of this aberrated (non-telecentric) ray and the image plane, will drift with defocus. Finally, an intermediate sized feature will behave somewhere between the two cases described above. This general trend, however, becomes more complicated when the illuminator is specifically optimized for a particular feature size or orientation, such as when resolution is enhanced with off-axis illumination schemes.

2.2.1.2. Electromagnetic interaction with mask topography

A nuisance to the operation of any phase shifting mask technology is the electromagnetic interaction of light as it propagates through the three-dimensional mask topography. This interaction is an unavoidable constraint set by Mother Nature, manifest in the fundamental physics represented by Maxwell's equations and the boundary conditions associated with the particular topography.

Rigorous finite difference time domain (FDTD) simulation, where Maxwell's equations are solved iteratively, can predict with great accuracy this interaction quantitatively. However, its effects have been described qualitatively in various ways. Wong [95] observed that near material interfaces electromagnetic fields tend to concentrate in higher index materials. This results in what he first described as the imbalance effect between phase-shifted and non-shifted regions. Adam [3] offered two complimentary explanations for why fields concentrate in higher index materials near interfaces. First, he showed that since fields propagate faster in air than in glass, a 'shock wavefront' of Cherenkov radiation occurs down the air-glass interface. This creates Huygens' spherical sources near the boundary on the air-side prior to the glass-side. Thus, these sources radiate into the glass and their fields interferometrically interact with fields scattered from a nearby corner. In other words, fields are 'sucked' into the higher

index material. The net effect is a plane wave propagating into the glass at an angle determined by the ratio of refractive indexes ($\phi=\arcsin(n_{air}/n_{glass})$. Alternately, this can be described in the context of total internal reflection, where the material interface serves as a one-way valve for light propagating at certain angles. All propagating waves may cross from the air to the glass, but only waves at angles greater than the critical angle may traverse from the glass to the air side. Likewise, the normally incident plane wave that propagates parallel to the boundary will induce the field on the glass side to 'take off' at an angle equal to the critical angle. This critical angle turns out to be identical to the one derived from Cherenkov radiation.

The net effect of this unavoidable electromagnetic interaction is a distortion of the fields transmitted through the photomask compared to the ideal thin mask case. Depending how these distorted fields propagate to the far field, this effect can have a sizable impact on how the mask pattern images into photoresist. The 3-D topographies of the PSM monitors developed in this thesis are generally much more complex than standard photomasks for I.C. manufacturing. Thus, great attention must be paid to understanding these effects and the manner in which they affect the practical application of the PSM monitors. TEMPEST [85] and SPLAT, an FDTD simulator and an aerial image simulator which were both developed at UC Berkeley – or Panoramic Software [98], a commercialized version of the two, are often used in this dissertation to investigate these effects. Comparison of thick mask (TEMPEST) simulation to a thin mask simulation reveals the extent that EM effects play.

2.2.1.3. Mask making limitations

In addition to the limits of Mother Nature, the limits of mankind's ability to faithfully fabricate the correct mask topography present additional – and often more debilitating – constraints on imaging. As will be shown numerous times throughout this thesis, the randomness inherent to the mask fabrication process appears to be, at present day, the primary limitation of many of the monitoring techniques developed. However, in some cases, reasonable monitoring is achieved by first manufacturing the mask to the best tolerances possible and then calibrating the test mask to filter imperfections from the measurement data.

It is noted that the monitors developed in this thesis are non-standard for state-of-the-art mask fabrication. The four-phase chromeless topography with sub-wavelengh features presents unique challenges to the mask maker. The test reticles fabricated and donated to UC Berkely by both Photronics and Toppan were generally made within the specifications required by today's IC industry. However, since many of the monitors operate by maximizing proximity effects at a single image location, they tend to amplify inevitable imperfections in mask making.

2.2.2. Test reticles for lithographic characterization

Many techniques exist to characterize the various components of a lithography system such as interferometry, scatterometry, atomic-force metrology, ellipsometry, etc. However, most techniques that are effective at quantifying the imperfections in a single element of the system require they be done before tool assembly, or perhaps during disassembly for tool maintenance. Furthermore, the details of the imperfections of a single component are often irrelevant, as the components functionality ultimately depends on how it interacts with the rest of the system. Thus, the use of *in-situ* monitoring, where the characteristics are extracted from a fully assembled tool, is generally the most useful and trusted characterization approach.

Most modern scanners come equipped with a series of on-board monitors to enable periodic characterization of various effects. However, it is usually preferred to also have an independent characterization method that can be used to compare the performance of multiple tools and to track their behavior over time. Since the end user of a tool typically only has access to the wafer and reticle stages, the use of test reticles – special test masks that contain arrays of patterns designed to be each sensitive to a single effect – are generally the method of choice. Somewhat related are test reticles used in conjunction with OPC, where arrays of layout-like clips are imaged to help calibrate imaging models used in OPC.

2.2.2.1. The test reticle market

Although test reticles are commonplace in the semiconductor manufacturing and are critical in maintaining acceptable lithographic performance, the test reticle market is a

relatively small and diffuse market sector within the semiconductor industry. By one estimate[1], the market size is roughly $20M/year and has generally had a steady growth of about 10-20% per year for the past twenty years. However, the variety of sources for test reticles - and types of end customers - makes a strict definition and size of the market hard to assess.

Test reticle suppliers generally fall into one of four categories. First, there are two companies who are primarily in the business of designing and selling test reticles: Benchmark Technologies, Inc. and Litel Instruments, although they generally do not have competing product lines. Benchmark sells a large suite of products aimed at enabling the repeatability and stability of various lithographic qualities across the imaging field, from tool-to-tool, or over time [96]. Litel offers two product lines, one for quantifying projection lens aberrations and one for characterization of the illumination angular uniformity and distribution (also referred to as the source-image, which is also the aim of the monitors described in Chapters 3 and 4 of this thesis) [97]. The second category of test reticle suppliers are the companies that manufacture and sell the lithography tools, with ASML, Nikon, and Canon being the primary vendors. Their presence in the test reticle market is not necessarily to obtain revenues directly from test reticle sales, but to serve as an enabler for the much more high-dollar sales of lithographic scanners, which may cost in excess of $30M per tool. As resolution requirements become more advanced and customers are made aware of the impact that a particular tool component may have on imaging capability, they tend to demand more monitoring capabilities be included with a scanner purchase. Aside from the occasional replacement part, these test reticles are typically included with the price of the scanner. In some cases, these equipment vendors may include reticles from a reticle vendor (i.e. ASML sometimes sells Benchmark products with a scanner).

---

[1] Most information in this section is from a conversation between the author and Patrick Reynolds, President and co-founder of Benchmark Technologies, Inc.

The third source of test reticles in the industry are the electronic design automation companies who provide the software used to design layouts and prepare them for the manufacturing flow. As real manufacturing data is critical for the models that underlie their algorithms, they often design and distribute test reticles to calibrate these models. Again, they are supplied not necessarily as a source of revenue, but to enable software sales. Finally, the fourth source of test reticles is much more difficult to quantify, consisting of any company with the capability to design and fabricate a reticle with test patterns. For instance, most of the larger semiconductor manufacturers create their own test reticles in-house to some extent. Depending on their capabilities and resources, it may be cost effective to make their own, rather than to buy from a reticle vendor.

Aside from the obvious semiconductor manufactures, there are a variety of potential customers for test reticles. Equipment vendors, photoresist suppliers, software developers, universities and others all may have needs for specialized reticles. Additionally, there are a variety of adjacent markets where the expertise of a test reticle vendor, such as Benchmark, is useful. For example, they often leverage their knowledge of the intricate mask manufacturing flow to provide other services for reticles or other precision optical elements. Additionally, there are often synergies with the adjacent test wafer market (specialized wafers for calibration of wafer fabrication equipment such as plasma etching, chemical-mechanical polishing, etc.).

The sales and customer support aspect of the test reticle market is highly technical, often requiring individual attention and the development of a customized product. In some cases, accompanying software is required to analyze measurement data; however, the software is generally not a separate product and the two are bundled into one product solution. More capable customers often prefer to develop their own software and data reduction techniques that abide by their processes. Although it can often be argued that a test reticle product may save the customer billions of dollars by increasing yield, the pricing of test reticles is generally limited to the cost of the reticle, plus a small margin. Thus, test reticles likely fall in the range of $5,000 to $150,000 each, depending on the complexity and level of engineering effort required.

Finally, it is noted that – at least from one vendor's perspective – intellectual property (IP) enforcement has not been a primary concern within the semiconductor industry for the past decade or two. Generally, the money saved by infringing on IP for test reticles is likely not worth the risk of being labeled with the resulting reputation, if caught. However, as in most high-tech markets, the rapid emergence of China is steadily strengthening concerns over IP protection.

2.2.2.2. Test reticles designed and fabricated for this thesis

To improve feature resolution and process robustness, the photomask has undergone evolution from a simple binary chrome-on-quartz stencil to more complex structures such as the phase shift mask (PSM). As discussed earlier, in a PSM, selective etches into the quartz improve imaging by manipulating the scattered wavefront. The monitors developed in this thesis take this one step further. As indicated in Figure 2-8a, patterns in chrome are combined with multiple phase etched regions. This engineers a wavefront that creates an image-plane response sensitive to only the desired optical effect. Data is then collected from the images that are formed in the photoresist. A sample mask topography and corresponding mask layout is shown in Figure 2-8b. Colors refer to the amount of etch into the quartz and thus, the phase shift of the local wavefront, as was quantified by equation 2-21.

As a contribution to the Feature Level Compensation and Control grant, a University of California Discovery Project, both Photronics, Inc. and Toppan Photomasks (formerly Dupont Photomasks) periodically donate an industrial-quality photomask. This has been a critical component of this thesis and has enabled the experimental verification of the scientific principles of the monitors developed in this thesis. Furthermore, it has helped in estimating the achieved and potential future capabilities of these monitors in light of the non-idealities due to realistic imaging conditions previously discussed in this chapter.

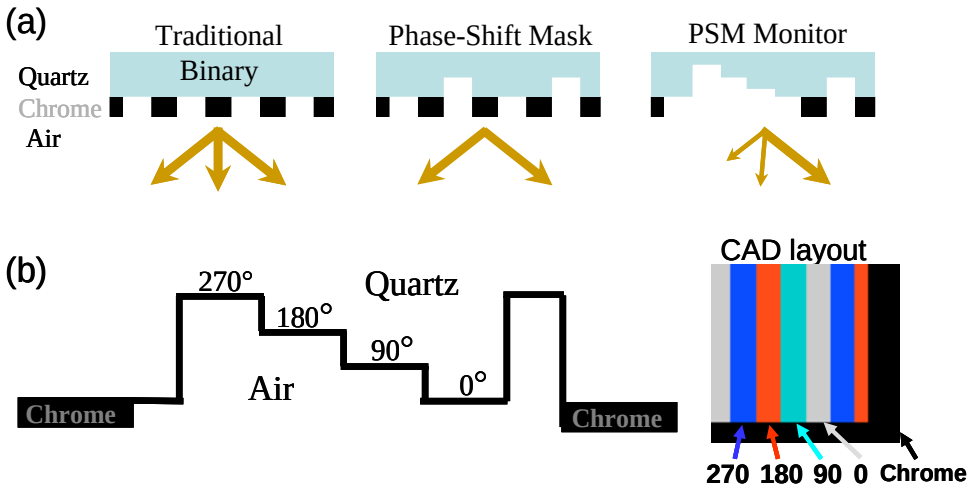

Figure 2-8. Concept of PSM monitors

(a) Evolution from binary mask to PSM monitors. PSM monitors engineer a wavefront for sensitivity to an optical effect. (b) Depth profile and CAD layout of 4-phase topography.

The three test reticles shown in Figure 2-9a have been designed by the author and have integrated not only the monitors discussed in this dissertation, but have encompassed the work of about fifteen students from various research areas within semiconductor manufacturing. An overview of the three reticles is provided in Table 2-3.

Test Reticle	Manufacturer	λ(nm)	NAs	Purpose	Experiments conducted at:	Notes
A	Photronics	248	.5-.8	illumination monitors (LPG, LPR) PSM performance (IPM) others (aberrations, CMP, metrology, resist, plasma etch)	ASML Photronics UCB microlab	* 4-phase * all Cr removed first * 180&270 etched first
B	Photronics	193	0.5-1.4	polarization monitors (RPG) illumination monitors (LPG, LPR) PSM performance (IPM) others (aberrations, shuttle design, flare, fogging, CMP, scatterometry, resist)	Nikon Photronics AMD	* 4-phase * all Cr removed first * 90&270 etched first
C	Toppan	193	0.93	polarization monitors (PEPA) others (aberrations, scatterometry, shuttle design, polarization-sensitive layout clips)	Nikon Toppan AMD	* backside pinhole array * 4-phase * Cr removed as needed * 90&270 etched first

Table 2-3. Test reticles designed and fabricated for this thesis.

The basic fabrication procedure for the four-phase topography is shown in Figure 2-9b. With traditional top-down processing, it takes $N = \ln_2 S$ process steps to produce S

phase regions [64]. The four phase regions of the original design are fractured into two process steps, one consisting of the 90 and 270 region and the other consisting of the 180 and 270 region. The example in Figure 2-9b shows the 90-270 region patterned and etched first to 90 degrees; followed by the 180-270 region patterned and etched another 180 degrees. Note that is possible also to reverse the order of the two process steps. In either case, the final mask topography will be subject to the ability to align these two process steps. Misalignments of 3nm to 60nm were observed in the three test reticles. The chrome may be etched first all at once (as in the Figure), or the chrome can be removed as needed in order to use it – whenever possible –as the etch mask for each phase etch. The three reticles in this thesis were made with three variations of this process, as outlined in Table 2-3. For reticles A and B, the chrome was patterned with electron beam and etched, then each subsequent phase etch was patterned with a laser write tool. Reticle C, however, used electron beam to pattern each phase etch region and used chrome as the etch mask whenever possible. This resulted in slightly better pattern fidelity and less alignment error between process steps.

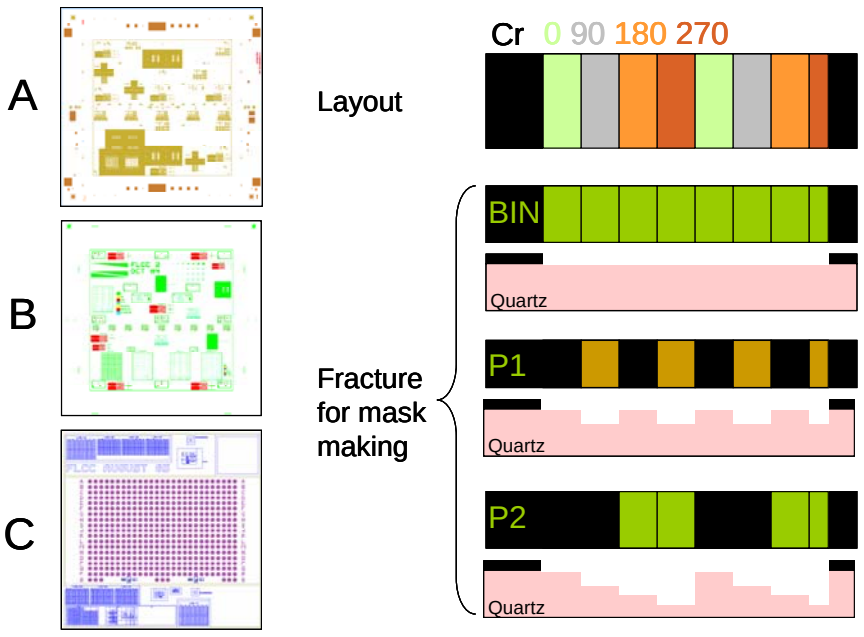

Figure 2-9. (a) Three test reticles designed and fabricated for this thesis. (b) Sample process flow to fabricate 4-phase topography.

Finally, it is possible also to construct the multi-phase mask topography with a direct-write strategy instead of with conventional mask making procedures. For example, electron-beam can be used to directly write patterns in a substance such as hydrogen silsesquioxane (HSQ), a spin-on-glass which behaves like a negative photoresist. HSQ becomes insoluable upon exposure and remains intact after development. Since this spin-on-glass has optical properties that closely resembling silicon dioxide or quartz, it can be used as the basis for creating phase shifting mask patterns. Thus, the phase-shifting monitors developed in this thesis could potentially be added to a traditional photomask with a one-step process. Researchers at MIT have employed this strategy to directly write phase shifting zone plates in the development of a maskless lithography technique [84]. This author, in research for a Masters degree [62] investigated this with some success for the linear phase rings discussed in Chapter 2.

3 Monitoring Illumination 1: Linear Phase Grating

In this chapter, a phase shifting mask pattern consisting of a linear phase grating is introduced as a potential tool to measure or monitor illumination angular distribution and uniformity in optical projection printing. An implementation as simple as four phase steps serves to steer the illumination into and out of the pupil at an angle determined by the period of the grating. The total intensity captured within the pupil is recorded in resist, allowing for a fast analysis of the illuminator's fill of the pupil. The advantage over existing techniques lies in the fact that the analysis of the source has been transferred to the design of the mask pattern, where multiple gratings are used to sample various portions of the illuminator. Illumination pupil-fill may be monitored across the field, tool-to-tool, or over time, or can be compared to the intended design.

This chapter begins by providing a brief historical account of other methods developed to monitor illumination. An alternate monitoring technique based on the Linear Phase Grating (LPG) is then introduced and discussed, assuming ideal diffraction from the four-phase grating. Experimental results at 193nm and 248nm wavelengths are then shown to validate the technique's scientific principles as well as to uncover unavoidable non-idealities due to realistic imaging conditions. The primary non-idealities are the electromagnetic interaction with mask topography, mask making imperfections, and a signal-to-noise ratio inherent to the LPG operation due to imaging with partially coherent imaging. These limitations are explored and various techniques are proposed to compensate for them in both design and data analysis. Additionally, a calibration and measurement procedure for the practical application of the LPG illumination monitor is outlined based on a modified version of Abbe's method. Finally,

it is concluded that due to mask making requirements and the angular-frequency dependence of the grating's diffraction efficiency, this technique is primarily useful for monitoring intensity balance in dipole or quadrupole illumination schemes. Although it will likely not outperform existing commercially available techniques, an understanding of the LPG provides a useful background for the other illumination monitor and the polarization monitors discussed in Chapters 4 and 5.

3.1. Historical evolution and existing techniques

Goodman and Rosenbluth offer an excellent background of the need for illumination monitoring in their 1988 discussion of the impact of condenser aberrations in Kohler illumination [28]. Here, they introduce the concept of the local effective source and discuss further how condenser lens aberrations can degrade system telecentricity. In the mid '90s, Borodovsky first proposed evidence that variations in the local value of partial coherence were responsible for across chip linewidth variance [5]. The local value of partial coherence is also referred to as sigma, the pupil-fill, or the source image, and is a measure of the spatial extent that the illuminator fills the pupil. By comparing simulation to experimental results, Borodovsky showed the influence that variations in sigma had on different features, noting the discrepancy between isolated and nested lines. He proposed a technique to measure sigma with a test pattern, called the proximity structure, consisting of periodic lines and spaces of a single linewidth and variable pitch. The printed linewidth's behavior through pitch depends on sigma, thus sigma is determined by comparing printed proximity structures to simulation. The result was a 'coherence map' of the field and helped explain across chip linewidth variance unexplainable by other phenomena.

Soon thereafter, Progler and Kirk offered additional support that the illumination pupil fill must be closely monitored and presented a measurement technique based on the useful concept of the pinhole camera [74],[41]. An out of focus pinhole, usually on the backside of a standard photomask, helps to create an image of the pupil-fill on the wafer. As the pinhole is exposed through dose, a series of source-images are created in resist. These images are then photographed, digitized, and subsequently converted into a three-dimensional dose contour map. This contour map may then be integrated over to

determine the angular distribution of the illuminator's fill of the pupil. Additionally, clever variations of the pinhole camera have emerged, such as Sato's grating pinhole [80], and Litel's Source Metrology Instrument [48]. Although some resolution is lost via the limitations of the pinhole camera and its convolution with the source-image, these techniques generally give a fair description of the source after compilation of and integration over the dose contour map.

Although the pinhole camera technique is most prevalent in industry, other methods have been reported in the latter half of the 1990s. For example, Grodnensky proposed a variation of the proximity structure that takes advantage of the internal focus detection system of a Nikon stepper to automatically measure the height of periodic diamonds, which is sigma dependent [30]. Also, a phase shifting focus monitor developed by IBM was found to have a sigma-dependent behavior. Thus, at best focus, the monitor can detect variations in sigma across the field [75]. Additionally, Watson described a technique using multiple apertures at the source plane and an image plane CCD to measure partial coherence. He concluded that a single number could not accurately characterize partial coherence (sigma). Rather, it varies across the field in a complex manner [90].

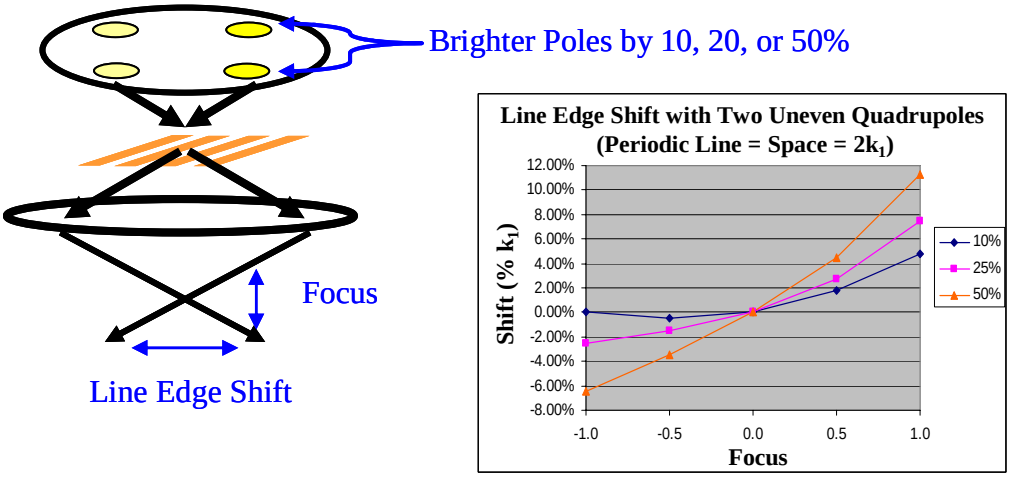

Figure 3-1: Effect of unbalanced source

Potential focus dependent shift of feature placement due to unbalanced quadrupoles. Feature is line = space = 2 x k1.

To illustrate the importance of balanced illumination pupil-fill, an example using quadrupole illumination is shown in Figure 3-1. Here two of the poles are brighter than the other two by either 10, 20, or 50 percent. Dense lines and spaces twice as large as the resolution limit allows are simulated. It is noted that process latitude is lost, seen as a focus-dependent shift of the feature placement. Thus, a line placement budget of 4% of the minimum feature size would require the poles to be balanced to within ±10%. Other consequences of improper illumination are shown in literature [5][74][41].

3.2. Linear phase grating (LPG)

3.2.1. LPG pattern derivation

The monitoring technique proposed in this chapter is based on the linear phase grating (LPG). Illustrated in Figure 3-2a, the LPG consists of four successive phase-shift regions, etched linearly in a chrome-less mask. The phase regions are etched to a depth according to the following relationship:

$$\boldsymbol{d} = \frac{\Phi\lambda}{360(\boldsymbol{n}-1)} \qquad \text{Eq. 3-1.}$$

where d is the etch depth in nm, Φ is the desired phase shift in degrees, λ is the wavelength in nm, and n is the index of refraction of the quartz. Since light travels faster in air than in the quartz, the wavefronts emerging from the three etched regions are advanced by multiples of λ/4 from the 0° region. Thus, this four-phase mask topography serves to diffract an incident plane wave into, ideally, only the +1 and higher orders. Notably, destructive interference from opposite and adjacent phases prevents radiation in the –1 or 0 orders.

Approximating the three dimensional structure as a two-dimensional thin mask, the ideal far field diffraction pattern due to coherent illumination can be derived as the Fourier transform of the mask function. With the four regions of the grating defined by the variables (A, B, C, D) in Figure 3-2b, the periodic thin mask M(x) is described by:

$$M(x)=\left[\begin{array}{l}|A|e^{i\varphi_A}\cdot \mathrm{rect}(\frac{x}{d_A}-\frac{d_A}{2})+|B|e^{i\varphi_B}\cdot \mathrm{rect}(\frac{x}{d_B}-(d_A+\frac{d_B}{2})) \\ +|C|e^{i\varphi_C}\cdot \mathrm{rect}(\frac{x}{d_C}-(d_A+d_B+\frac{d_C}{2}))+|D|e^{i\varphi_D}\cdot \mathrm{rect}(\frac{x}{d_D}-(d_A+d_B+d_C+\frac{d_D}{2}))\end{array}\right]\otimes comb(\frac{x}{P})$$

Eq. 3-2.

where |A|, and φ_A describe the amplitude and phase of fields after propagation through region A of the mask, d_A is the width of region A, and P is the period of the four phase grating. The far field diffraction pattern in frequency (*f*) space is thus:

$$O(f)=\left[\begin{array}{l}|A|e^{i\varphi_A}\cdot\frac{d_A}{P}\mathrm{sinc}(fd_A)\cdot e^{-i2\pi f\frac{d_A}{2}}+|B|e^{i\varphi_B}\cdot\frac{d_B}{P}\mathrm{sinc}(fd_B)\cdot e^{-i2\pi f(d_A+\frac{d_B}{2})} \\ +|C|e^{i\varphi_B}\cdot\frac{d_C}{P}\mathrm{sinc}(fd_C)\cdot e^{-i2\pi f(d_A+d_B+\frac{d_C}{2})}+|D|e^{i\varphi_B}\cdot\frac{d_D}{P}\mathrm{sinc}(fd_D)\cdot e^{-i2\pi f(d_A+d_B+d_C+\frac{d_D}{2})}\end{array}\right]\cdot\delta(f+n/P)$$

Eq. 3-3.

where $n=[\ldots -2,-1,0,+1,+2\ldots]$. Section 3.4.1 will revisit this analysis by approximating the diffraction from the three-dimensional topography with this thin mask approximation.

Given an incident scalar electric field E_0, the +1 diffraction order is thus

$$E_{+1}=t_{+1}\cdot E_0\,\mathbf{exp}(ik_x x) \qquad \text{Eq. 3-4.}$$

where t_{+1} is the +1 order scattering coefficient and the scattered wavevector ($\mathbf{k}_x$) is related to the incident wavevector ($\mathbf{k}_0$) and the period of the four phase grating as

$$k_x=k_0\,\mathbf{sin}(\theta)=\frac{2\pi\cdot M}{P} \qquad \text{Eq. 3-5.}$$

θ is the angle relative to normal that the +1 order is scattered into the pupil and is related to tool numerical aperture as

$$\mathbf{sin}(\theta)=\Delta r\cdot NA \qquad \text{Eq. 3-6.}$$

where $\Delta\boldsymbol{r}$ is the relative pupil shift in pupil coordinates. Thus, the period of the grating determines where the +1 order will be scattered into the pupil as:

$$P = \frac{M\lambda}{\Delta r \cdot NA} \qquad \text{Eq. 3-7.}$$

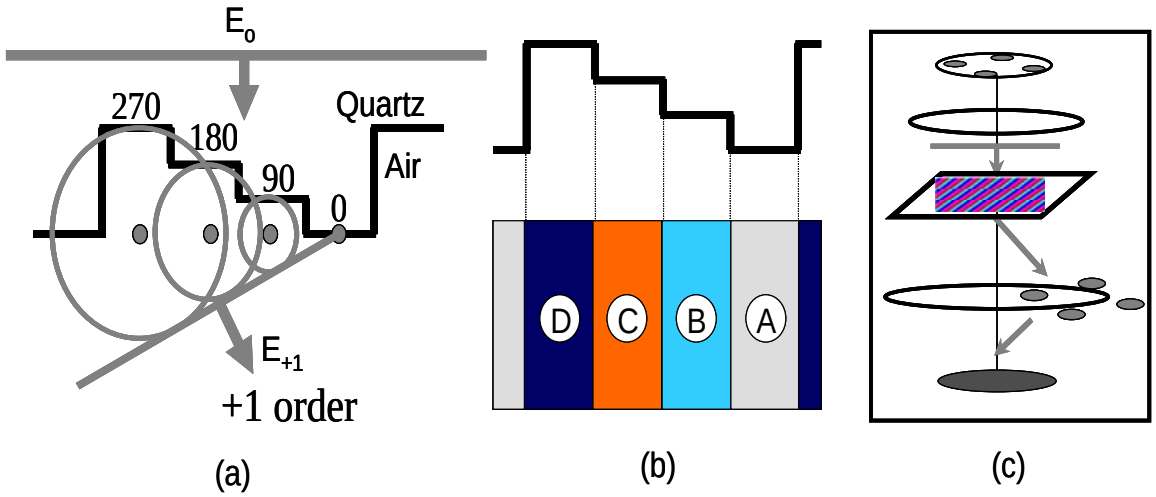

Figure 3-2. The linear phase grating (LPG)

The LPG (a) diffracts light into only the +1 and higher orders. (b) Thin mask approximation to 3-D mask topography. (c) The pupil is used to clip only a certain portion of the source-image depending on the orientation and period of the LPG.

3.2.2. LPG as an illumination monitor

Figure 3-2c shows an LPG at the reticle (object) plane directing a quadrupole illumination scheme into the pupil at an angle determined by the period of the grating. As discussed in Section 2.1.1, Kohler illumination systems are typically used in lithography to produce spatially invariant imaging. One condition of this illumination scheme is that the condenser optics form an image of the source in the projection lens entrance pupil, typically referred to as the source pupil-fill [28]. Thus, with an appropriate choice of the LPG period and orientation, the pupil is used as an aperture to clip a certain portion of the illumination pupil-fill. In the case of Figure 3-2c only one pole, which is ideally 25% of the illuminator, is captured within the pupil. This total intensity captured within the pupil is then recorded at the wafer plane via the clearing dose of the resist. The ideal measurement consists of simply determining whether or not the resist has cleared, since the incident radiation results from a single DC component from the +1 diffraction order.

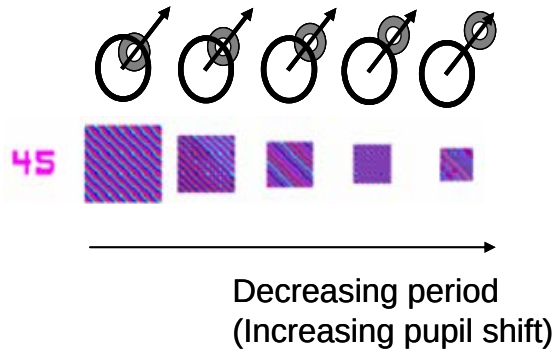

Figure 3-3. Concept of pupil shift

Multiple LPGs sample various portions of the illuminator depending on the period and orientation of the LPG.

To characterize the illumination pupil-fill, multiple LPGs are strategically placed on the mask with various grating periods and orientations. As in the example for annular illumination in Figure 3-3, each LPG serves to shift the pupil-fill by a different amount, thus measuring the intensity in a particular region of the pupil. Since the clearing dose of the resist depends on total intensity captured within the pupil, each LPG will clear at a different dose. This clearing dose for each LPG is recorded as the signal and used as either a quick check for source symmetry or to recreate the shape of the illuminator.

3.2.3. Mask design and resist through dose

The complexity of the mask design is dependent on the desired resolution of the measurement. A simple design to check for intensity balance of quadrupole illumination is shown in Figure 3-4a. Each of the four gratings consist of about 10 periods and are oriented such as to isolate and measure an individual pole. Assuming a positive resist, the four gratings will all clear simultaneously as the dose is increased if the poles are balanced, as in Figure 3-4b. However, if the poles are unbalanced, each grating will clear at a different dose (Figure 3-4c), directly proportional to the total intensity of that pole. Thus, a cursory inspection of a dose-matrix wafer with a low magnification optical microscope will determine if the poles are balanced. If they appear to be unbalanced, then the exact imbalance can be quantified by noting the dose at which each grating clears.

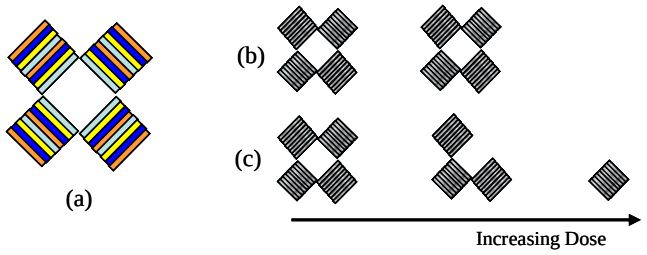

Figure 3-4. LPG Quadrupole Monitor

Four LPGs oriented at the 45°'s serve to isolate and measure individual pole intensities. Comparison between how the (a) mask pattern prints in resist with increasing dose for (b) balanced and (c) unbalanced quadrupoles.

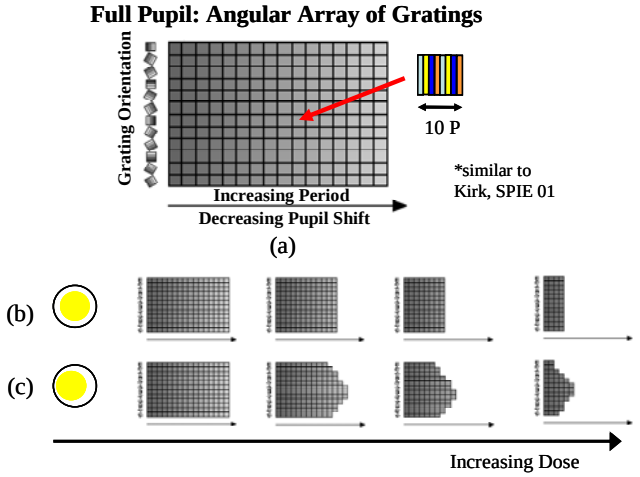

Figure 3-5: LPG full pupil-fill monitor

Angular array of linear phase gratings allow for a full-pupil measurement of illumination angular distribution. The (a) mask pattern prints in resist in a manner representative of the illumination distribution. Shown here is a comparison between a (b) symmetric top hat and an (c) asymmetric top hat.

A more complex mask design, such as the angular array shown in Figure 3-5 (inspired by Kirk, reference [42]), enables measurement of the full angular distribution of the pupil-fill. Each square of the array contains approximately 10 periods of a particular grating. Horizontally, the grating periods are increased such as to cause less of a pupil shift. Vertically, the orientations of the gratings are rotated as to 'walk' the illumination out of the pupil at multiple angles. As with the quadrupole monitor, the manner in which this pattern prints clearly displays source symmetry or asymmetry. Figure 3-5b compares

how the pattern prints through dose for a symmetric and an asymmetric top-hat source. With a symmetric source, each grating of a particular period will clear at exactly the same dose, regardless of its angular orientation. A non-symmetric source, however, will create corresponding non-rectangular resist images such as in Figure 3-5c.

3.2.4. Ideal geometric 'CIDOC' and source reconstruction

This section discusses reconstruction of the source from a series of resist images, assuming that a perfect geometric image of the source is created in the pupil by the +1 diffraction order. As the grating period is decreased, the spatial frequency of the +1 order will increase, resulting in a greater shift within the pupil. Thus, successively decreasing periods of the horizontal row of gratings in Figure 3-5 essentially 'walk' the illumination out of the pupil. With increasing pupil shift, the total intensity captured within the pupil declines. This information recorded in resist can be translated into a 'captured intensity drop-off curve' (CIDOC) as a function of pupil shift, wave number, or grating period, as shown in Figure 3-6. Rotation of the grating's orientation allows for the construct of multiple CIDOCs for various shift axes.

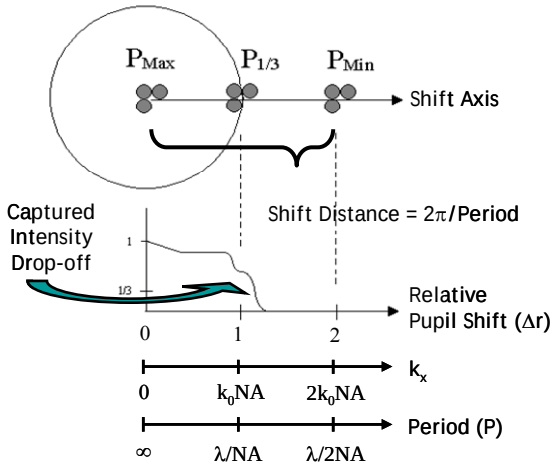

Figure 3-6: Captured intensity drop-off curve (CIDOC)

CIDOC created at a specific shift axis by multiple linear phase gratings with varying period.

Simulation of a fictitious three-pole illuminator clearly illustrates this principle in Figure 3-7. By shifting the unorthodox illuminator out of the pupil at various angles, a

series of CIDOCs are obtained. Analysis of these curves relays important information about the source and can be done in one of two ways. First, these curves can simply be compared to each other or to curves from other field locations, providing a fast, qualitative method to check for source symmetry and across field uniformity. Alternatively, analyzing the rate at which these CIDOCs decline allows for a quantitative analysis of the angular distribution of the actual pupil-fill. As shown in Figure 3-8, differentiating the ideal CIDOC results in a 'pupil-fill density profile' for a particular cut-line in the pupil. These profiles can be converted into a reconstruction of the source by modifying a technique often used in medical imaging, parallel beam reconstruction.

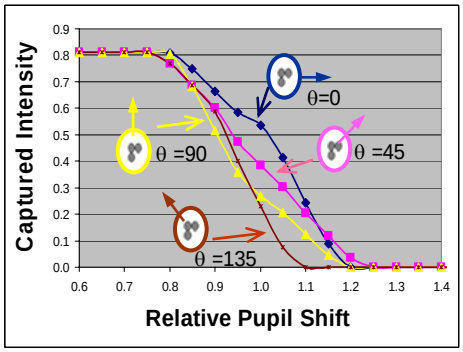

Figure 3-7: Simulated CIDOC example

Simulation of a fictitious three-pole illuminator gives a series of captured intensity drop-off curves for multiple shift axes.

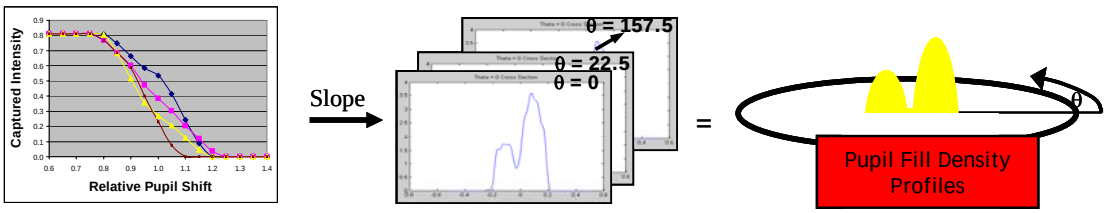

Figure 3-8: Pupil-fill density profile

Differentiation of the captured intensity drop-off curve gives a pupil-fill density profile for a particular cut-line in the pupil.

Parallel beam reconstruction is used to reconstruct the source-image from CIDOCs of multiple shift angles by taking advantage of the Fourier slice theorem. This

theorem states, “the Fourier transform of a parallel projection of an image *f(x,y)* taken at an angle θ gives a slice of the two-dimensional transform, F(u,v), subtending an angle θ with the u-axis.” In other words, we take the Fourier transform of the 1-D density profiles, back-project them onto a 2-D background, and then take the 2-D inverse Fourier transform to get the measured pupil-fill [40]. The accuracy of this reconstruction is clearly dependent on the number of gratings used.

To illustrate this reconstruction, a series of LPGs were simulated with SPLAT using the unorthodox tri-pole illuminator used as an example in this chapter. A thin mask approximation was used, producing a constant intensity at the wafer for each grating and thus creating an ideal geometric CIDOC. A Matlab script, written based on the Fourier slice theorem, then converted this series of LPG intensities into a reconstruction of the original source. An example of such a reconstruction from eight angles and a pupil shift increment of 0.05 is shown in Figure 3-9. Note that the algorithm used in this example assumes that the pupil-edge can be approximated by a straight knife-edge. This results in a decent reconstruction for the illuminator used in this example, which is confined to the center of the pupil. Source reconstruction for larger illumination schemes would require the 1-D density profiles to be compensated to account for the circular nature of the pupil-edge and for the back projection of their Fourier transforms be mapped onto a circular geometry.

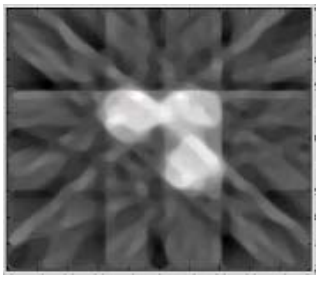

Figure 3-9: Reconstruction of the source using parallel beam reconstruction.

It is assumed then that as long as the ideal geometric CIDOCs can be obtained, an accurate reconstruction of the source – or more simply, a quick check of source symmetry - is possible. Of course, various realistic imaging conditions prevent

measurement of the ideal geometric CIDOCs. The remainder of this chapter will show some of these non-idealities and propose techniques to extract the ideal CIDOC from non-ideal data.

3.3. Experimental results

The mask pattern shown in Figure 3-10a was used to test this concept experimentally in a 0.63 NA scanner with a wavelength of 248nm and a 0.80NA scanner with a wavelength of 193n. Here, multiple LPGs are arranged with five different periods and six different orientations. Taking the top row of LPGs as an example and considering an annular illuminator with inner and outer radii of 0.3 and 0.6 pupil coordinates, the cartoon in Figure 3-10b shows how each grating serves to capture a different portion of the illuminator within the pupil. With the individual phase ledges, the smallest features of the grating, ranging from 525nm to 225nm for a 248nm wavelength, the illuminator is shifted out of the pupil between 0.75 and 1.75 pupil coordinates. Thus, each grating is expected to clear the photoresist at different exposure doses.

Figure 3-10c shows top-view images of sample LPGs on the reticle with a scanning electron microscope (SEM). Further detail from an atomic force microscope (AFM) measurements is seen in Figures 3-10d and 3-10e showing roughly the desired stair-step profile. The small lip on the 90 degree phase ledge of this chromeless phase boundary appears to be due to a small 35nm overlay error during the second phase etch. This, however, is well within the specification limits of the tool used to write the mask. It is of concern because it may cause orientation dependant imaging effects. Additionally, the fact that the 270 degree phase ledge in Figure 3-10e does not appear to reach a full 270 degree depth is likely an artifact of the 250nm AFM tip that was used, which was only slightly smaller than the trench being measured. Thus, no representative profiles of LPGs smaller than this one were possible.

The first experimental verification of the LPG was done on a Zeiss AIMSFAB248 Aerial Image Measurement System. Again considering the first row of LPGs in the mask pattern with annular illumination, Figure 3-10f compares aerial image cutlines through each of the five LPGs. As expected, the average intensity does decrease with increasing

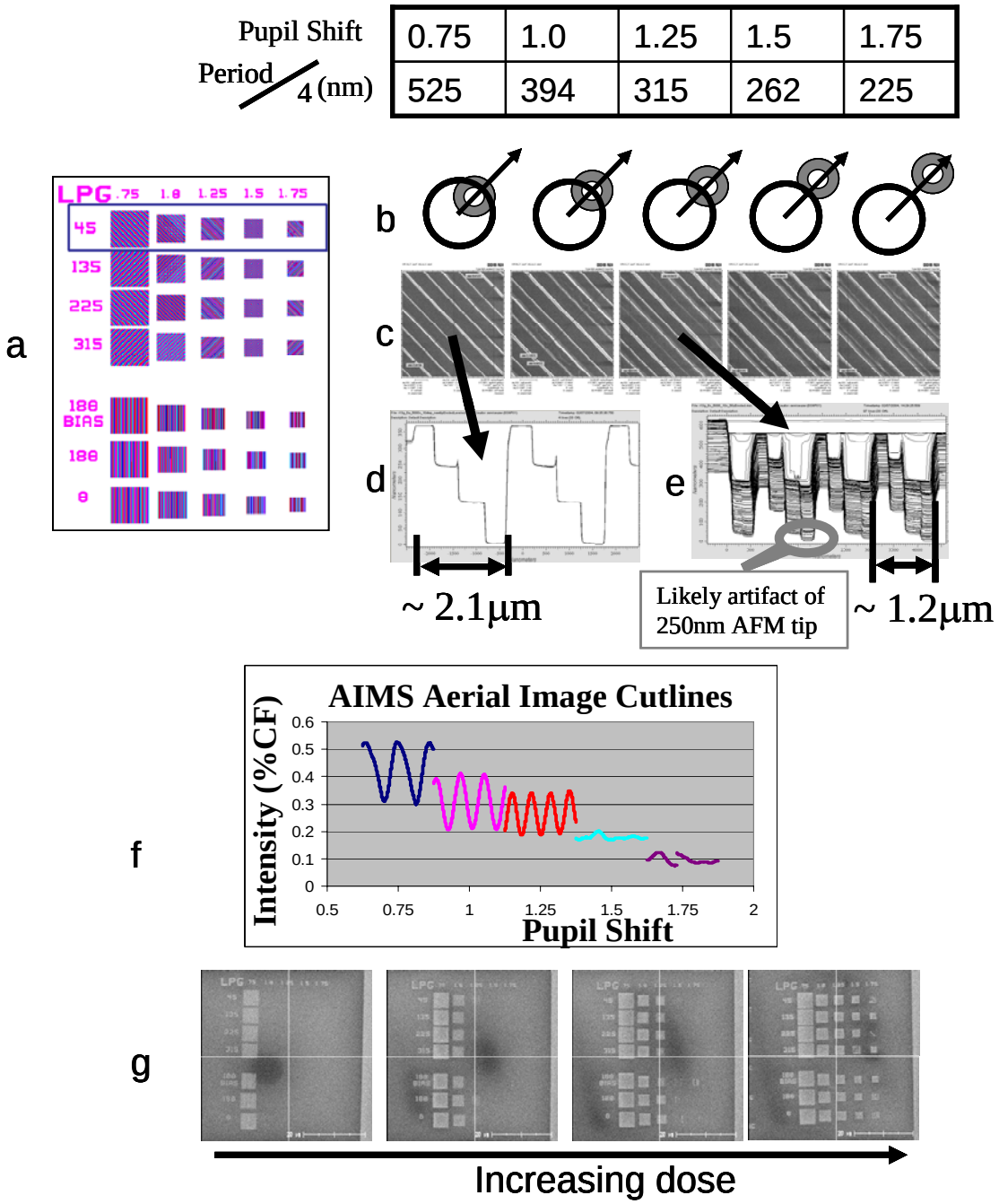

Figure 3-10. LPG experimental verification

(a) Mask layout consists of multiple LPGs of various periods and orientations each causing (b) a different portion of the illuminator to be captured within the pupil. (c) SEM and (d,e) AFM measurements confirm the desired stair-step profile, although some measurements were limited by the 250nm size of the AFM tip. (f) AIMS aerial image cutlines and (g) resist patterns printed with increasing exposure dose show the desired effect.

pupil shift. However, the contrast seen within the image is an unwanted effect and is due to a combination of the electromagnetic interaction of light with the three-dimensional mask topography and of the inability of the mask maker to fabricate a perfect topography.

These effects and ways to compensate for them are described further in the next section. One method to compensate for them is by simply biasing the geometry of the grating. This biasing was demonstrated with the fifth row of LPGs in this mask layout (Figure 3-10a), where enlarging the 270 degree phase ledge relative to the 0 degree ledge resulted in slightly lower contrast. It is also noted that, considering the size of the illuminator under analysis in this example, the two smallest gratings should diffract little or none of the annulus into the pupil. However, the roughly constant intensity in their images is likely dominated by the unwanted light in the -1 and 0 diffraction orders.

Finally, images in photoresist from a 4x ASML PAS 5500/800 KrF (NA = 0.63) scanner with this same mask layout are shown in Figure 3-10g. As expected, each of the gratings clear at different doses relative to the portion of the illuminator captured within the pupil. Thus, a quick method of monitoring source symmetry could be to compare the doses at which each LPG in a column (same period, different orientation) clear the resist threshold. Ideally, for an asymmetric source, some LPGs in that column should clear before others depending on the degree and orientation of the asymmetry.

Figure 3-11 shows a comparison of experimental CIDOCs from both AIMS measurements and printing in resist to SPLAT simulation for two illumination conditions. SPLAT simulation was conducted with a thin-mask approximation, thus the data represents ideal geometric CIDOCs. In both examples, there appears to be a good match when the period is above 1.3μm, or when the individual phase ledges (smallest feature) are slightly larger than a wavelength. The mismatch at smaller periods is likely a result of both electromagnetic effects and mask making limitations and will be discussed further in the next section.

Additionally, these patterns were used to investigate quazar and conventional illuminators resulting in similar conclusions. However, when considering the four LPGs

oriented at different diagonals (first four rows in Figure 3-10a) with quasar illumination, slightly different clearing doses were seen between the four gratings of the same period. However, for this uncalibrated data, comparison with an existing on-board ASML technique using the concept of the pinhole camera introduced in Section 3.1 led to the conclusion that mask orientation dependent effects were larger than the actual illumination imbalance. However, it appears as though, in this uncalibrated experiment, the LPGs were able to measure intensity balance among poles to within about 5%. Again, the next section will address this and show how pre-calibrating the test mask can account for this effect during data analysis.

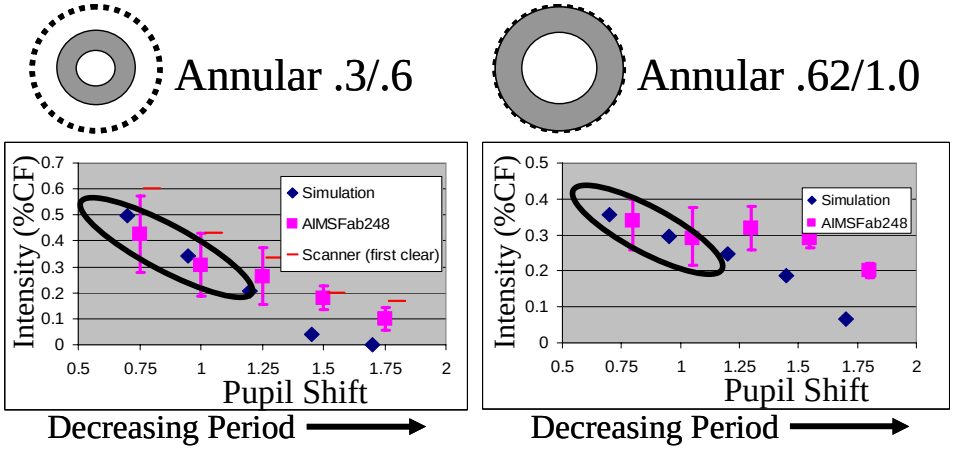

Figure 3-11. Experimental CIDOCS

Experimental results for two illumination conditions agree closely with simulation for periods lower than 1.3μm, or when the smallest features are roughly larger than a wavelength.

A primary advantage of this technique is that the patterns are sufficiently large and can be monitored with a low powered optical microscope. The analysis done in this section was primarily based on SEM measurements, but the patterns were easily seen with a microscope having a magnification of 10x to 100x.

3.4. Non-idealities and methods to compensate for them

As discussed in the previous section, various factors contribute to the non-ideal behavior of the LPG illumination monitor. This section explores the causes and impact of the three most significant non-idealities and discusses methods to either pre-

compensate the mask design or bias the experimental data to counteract these effects. Table 3-1 summarizes the three non-idealities and their primary work-arounds.

Non-ideality	**Primary compensation method**
Electromagnetic interaction with mask topography	3-D optical proximity correction
Mask making limitations	Experimentally calibrate diffraction orders
LPG signal-to-noise due to partially coherent illumination	Compensate signal based on SNR and MOD analysis

Table 3-1. LPG non-idealities and work arounds

3.4.1. Electromagnetic interaction with mask topography

Section 2.2.3.1 introduced the unavoidable electromagnetic (EM) interaction that occurs as light propagates through a three-dimensional mask topography. It was shown that fields are 'sucked' into the higher index material as light propagates down the material boundary. As LPG feature sizes are on the order of the wavelength of light they are designed for, understanding this EM effect is of great importance to understanding the practicality of the LPG illumination monitor. Unpolarized light is considered here. For a discussion of the polarization dependence of this effects, see Section 5.5.1.1.

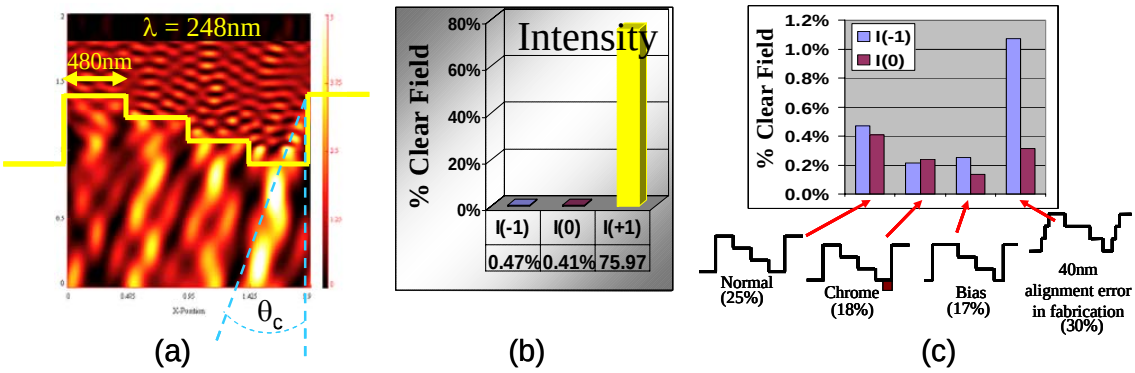

Figure 3-12. Electromagnetic interaction with mask topography

EM interaction with mask topography produces a bright spot at the foot of the 0° phase ledge in the near field. Induced off-axis wave propagation at an angle θc is observed within the glass and is described in the text. (b) Although intensity in the unwanted diffraction orders (0, -1) is small in the far field, interference effects produce unwanted contrast in the image. (c) Feature biasing or adding chrome are methods to reduce the unwanted orders.

A near field simulation using TEMPEST, a FDTD simulator developed at UC Berkeley [85], of a LPG is shown in Figure 3-12a. The simulation illustrates the manner in which fields are 'sucked' into the steep vertical sidewalls, resulting in a hot spot on the foot of the 0° phase ledge. Additionally, the off-axis angle of propagation is observed within the glass of the 0° region and is roughly equal to the critical angle of total internal reflection, as described by Adam [3].

The effect of this EM interaction is to diffract light into the unwanted 0^{th} and -1^{st} diffraction orders, as shown in Figure 3-12b. Although the intensities of these orders are only about 0.5% of that of the intended +1 order, they are sufficient to cause considerable modulation as light interferes on the wafer plane, as was seen in Figure 3-10f. Minimizing these unwanted orders will minimize the unwanted contrast in resist, thus minimize the experimental error associated with the LPG illumination monitoring technique.

The primary method to minimize these unwanted orders is to modify the 3-D topography either by biasing the feature sizes, adding chrome to balance transmission among regions, or by optimizing the phase etch depths. Figure 3-12c shows a slight decrease in the unwanted orders (and thus in the unwanted contrast) from simply biasing the features or applying chrome to portions of the 0° region. The third test mask designed and studied in this thesis, which is discussed primarily in Chapter 5 in the discussion of a polarization monitoring technique, employed a global optimum of the four phase etch depths.

Figure 3-13 compares the near fields and far field diffraction orders of a thin mask, a thick mask, and a thin mask approximation to the thick mask using the theory derived in Equation 3-3 with the parameters defined in the figure. Although the near fields differ greatly, the thin mask approximation produces similar amplitudes of the diffracted orders. The phases are not similar; however, it will be shown in section 3.5 that the phases are of secondary importance to the functionality of the LPG monitors.

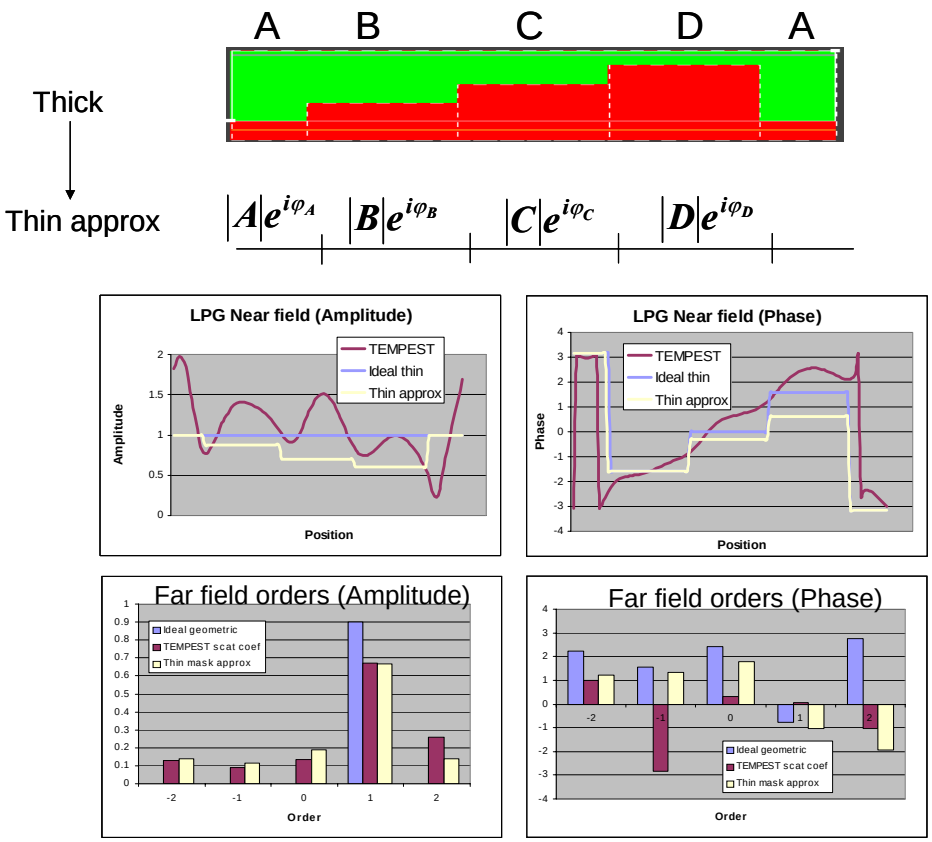

Figure 3-13. LPG thin mask approximation

(a) Approximation of thick mask scattered orders with the thin mask approximation described in Section 3.2 with (magnitude, phase) of regions A (1,0), B(0.87,0.5π), C (0.7,0.9π), and D (0.6,1.2π). Region dimensions are assumed identical. (b) Near field and (c) far field order comparison of TEMPEST, thin mask, and thin mask approximation. Far field order phase differences are shown later to be immaterial. Simulated parameters: P = 1.108um, pupil shift = 0.75, λ = .193, NA = .93, M = 4.

3.4.2. Mask making limitations

In addition to the EM interaction dictated by nature, another factor that deteriorates the diffraction efficiency of the LPG is the limitation of mankind to fabricate an ideal 3-D structure. LPGs were fabricated on three separate test reticles during the research for this dissertation, each with a slight variation of the fabrication process described in Section 2.2.2.2. As fabrication of four-phase reticles with a mixture of chromeless, alternating, and binary features is non-standard, the process was a learning experience for both mask manufactures (Photronics, Inc. and Toppan (Dupont) Photomasks). Many of the mask making limitations listed in Table 2-2 were observed,

although most fell within specifications of current state of the art photomask fabrication requirements.

Figure 3-14a attempts to deconvolve the relative impact of these mask making limitations with the electromagnetic effects described in the previous section. Comparing thin mask simulation to thick mask simulation of LPG behavior through pitch for annular illumination shows the relative impact of EM effects (solid line). However, comparing the thick mask simulation to experimental results from an AIMS tool indicates the additional degradation due to mask making limitations(dashed line). This analysis suggests that for this first test reticle, the primary limitation appears to be due to misalignment in the fabrication process, which is seen as a loss of pattern fidelity in Figure 3-14b. Misalignment was on the order of 30nm (reasonable for current state-of-the-art) for test reticle A and 50nm for test reticle B, which are evident from the extra quartz on the 90 degree phase ledge in Figure 3-14b. This misalignment appears to impact the electromagnetic performance of smaller features more so than larger features, as seen in Figure 3-14a.

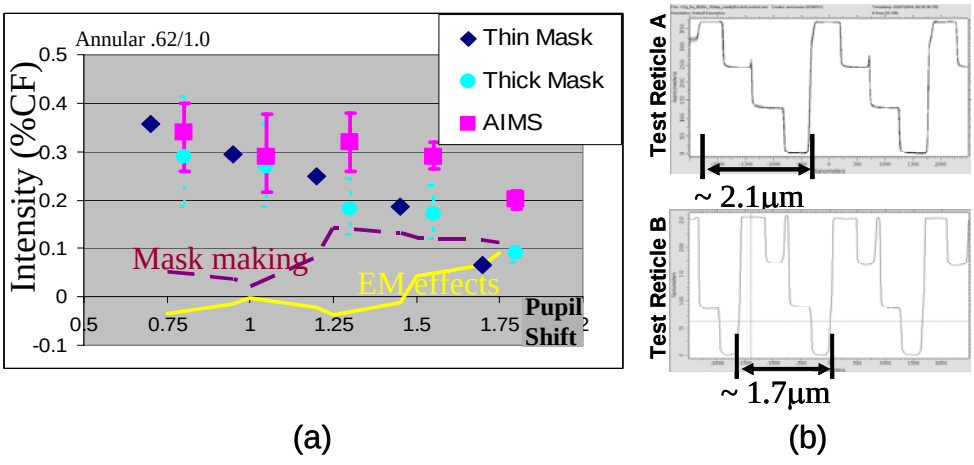

Figure 3-14. Deconvolving electromagnetic and mask making effects

(a) Comparison of thin mask simulation, thick mask mask simulation, and experimental AIMS results implies that mask making limitations are a larger effect than EM effects for this first test mask. (b) AFM measurements illustrate how misalignment in the mask fabrication process affects the 3-D pattern fidelity for test reticles A (~30nm misalignment) and B (~50nm misalignment).

Other than improvements in the mask making process, the primary means to account for these mask making limitations is to calibrate the test mask after fabrication. This can be accomplished either by analyzing the images of an LPG array with a series of known (calibrated) illumination states or – more likely - by measuring the diffracted orders on a lab bench with a laser source and a series of CCD detectors, similar to that described in [9]. Section 3.5 will describe how these experimentally determined diffraction orders can be used to bias the data for a more accurate measurement of the tool's illumination.

3.4.3. Effects of partially coherent illumination

In addition to EM effects and mask making limitations, an additional measurement error arises due to the use of partially coherent illumination. As shown in Figure 3-15a, the ideal LPG behavior produces a single diffraction order and thus a constant DC intensity in photoresist. However, the leakage of fields into the unwanted diffraction orders (from a combination of EM and mask making effects) produces modulation at the wafer. This is due to the coherent interference of orders captured by the pupil from a single source point and is as shown in Figure 3-15b for an arbitrary source point within an annular illumination scheme. However, the final image intensity is the sum of the image intensities of all incoherent source points (Figure 3-15c). Thus, the deviation of the final image intensity from the ideal DC intensity will also depend on the angular distribution of illumination frequencies used – since the orders captured by the pupil will vary for different illumination frequencies. The next section will describe a procedure to account for these three primary non-idealities by compensating the measured signal to estimate the ideal geometric signal.

3.5. LPG calibration and measurement procedure: modified Abbe's theorem

This section will describe a procedure for calibrating the test mask and finding the best estimate of the ideal DC (geometric) signal for each LPG exposed with an arbitrary illumination scheme. A modified version of Abbe's theorem [1] is used to calculate the image intensity from experimentally determined diffraction orders. By comparing this intensity distribution to the DC signal expected with just the ideal +1 diffraction order, a procedure is derived to convert the measured signal (lowest dose where photoresist

begins to clear) into the compensated signal. The compensated signal is the estimate of the ideal geometric signal, which can then be used to either reconstruct the source or to check for source symmetry following the methods described in Section 3.2.4. Calibration of the test reticle is critical to filter out artifacts of the measurement such as orientation and polarization dependent effects.

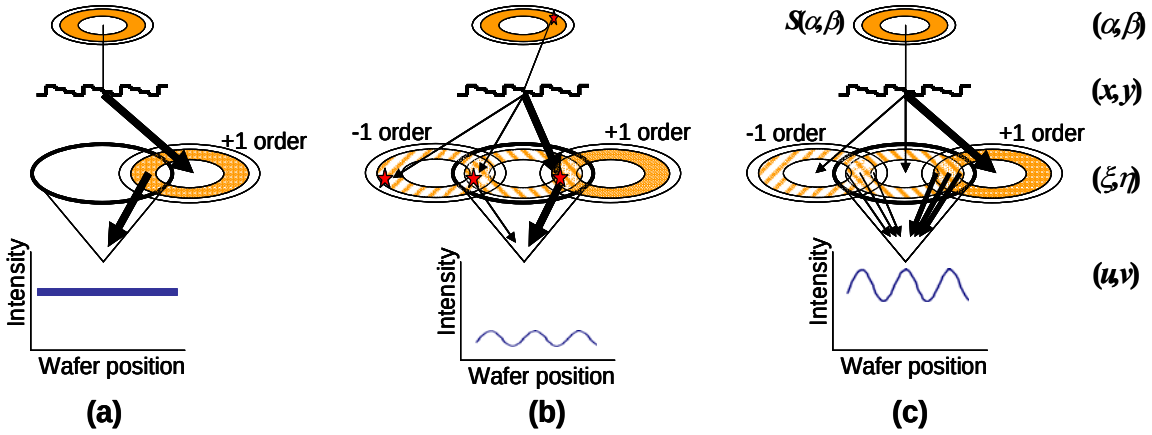

Figure 3-15. LPG analysis with modified Abbe's method

(a) Ideal LPG behavior produces only a +1 diffraction order and DC intensity at wafer. (b) Mask topography effects and mask making limitations couple light into the unwanted (0, -1) orders. The resulting image plane interference of orders captured by the pupil from diffraction from each source point causes modulation at the wafer. (c) The net image intensity is simply the sum of image intensities from each incoherent source point.

Step 1: Measure scattering coefficients: First, the magnitudes of the lowest five polarization-dependent scattering coefficients are determined experimentally, in a manner similar to that described in reference [8]. Although the coefficients from multiple angles of incidence can be measured and easily integrated into this analysis, it is assumed here that scattering coefficients (t_n) are constant with angle of incidence:

$$\tilde{t}_n(\alpha,\beta,\Delta r,\varphi) \cong \tilde{t}_n(\alpha=0,\beta=0,\Delta r,\varphi) = \begin{bmatrix} t_{n,x} \\ t_{n,y} \end{bmatrix} \qquad \text{Eq. 3-8.}$$

where $n = [-2,-1,0,+1,+2]$ and α and β are source coordinates defined in Figure 3-15c. Δr and φ are the desired pupil shift amount and orientation, respectively, and are related to LPG period as:

$$P(\Delta r) = \frac{M\lambda}{\Delta r \cdot NA} \quad , \quad \begin{matrix} P_Y = P\,\mathbf{sin}(\varphi) \\ P_X = P\,\mathbf{cos}(\varphi) \end{matrix} \quad , \quad \begin{matrix} \Delta r_y = \Delta r \cdot \mathbf{sin}(\varphi) \\ \Delta r_x = \Delta r \cdot \mathbf{cos}(\varphi) \end{matrix} \qquad \text{Eq. 3-9.}$$

where M, λ, and NA are the magnification, wavelength and numerical aperture of the scanner. A minimum pupil shift of 0.5 is assumed to ensure no orders other than the lowest five are captured by the pupil.

Step 2: Choose a source configuration: The polarization-dependent angular distribution of the source field (S) and intensity (I) are described by:

$$\tilde{S}(\alpha,\beta) = \sqrt{\tilde{I}_S(\alpha,\beta)} = \begin{bmatrix} S_X(\alpha,\beta) \\ S_Y(\alpha,\beta) \end{bmatrix} \qquad \text{Eq. 3-10.}$$

where ˜ indicates a vector quantity consisting of orthogonal (x and y) polarization components.

Step 3: Employ modified Abbe's method to calculate image intensity: The fields scattered from a given LPG (Δr,φ) for a particular diffracted order (n) with scattering coefficient in the pupil plane (ε,η) due to a single source point (α,β) are then:

$$\begin{aligned} \tilde{E}_n(\alpha,\beta,\xi,\eta,\Delta r,\varphi) &= \tilde{S}(\alpha,\beta)\cdot\tilde{t}_n(\Delta r,\varphi)\cdot\delta(\xi + n\cdot\Delta r_x, \eta + n\cdot\Delta r_y) \\ &= \begin{bmatrix} S_X(\alpha,\beta) \\ S_Y(\alpha,\beta) \end{bmatrix} \cdot \begin{bmatrix} t_{n,x}(\Delta r,\varphi) \\ t_{n,y}(\Delta r,\varphi) \end{bmatrix} \cdot \delta(\xi + n\cdot\Delta r_x, \eta + n\cdot\Delta r_y) \end{aligned} \qquad \text{Eq. 3-11.}$$

Applying the pupil as a low pass filter, the fields exiting the pupil are:

$$\tilde{E}_n'(\alpha,\beta,\xi,\eta,\Delta r,\varphi) = \tilde{E}_n(\alpha,\beta,\xi,\eta,\Delta r,\varphi)\cdot P(\xi,\eta) \qquad \text{Eq. 3-12.}$$

where $S(\alpha,\beta)$ and E_n' are illustrated in Figure 3-16a for annular illumination where only portions of the +1 and -1 orders are captured by the pupil. The net fields in the pupil plane are the sum of all captured diffraction orders:

$$\tilde{E}'(\alpha,\beta,\xi,\eta,\Delta r,\varphi) = \sum_n \tilde{E}'_n(\alpha,\beta,\xi,\eta,\Delta r,\varphi) \qquad \text{Eq. 3-13.}$$

The field distribution on the image plane (u,v) is found by integrating over all spatial frequency components (which each correspond to the fields at a particular pupil location), when propagated to the image plane:

$$\tilde{E}'(u,v,\alpha,\beta,\Delta r,\varphi) = \iint_{pupil} d\xi d\eta \sum_n \tilde{E}'_n(\alpha,\beta,\xi,\eta,\Delta r,\varphi)\cdot \mathbf{exp[}\, j\cdot(k_{x,n}u + k_{y,n}v)\mathbf{]} \quad \text{Eq. 3-14.}$$

where the propagating wave vectors in the image plane are defined as:

$$k_{x,n} = \frac{2\pi\alpha}{M\lambda/NA} + n\Delta r_x \quad , \quad k_{y,n} = \frac{2\pi\beta}{M\lambda/NA} + n\Delta r_y \quad \text{Eq. 3-15.}$$

and the image-plane intensity for a given source point is:

$$\tilde{I}(u,v,\alpha,\beta,\Delta r,\varphi) = \left|\tilde{E}'(u,v,\alpha,\beta,\Delta r,\varphi)\right|^2 \quad \text{Eq. 3-16.}$$

Integrating over all source points yields the final image intensity in vector form:

$$\tilde{I}(u,v,\Delta r,\varphi) = \iint_{source} \tilde{I}(u,v,\alpha,\beta,\Delta r,\varphi) d\alpha d\beta = \begin{bmatrix} I_x(u,v,\Delta r,\varphi) \\ I_y(u,v,\Delta r,\varphi) \end{bmatrix}$$

$$= \iint_{source} d\alpha d\beta \left| \begin{array}{l} \iint_{pupil} d\xi d\eta \sum_n \tilde{S}(\alpha,\beta)\cdot \tilde{t}_n(\Delta r,\varphi)\cdot \delta(\xi + n\Delta r_x, \eta + n\Delta r_y)\cdot P(\xi,\eta) \\ \cdot \mathbf{exp\{}\, j\cdot \mathbf{[}(\frac{2\pi\alpha}{M\lambda/NA} + n\Delta r_x)u + (\frac{2\pi\beta}{M\lambda/NA} + n\Delta r_y)v\mathbf{]\}} \end{array} \right|^2 \quad \text{Eq. 3-17.}$$

And the total intensity is the incoherent sum of that from each polarization component:

$$I(u,v,\Delta r,\varphi) = I_x(u,v,\Delta r,\varphi) + I_y(u,v,\Delta r,\varphi) \quad \text{Eq. 3-18.}$$

which is, for convenience, normalized to the clear field:

$$I_{CF}(u,v,\Delta r,\varphi) = \frac{I(u,v,\Delta r,\varphi)}{I(clearfield)} = \frac{I(u,v,\Delta r,\varphi)}{\iint_{source} d\alpha d\beta \cdot I_S(\alpha,\beta)} \quad \text{Eq. 3-19.}$$

Figure 3-16b shows an example of a calculated interference pattern of annular illumination using the above procedure. The polarization-dependent scattering

coefficients were simulated rigorously with TEMPEST, although in practice they would be measured experimentally.

Step 4: Calculate S_{+1} (wafer intensity for only +1 order): The above procedure yields the S_{+1} intensity value when only one diffracted order is used (i.e. $t_n = 0$ for n = -2,-1,0,2). An example is shown in Figure 3-16b.

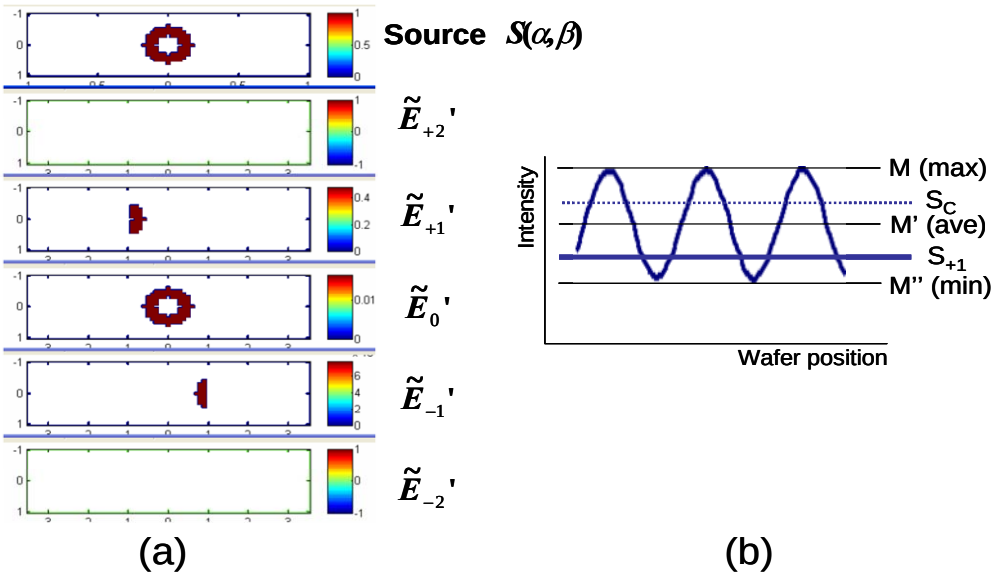

Figure 3-16. Estimate of the geometric signal with modified Abbe's method

(a) Representation of the source-images diffracted and filtered by the pupil. (b) Modified Abbe's theorem results in calculated image intensity modulation compared with the DC term expected from only the +1 order (S+1). Process discussed in the text produces SC, the estimate of the geometric signal needed for pupil-fill characterization.

Step 5: Determine SNR and MOD factors: The signal is compared to the noise in the SNR factor and the unwanted remaining modulation is defined by the MOD factor as:

$$SNR = \frac{S_{+1}}{\text{ave} - S_{+1}} \quad , \quad MOD = \frac{S_{+1}}{\max - \min} \qquad \text{Eq. 3-20.}$$

where high SNR and low MOD factors are desired.

Step 6: Determine average SNR and MOD factors: The above procedure is used to average the SNR and MOD factors for multiple realistic illumination configurations for each LPG.

Step 7: Monitor arbitrary illumination scheme with test reticle: Once the above calibration is complete, the test reticle can be used to monitor any realistic arbitrary illumination scheme. For each LPG, the measurement consists of determining the smallest dose that just causes the resist to clear. This corresponds to the greatest image intensity of the interference pattern when plotted as a percent of the clear field, as illustrated by M in Figure 3-16b.

The average intensity (M') is estimated from the SNR and MOD factors:

$$M' = M\left(1 + \frac{SNR \diagup 1 + SNR}{2 \cdot MOD}\right)^{-1} \qquad \text{Eq. 3-21.}$$

the compensated signal, or estimate of the ideal geometric signal, is then:

$$S_C = M'\left(\frac{SNR}{1 + SNR}\right) \cdot \frac{1}{T_{+1}} \qquad \text{Eq. 3-22.}$$

where $T_{+1} = \left|t_{+1}\right|^2$ accounts for energy lost in diffraction to orders other than the +1 order. For the ideal thin mask case, $T_{+1} = 0.81$.

Figure 3-17 shows a simulated example of the calibration for a series of five LPGs of decreasing period. The SNR and MOD factors are found for several realistic illumination configurations and the average is taken. Figure 3-18 then applies this calibrated data to two test cases, one for annular illumination and one for cross-quadrupoles. The captured intensity drop-off curve (CIDOC) from the compensated signal (S_C) is clearly a better estimate of the ideal geometric signal than the raw measurement data (M). The S_C CIDOC can then be used to either recreate the source shape or as a check for source symmetry.

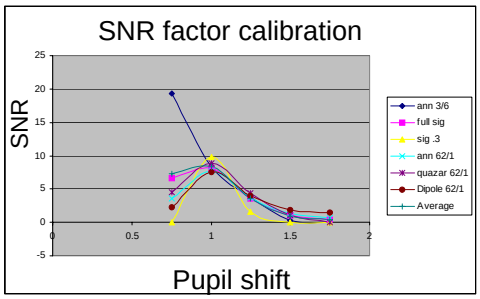

(a)

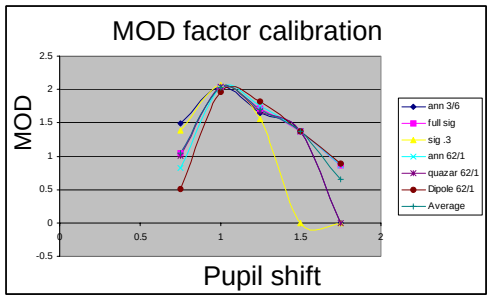

(b)

Calibration Factors:

Shift	SNR	MOD
0.75	22.700	1.044
1	8.389	2.028
1.25	3.533	1.695
1.5	0.953	1.373
1.75	0.438	0.653

(c)

Figure 3.17. Example of test mask calibration

(a) SNR and (b) MOD factors calculated from TEMPEST diffraction orders for various illumination configurations. (c) Calibration SRN and MOD factors are found as the average of all illumination configurations.

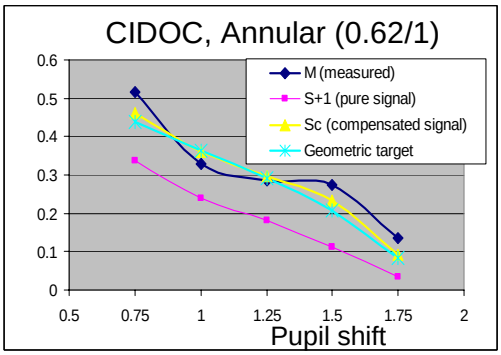

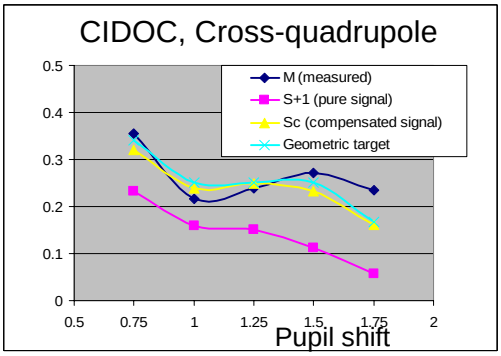

Figure 3-18. Two simulated cases of LPG calibration and measurement procedure

Measurement data is filtered to compensate signal, which is shown to produce a better estimate of the targeted geometric CIDOC.

Finally, it is noted that it is sufficient to calibrate the LPG with only the magnitudes of the scattering coefficients. Since the image intensity is primarily determined by the large +1 order, the 0 and -1 orders serve to induce modulation in the image. Generally, the modulation amount is determined by the magnitudes of the unwanted orders, while the locations of the interference pattern fringes are determined by the phases. Since absolute position of the image is irrelevant, the phases can generally be

neglected. This allows calibration of the diffraction orders with a simple apparatus consisting of CCD detectors unable to track the rapid oscillations (and thus the phase) of the scattered orders.

3.6. Summary and overall assessment

A phase shifting mask pattern, the linear phase grating, has been introduced as a potential tool to measure or monitor illumination angular distribution. Its advantage over existing techniques lies in the fact that the analysis of the source has been transferred to the mask pattern. After calibration of the test reticle and filtering out mask irregularities, inspection of a single dose-matrix wafer with a low magnification optical microscope displays signs of source irregularity. If signs of irregularity are found, the capability exists for the user to complete a more in-depth analysis of the source intensity distribution. Illumination pupil-fill may be monitored across the field, tool-to-tool, or over time, or can be compared to the intended design. Mask requirements, mask making limitations and electromagnetic performance issues have been discussed. Although the LPG pushes the limits of conventional mask making, fabrication is feasible and imperfections may be accounted for by proper mask calibration.

Finally, to assess the practicality of the LPG as an illumination monitor, its ability to measure two attributes of the illuminator are considered: the intensity balance of symmetric pupil locations (i.e. balance between two dipole locations) – and the resolution capable in pupil coordinates (i.e. to measure if the dipoles are in the right place). Without calibration, the LPG is unreliable for either of these measurements due to the inevitable orientation-dependent mask topography effects which impact the diffraction efficiencies for different LPGs. The un-calibrated experiments conducted for Chapter 3 estimated the LPGs were able to measure intensity balance to with 5%; sub-par for industry requirements. However, with proper calibration, it is likely that this technique could measure intensity balance between symmetric source-image locations to within 2 or 3 percent. Resolution of the source-image measurement is a more difficult measurement, but could likely achieve a resolution of about 0.02 pupil coordinates. Higher resolution requires a larger number of LPGs, thus a more extensive calibration and experimental procedure. Of course, both measurements depend largely on the ability to faithfully

measure the calibrated diffraction orders and in minimizing experimental error. Additionally, they will both be a function of the angular frequency content of the illuminator (i.e. the partial coherence), as the SNR and MOD factors discussed in the previous section are frequency dependent. With a larger number of frequencies, more averaging occurs, thus the less reliable the measurement is.

To conclude, the LPG may be useful for some applications such as a quick check for intensity balance between dipoles or quadrupoles. However, due to the frequency-dependence of the LPG behavior, it is likely not practical enough to outdo techniques that are currently used in the industry for a full source-image measurement. Generally, these techniques are based on the pinhole camera concept described in Section 3.1. However, understanding the LPG is useful, in that it forms a critical component of the LPR illumination monitor discussed in the next chapter and of the polarization monitors of Chapter 5. An LPG-like four-phase grating embedded within the polarization monitors will, with the assistance of an aperture in the backside of the photomask, enable them to analyze light from only a particular illumination frequency. In that case, partial coherence effects are irrelevant and faithful calibration of the mask is more successful in enabling an accurate measurement.

4 Monitoring Illumination 2: Linear Phase Ring

An alternate method to monitor illumination angular uniformity and distribution using phase shift masks is presented in this chapter. The Linear Phase Ring (LPR), consisting of an Airy pattern multiplied by a linear phase progression, leverages proximity effects to create a signal in photoresist dependent on a single illumination angular frequency. The proximity effect spill-over from the pattern rings is in phase at the center position only for illumination from the designed off-axis illumination direction. Thus, a quantitative analysis of the intensity in a particular pupil location is available by measuring intensity at the center of the pattern. For analysis of certain small illuminators, a sub-printable, interferometric probe placed at the LPR center increases signal strength and sensitivity. LPR operation is similar in principle to receiving a signal with a circular aperture antenna, except that the summation is weighted by the proximity spillover. The key issues are signal strength, angular discrimination, and orthogonality to aberrations. A theoretical analysis is presented first and image simulation studies are made of an implementation based on four-phase mask making. Theory predicts the signal strength to be high (about 1/3 to 1/5 of the clear field intensity per ring), the angular discrimination to be good (about 0.5/ring number), and that LPRs are reasonably unaffected by aberrations. Experimental results from a four-phase test reticle are reported, validating the scientific principles and shedding light on signal lost due to realistic imaging conditions such as electromagnetic effects and mask making limitations.

The advantage of this technique is that analysis of the illuminator has been transferred to the mask pattern. Unlike the LPG monitor of the previous chapter, each LPR is designed to create a signal for only a single illumination frequency incident on the

mask. Thus, with proper calibration it allows for a fast and easy measurement of illumination schemes such as quadrupole and dipole. However, signal strength relative to the clear field intensity decays with larger values of partial coherence. The measurement only consists of determining intensity at the center of the LPR as a dose to clear in photoresist. Furthermore, the LPR can be used on a special test mask or embedded in the scribe line of an actual production mask layout, although cost may be an issue.

Section 4.1 introduces the concept of the LPR and shows how it acts as a detector for illumination in a particular location of the pupil. In Section 4.2, a theory of the LPR's sensitivity, based on the proximity effect, is developed and predicts the amount of electric field coherently spilled into the center of the pattern. This theory is then applied to develop measurement schemes for various illumination configurations in Section 4.3. Additionally, a slight variation is presented to compare temporal coherence between two symmetric illumination frequencies. Experimental verification of the LPR technique is reported in Section 4.4 and a discussion of relevant imaging limitations and methods to compensate for them are discussed in Section 4.5. Calibration of the test mask is required. It is concluded that the calibrated LPR may be advantageous for a quick check of intensity balance between poles of a dipole or quadrupole illuminator with sensitivity capable of monitoring intensity balance between dipoles to within about 2%.

4.1. Concept: Linear Phase Ring

The linear phase ring (LPR) takes advantage of reciprocity and the optical proximity effect to create a spatial frequency dependant signal on the wafer. The optical proximity effect is the well known electromagnetic influence of one mask location onto a nearby reciprocal wafer location. This influence is manifested in the point spread function which, for a circular pupil, is found to be in the form of an Airy pattern with dimensions dependent on the wavelength of light and numerical aperture of the optics. Thus, due to the circular nature of the lenses in a lithographic imaging system, an arbitrary clear field location B in the object plane (reticle) will contribute electric field to any other arbitrary location C in the image plane (wafer) dependent on the magnitude and phase of the point spread function at location C, centered on point B, as shown in Figure 4-1a. This is commonly known as the proximity effect. By reciprocity then, the net

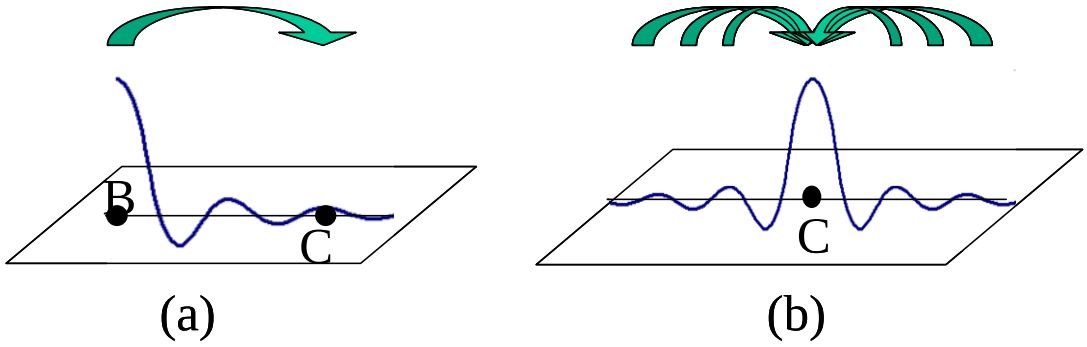

Figure 4-1. The concept of reciprocity

(a) The proximity effect spill-over from location B to C is found by the magnitude and phase of the point spread function (PSF) at C, centered on B. (b) Reciprocity dictates that the net influence of all mask locations on location C is found as the integral over the PSF, centered on C.

influence on point C by any and all mask locations is found by integrating over the entire point spread function, when centered on point C, as in Figure 4-1b.

To leverage this concept of reciprocity, a mask pattern is created resembling the Airy pattern (concentric rings of 0 and 180 degree phase), as in Figure 4-2a. Thus, the proximity effect spill-over from the surrounding rings to the central position will add collinearly for normally incident plane wave illumination, which corresponds to a small illumination spot in the center of the illuminator (Figure 4-2c). Conversely, if the illumination spot is off-axis, then the spill-over from the obliquely incident plane wave will not add collinearly, thus decreasing the signal (Figure 4-2d). In other words, this pattern is a detector for an on-axis illumination spot.

This mask pattern can be altered to detect an illumination ray from any location in the pupil. First, the Airy function is multiplied by a constant linear phase corresponding to the desired target location. The LPR mask pattern is then realized as the phase of this expression, as follows:

$$\Phi_{\mathrm{LPR}}(x,y) = Phase\left[Airy(x,y)\times e^{+j\varphi_{\mathrm{target}}(x,y)}\right] \qquad \text{Eq. 4-1.}$$

where

$$\varphi_{\text{target}}(x,y) = \frac{2\pi T_x}{\lambda / NA}x + \frac{2\pi T_y}{\lambda / NA}y \qquad \text{Eq. 4-2.}$$

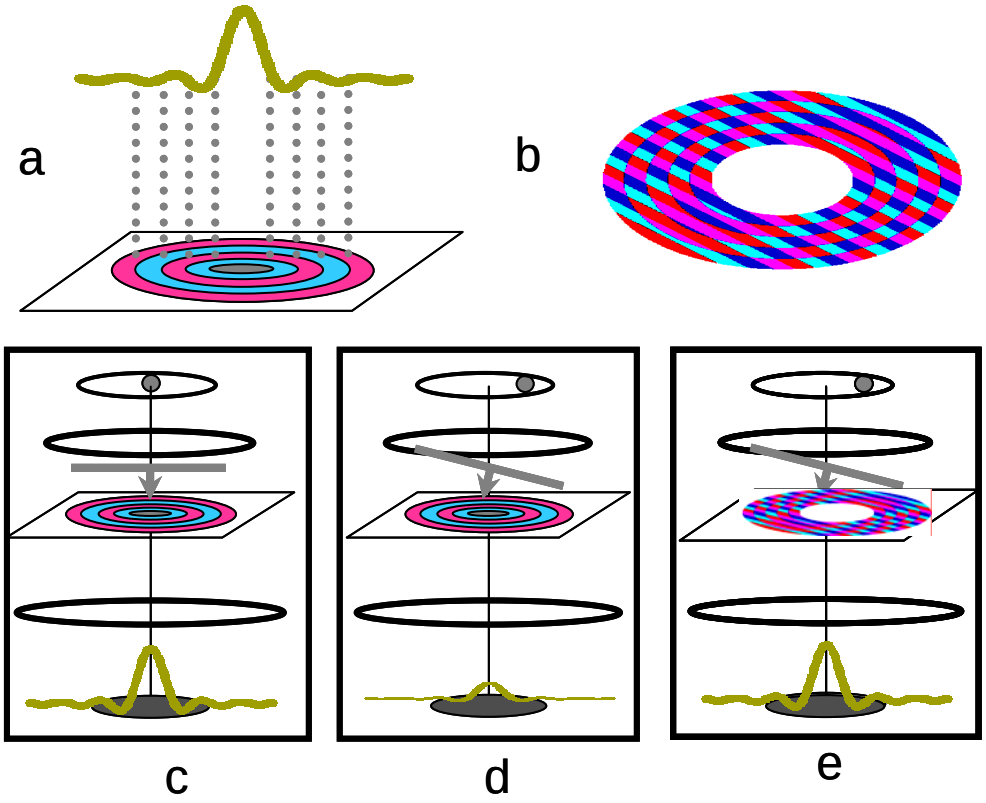

Figure 4-2. The Linear Phase Ring Illumination monitor

(a,c,d) A mask pattern that resembles the Airy pattern serves to maximize proximity effect spill-over into the center position for only an on-axis illumination spot. (b,e) The linear phase ring (LPR), consisting of an Airy pattern multiplied by a linear phase, serves a detector for an off-axis illumination spot.

An example mask pattern, shown in Figure 4-2b, becomes a detector for an illumination ray located at position (T_x, T_y) in the pupil, normalized to the numerical aperture (NA) of the projection lens. The ideal phase distribution has been rounded to the nearest 90º to comply with conventional mask making capabilities. However, a test mask with finer phase steps might also be directly written with an electron beam in a resist system such as HSQ, potentially offering a very cost effective method to fabricate LPRs and other PSM test structures [26]. Figure 4-2e shows how an incident plane wave from the target design illumination location is redirected to coherently spill electric field into the center position. The intensity in the center position will achieve a maximum when an

illumination ray coincides with the target design (T_x, T_y) and will decrease with increasing angular deviation from that location.

Since the linear phase variation for each illumination pupil position is unique, an LPR designed for a certain illumination location will be orthogonal to all other pupil locations. Furthermore, the mask design will generally be orthogonal to Zernike polynomials and will be unaffected by lens aberrations. However, it is noted that in some single-ring applications the LPR will be sensitive to rotationally symmetric aberrations such as defocus.

The dimensions of interest for the LPR are the radius, linear phase period, probe size and phase etch depth shown in Figure 4-3. The ring outer radius of the Nth ring is determined by the Airy pattern as approximately:

$$R_{out}(N) \cong (0.6 + 0.5N)\frac{M\lambda}{NA} \qquad \text{Eq. 4-3.}$$

where M is system magnification. The period of the phase regions is dependent on the target design illumination spot (σ_{Target}) as:

$$P = \frac{1}{(\sigma_{Target})}\frac{M\lambda}{NA} \qquad \text{Eq. 4-4.}$$

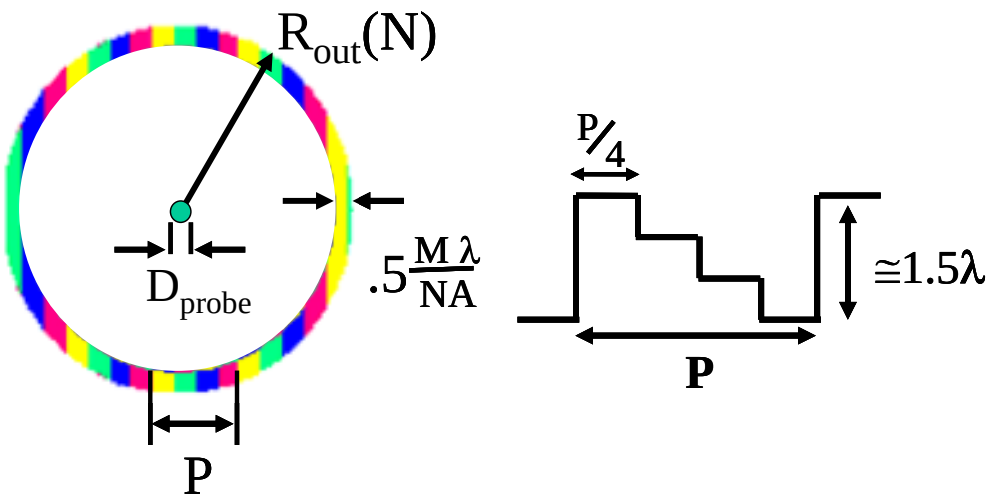

Figure 4-3. LPR dimensions

If used, the diameter of an interferometric reference probe is arbitrary, but must be designed appropriately to provide a signal on order of that from the pattern for the illuminator under analysis. Generally, the probe diameter will be about 0.4 Mλ/NA. Finally, the maximum phase depth for the 270° region is about 1.5λ, assuming an index of refraction of 1.5. Manufacturability will be discussed in Section 4.5.

4.2. Theory: LPR sensitivity

In order to design the LPR for a particular application, we first develop a theory for the sensitivity of the pattern to the incident illumination. Sensitivity is defined as the change in center intensity (from the maximum) as the actual illumination ray (from σ_x, σ_y) deviates from target design (T_x, T_y). The proximity effect spillover from any location B to the center of the pattern is found by considering at location B the magnitude and phase of the Airy function (centered at C), the phase of the incident illumination ($\Phi_{illum}(B)$), and the phase change induced by the LPR ($\Phi_{LPR}(B)$) as follows:

$$E_{B\Rightarrow C} = Airy(B) \times e^{j\Phi_{illum}(B)} \times e^{-j\Phi_{LPR}(B)} \qquad \text{Eq. 4-5.}$$

where

$$\Phi_{illum}(B) = \frac{2\pi\sigma_x}{\lambda / NA} x_B + \frac{2\pi\sigma_y}{\lambda / NA} y_B \qquad \text{Eq. 4-6.}$$

The amount of electric field spill-over will, in general, be a complex number. However, since the lens system is real, to determine the influence of the entire target on the center position, we simply take the real part of this function integrated over the LPR area:

$$E_C = \int_{LPR} Airy(x,y) \times \cos[\Phi_{illum}(x,y) - \Phi_{LPR}(x,y)] \qquad \text{Eq. 4-7.}$$

The main point of interest here is that the LPR's sensitivity is only a function of the difference between the actual illumination (σ_x, σ_y) and the target design (T_x, T_y), as well as the number of rings in the LPR.

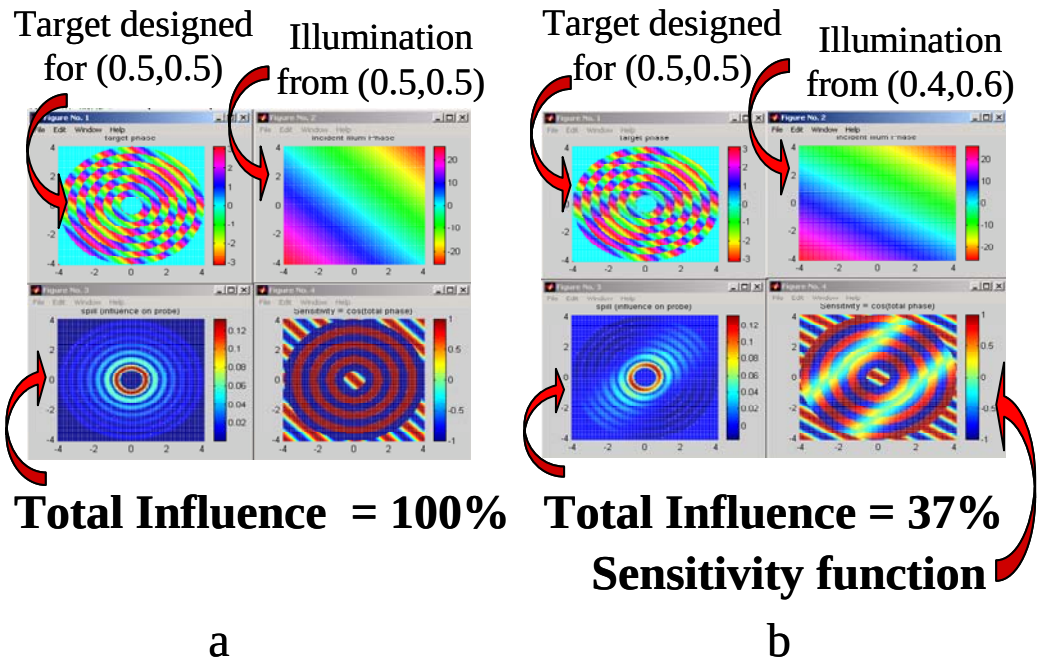

Figure 4-4. Representation of LPR influence function

The LPR designs, the phase progressions of given incident plane waves, and the resulting influence functions and sensitivity functions are depicted for (a) illumination from the target design and (b) illumination from a slightly off-design location.

To gain a visual understanding of the above relations, Figures 4-4a and b show how a target behaves differently for illumination from different locations. The top left portion of both figures is an ideal LPR designed for illumination with coordinates (T_x = 0.5, T_y= 0.5). The top right portion shows the phase variation across the mask for actual illumination from two locations (Figure 4-4a: σ_x = 0.5, σ_y = 0.5; Figure 4-4b: σ_x = 0.4, σ_y = 0.6). The difference between these two scenarios is seen clearly in the bottom left portion of the figures as the total influence. This influence function is a representation of the amount of electric field that would coherently spill into the center position from each location in the target. Thus, integrating over this function will determine the relative coherent spillover of the LPR. We see that illumination from the target design location (Figure 4-4a) results in 100% of the maximum influence, whereas illumination from the alternate location contributes only 37% of the maximum. These numbers refer to the electric field at the center position and the expected measured intensity is simply the square of the electric field.

To gain a better understanding of how sensitivity depends on LPR design, we consider the electric field contribution to the center position ring by ring. The above relation can be rewritten as follows to show the influence of each ring:

$$E_A = \sum_N \frac{2}{\pi}(.5\frac{\lambda}{NA})(2\pi r_N)\frac{J_1(2\pi r_N)}{(2\pi r_N)} \int_{N^{th}\ ring} \cos[\Phi_{illum}(x,y) - \Phi_{LPR}(x,y)] \qquad \text{Eq. 4-8.}$$

The first part of the expression is the maximum electric field contribution from the N^{th} ring, or the total area under that ring of the Airy pattern. The second part is the sensitivity function. A plot of this function reveals the LPR sensitivity as a function of total rings, and is shown is Figure 4-5. Figure 4-5a shows that the relative sensitivity increases with the use of more rings. However, the total intensity at the center location (Figure4-5b) also increases, resulting in a huge signal of about 10 times the clear field for an LPR with all 11 rings.

Improvement in sensitivity at the expense of the excess signal is attained by simply eliminating some of the inside target rings. Furthermore, the addition of an interferometric reference probe, a small sub-printable feature at the center of the mask pattern, can allow for improved sensitivity due to the coherent addition of the electric field from both pattern and probe. For a single ray of illumination, the intensity in the center position becomes: $I_C = (E_{probe} + E_{pattern})^2$ and the gain due to the presence of the probe is: Gain = 2 (E_{probe} / $E_{pattern}$).

However, the use of the probe has both advantages and disadvantages, and is useful only when the size of the illuminator under analysis is fairly small. For a small illumination spot resulting in a single illumination ray, the use of a probe and hollow pattern has both increased angular discrimination and signal detection. Figure 4-5c shows an example of an LPR with a probe and only the 9^{th} ring. Sensitivity of this one ring LPR with probe is compared to an LPR consting of only a 5^{th} ring and probe in Figure 4-5d. The signal in this case becomes the center intensity from both pattern and probe compared to the intensity of a nearby identical, but isolated, probe. Iso-probe intensity is shown as a straight line, constant with angular deviation. Larger ring radius results in better angular discrimination, which is also evident mathematically by equation

3-8 as increasing ring number (N) is considered. For single ring targets with a probe, the theoretical resolution of the LPR is approximately inversely proportional to the size, and is given in pupil coordinates roughly as 0.5/ring number.

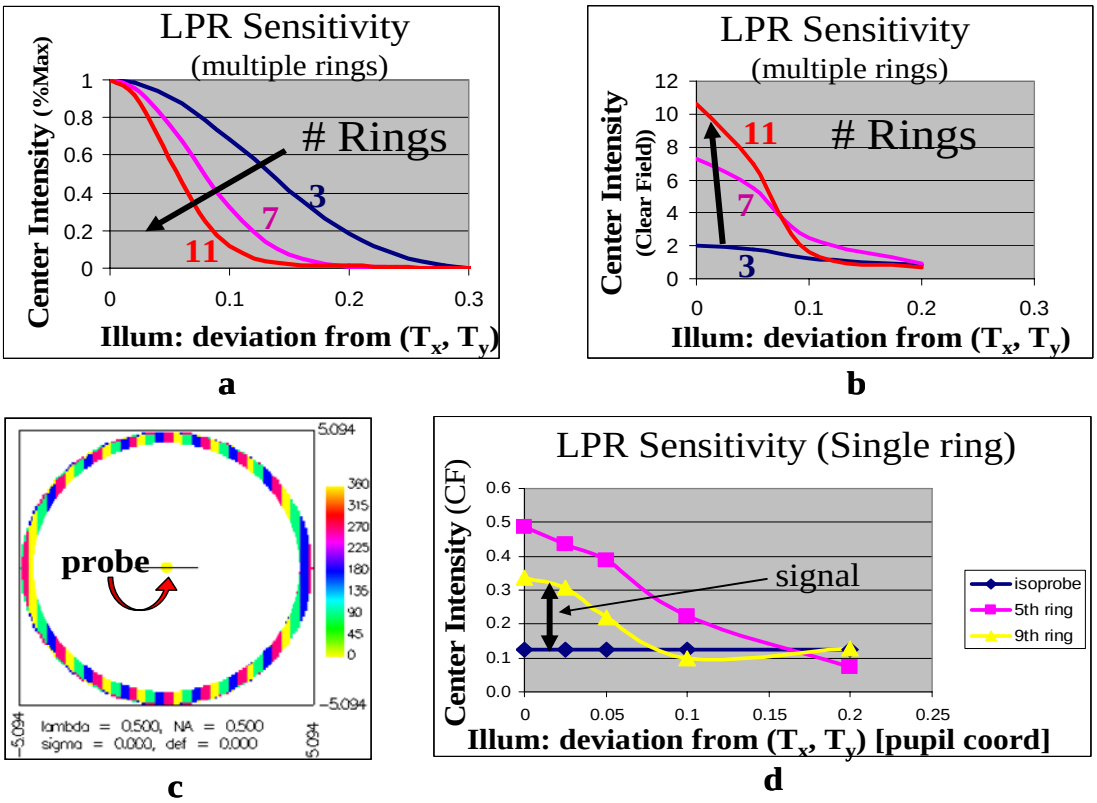

Figure 4-5. LPR sensitivity as a function of the number of rings

(a) Relative intensity shows increasing sensitivity for larger targets and (b) absolute intensity shows very large signals with increasing ring count. However, signal can be traded for sensitivity by using (c) a single ring target with an interferometric probe. (d) Sensitivity comparison of two single ring LPRs is shown, using an isolated probe as a reference. Probe is useful only for small illuminators.

The disadvantage of the probe appears when the illuminator under analysis is large. For example, if two small dipoles are considered, the pole from a location different than the target design will contribute electric field to the center position through the probe, but not the pattern. Thus, illumination from any other location will add an incoherent, noisy probe contribution as follows: $I_C = (N\text{-}1)\, I_{probe} + (E_{probe} + E_{pattern})^2$, where N-1 is the number of rays from locations other than the target design. Clearly, the incoherent probe contributions begin to drown out the pattern signal as the illuminator

size increases and the probe becomes ineffective. Thus, a probe should only be used for small illuminators. Since a probe is not used for large illuminators, no incoherent noisy contributions to the center intensity exist from rays other than from the target design. Therefore illumination from other locations will not effect the measurement when no probe is used.

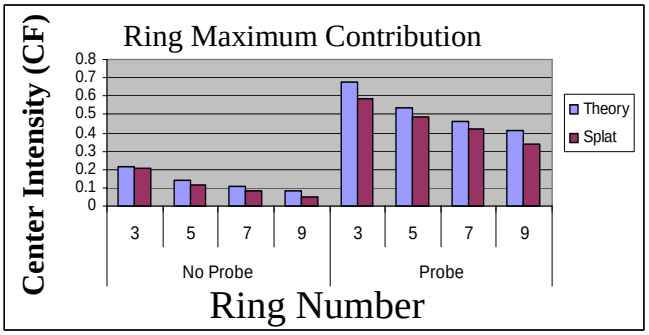

a

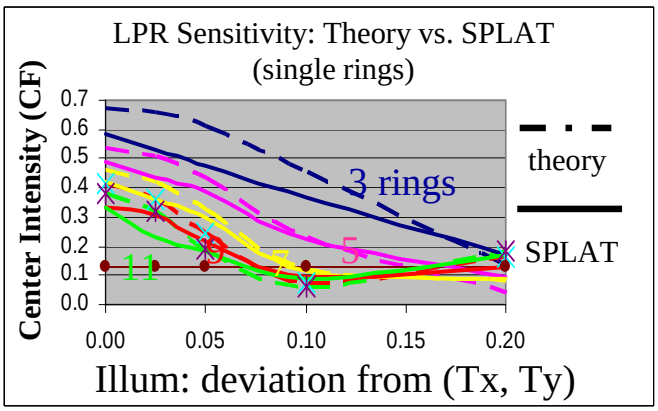

b

Figure 4-6. LPR theory vs. simulation

Theoretical (a) maximum single ring contribution and (b) sensitivity are compared to thin mask (SPLAT) simulation. The theory, based on the proximity effect, slightly over-predicts signal strength for explained reasons.

To determine the validity of the proximity effect theory of target sensitivity, the theory for a single ring pattern with and without the probe is compared to a thin mask SPLAT simulation in Figure 4-6. With a single ray illuminator, the maximum ring contribution is shown in Figure 4-6a and the LPR's behavior through illumination pupil shift is displayed in Figure 4-6b. We see that, although relatively accurate, the theory

always predicts a higher intensity than is seen in simulation. This is likely due to the assumed sinusoidal shape (factor of $2/\pi$) in the theory and the fact that the SPLAT input files used were generated from a rectangle-fitting algorithm. Finally, for an LPR designed for off-axis illumination, the obliquity factor may decrease the actual amount of energy incident on the mask.

4.3. LPR applications

4.3.1. Dipole monitor

The theory developed for target sensitivity clearly shows a trade-off between angular discrimination, signal strength, the number of target rings, the probe size (if any), mask complexity, and the physical extent and location of the illuminator under analysis. Thus, optimization of these parameters must be considered in designing a monitor for a particular application. As an example, a dipole illuminator with relatively small spot sizes ($r_{spot} = 0.1$) is first considered.

First, Figure 4-7a shows how two LPRs can be used on a special test mask, each pattern optimized for one dipole. The relatively small nature of the dipoles allows for the use of a probe to increase signal sensitivity. Theoretically a target with only the 9^{th}, 10^{th}, and 11^{th} rings allows for a reasonable pattern to probe signal ratio, while attaining excellent angular discrimination. The mask would be exposed through dose in photoresist. Simple observation of the resist pattern with an optical microscope, or perhaps with an automated CD-SEM, allows for comparison between both poles of the dipole. If both center positions cross the resist exposure threshold and print at the same dose, then the dipoles are balanced. However, if one LPR center prints before the other, then the dipoles are unbalanced by an amount quantified by the two clearing doses.

Secondly, these targets could be placed in the scribe line of a production mask layout and referred to during manufacturing if an error in illumination is suspected. For example, Figure 4-7b shows multiple sets of two LPRs placed in the scribe line. Among the different sets would be a range of pattern and probe (if needed) designs offering varying signal strength. Thus, if the dipoles are indeed unbalanced, there will likely be a set of targets where one probe prints, but the other does not. This ability to monitor the

state of illumination during manufacturing is unique to this technique, although the manufacturing cost associated with four phases may be an issue.

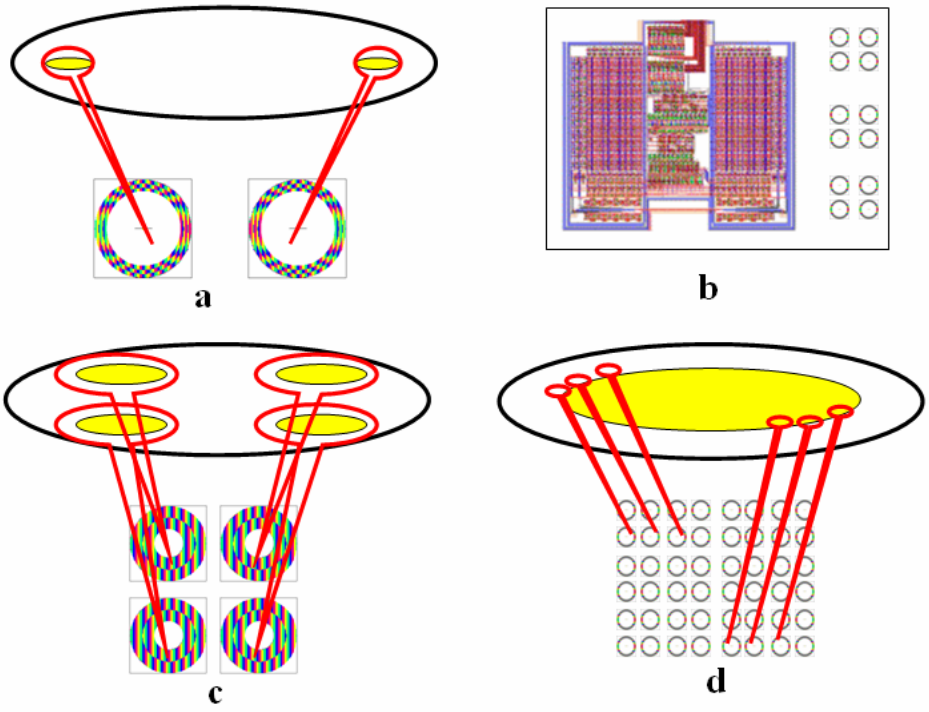

Figure 4-7. LPR applications

(a) A dipole illuminator can be monitored with two mask patterns on a special test mask or (b) in the scribe line of a production mask layout. Flexibility in LPR design allows measurement of other illumination schemes, such as (c) quadrupole or (d) an arbitrary full-pupil illuminator.

4.3.2. Quadrupole or full pupil monitor

Other types of illumination conditions may be measured simply by altering the LPR design. For example, quasar illumination or quadrupoles similar those seen in Figure 4-7c can be characterized on a test mask with four targets. Due to the larger extent of the poles a probe is likely ineffective due to excess incoherent contributions it would provide. Furthermore, a high degree of angular selectivity is not desired since each target is intended to detect a relatively large portion of the pupil. Thus, targets with only the 2nd and 3rd rings and no probe might be most effective. Again, this test mask would be exposed through exposure dose and the doses at which the center positions print

are compared. In a balanced quadrupole, all four locations should print at the same dose, neglecting for now orientation-dependent mask making effects.

Furthermore, arranging a large number of LPRs on a mask, as shown in Figure 4-7d, will allow for a more general pupil characterization. Depending on the desired resolution, each target would be appropriately designed to be sensitive only to a particular region of the pupil. As an example, the signal from a target consisting of only the 9^{th}, 10^{th}, and 11^{th} rings (no probe) will decrease 30% of the clear field for a pupil shift of only 0.02. Thus each LPR responds only to intensity in a certain small pupil location, quantified by the dose at which its center prints. Analysis of a large number of appropriately designed LPRs provides a means to measure the full pupil-fill. However, this LPR application potentially adds cost and mask complexity and would generally not have an advantage over existing techniques.

As the relationship between LPR target geometry and angular discrimination should be clear at this point, an analogy to the directional gain achieved by an array of antennas is made. Just as multiple antennas, arranged appropriately in three-dimensional space, allow for detection of a signal from a smaller solid angle, rings of increasing radius allow for discrimination of illumination between smaller source spots.

Furthermore, a test mask with appropriate LPR designs could be used in conjunction with the pinhole camera technique to identify the absolute energy in a particular portion of the lens. By requiring overexposing the out-of-focus pinholes by up to 100 times the clear field dose, the pinhole-camera technique is often useful only for comparing relative intensities for various pupil locations. The LPR, however, allows for easier measurement of absolute local intensities in a particular pupil location at realistic operational doses. A combination of multiple techniques (pinhole camera, grating pinholes, linear phase gratings, and linear phase rings) will likely give the most accurate measurement.

4.3.3. Application: Temporal coherence monitor

A final application, based on a variation of the LPR, is to measure the degree of temporal coherence between two pupil locations. Ideally in Kohler illumination, all source points are completely temporally incoherent. This if often achieved by routing a coherent light beam (for example, from a KrF pulsed laser) through a diffuser and light pipe. However, it may be of interest if the diffuser and light pipe fail to completely randomize the light incident on a mask pattern. This could result in unwanted ringing in the aerial image and degrade feature printability.

The LPR was designed by taking the phase of the Airy pattern, multiplied by a linear phase associated with one pupil location. However, if the LPR design is the phase of an Airy pattern multiplied by the difference in linear phase from two symmetric pupil locations, we get the following expression for the electric field spilled into the center of the pattern:

$$E_C = \int_{time} \int_{\mathrm{LPR}} [Airy(x,y) \times (e^{j\Phi_{\mathrm{LPR}}(x,y)} - e^{-j\Phi_{\mathrm{LPR}}(x,y)})] \times (e^{j\Phi_{\mathrm{illum}}(x,y)} + e^{-j\Phi_{\mathrm{illum}}(x,y)} e^{-j\varphi(t)}) \quad \text{Eq. 4-9.}$$

The term in brackets is the LPR design, which for symmetric target design locations, simplifies to $Airy(x,y) \times 2j\,\mathbf{sin}(\Phi_{\mathrm{LPR}}(x,y))$.

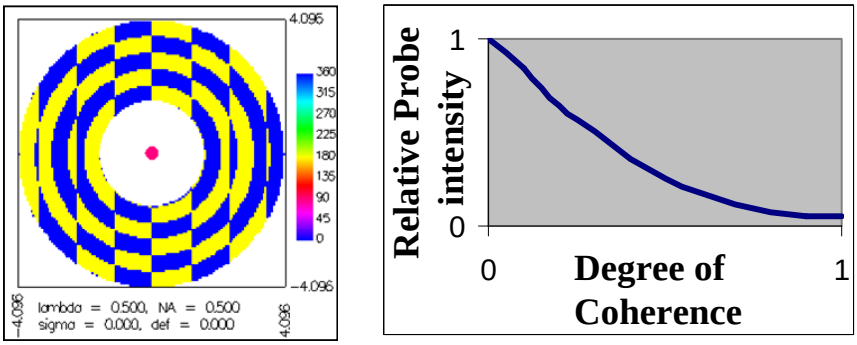

Figure 4-8. Temporal coherence monitor

(a) Mask pattern and (b) relative sensitivity to degree of coherence between two symmetric pupil locations.

When the phase of the term in brackets is realized on a mask, we see in Figure 4-8a that the design only requires two phases for the pattern rings. However, a 90º probe is required to interact with and measure the imaginary portion of the expression above since we are only concerned with a difference in phase. Thus, considering illumination only from the two symmetric target design locations and assuming comparable intensities, the degree of coherence between the locations is measured. If the illumination from these two pupil locations are completely temporally coherent (i.e. $\varphi(t)$ is constant with time), then the target will cause the electric fields spilled from the two illumination locations through the pattern to destructively interfere at the probe position. Probe intensity will be at a minimum and will be due to only the probe contributions. Conversely, if the two locations are completely temporally incoherent ($\varphi(t)$ is random), as they should be, the target will simply average the two location intensities. A theoretical plot of this behavior is seen in Figure 4-8b, which displays the decrease in probe position intensity with an increasing degree of coherence.

4.4. Experimental verification

This section reports a set of experiments that validates the scientific principles of the LPR technique. The next section will identify discrepancies between theory and experiment and discuss methods to compensate for various non-idealities. Figure 4-9a shows an SEM of a four-ring, four-phase, LPR designed for a 248nm wavelength tool with a numerical aperture (NA) of 0.5 and reduction of 5x. Again, a cutline from an AFM measurement shows roughly the desired profile. Experimental evidence of the LPR's scientific principle is seen in Figure 4-9b c where this same mask pattern is exposed in an AIMS tool under two different illumination conditions. The pattern is designed to 'detect' light from an area in the pupil approximated by the drawn circle. As expected, when no light is present in that region as with coherent illumination ($\sigma = 0.3$), then a cutline through the center of the aerial image remains essentially flat. However, when light is present in that region, as in the case of a large annular illuminator, then light is 'spilled' into the center. This effect is seen as a local peak in intensity. It is noted that the intensity peak in this case is only about 3% of the clear field intensity. This pattern was specifically designed to monitor quadrupole illumination and the fact that much of

the annular illuminator is not being detected serves to simply decrease the measurement intensity. In other words, if this pattern were to be illuminated with quadrupoles, then the signal would be expected to be about two to three times larger.

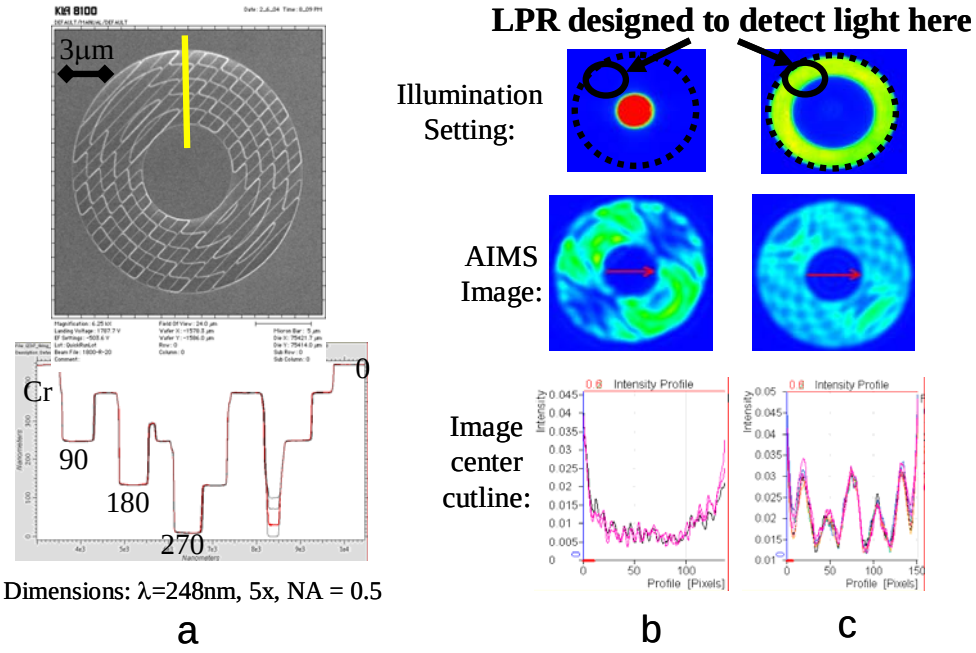

Figure 4-9. LPR experimental results

(a) SEM and AFM measurements of a four-ring, four-phase LPR on the mask show the desired profile. AIMS aerial images of this mask pattern under (b,c) two illumination conditions show the desired effect of light spilled into the center when illumination is present where the LPR is designed to detect.

To test a potential practical application of the LPR, multiple two-ring LPRs were fabricated on the same four-phase reticle as the LPGs, in the configuration shown in Figure 4-10a. In the vertical direction, the periods of the linear phase progression within the rings decrease so as to sample a portion of the pupil further from the center. In the horizontal direction, the two columns of LPRs use different rings of the Airy pattern. The LPRs in this mask configuration each detect light from the different pupil positions shown in Figure 6b against quazar illumination.

An example of how the LPR prints in photoresist when illumination is present where the pattern is designed to detect is shown in Figure 4-10c. The only aspect that is important is the dose at which the center position begins to print. This dose, when

expressed in terms of the clear field intensity, reflects the signal strength and is used to compare intensities from various pupil locations. The plot in Figure 4-10d shows the signal strength from the LPRs of the mask configuration of Figure 4-10a. As expected, the signal strength is greatest when the pattern is designed to detect illumination from the location where the quazar is located. Additionally, it is seen that larger rings spill less light into the center, decreasing signal strength.

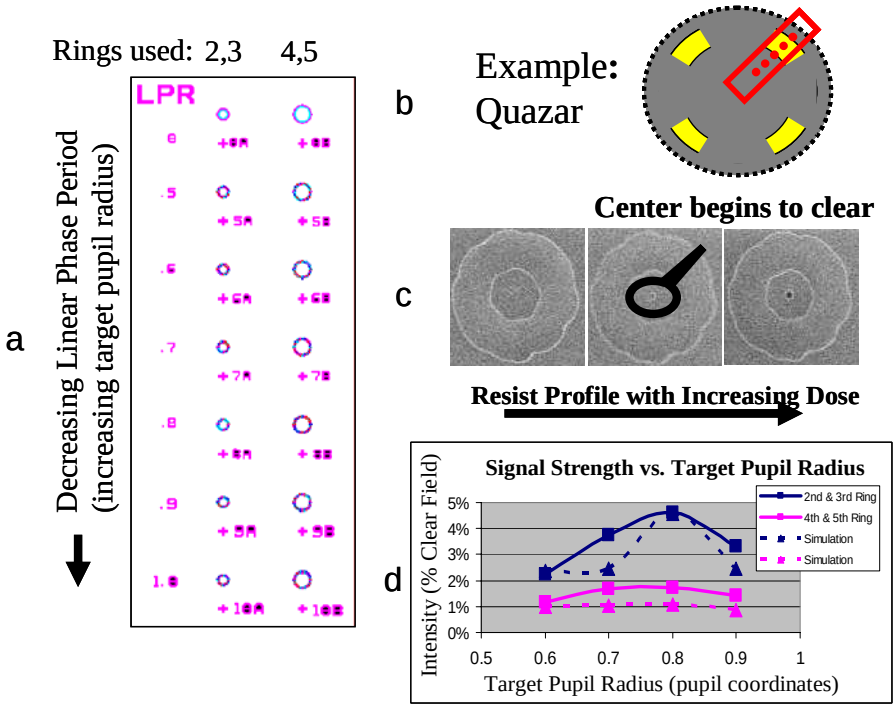

Figure 4-10. LPR Experimental results

(a) Multiple LPRs on the mask each serve to detect light from (b) different locations in the pupil. (c) Resist patterns are analysed to find the clearing dose of the central position. (d) Signal strengths of each LPR are compared to simulation, showing the desired effect.

4.5. Practical analysis of LPR non-idealities and compensation methods

As with the Linear Phase Grating, electromagnetic interaction with mask topography and mask making limitations are sure to be of concern due to the sub-resolution feature requirements of the multiple phase shift regions of the LPR. Figure 4-11 attempts to deconvolve these two effects using simulation and the experimental data reported in the previous section. Comparison of the thin mask and thick mask

simulations reveals the expected loss in signal and sensitivity due to EM effects. Comparison between the thick mask simulation and experimental data uncovers additional loss in signal and sensitivity, which is primarily attributed to limitations of mask making capabilities. A loss of roughly 40% of the peak signal and 60% of the maximum sensitivity (slope) is observed between the thin mask simulation and actual experiment. Section 4.2 (Figure 4-6) showed good agreement between thin mask simulation and the theory developed in this chapter. Thus, when adjusted for this signal and sensitivity loss, this theory appears to be relevant to reality.

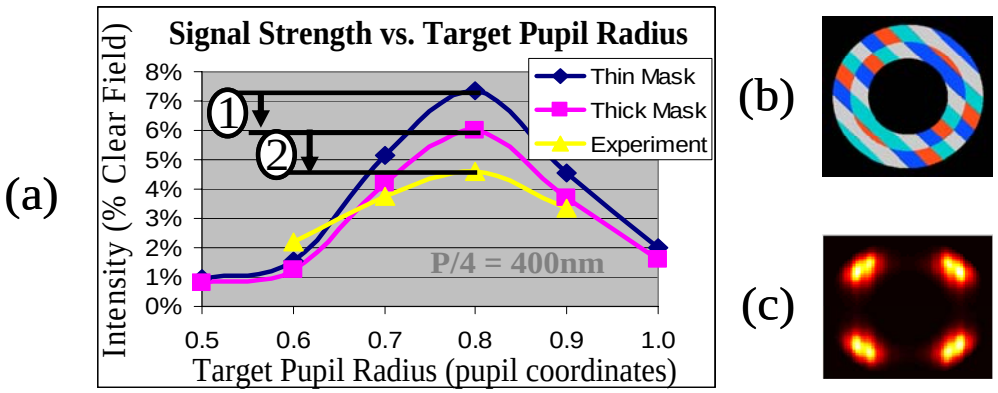

Figure 4-11. Electromagnetic effects vs. mask making limitations

(a) Signal loss due to (1) electromagnetic interaction with mask topography and (2) mask making limitations of a (b) two ring LPR monitoring (c) quazar illumination.

Additional experimental measurements were made attempting to detect an imbalance between the poles of the quazar illuminator by considering four similar LPRs oriented at different diagonals. However, trends in the variation in signal strength did not agree with measurements done with a pinhole camera technique [41]. Orientation dependent mask non-uniformities due to slight (and inevitable) alignment errors in the fabrication process appear to have caused greater measurement error than the imbalance of the illuminator under analysis. Thus, calibration of the test reticle is essential to the practical application of the LPR monitoring technique. Calibration would consist of exposing the LPR array with a series of well-calibrated, coherent off-axis illumination spots and comparing the measured signal to that of a thin mask simulation. The ratio of

these two measurements defines $M_e(T_a)$, the thick mask factor for the angular frequency component from location T_a in the source, used below in equation 3-10.

Equation 3-8 described the theoretical electric field signal for an off-axis coherent illumination spot. In addition to signal lost to mask effects, the nature of the partially coherent illumination scheme will have an impact as well. Accounting for all of these effects, the final signal intensity for an LPR without probe can be expressed as:

$$I_C \approx \underbrace{M_e(T_a)}_{\text{Thick mask factor}} \underbrace{\frac{1}{A_\sigma^2}}_{\text{Source size}} \sum_{i^{th}ring} \left[\underbrace{\left(\frac{2}{\pi} \right)}_{\text{Max ring influence}} \underbrace{\left(.5 \frac{\lambda}{NA} (2\pi r_i) \frac{J_1(2\pi r_i)}{(2\pi r_i)} \right)}_{\text{Max ring influence}} \underbrace{\left(\pi \frac{(\lambda / NA)^2}{64 r_i^2} \right)}_{\text{Detection zone } (a_i)} \underbrace{\left(\frac{a_i \cup A_\sigma}{a_i} \right)}_{\text{Zone / source overlap}} \underbrace{\Gamma_a}_{\text{Zone intensity}} \right]^2$$

Eq. 4-10.

where A_σ is the total area of the source-image and r_i is the radius of the i^{th} LPR ring. The detection zone (a_i) is defined as the region in the source that will cause spill-over to occur and is depicted in Figure 4-12. Note that larger rings achieve a smaller detection zone, although their maximum ring influence is less. In actuality, the detection zone is a Gaussian shaped function as seen in Figure 4-5, but has been approximated here as a circle corresponding to the full-width half-maximum of the distribution. If desired, a pinhole in a layer of chrome on the backside of the reticle can be used to ensure that only

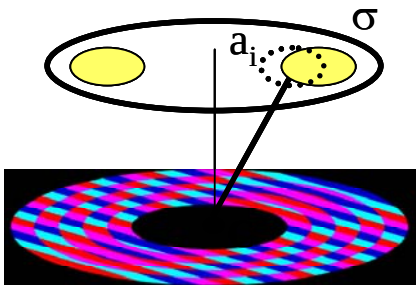

Figure 4-12. LPR detection zone

The radius and number of rings used determines the size of the zone within the source that the LPR can detect. Total spill-over is determined by the overlap of this zone with the actual source.

light from within a defined region is incident on the LPR. The backside pinhole concept will be discussed further in Chapter 5. Γ_a is the intensity of the source that falls within the detection zone, compared with the total intensity of the source. Thus, the value for I_C is the signal intensity as a percent of the clear field intensity. $M_e(T_a)$, as discussed earlier, accounts for the EM and mask making effects. As with the linear phase grating, biasing the features of the four phase grating can help alleviate some of the signal lost due to EM effects, thus increase the thick mask factor and the measurement signal.

A general conclusion that can be drawn from equation 3-10 is that the LPR, when properly calibrated, is more apt at monitoring intensity balance between various illumination frequencies than at determining the absolute shape of a source map. Intensity balance between to off-axis locations of interest (perhaps between two dipole locations) is found simply by analyzing the signals of two calibrated LPRs designed for the appropriate off-axis spatial frequencies. This is a measurement of the total intensity within the detection zone. However, since the slope of the intensity signal curve (Figure 4-11) is zero at the target design location (σ_c=0.8), the sensitivity to variations in source spot location at this point is zero. Thus, accurately mapping the angular distribution of the entire source would take many LPRs and be a rather cumbersome measurement.

Additionally, the signal strength relative to the clear field intensity depends on the ratio between the detection zone (a_i) and the total size of the illuminator (A_σ). Light from any illumination angular frequency that is not captures within the detection zone is light that does not contribute to the measurement, but does contribute to the clearing of a large open area. Thus, this technique is most useful for illumination schemes with small values of partial coherence such as dipoles or perhaps quadrupoles.

Finally, it is noted that most of the LPRs experimentally investigated in this chapter consisted of only two rings, giving a maximum signal of about 4% of the clear field intensity for quazar illumination (which corresponds to roughly 8% for dipoles). However, it is predicted that with, for example, a six-ring LPR, the maximum signal strength should increase to roughly 44% of the clear field intensity for dipole illumination. This can be compared with the ideal theoretical sensitivity of about 300%

of the clear field signal, extrapolated from Figure 4-5b. Thus, roughly 85% of the signal is lost due to all limitations, primarily mask making limitations, EM effects and partial coherence effects. Of course, there exists a design trade-off between signal strength and the size of the detection zone, which is tunable by varying the number of LPR rings in the test reticle design.

4.6. Summary and Discussion

The linear phase ring has been introduced to create a central peak intensity for monitoring the intensity in a particular illumination angular frequency. The available signal and illumination angular discrimination allow flexibility in the LPR design, although for practical signal strength it is most advantageous for monitoring dipoles or quadrupoles. Mask calibration is required and the measurement involves simply determining the intensity at the center of the pattern's image. Simulation studies of a four-phase implementation show a possible signal of roughly 44% of the clear field for measuring the intensity of the poles of a dipole illumination scheme with a six-ring LPR. Assuming the resist process and measurement extraction is reliable to within 1% of the clear field, then this suggests the LPR – when properly calibrated – is capable of monitoring intensity balance between dipoles to within about 2%. However, it is likely not practical for a full source-image measurement, as that would require a very large number of LPRs. The signal levels can be designed to be sufficiently high that the monitors can be used directly in production without special exposure conditions. A similar target with only two phases has also been introduced to measure the degree of temporal coherence between two pupil locations.

5 Monitoring Polarization: PSM Polarimetry

A technique using phase shifting test mask patterns is introduced for monitoring polarization of the illumination in high-NA and immersion projection printing systems. This technique is likely a commercially viable solution, as it promises to meet industrial specifications and is the only known *in-situ* technique that does not require special equipment.

A set of test mask patterns are derived from high-NA proximity effects and serve to scatter light into high angle spatial frequencies. This creates a central intensity dependent only on the local state of polarization. A test mask consisting of multiple patterns is proposed to monitor the polarization from any arbitrary illumination scheme. Proper calibration of the test reticle enables reasonable mask making limitations and mask topography effects to be tolerated. A set of linear equations enable determination of the Stokes parameters from a series of resist images. A series of simulation and experimental studies validate the scientific principles of this technique and provide insight into practical limitations due to realistic imaging conditions. Various potential improvements to the design, fabrication of the mask, and experimental setup are discussed. Additionally, to decrease measurement time, a design modification and double exposure technique is proposed to enable electrical detection of the measurement signal.

Section 5.1 begins by deriving the polarization monitors – or in polarimetry terminology, polarization analyzers – from theory of coherent high-NA imaging. They exist in two embodiments, the Radial Phase Grating (RPG) and the Proximity Effect Polarization Analyzers (PEPA), and operate by taking advantage of what is typically an

unwanted side-effect of high-NA imaging: the transformation of the radial pupil polarization component into an electric field component oriented normal to the wafer surface. The analyzers create measurable normal-component signals in resist by engineering which incident polarization component becomes subject to high-NA effects. Section 5.2 adapts theory from the field of imaging polarimetry and presents a method to monitor the Stokes parameters from the resist images of a series of analyzers on a calibrated test mask. Calibration is essential and enables a reasonable polarization measurement in the face of fairly severe mask topography effects and mask making limitations. A set of six analyzers allows for a complete characterization of the polarization state of incident illumination, although less patterns are likely sufficient for optical lithography. Simulated examples for on-axis and off-axis illumination illustrate the concept. Section 5.3 describes a test reticle design that enables polarization characterization of the full angular extent of the illuminator by employing a pinhole aperture in a backside layer on the test reticle.

Experimental results from two test reticles are reported in Section 5.4, displaying polarization sensitivity of both the on- and off-axis monitors and illustrating the calibration and measurement procedure. The first reticle employed the RPG analyzers and special apertures in the tool for illumination angular frequency selection and showed a sensitivity of about 0.3 percent of the clear field per percent change in polarization state. The second reticle employed the more sensitive PEPA analyzers, a backside pinhole array for frequency selection and a more robust experimental setup. Although the backside pinhole layer was initially misaligned, the results indicate that the current design is capable of measuring linear polarization with a sensitivity of about 1 percent of the clear field intensity per percent change in polarization state. Although many aspects of the technique have yet to be optimized, this sensitivity implies a measurement of the Stokes parameters to within about 0.03 to 0.04, corresponding to a polarization measurement to within 2%. Section 5.5 discusses relevant imaging limitations. The impact of systematic and random errors are discussed, as well as various sensitivity detractors, notably mask topography effects since mask features are on the order of the wavelength of light. Various potential improvements, as well as a comparison to existing

techniques, are offered in Section 5-6 and may lead to a sensitivity of 2 percent of the clear field intensity per percent change in polarization state and a corresponding Stokes measurement to within 0.02. Finally, Section 5-7 describes how a double exposure and pattern transfer to a conducting layer enables electrical detection of the signal, offering a much faster means of data collection than analyzing photoresist images with a scanning electron microscope (SEM).

At the current time, the only other known technique to monitor polarization is an on-board technique being developed by Nikon, called the Apollo Polarization Measurement System [23]. Collaboration with Nikon in this research has enabled the PSM polarization analyzers to be calibrated using Apollo. It is concluded that the likely measurement sensitivity of PSM Polarimetry makes it a commercially viable technique to independently verify tool polarization control and to provide a benchmark for comparison over time or from tool to tool.

5.1. PSM polarization analyzers: Pattern derivation

5.1.1 Concept and pattern evolution

The polarization analyzers exist in two embodiments and are illustrated in Figure 5-1. First, to demonstrate the high-NA vector effect employed by these monitors, a periodic alternating phase linear grating, as shown in Figure 5-1a, is imaged with coherent illumination ($\sigma = 0.1$) and orthogonal polarization states in Figure 5-2. At high numerical aperture, the resulting two-beam interference pattern becomes sensitive to incident polarization state. The incident state which becomes the TE component in the pupil produces perfect image contrast, whereas the TM component suffers degraded or reversed image contrast. Thus, tracking the intensity of the one of the nulls of the interference pattern is a simple means to monitor polarization state. The vector diagrams in Figure 2 show that at the peaks of the interference at the wafer plane, the x and y components add and the z-components subtract, or:

$$I_{Peak} = E_{0y}{}^2 + (2E_{0x}\cos(\theta))^2 \qquad \text{Eq. 5-1.}$$

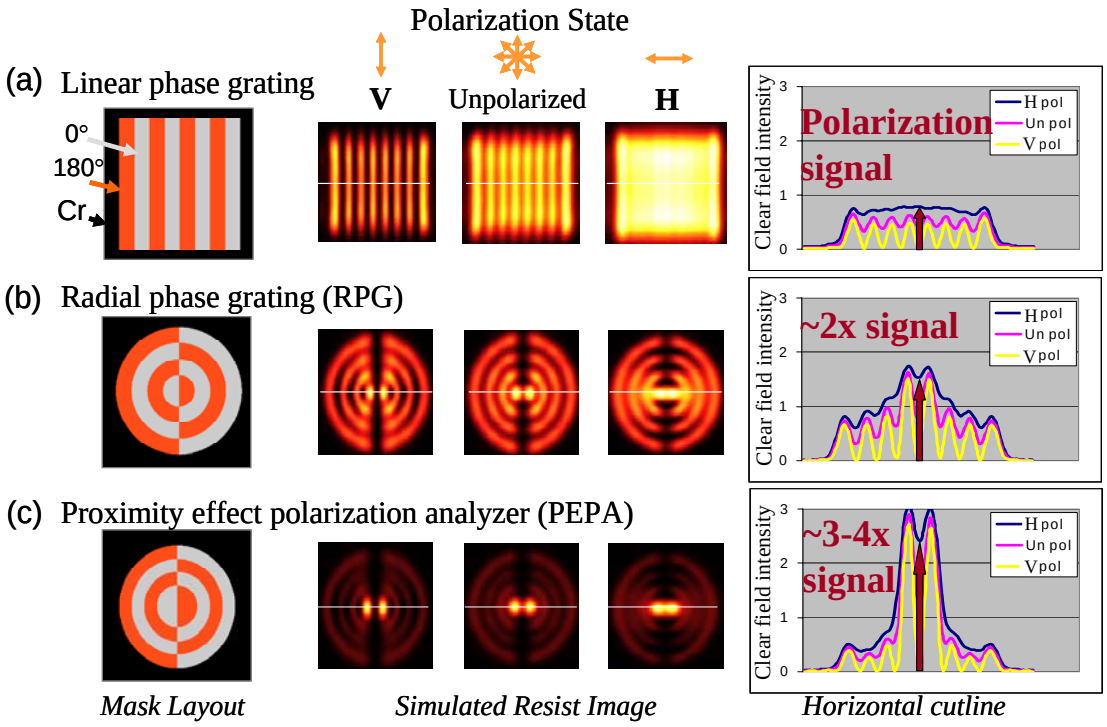

Figure 5-1. PSM polarization analyzers

(a) Monitoring the nulls of an alternating phase periodic linear grating provides a polarization dependent signal. (b) The image center of a periodic radial phase grating (RPG) offers a 2x improvement in signal strength. (c) The optimum pattern is derived from proximity effects (PEPA) enabling a 3-4x signal improvement.

Likewise, the nulls occur when the x- and y-components subtract and the z-components add, or:

$$I_{Null} = (2E_{0x}\,\mathbf{sin}(\theta))^2 = (2E_{0x}NA)^2 \qquad \text{Eq. 5-2.}$$

Approximating the two diffracted orders as $2/\pi$ times the fields incident upon a line-equal-space mask, this is, for the case of unpolarized or circularly polarized light, roughly:

$$I_{Null} = 0.8NA^2 I_{CF} \qquad \text{Eq. 5-3.}$$

Thus, ideally the intensity of the nulls with respect to the clear field intensity (I_{CF}) is solely a function of the numerical aperture. Note that the desired NA that light is scattered to results from the period of the grating as:

$$P = \frac{M\lambda}{NA(scattered)} \qquad \text{Eq. 5-4.}$$

where M is the tool magnification and λ is the illumination wavelength. Since the intensities of the nulls are dependent on only one polarization component, a simple linear polarization monitor may consist of two Alt-PSM gratings oriented perpendicular to each other.

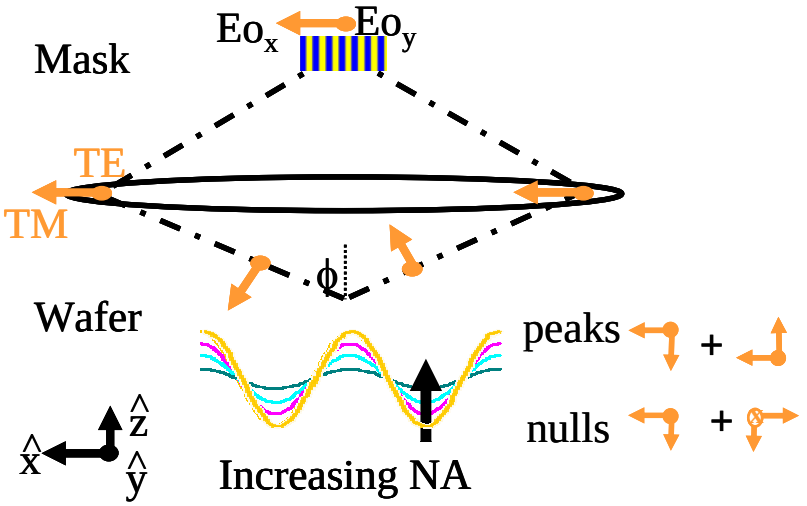

Figure 5-2. High-NA vector effects

High-NA imaging produces a z-component of electric field at the image plane from TM polarized light in the pupil plane. The monitors proposed in this paper take advantage of this effect by engineering which mask plane polarization component produces this z-component signal. The z-component from opposing diffraction orders adds coherently in the nulls of the interference pattern.

5.1.1.1 Radial phase grating (RPG)

An improved monitoring scheme with increased signal strength and measurement sensitivity is possible by altering the mask pattern to focus energy to a central location. This can be achieved by generalizing the above concept from a periodic grating in a linear direction to a periodic grating in the radial direction. This Radial Phase Grating (RPG) is shown in Figure 5-1b. The measurement consists of determining the intensity at the center of the pattern on the wafer. The pattern is constructed with an odd function along any radial cutline such that the E_x and E_y components contribute nothing at the

center. Thus, the electric field at the center ideally has only a z-component (resulting from high-NA effects) and is written as:

$$E_Z(center) = -j(2E_{0x}NA)^2 \int_0^{\varphi} \cos(\varphi) \qquad \text{Eq. 5-5.}$$

Comparing this to the simple linear grating,

$$E_Z(center) = E_Z(null, \text{linear grating}) \bullet 2 \qquad \text{Eq. 5-6.}$$

where φ is defined as the spatial angle of the pattern and is set to a maximum of 90°. Thus, the RPG offers roughly a factor of 2 improvement in signal strength over the simple linear case.

5.1.1.2 Proximity effect polarization analyzers (PEPA)

An additional improvement is provided by maximizing proximity effects in the form of the Proximity Effect Polarization Analyzers (PEPA), shown in Figure 5-1c. The PEPA maximizes the coherent spill-over of electric fields oriented normal to the wafer surface, thus maximizing the polarization-dependent high-NA signal. Similar to the derivation of Section 2.1.1.2, the z-component of the electric field at the image plane due to high-NA effects can be shown to follow the relation:

$$E_z(x) = \sin(\theta) E_{TM}(x) = \frac{NA}{n_{resist}} E_{TM}(x) = \frac{k_x}{k_0} E_{TM}(x) = \frac{j}{k_0} \frac{\partial}{\partial x} E_{TM}(x) \qquad \text{Eq. 5-7.}$$

where k_x is the propagation vector along the wafer. Thus, the z-component of the electric field is proportional to the spatial derivative of the low-NA, or scalar, component that is parallel to the TM component (which is, in this case, the x-component). As an example, the electric field z-component of a 2-beam interference pattern will behave sinusoidally, resulting in a reversed image intensity distribution compared to the traditional low-NA cosine image.

Considering three dimensions, the point spread function that describes proximity effects can be differentiated in the x- and y-directions to form two polarization-

dependent, E_z point spread functions. These PSFs are shown in Figure 5-3b and illustrate the polarization-dependent proximity effect for the, typically unwanted, z-component of light. The concept of reciprocity implies that an object pattern resembling the E_z PSF, as shown in Figure 5-3c, will have the maximum coherent 'spill-over' of z-component light into the center of the image. In other words, this pattern becomes a detector for one polarization component where the measured signal is the intensity at the center of the pattern's image. Two patterns oriented perpendicular to each other become a means of comparing the amount of light in orthogonal polarization components. The arrows in Figure 5-3c depict the polarization components for each pattern that result in the TM component in the pupil, and thus the z-component signal on the wafer. This signal is extracted from photoresist measurements as the dose to clear of the center of the image, as shown in Figure 5-3d. The dimension for the inner ring radius and each outer ring's width are:

$$r_{inner} = \frac{0.85M\lambda}{NA} \quad , \quad width_{outer} = \frac{0.5M\lambda}{NA} \qquad \text{Eq. 5-8.}$$

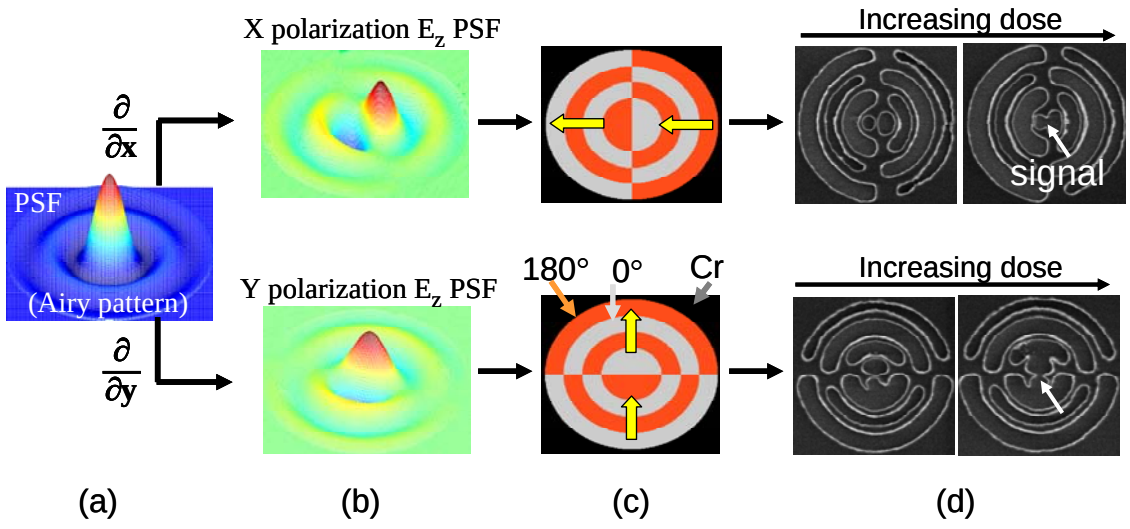

Figure 5-3. Derivation of the PEPA analyzer

The spatial derivative of the (a) low-NA PSF results in (b) two polarization-dependent z-component point spread functions (PSFs). (c) The corresponding mask patterns are thus the most sensitive to one polarization. (d) The dose to clear of the image center is considered the signal (resist image is shown for an RPG).

5.1.2 On-axis, linear polarization analyzers

When imaged in a slow detector such as photoresist, both the RPG and PEPA analyzers derived in the previous sections serve to sample a single, time-averaged, linear polarization component for coherent on-axis (small sigma) illumination. Since light is a transverse electromagnetic wave, the state of polarization can be described by either two orthogonal vector components (consisting each of a magnitude and phase) – or the time averages of four components (two orthogonal and the two bisectors of those orthogonal components). Thus, the complete state of linear polarization can be monitored with a set of four analyzers oriented at, for example, 0°, 45°, 90°, and 135°. Section 5.2 will develop this concept further.

The theoretical response of a set of analyzers to change in linear polarization state is shown in Figure 5-4. The field at the image center of the pattern of Figure 5-4a is proportional to only the x-polarization of the incident illumination and:

$$I(center, \text{Figure } 5\text{-}4a) = \frac{R^2}{R^2+1}\kappa \cdot NA^2 I_{CF} \qquad \text{Eq. 5-9.}$$

where κ is a scaling factor depending on various factors such as which analyzer is used, the number of rings used in the pattern, illumination partial coherence and, potentially, to account for realistic sensitivity detractors such as those discussed in Section 5.5.1. Conversely, Figure 5b is dependent only on the y-polarization:

$$I(center, \text{Figure } 5\text{-}4b) = \frac{1}{R^2+1}\kappa \cdot NA^2 I_{CF} \qquad \text{Eq. 5-10.}$$

R is defined as the ratio of x- to y-polarization:

$$R = \frac{E_{OX}}{E_{OY}} \qquad \text{Eq. 5-11.}$$

Thus, comparing the intensities at the center of these two patterns is a means to determine the ratio of linear polarization. The graphs corresponding to Figures 5-4a and 5-4b show the theoretical central intensity behavior for RPGs with various NAs, where NA is again related to the period of the RPG.

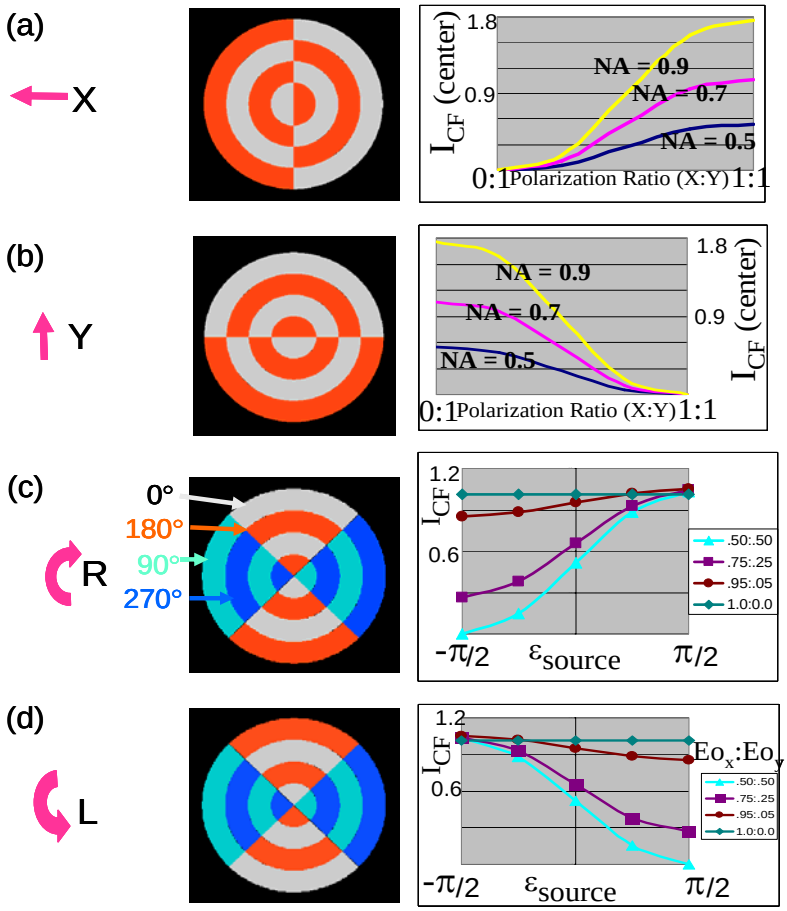

Figure 5-4. On-axis analyzers

Four variations of the RPG serve to: (a,b) monitor ratio of linear polarization (Eox:Eoy) and (c,d) monitor degree of circular polarization (εsource). Theoretical signal behavior is shown.

Figure 5-5 shows a thick mask simulation in resist (Panoramic software) of an on-axis PEPA analyzer designed to measure linear polarization in the x-direction. The signal is considered the intensity at the center of the resist image and is shown to be very sensitive to orthogonal incident polarization states. Also, it is noted that for this example, the measurement consists of detecting the intensity in a saddle – with peaks on one side and nulls on the other.

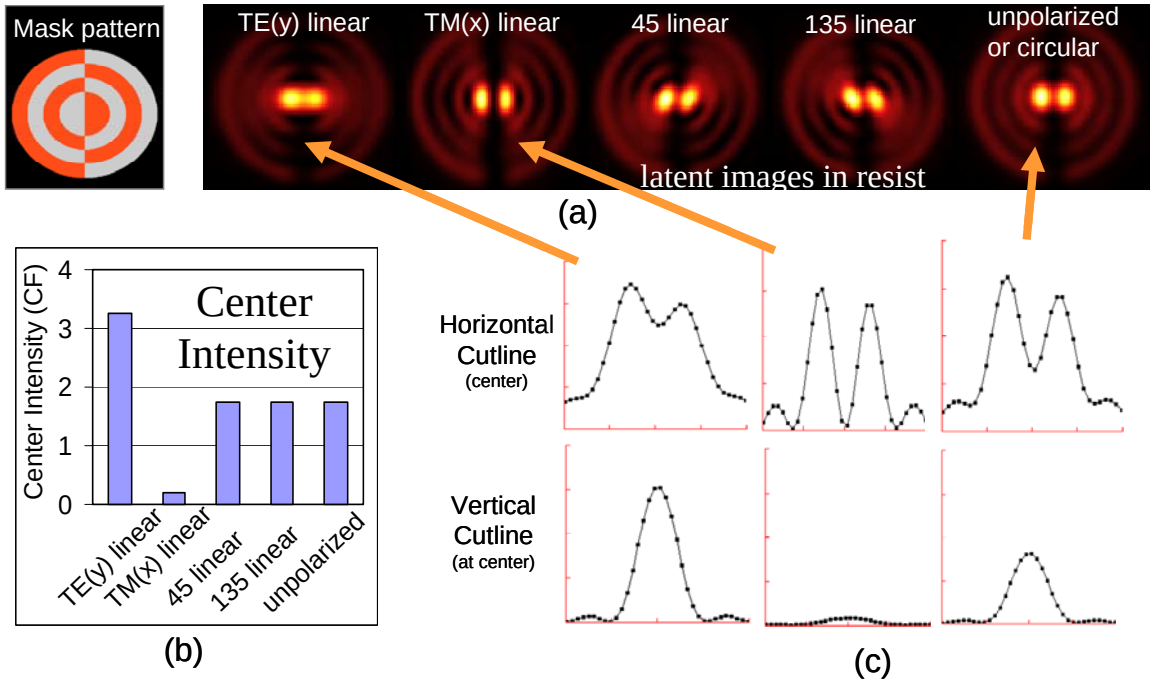

Figure 5-5. Simulation of on-axis linear PEPA analyzer

(a) Simulated latent resist images for one analyzer under various illumination conditions show (b) good sensitivity to polarization. (c) The measurement consists of determining the intensity at the center of the image, which is shown to be a saddle. (resist stack: resist: n = 1.7, k = 0.018, 225nm ; ARC: n = 1.5, k = 0.54, 35nm)

5.1.3 Circular polarization analyzers

Analysis thus far has only considered linear polarization, where there is no temporal phase relationship between the x- and y-polarization components. However, to consider this possible phase relationship for circularly or elliptically polarized light, the incident electric field is written as:

$$E_0 = E_{0X}\,\mathbf{exp[}\,j\varepsilon_{source}\,\mathbf{]}\hat{x} + E_{0Y}\,\hat{y} \qquad \text{Eq. 5-12.}$$

Monitoring this phase relationship, which determines the degree of circular polarization, is possible with a set of modified analyzers. This pair of patterns is shown in Figures 5-4c and d and consists of four phases, introducing 90 and 270 degree portions. Thus, the pattern center forms a vortex where a normally incident plane wave is circularly rotated in a corkscrew-like manner. The only difference between the two patterns is the direction of rotation, either right- or left-hand circular.

Although the center of a vortex is typically a null in intensity, the fact that the Alt-PSM grating scatters energy predominantly to the outside of the lens system, high-NA effects dominate at the center of the vortex in the image:

$$E_Z(\text{vortex center}) \propto NA[E_{0X}e^{j(\varepsilon_{source}-\varepsilon_{pattern})} + E_{0Y}] \qquad \text{Eq. 5-13.}$$

Thus, once E_{ox} and E_{oy} are determined with the linear analyzer, the degree of circular polarization (related to ε_{source}) is determined by measuring the intensity at the center of the two circular analyzers. Two patterns are necessary to determine both the magnitude and sign of the phase relationship. Note that the phase angle induced by the pattern ($\varepsilon_{pattern}$) is either $\pi/2$ or $-\pi/2$, depending on the direction of the pattern's vortex rotation. The graphs corresponding to Figures 5-4c and d show the predicted intensity at the pattern center as a function of ε_{source} for various linear polarization ratios of an RPG designed for an $NA_{desired}$ of 0.7.

Another explanation for the behavior of the circular polarizaiotn analyzers is found in an analogy to an apparatus used to monitor circular polarization of a collimated laser beam on a lab bench. Typically, a sequential polarizer, rotator (quarter wave plate), and CCD detector, as shown in Figure 5-7a, are used to sample specific polarization states depending on the order and orientation of the elements. The PSM circular analyzer can be thought of as a superposition of a polarizer and quarter wave plate. The resist serves as the detector.

5.1.4 Off-axis polarization analyzers

To monitor off-axis illumination, the monitors shown in Figure 5-4 are modified by multiplying them by a four-phase linear phase progression (0°, 90°, 180°, 270°), as shown in Figure 5-6. The four-phase grating, described further in Chapter 3, serves to diffract the incident plane wave into only the +1 and higher orders. In other words, it redirects the light into the pupil at an angle determined by the period of the four-phase grating. Consequently, the period is chosen to correspond to the desired off-axis measurement location (σ_c) by:

$$P(4-phase) = \frac{M * \lambda}{\sigma_C * NA} \qquad \text{Eq. 5-14.}$$

Thus, the off-axis analyzers combine two effects to monitor polarization: redirection by the four phase grating and high-NA diffraction by the radial pattern to produce the polarization dependent z-component signal at the wafer. Again, multiple orientations of the radial aspect of the pattern serve to sample different polarization components. For example, the analyzer illustrated in Figure 5-6 is designed to monitor TE polarization from an off-axis frequency in the x-direction.

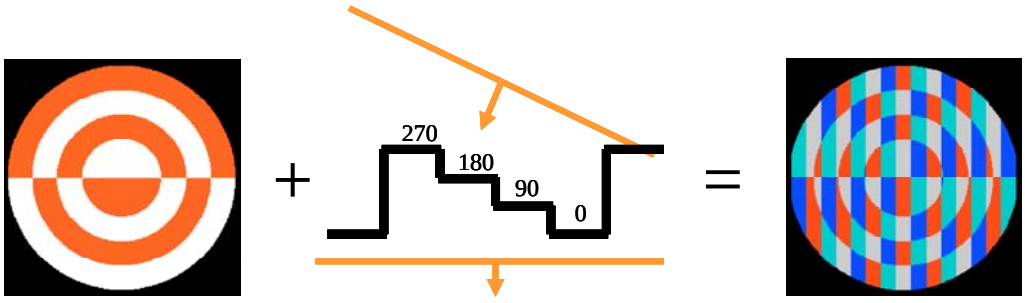

Figure 5-6. Off-axis analyzer

Polarization from a off-axis illumination is monitored by multiplying the on-axis analyzer by a four-phase linear phase progression corresponding to the off-axis angular frequency. This example shows a PEPA designed to monitor TE polarization from off-axis illumination in the x-direction.

5.2. PSM Polarimetry: Monitoring polarization with multiple analyzers

A set of four calibrated PSM analyzers is theoretically sufficient to completely characterize the state of incident polarization in high-NA projection printing systems. However, fewer analyzers are likely sufficient for the needs of optical lithography where only the linear polarization states that correspond to the orientation of features in the IC design are typically of interest. The theory described in this section is familiar to the field of polarimetry and closely follows that illustrated by Chipman [11]. In polarimtery, a set of analyzers are used to each measure the flux (F) of one polarization component in the incident light. On a lab bench, this is typically accomplished with a time-sequential series of arrangements of a polarizer, rotator (quarter wave plate) and CCD detector, as in Figure 5-7a. PSM polarimetry employs instead a series of mask patterns arranged spatially on the test reticle. To account for the fact that the analyzers will not consist of

perfect polarization elements, the analyzers are first calibrated, producing a polarimetric measurement matrix (W) for each set of analyzers. This calibration data is then used to determine the measured Stokes parameters (S_m) describing the polarization state from any arbitrary illumination by solving a set of linear equations. Calibration is accomplished by illuminating the polarimeter with a series of known polarization states. It is noted that accurate calibration will alleviate imperfections introduced by mask topography effects such as vector effects and mask making limitations. Thus, reasonable mask making errors such as layer-to-layer misalignment and phase etch inaccuracies will be tolerated.

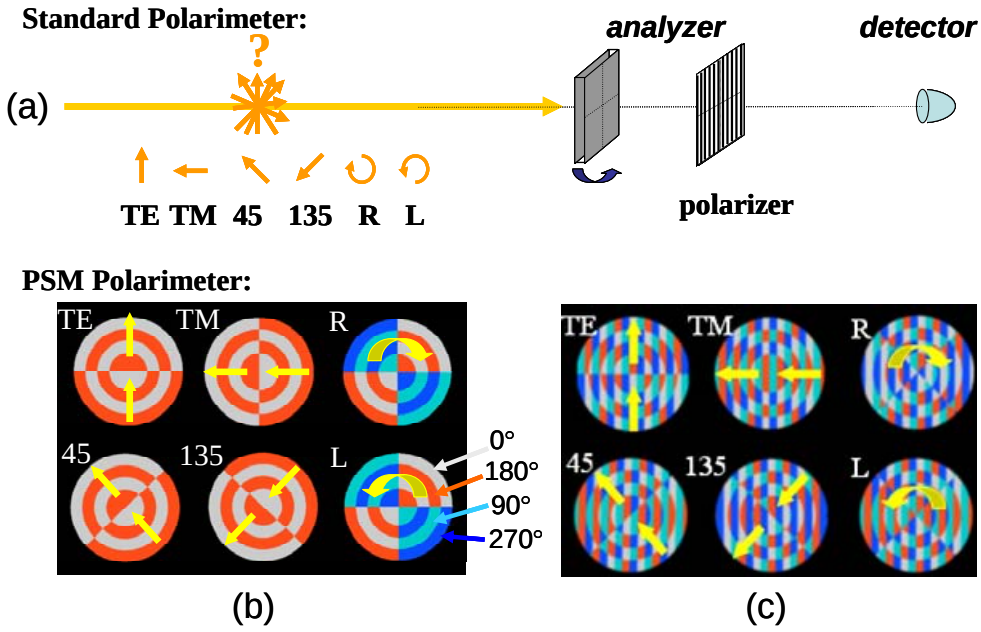

Figure 5-7. Standard and PSM polarimeter

(a) A typical lab bench polarimeter consists of six time-sequential combinations of a rotator, polarizer and CCD detector. A PSM polarimeter is comprised of six PSM analyzers arranged spatially on a test reticle for (b) on-axis illumination or (c) off-axis illumination. When properly calibrated, resist images of the polarimeters determine the Stokes parameters.

In the Mueller calculus, commonly used in polarimetry, the Stokes vector (**S**) is used to completely describe the polarization state of light. This vector is defined relative to six flux measurements (P) performed on the light with ideal polarizers placed in front of a detector. The Stokes vector is defined as:

$$\mathrm{S} = \begin{bmatrix} s0 \\ s1 \\ s2 \\ s3 \end{bmatrix} = \begin{bmatrix} P_{TE} + P_{TM} \\ P_{TE} - P_{TM} \\ P_{45} - P_{135} \\ P_R - P_L \end{bmatrix} \qquad \text{Eq. 5-15.}$$

where P_{TE}, P_{TM}, P_{45}, P_{135}, refer to the measured flux from an ideal linear polarizer oriented at 0, 90, 45, and 135 degrees and P_R, P_L refer to that from ideal right and left circular polarizers. In other words, this is the true flux of light in each polarization component. Note that the coordinate system of TE/TM is used here (as opposed to H/V or X/Y) to account for incident angles resulting from the use of circular apertures in projection printing, an important distinction for the off-axis analyzers that were introduced in the Section 5.1.4. The 0 degree axis is defined here in the direction of the TE component (or for the on-axis case, in the y-direction).

5.2.1. Mask layout and calibration

Figure 5-7b and c show the proposed set of six analyzers that are defined here as complete PSM polarimeter for on- or off-axis illumination. In each, the four patterns on the left each create a signal dependent on a particular linear polarization component, where as the two on the right monitor right and left circular polarization, respectively. An incomplete polarimeter would consist of fewer patterns and can be designed to just measure the Stokes parameter of interest (which, for optical lithography would typically be S_1 / S_0).

5.2.1.1. Calibration with ideal source

To calibrate the imperfect analyzers with perfect illumination conditions, each analyzer is first characterized by an analyzing vector (**A**), containing four components defined in a manner analogous to a Stokes vector. Defining $F_{TE,TM}$ to be the actual flux measurement taken by the TE analyzer when one unit of TM polarized light is incident, the analyzing vector (A) of a single analyzer is defined as:

$$\mathbf{A}_{\mathrm{TE}} = \begin{bmatrix} a_{0,TE} \\ a_{1,TE} \\ a_{2,TE} \\ a_{3,TE} \end{bmatrix} = \begin{bmatrix} F_{TE/TE} + F_{TE/TM} \\ F_{TE/TE} - F_{TE/TM} \\ F_{TE/45} - F_{TE/135} \\ F_{TE/R} - F_{TE/L} \end{bmatrix}, \quad \mathbf{A}_{\mathrm{TM}} = \begin{bmatrix} a_{0,TM} \\ a_{1,TM} \\ a_{2,TM} \\ a_{3,TM} \end{bmatrix} = \begin{bmatrix} F_{TM/TE} + F_{TM/TM} \\ F_{TM/TE} - F_{TM/TM} \\ F_{TM/45} - F_{TM/135} \\ F_{TM/R} - F_{TM/L} \end{bmatrix} \quad \ldots \qquad \text{Eq. 5-16.}$$

where the response ($F_{TE,arb}$) of the single TE analyzer to an arbitrary polarization state (S_{arb}) is:

$$F_{TE,arb} = \mathbf{A}_{\mathrm{TE}} \bullet \mathbf{S}_{\mathrm{arb}} = a_{0,TE} s_{0,arb} + a_{1,TE} s_{1,arb} + a_{2,TE} s_{2,arb} + a_{3,TE} s_{3,arb} \qquad \text{Eq. 5-17.}$$

The analyzing vectors of the six PSM analyzers are grouped together in the polarimetric measurement matrix (**W**), which completely characterizes the imperfections of the polarimeter and is defined as follows:

$$\mathrm{W} = \begin{bmatrix} \mathbf{A}_{TE}^{T} \\ \mathbf{A}_{TM}^{T} \\ \mathbf{A}_{45}^{T} \\ \mathbf{A}_{135}^{T} \\ \mathbf{A}_{R}^{T} \\ \mathbf{A}_{L}^{T} \end{bmatrix} = \begin{vmatrix} a_{0,TE} & a_{1,TE} & a_{2,TE} & a_{3,TE} \\ a_{0,TM} & a_{1,TM} & a_{2,TM} & a_{3,TM} \\ a_{0,45} & a_{1,45} & a_{2,45} & a_{3,45} \\ a_{0,135} & a_{1,135} & a_{2,135} & a_{3,135} \\ a_{0,R} & a_{1,R} & a_{2,R} & a_{3,R} \\ a_{0,L} & a_{0,L} & a_{0,L} & a_{0,L} \end{vmatrix} \qquad \text{Eq. 5-18.}$$

5.2.1.2. Calibration with known imperfections in source

In the likely event that the light used to calibrate the analyzers is not perfect (but measured via an independent means), the **W** matrix is calculated as follows:

$$\mathbf{W} = [inverse(\mathbf{S}_c) \cdot \mathbf{F}_c]^T \qquad \text{Eq. 5-19.}$$

where *T* indicates the matrix transpose. Assuming first that only the S_1/S_0 parameter is of interest (see Figure 5-12) only two patterns are used and S_c is defined as the Stokes calibration matrix:

$$\mathbf{S}_c = \begin{bmatrix} S_{0,TE} & S_{1,TE} \\ S_{0,TM} & S_{1,TM} \end{bmatrix} \qquad \text{Eq. 5-20.}$$

$S_{1,H}$ is the (calibrated) S_1 Stokes parameter of the actual horizontal illumination setting. F_c is defined as the Flux calibration matrix:

$$\mathbf{F}_c = \begin{bmatrix} F_{TE,TE} & F_{TM,TE} \\ F_{TE,TM} & F_{TM,TM} \end{bmatrix} \qquad \text{Eq. 5-21.}$$

where $F_{TM,TE}$ is the measured signal for the TM-analyzer exposed with the TE illumination setting.

Instead of measuring one Stokes parameter with two patterns, it is possible to measure two parameters with four patterns. Although this requires more calibration exposures and measurements, it theoretically provides a more robust measurement by offering more redundancy in the measurement and reducing the impact of experimental error. Although the matrices are larger, the math is similar. S_c is defined as the Stokes calibration matrix:

$$\mathbf{S}_c = \begin{bmatrix} S_{0,TE} & S_{1,TE} & S_{2,TE} \\ S_{0,TM} & S_{1,TM} & S_{2,TM} \\ S_{0,45} & S_{1,45} & S_{2,45} \\ S_{0,135} & S_{1,135} & S_{2,135} \end{bmatrix} \qquad \text{Eq. 5-22.}$$

F_c is defined as the Flux calibration matrix:

$$\mathbf{F}_c = \begin{bmatrix} F_{TE,TE} & F_{TM,TE} & F_{45,TE} & F_{135,TE} \\ F_{TE,TM} & F_{TM,TM} & F_{45,TM} & F_{135,TM} \\ F_{TE,45} & F_{TM,45} & F_{45,45} & F_{135,45} \\ F_{TE,135} & F_{TM,135} & F_{45,135} & F_{135,135} \end{bmatrix} \qquad \text{Eq. 5-23.}$$

Since S_c is not a square matrix, the inverse is undefined. Thus, the pseudo-inverse provides the best estimate and the W matrix is calculated as:

$$\mathbf{W} = [inverse(\mathbf{S}_c{}^T \cdot \mathbf{S}_c) \cdot \mathbf{S}_c{}^T \cdot \mathbf{F}_c]^T = \begin{bmatrix} a_{0,TE} & a_{1,TE} & a_{2,TE} \\ a_{0,TM} & a_{1,TM} & a_{2,TM} \\ a_{0,45} & a_{1,45} & a_{2,45} \\ a_{0,135} & a_{1,135} & a_{2,135} \end{bmatrix} = \begin{bmatrix} \mathbf{A}^T{}_{TE} \\ \mathbf{A}^T{}_{TM} \\ \mathbf{A}^T{}_{45} \\ \mathbf{A}^T{}_{135} \end{bmatrix} \qquad \text{Eq. 5-24.}$$

where A_{TE} is the analyzing vector for the TE-analyzer.

5.2.2. Calculating the Stokes parameters

Once the polarimeter is calibrated by **W**, the Stokes vector of any arbitrary illumination ($\mathbf{S}_A$) is theoretically related to the measured flux values from the set of, for example, six analyzers (**F**) by:

$$\mathbf{F} = \begin{bmatrix} F_{TE} \\ F_{TM} \\ F_{45} \\ F_{135} \\ F_R \\ F_L \end{bmatrix} = \mathbf{W}\mathbf{S}_{\text{arb}} \quad \text{or, likewise:} \quad \mathbf{F} = \begin{bmatrix} D_{CF}/D_{TE} \\ D_{CF}/D_{TM} \\ D_{CF}/D_{45} \\ D_{CF}/D_{135} \\ D_{CF}/D_R \\ D_{CF}/D_L \end{bmatrix} = \mathbf{W}\mathbf{S}_{\text{arb}} \qquad \text{Eq. 5-25.}$$

where D_{CF}/D_{TE} refers to the dose that causes the resist in the center of the TE analyzer image to clear, relative to the clear field.

Finally, to determine the Stokes parameters of the actual illumination:

$$\mathbf{S}_m = \mathbf{W}^{-1}\mathbf{F} \qquad \text{Eq. 5-26.}$$

which will be a complete or partial measurement depending on the number of analyzers used. $\mathbf{S}_m$ refers to the measured Stokes vector to account for errors between the calibrated and actual $\mathbf{W}$. Without errors, $\mathbf{S}_m$ would be equal to the actual $\mathbf{S}_{\text{arb}}$. A complete polarimeter was defined here as having six analyzers (Figure 5-7) to minimize the impact of noise, however four is the minimum needed to form a complete polarimetry measurement. If more than four analyzers are used, $\mathbf{W}$ is not a square matrix, thus $\mathbf{W}^{-1}$ is not unique, and $\mathbf{S}_m$ is overdetermined by the measurements. A least squares estimate for $\mathbf{S}_m$ determines the optimum $\mathbf{W}^{-1}$ to be the psuedoinverse ($\mathbf{W}_p^{-1}$) of $\mathbf{W}$ as $\mathbf{W}_p^{-1} = (\mathbf{W}^T\mathbf{W})^{-1}\mathbf{W}^T$. Thus, the best estimate of S_m is:

$$\mathbf{S}_m = (\mathbf{W}^T\mathbf{W})^{-1}\mathbf{W}^T\mathbf{F} \qquad \text{Eq. 5-27.}$$

5.2.3. Simulation studies

In this section the theory previously described will be applied to two practical examples via simulation studies. First, an example of monitoring polarization from an on-axis cone of light is shown using the set of analyzers introduced in Figure 5-7a. Next, the analyzers are modified to detect polarization from an off-axis cone of light by introducing the four phase, linear phase progression into the patterns. All simulations have been performed with TEMPEST Panoramic, accounting for the true vector nature of light, with the following parameters: wavelength (λ) of 193nm, NA of 0.93, magnification (M) of 4, and monopole illumination with σ = 0.1. The resist stack

consisted of 225nm resist (n = 1.7, k = 0.018) and 35nm of antireflective coating (n = 1.5, k = 0.54). This resist stack was chosen due to its availability, however it is noted that increased sensitivity can be achieved by tuning the resist parameters.

5.2.3.1. Simulated Example 1: On-Axis Polarimeter

First, the set of six analyzers shown in Figure 5-7a are simulated with on-axis illumination under seven ideal illumination conditions: TE(0°) linear, TM(90°) linear, 45° linear, 135° linear, Right circular, Left circular, and unpolarized light. The resulting measured flux values (intensity at the center of the image relative to the clear field) are listed in Table 5-1.

		Incident polarization state						
		linear				circular		un-
		TE	TM	45	135	R	L	polarized
analyzer	TE	3.27	0.19	1.73	1.73	1.73	1.73	1.73
	TM	0.19	3.27	1.73	1.73	1.73	1.73	1.73
	45	1.73	1.73	3.27	0.19	1.73	1.73	1.73
	135	1.73	1.73	0.19	3.27	1.73	1.73	1.73
	R	1.37	1.76	1.43	1.71	2.99	0.15	1.57
	L	1.76	1.37	1.43	1.71	0.15	2.99	1.57

Table 5-1. Simulation measurements for calibration of on-axis polarimeter (in units of clear field intensity)

		Analyzer Vectors (A)			
		ao	a1	a2	a3
Analyzer	TE	3.46	3.08	0	0
	TM	3.46	-3.08	0	0
	45	3.46	0	3.08	0
	135	3.46	0	-3.08	0
	R	3.13	-0.39	-0.28	2.84
	L	3.13	0.39	-0.28	-2.84

Table 5-2. Calculated W matrix for on-axis polarimeter

Note that the linear polarization analyzers are slightly more efficient at creating a polarization-dependent signal than the circular analyzers. This is because the 90 and 270 regions in the circular analyzers introduce additional mask topography effects and a net decrease in coherent addition of z-component light at the center of the pattern. Although all analyzers do not behave as perfect polarizers, calibration of the polarimetric measurement matrix (W) enables the set of six patterns to accurately characterize an actual illumination scheme. The resulting W matrix is listed in Table 2.

To simulate an example that may be of practical interest, the response of the on-axis polarimeter to two illumination conditions is considered. First, if the illuminator design is intended to produce light that is 80% TE (y) polarized (where the remaining 20% is unpolarized), then the intended Stokes parameters and expected measured flux values are:

$$\mathbf{S}_{\mathbf{int}\,ended} = \begin{bmatrix} 1 \\ 0.8 \\ 0 \\ 0 \end{bmatrix} \qquad \mathbf{F}_{predicted} = \begin{bmatrix} 2.96 \\ 0.50 \\ 1.73 \\ 1.73 \\ 1.41 \\ 1.73 \end{bmatrix} (CFIntenstiy)$$

However, suppose the actual measurements produce the flux values below (a simulated example using 70% TE(y) polarized light). Calculations with the calibrated W matrix show the measured illumination condition to be 69.8% TE (y) polarized. The resulting error is only about 0.2%.

$$\mathbf{F}_{actual\,(simulated)} = \begin{bmatrix} 2.81 \\ 0.66 \\ 1.73 \\ 1.73 \\ 1.43 \\ 1.71 \end{bmatrix} (CFIntensti\,y) \qquad \mathbf{S}_{m,actual\,(calculated)} = \mathrm{W}^{-1}F = \begin{bmatrix} 1 \\ 0.698 \\ 0.000 \\ -0.001 \end{bmatrix}$$

The two conditions are compared in Figure 5-8a, showing that the signal provided by both the TE and TM analyzers change by about 15% of the resist clear field (i.e. 2.96 – 2.81 and 0.50 – 0.66) for this 10% variation in the TE component, which corresponds to a 5% variation in the S_1/S_0 Stokes parameter. Thus, if calibrated accurately, this 4-ring on-axis polarimeter is likely to measure polarization with a sensitivity of over 3 percent of the clear field per percent change in polarization. Generally, variations of about one percent of the clear field in resist are measurable. Simulation capabilities restricted this analysis to the 4-ring analyzers shown in Figure 5-7. However, depending on the coherence of the illumination, more rings can provide greater signal.

5.2.3.2. Simulated Example 2: Off-Axis Polarimeter

The second example considered in this section is of a set of analyzers designed to monitor polarization from off-axis illumination, shown in Figure 5-7b. Again, the arrows in Figure 5-7b indicate which polarization component is being measured. This example shows the necessity of pre-calibrating the analyzers and, although the mask topography effects are much more severe than the on-axis analyzers, shows the measurement to be as

accurate. To counteract mask topography effects, the actual etch depths for the phase shifted regions were optimized to be 95°, 195°, and 300° for this example [69].

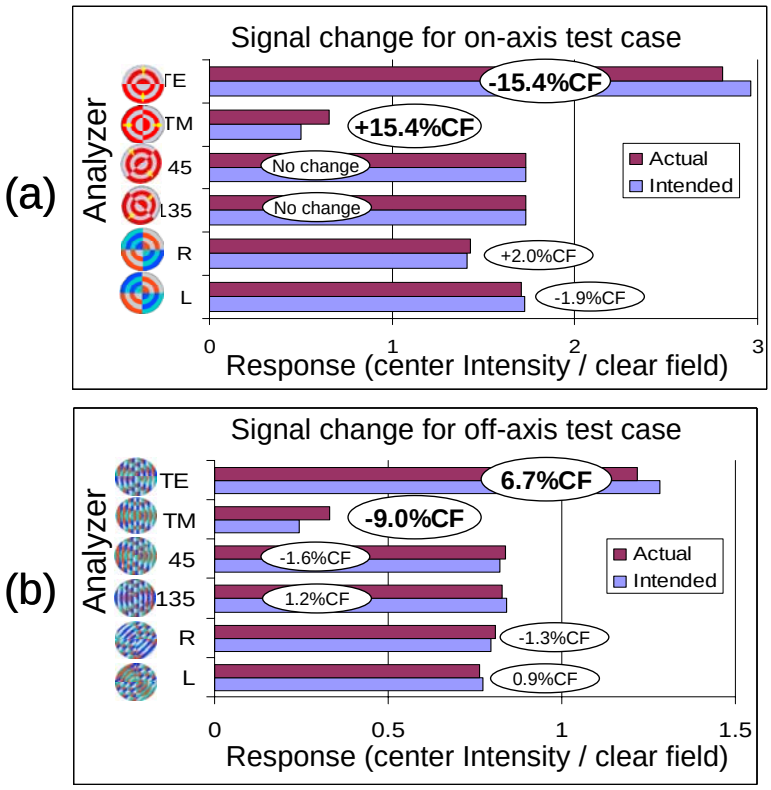

Figure 5-8. Simulated on- and off-axis examples

Perturbation of the response of six analyzers for two simulated (a) on-axis and (b) off-axis illumination conditions: Intended (80% TE polarized, 20% unpolarized), and Actual (70% TE polarized, 20% unpolarized). The signal for this 5% variation in the S1/S0 parameter is roughly (a) 15% of the clear field for the on-axis case and (b) 7.5% for the off-axis case.

A practical example similar to that used for the on-axis monitor was simulated. The only difference being the modifications to the patterns and that the monopole center was moved to $\sigma_c = 0.81$. The resulting flux measurements and calculated W matrix are listed in Table 3.

		Incident polarization state						
		linear				circular		un-
		TE	TM	45	135	R	L	polarized
analyzer	TE	1.42	0.11	0.92	0.58	0.58	0.92	0.75
	TM	0.06	1.83	0.96	0.96	0.96	0.96	0.96
	45	0.79	1.10	1.80	0.10	0.85	1.04	0.95
	135	0.87	0.62	0.07	1.41	0.65	0.83	0.74
	R	0.77	1.02	0.98	0.82	1.70	0.10	0.90
	L	0.79	0.61	0.75	0.65	0.15	1.25	0.70

Table 5-3. Simulation measurements for calibration of off-axis (σ_C = 0.81) polarimeter (clear field intensity)

		Analyzer Vectors (A)			
		ao	a1	a2	a3
analyzer	TE	1.53	1.31	0.34	-0.3
	TM	1.89	-1.8	0	0
	45	1.89	-0.3	1.7	-0.2
	135	1.49	0.25	-1.3	-0.2
	R	1.79	-0.25	0.16	1.60
	L	1.40	0.18	0.10	-1.10

Table 5-4. Calculated W matrix for off-axis polarimeter

Considering again the practical example where the illuminator design is intended to produce dipoles with 80% TE polarized light (20% unpolarized), the expected Stokes parameters and measured flux values would be:

$$\mathbf{S}_{\mathbf{int}\,ended} = \begin{bmatrix} 1 \\ 0.8 \\ 0 \\ 0 \end{bmatrix} \qquad \mathbf{F}_{predicted} = \begin{bmatrix} 1.28 \\ 0.24 \\ 0.82 \\ 0.84 \\ 0.79 \\ 0.77 \end{bmatrix} \mathbf{(}CFIntensti\,y\mathbf{)}$$

However, if the actual illumination was only 70% TE polarized light, then the measured flux values are simulated to be as shown below. Calculations using the derived set of linear equations and the calibrated W matrix imply the actual light is 69.2% TE polarized, an error of less than 1%.

$$\mathbf{F}_{actual\,(simulated)} = \begin{bmatrix} 1.22 \\ 0.33 \\ 0.84 \\ 0.83 \\ 0.81 \\ 0.76 \end{bmatrix} \mathbf{(}CFIntenstiy\mathbf{)} \qquad \mathbf{S}_{m,actual\,(calculated)} = W^{-1}\mathbf{F} = \begin{bmatrix} 1 \\ 0.692 \\ 0.001 \\ -0.001 \end{bmatrix}$$

A comparison of the two conditions, shown in Figure 5-8b, predicts the TE and TM analyzers will change by +6.7 and -9.0 percent of the clear field, respectively. Thus, these 4-ring off-axis monitors are likely to measure polarization with a sensitivity of roughly 1.5 percent of the clear field per percent change in polarization. Again, although the different patterns behave differently, calibration of the W matrix allows for reasonable characterization of the actual illumination.

5.3. Test reticle design: Backside pinhole array

The PSM polarimeters require very coherent light for maximum sensitivity. Thus, they will work best when combined with an aperture to allow only a small cone of incident light (i.e. a small monopole). This can be achieved with a pinhole on the backside of the mask. Without the aperture, this technique is likely to only measure polarization for very small sigma (conventional), or perhaps small dipoles. Using pinholes on the back of the reticle will enable polarization characterization of the full illuminator. A proposed reticle design is depicted in Figure 5-9, showing the front and backside of the reticle for a particular field location. Multiple polarimeters are used in a cluster near each pinhole location, where each polarimeter has a unique period and orientation of the four-phase linear progression depending on its relative location to the pinhole, or likewise, the desired σ_C measurement. The location of each polarimeter is related to the cluster center, which is aligned with the pinhole, as:

$$r_{polarimeter} = t * \tan\left(\arcsin\left(\frac{NA * \sigma_C}{n_g * M}\right)\right) \qquad \text{Eq. 5-28.}$$

where t and n_g are the thickness and index of refraction of the reticle quartz substrate. Thus, the polarization quality of the full angular extent of the illuminator can be measured. This configuration may be repeated across the test reticle, allowing comparison across the field.

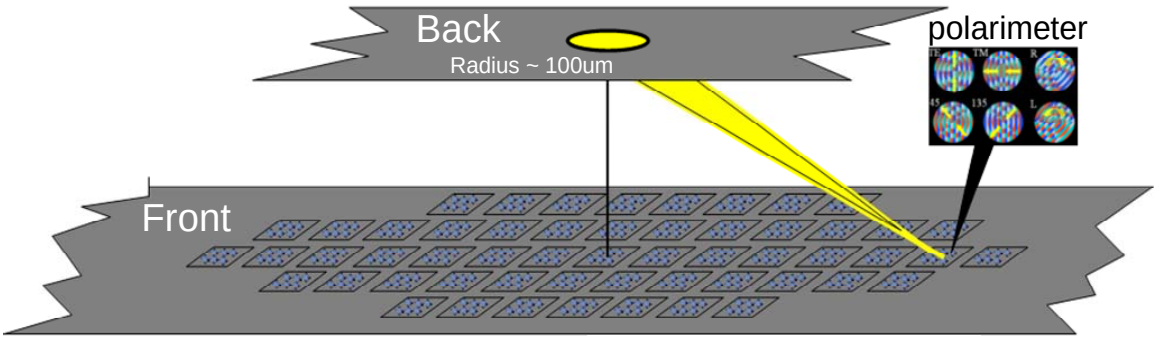

Figure 5-9. Proposed test reticle

Each field location contains a cluster of polarimeters in the vicinity of a pinhole in an opaque layer on the backside of the mask for illumination angular frequency selection.

To account for mask topography effects, calibration of each polarimeter is required resulting in a unique W matrix for each set of analyzers. Although proper simulation can determine the theoretical W matrices (as was done in the previous section), experimental determination of the W matrices is required to account for realistic mask making limitations. It is noted that the accuracy of the measurement will largely depend on the ability to calibrate W. The reticle would then be exposed at best focus through increasing exposure dose with the desired illumination scheme. For each analyzer, the dose that causes the resist to just clear relative to a nearby clear field dose is recorded as the signal.

5.4. Experimental results

To experimentally verify the scientific principles of these monitors, two test reticles were designed, fabricated, and exposed in scanners with multiple polarization conditions. In all experiments, the goal was to test for consistency between this technique and a Nikon proprietary technique, the Apollo polarization measurement system [23].

5.4.1. Test reticle B: Radial phase grating

Test reticle B, fabricated by Photronics, Inc. and donated to UC Berkeley, consisted of a series of RPGs arrayed on a four-phase reticle. Exposures were done on a Nikon 307E with a projection lens NA of 0.85, where special apertures were placed in the tool to achieve an effective sigma radius of 0.1 for on-axis and off-axis (σ_c = 0.81) illumination. The results are reported in this section, displaying polarization sensitivity of both the on- and off-axis monitors. Also, two examples of linear polarization measurements demonstrate the procedure for test mask calibration and how the system of linear equations introduced in Section 5.2.2 is employed for measurement of the Stokes parameters of an arbitrary polarization state.

Figure 5-10a depicts how the RPG serves to scatter light into pupil at an angle depending on the period of the RPG. SEM images of the photomask shows some degradation of pattern fidelity due to mask making effects in Figure 5-10b. Sample resist images of two orthogonal on-axis RPGs exposed with horizontal linear polarization are

shown in Figure 5-10c. The RPG dimensions are chosen to scatter light to an NA of 0.56. Of interest are the doses causing the center of the images to clear the resist threshold. Converted into a percent of the local clear field dose, this is recorded as the measurement signal. Figure 5-10c compares the signal of these adjacent monitors when exposed with nearly orthogonal polarization states, as measured by Apollo. Good symmetry in the behavior of both patterns and a sensitivity of about 0.33 percent of the clear field per percent change in polarization state is observed.

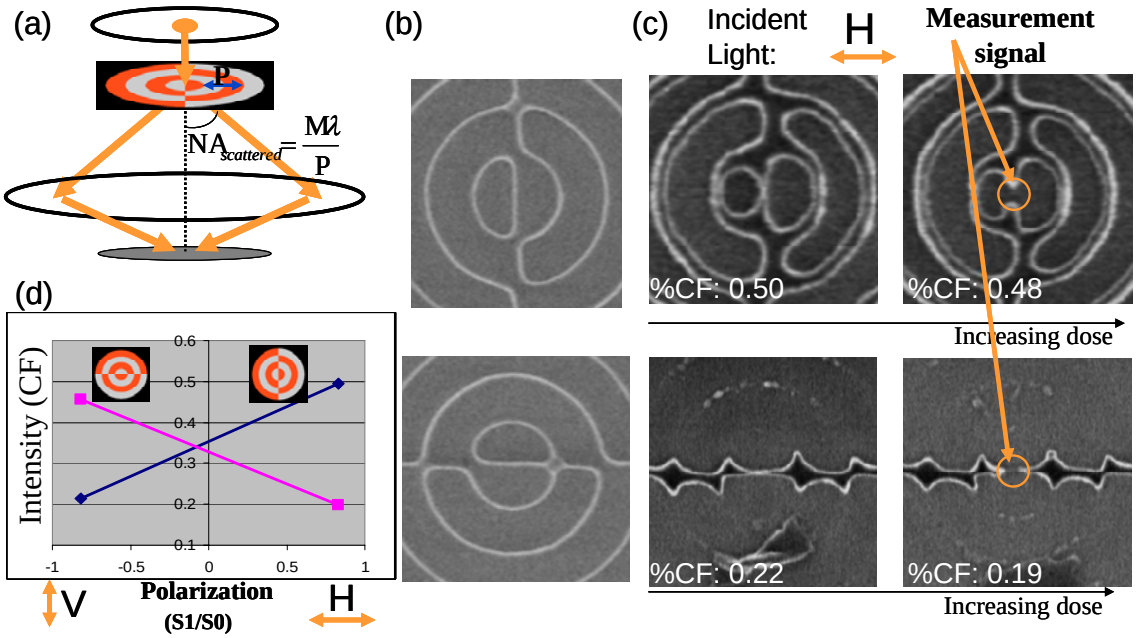

Figure 5-10. Experimental results of on-axis RPG

(a) Imaging of on-axis radial phase grating analyzers with a σ = 0.1 and aperture NAscattered = 0.56. (b) SEM from test reticle B. (c) Signal is extracted from resist images and (d) orthogonal analyzers provide symmetric behavior and a measurement sensitivity of about 0.33 percent of the clear field per percent change in polarization state.

The response of a set of off-axis RPGs designed for a σ_c of 0.8 is shown in Figure 5-11. Although the mask SEM and resist images are more intricate than the on-axis monitors, the example images of a TM analyzer and a TE analyzer exposed with TM polarized illumination display the measurement signals, where the dose causing the center of the image to clear is identified. Comparing the behavior of these monitors when exposed with orthogonal polarization states, Figure 5-11c shows a sensitivity of about

0.23-0.31 percent of the clear field per percent change in polarization state. This is only a loss of roughly 20% compared to the on-axis monitors and is promising in that these monitors are much more difficult to manufacture and suffer from worse mask topography effects. The fact that the two monitors behave differently is expected and is investigated further in the next section. Although these patterns behave very differently, only the absolute sensitivity is important as proper calibration of the test reticle takes into account differences in pattern behavior.

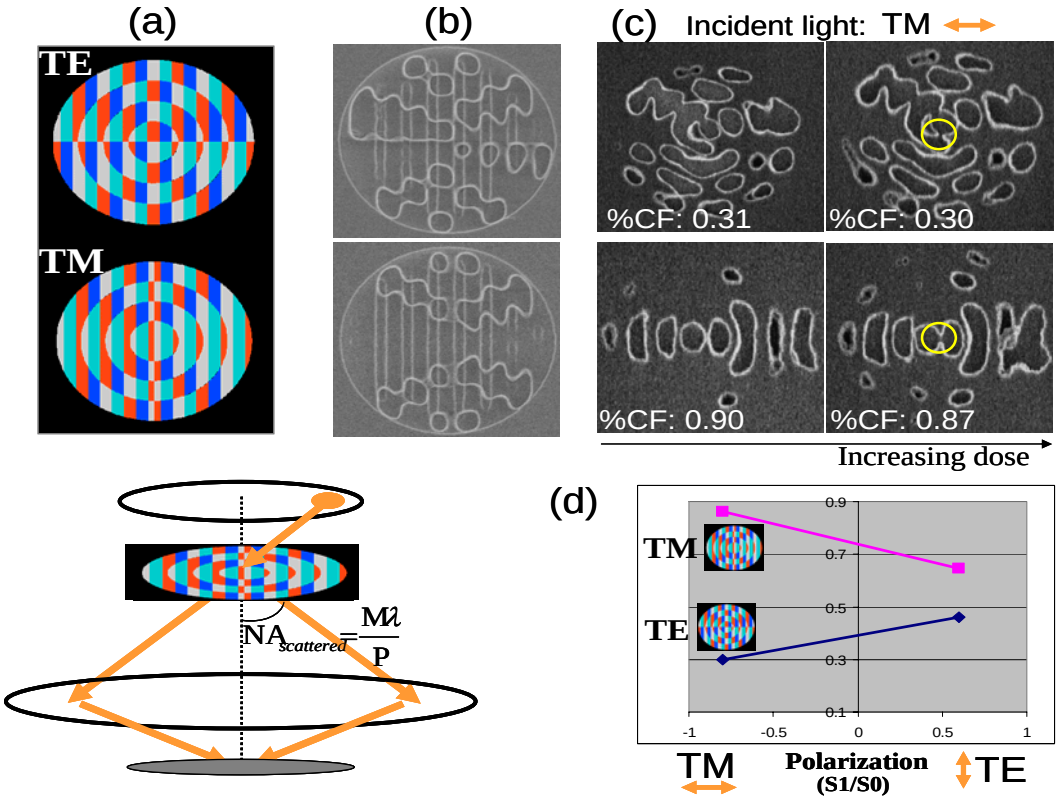

Figure 5-11. Experimental results of off-axis RPG.

(a) Off-axis illumination is monitored by incorporating into the rings of the RPG a four-phase linear phase progression. (b) SEM of mask patterns show difficulty in fabrication, however (c) resist images still show the desired effect. Extraction of the measurement signal and (d) comparison of the behavior of orthogonal patterns shows a sensitivity of about 0.23 to 0.31 for an off-axis monopole at $\sigma c=0.81$. Variations in pattern behavior are explained and accounted for in test mask calibration.

Two experimental examples are shown to test the theory described in Section 5.2.2. First, the two-pattern polarimeters shown in Figure 5-12 are employed for

measurement of only the S_1/S_0 or S_2/S_0 Stokes parameter. Three polarimeters located at the left, center and right side of the imaging field were exposed with as much variation as possible in polarization conditions. Making the bold assumption that each set of patterns behave identically across the field, the W matrix is calculated from one location. Assuming that this W matrix applies to other field locations, the Stokes parameter was calculated from the resulting photoresist measurements. The resulting measurements for both the set of X and Y analyzers (which measure the S_1/S_0 parameter) and the set of 45 and 135 analyzers (which measure the S_2/S_0 parameter) are shown in Figure 5-11. RPG and Apollo measurements agree quite well for the S_1/S_0 parameter and for the center of the field for the S_2/S_0 parameter. However, a 0.22 error is observed on the right side of the field for the S_2/S_0 measurement. This is most likely a result of assuming patterns behave the same across the field.

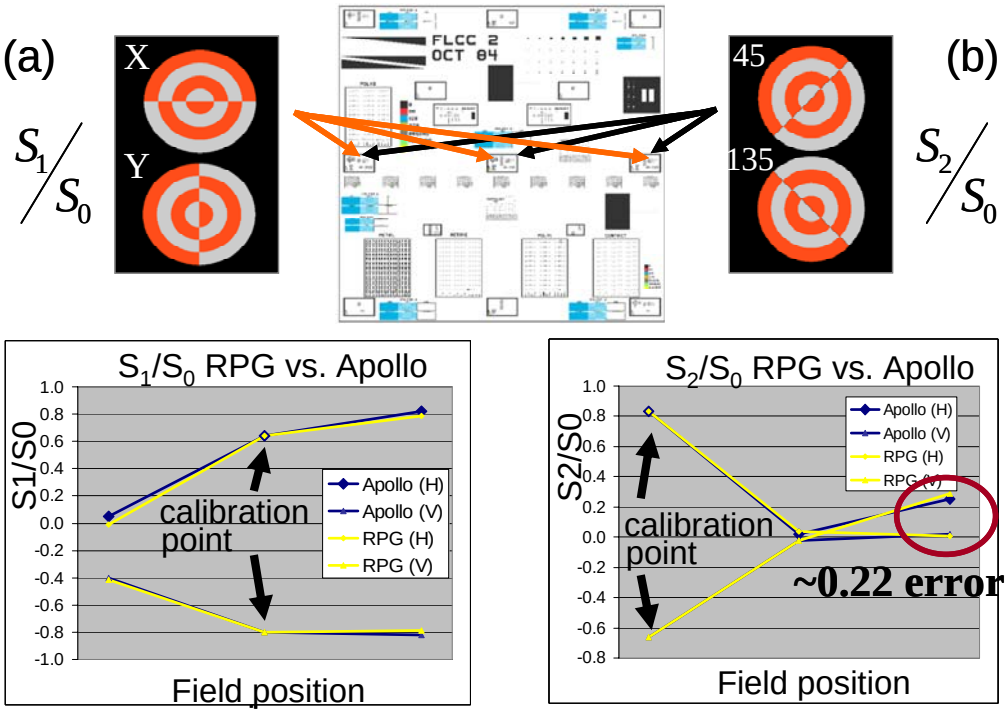

Figure 5-12. Monitoring one Stokes parameter with two RPG analyzers

By varying the polarization state across the field and analyzing sets of similar patterns, a two-pattern polarimeter is calibrated and is capable of approximately measuring either the (a) S1 or (b) S2 Stokes parameter. Assuming patterns behave alike across the imaging field is identified as the largest source of error in this initial experiment.

Additionally, the simultaneous measurement of both the S_1/S_0 and S_2/S_0 parameters is possible with the four-pattern polarimeter shown in Figure 5-13a. Although more analyzers require more measurements, they theoretically are more robust to experimental error. Figure 5-13b plots the results of this calibration and measurement scheme, using the S_1/S_0 and S_2/S_0 parameters as the axes. The four illumination conditions used to calibrate the monitors, as well as the Apollo and RPG measurements for two test illumination conditions (A and B) are shown. Agreement is generally within about 0.2. Discrepancies between experiment and theory are discussed in Section 5.5.

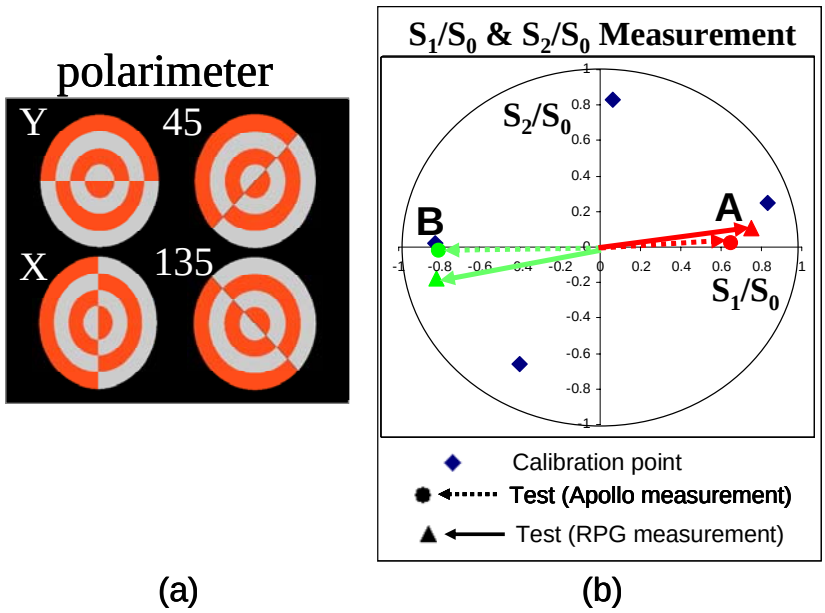

Figure 5-13. Experimental measurement of S_1/S_0 and S_2/S_0

A complete linear polarization measurement is conducted with (a) a set of four patterns. (b) Four illumination conditions from the right and left sides of the field are used to calibrate the polarimeter. Measurements at the center of the field are compared to the Apollo measurement system. Sources of error are discussed in the text.

5.4.2 Test reticle C: Proximity effect polarization analyzers

Test reticle C was fabricated and donated to UC Berkeley by Toppan Photomasks and experiments were conducted on a Nikon 308F. The mask layout, design of the polarization analyzers and the experimental setup were all more robust than in the first experiment, thus targeting a more sensitive polarization measurement of the full spatial

extent of any illumination scheme. Although this first attempt suffered a misalignment problem with a backside layer on the reticle, the achieved results indicate that a measurement sensitivity of about 1 percent of the clear field per percent change in polarization state is possible, once the alignment issues are corrected in the near future. This corresponds to a Stokes parameter measurement to within about 0.02 to 0.03.

Whereas the first reticle only targeted three illumination frequencies with the radial phase grating (RPG) analyzers, the second reticle employed arrays of polarimeters capable of monitoring all frequencies and consisting of the more sensitive proximity effect polarization analyzers (PEPA). The reticle concept was described in Figure 5-9, where a circular cluster of polarimeters were placed in the vicinity of a pinhole (radius ~ 100μm) in a backside layer of chrome. The backside pinhole, while enabling a full illuminator measurement with one photomask, does require large exposure dose values. To account for light lost due to the pinhole, the absolute tool dose values must be multiplied by the following overdose (OD) factor:

$$OD\_factor = \frac{\sigma^2}{r^2} \qquad \text{Eq. 5-29.}$$

where σ is the extent of the illuminator and r is the effective sigma due to the size of the pinhole. For example, r is approximately 0.1 for a pinhole with a radius of 100μm for a ¼ inch quartz mask designed for a 193nm tool. The OD factor used in this experiment was 94.09, corresponding to σ = .97 and r = .1.

The layout consisted of an array of 513 pinhole/cluster combinations with a variety of parameters varied in the design. These variations included three levels of optical proximity correction to account for mask topography effects, two pinhole sizes, nine programmed misalignments of the backside pinhole (aligned ± 50μm) and nine programmed layer-to-layer misalignment to account for expected overlay variations in the mask making process (aligned ± 30nm) . Figure 5-14a identifies the backside pinhole array on both the layout and a photograph of the reticle.

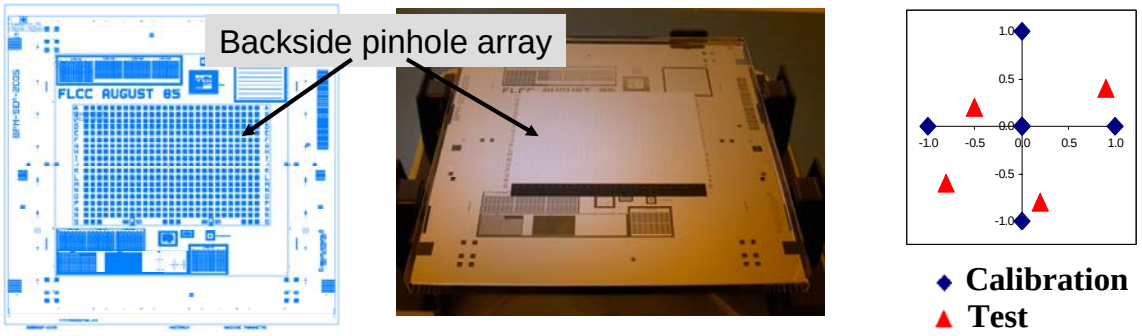

Figure 5-14. Test reticle C: reticle and experimental illumination conditions

(a) The second test reticle is capable of full illuminator characterization and consists of a backside pinhole array for frequency selection. The test mask consisted of 513 pinhole/cluster combinations, which were illuminated with (b) five calibration conditions and four test conditions.

To correctly calibrate each polarimeter, the reticle was exposed on a Nikon 308F with the five calibration polarization states identified in Figure 5-14b. This calibration would enable a **W** matrix to be calculated for each polarimeter. Four additional polarization states, also identified in Figure 5-14b, were used to test the measurement's correlation with the Apollo measurements.

Unfortunately, the initial exposures indicated roughly a 420µm misalignment in the backside pinhole layer, corresponding to about a 0.4 error in the illuminator location. The misalignment was evident by non-circular clusters in photoresist and measurable by identifying which polarimeters had not been exposed. This resulted in a loss of about 80 to 100% of the measurement sensitivity, depending on how a particular pattern was oriented relative to the misalignment (see Figure 5-23). Although a Stokes parameter measurement was not feasible, the patterns that did show sensitivity showed similar trends to a simulated case with a misaligned illuminator. For example, as in Figure 5-15, the Y-analyzer showed a sensitivity of about 0.15 percent of the clear field per percent change in polarization state. Simulation indicates that, for this pattern and misalignment, about 80% of the signal was lost. Thus, with corrected alignment, these monitors are expected to achieve a sensitivity of about 1 percent of the clear field per percent change

in polarization state. Following a similar analysis, the same conclusion is drawn from the 45-analyzer also displayed in Figure 5-15.

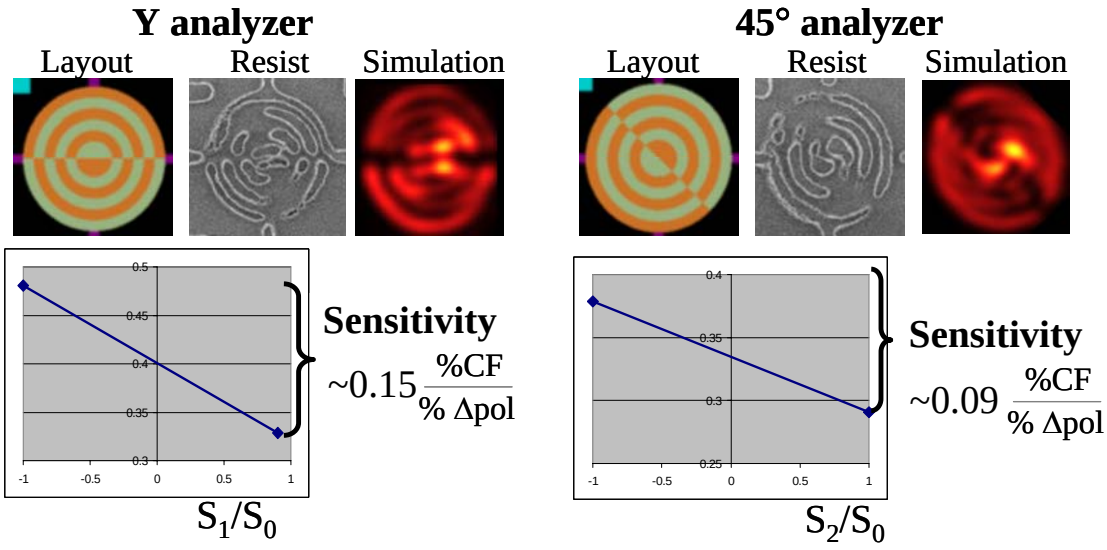

Figure 5-15. Reticle C experimental results

Although an initial 420μm pinhole misalignment decreased measurement sensitivity by 80-100%, the analyzer behavior correlated with simulation of a similar misaligned case. Theory predicts that, once the pinhole alignment is corrected, this reticle should achieve sensitivity of about 1 percent of the clear field per percent change in polarization state. This corresponds to a Stokes measurement to within 0.02 to 0.03. Further improvements are discussed in the text.

5.5. Analysis of relevant imaging limitations

Various effects due to practical imaging conditions undoubtedly limit the effectiveness of this polarization monitoring technique. These limitations are investigated in this section and can be divided into two categories: physical effects that decrease polarization sensitivity and experimental error (both systematic and random). As these limitations are discussed, suggested improvements will be presented by either adjusting the design, experimental setup, or fabrication of the photomask. The next section will comment on future potential of this monitoring technique.

5.5.1. Sensitivity detractors

There are a number of factors that serve to decrease the measurement sensitivity to polarization from the theoretical maximum, where this maximum is considered to be

from the aerial image of an ideal thin mask imaged with perfectly coherent illumination. The leading sensitivity detractors discussed in this section are electromagnetic mask topography effects, mask making limitations, resist stack effects, aspects of the particular RPG or PEPA design, alignment of the pinhole apertures (sigma location), and the need for a finite pinhole size (sigma size). Although all of these can be accounted for by proper calibration of the test reticle, they ultimately increase the measurements vulnerability to random and systematic errors and thus limit the resolution in which the Stokes parameters can be measured. The charts in Figures 5-16 to 5-19 are used to deconvolve some of these effects and Table 5-5 concludes with sensitivity estimates of previous and potential future designs.

5.5.1.1. Electromagnetic interaction with mask topography

As introduced in Section 2.2.1.2, electric fields propagating through a phase shift mask tend to accumulate in regions of higher index of refraction near material boundaries. Depending on feature size, this can impact on both the transmission and phase of light that emerges from a phase shifted feature. Thus, with multiple phase-etched regions with dimensions on the order of the wavelength of light, electromagnetic interaction with the mask topography is likely to be severe in PSM polarimetry.

To illustrate the impact of vector electromagnetic effects, aerial image thin and thick mask simulations are compared in Figure 5-16a for on-axis PEPA and RPG analyzers, in Figure 5-17a for off-axis RPG analyzers, and Figure 5-18a for off-axis PEPA analyzers. A few observations are evident from these plots:

1. On-axis monitors show about a 10% loss of sensitivity due to EM effects. This can be attributed to the fact that since light tends to accumulate in the high index material, the actual transmission (both magnitude and phase) after light propagates through the mask differs slightly from the ideal transmission function. Thus, the pattern fails to completely resemble the polarization proximity effect function and thus is less sensitive to polarization. Enlarging the shifted regions slightly will help alleviate this and is discussed further in Section 5.6.

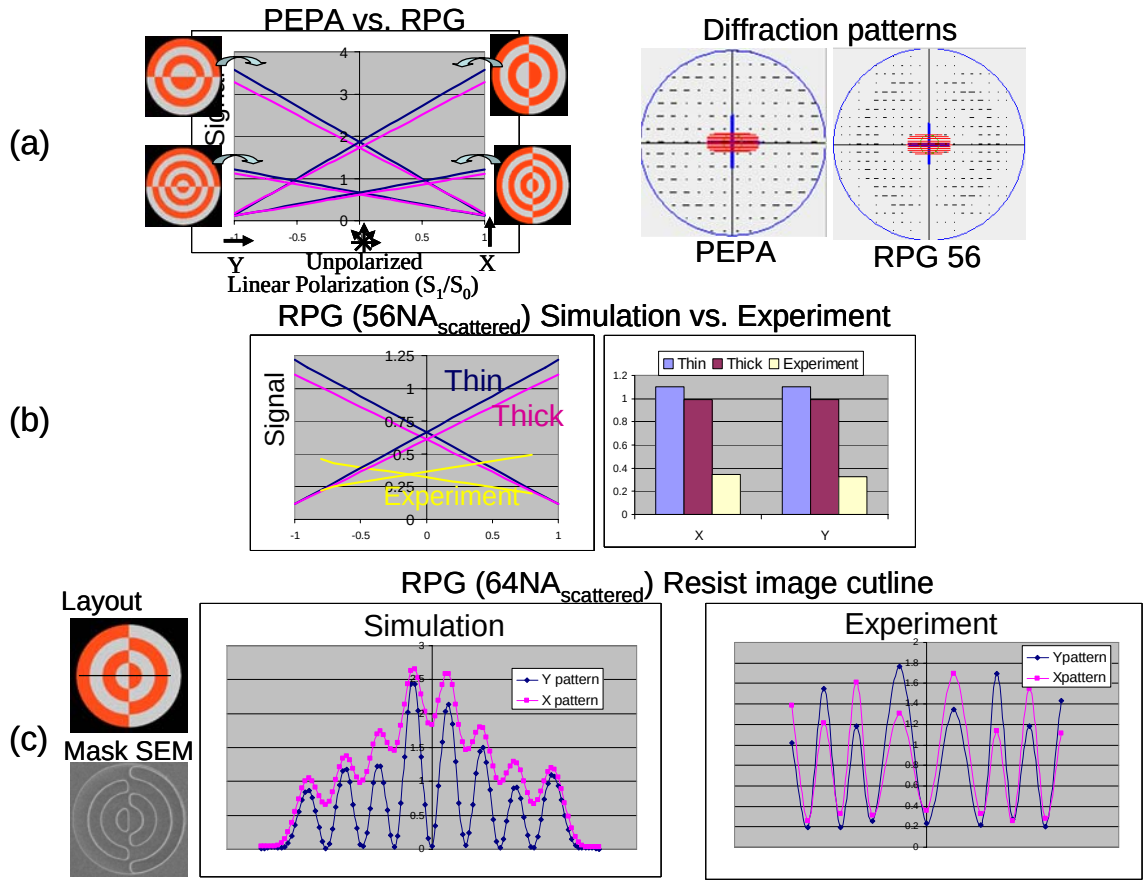

Figure 5-16. On-axis RPG & PEPA

(a) On-axis 4-ring PEPA shows roughly 3x signal over 6-ring RPG with NAscattered = 0.56 by more efficiently scattering light to high-NA. (b) RPG results show experimental sensitivity about 1/3 that of simulation. (c) Large differences are seen between simulation and experiment for RPG (64NAscattered), likely due to mask making imperfections.

2. Off-axis analyzers (both PEPA and RPG) show the TM analyzer to be more sensitive than the TE analyzer. This can be attributed to a combination of two effects:
    a. The design of the TM analyzer makes it inherently less susceptible to mask topography effects. The greatest part of the polarization dependent signal originates from the regions within the pattern that lie along a cutline in the direction of the polarization component being measured. For example, for the TM analyzers depicted in Figures 5-17 or 5-18, a majority of the signal arises from the regions to the left and right of the

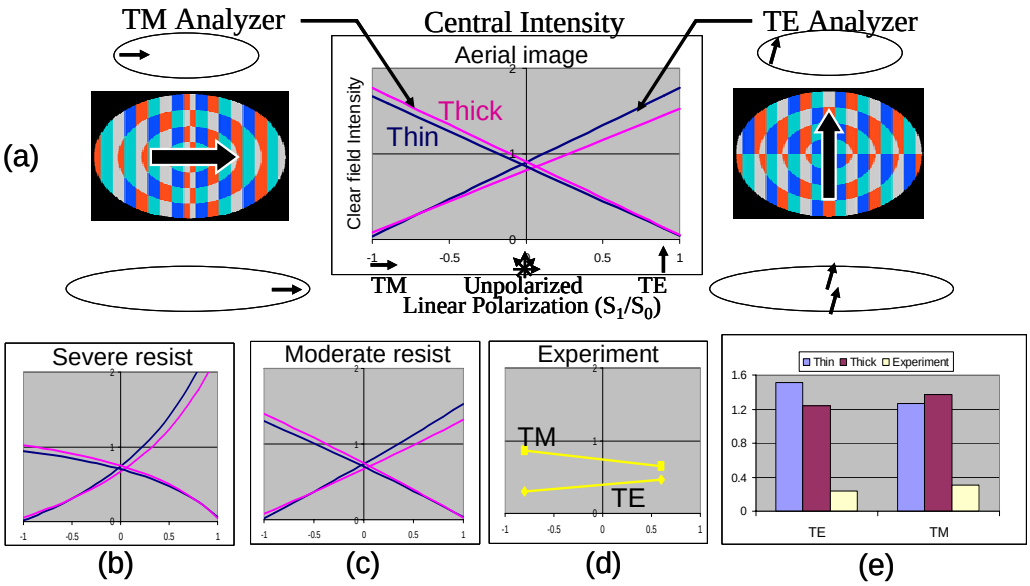

Figure 5-17. Off-axis RPG sensitivity: simulation vs. experiment

TE and TM RPG analyzers with NAscattered = 0.56 show different response to incident polarization for explained reasons for (a) aerial image, (b) resist image with severe resist polarization effects, (c) resist image with moderate resist polarization effects, and (d) experimental results from Reticle B. (e) comparison of analyzer sensitivity

center of the pattern (i.e. not from the top and bottom). Thus, close inspection of those regions of the patterns show the TE analyzer to have smaller and more severe phase steps. As evident by Figure 5-20, which illustrates the near fields just under each analyzer for the different polarizations, the TM analyzer's tranmitted fields more accurately replicate the desired thin mask transmission function. Thus, the TE analyzer's sensitivity is degraded more due to EM effects.

b. The four-phase progression is more effective at redirecting TM polarization than TE polarization. As shown in Figure 5-21a, FDTD simulation shows TM polarized light propagating smoother through a four-phase progression. This results in a smoother phase progression and less amplitude modulation in the near fields under the mask of Figure 5-21b. Thus, there will be less light lost to high-frequency scattering and more intensity in the +1 diffraction order (shown in Figure 5-23f). Therefore, the off-axis analyzers will be more effective at redirecting TM

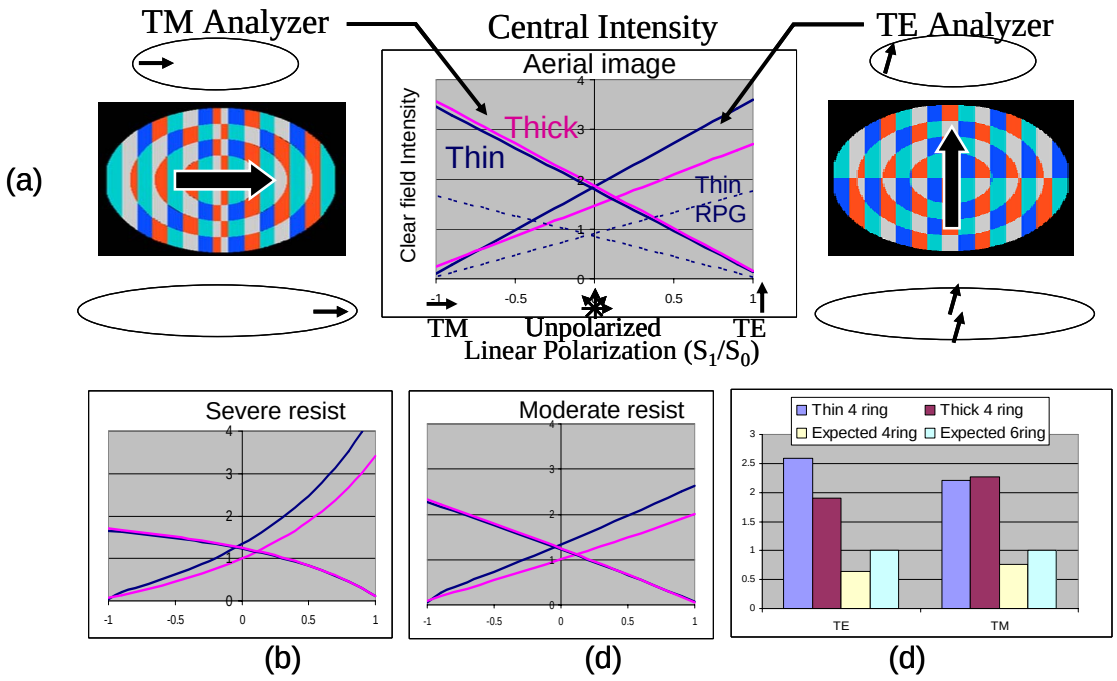

Figure 5-18. Off-axis PEPA sensitivity

TE and TM PEPA 4-ring analyzers show different response to incident polarization for explained reasons. Comparison of (a) aerial image shows 2x improvement over the RPG of Figure 5-17. Sensitivity in resist is shown with (b) severe and (c) moderate resist polarization effects. Simulation vs. expected experimental sensitivity for Reticle C design (once pinholes are aligned).

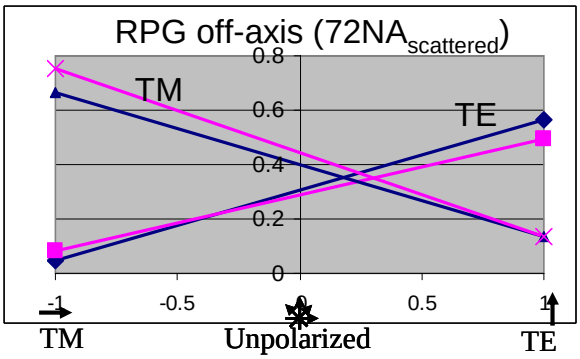

Figure 5-19. Effect of lack of orthogonality between RPG & PEPA

An asymmetry between analyzers is observed with smaller RPG dimensions and is likely due to the resulting lack of orthogonality to the proximity effect of z-component light. The TM analyzer receives a DC bias for explained reasons.

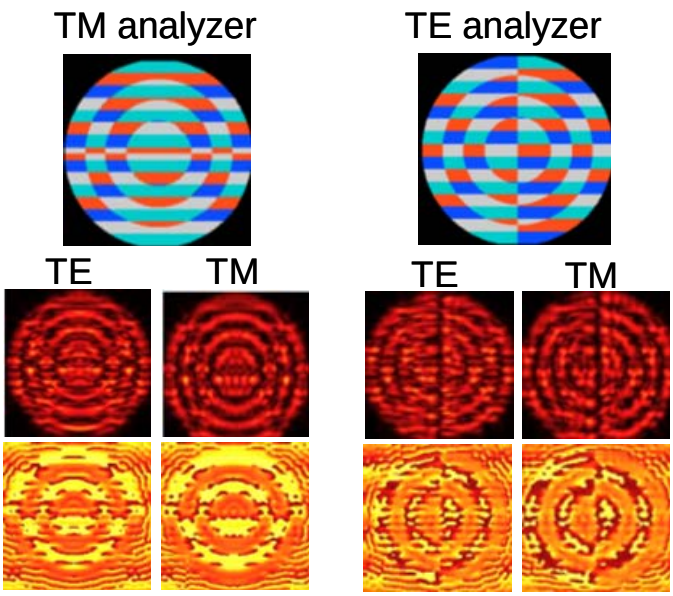

Figure 5-20. Polarization-dependent EM effect: PEPA near fields

Magnitude and phase of near fields under mask show how TM analyzer does a better job of replicating a thin mask transmission function, particularly in areas that impact the signal the most, and thus shows more sensitivity than the TE analyzer.

light down the center of the optical column. Since only the TM analyzer creates a signal from TM light, it is thus more sensitive than the TE analyzer. The difference in behavior between TE and TM polarizations as they propagate through the four-phase grating can be explained by Fresnel reflection and is illustrated in Figure 5-21c. As discussed in Section 2.2.1.2, the fact that light accumulates in high-index materials can be attributed to total internal reflection. Essentially, the material boundary serves as a one-way valve for electric fields propagating at angles greater than the critical angle, where angles are defined relative to the normal of the interface. However, when the angle of incidence is such that total internal reflection does not occur, there then becomes a difference in reflection coefficients between TE and TM light for both when light propagates from air to glass and from glass to air. In both cases, the TE reflection coefficient is greater than the TM coefficient. The three examples in Figure 5-21c illustrate how light from three different

Huygen's sources result in different polarization dependent transmission across the material interface. Thus, greater reflections will cause the fields to bounce around the mask topography to a greater extent with TE polarization. This results in more in interference effects, as was observed in Figure 5-21a. The dimensions used in Figure 5-21 correspond to an analyzer designed for $\sigma_c = 0.7$ and would be slightly worse with larger σ_c.

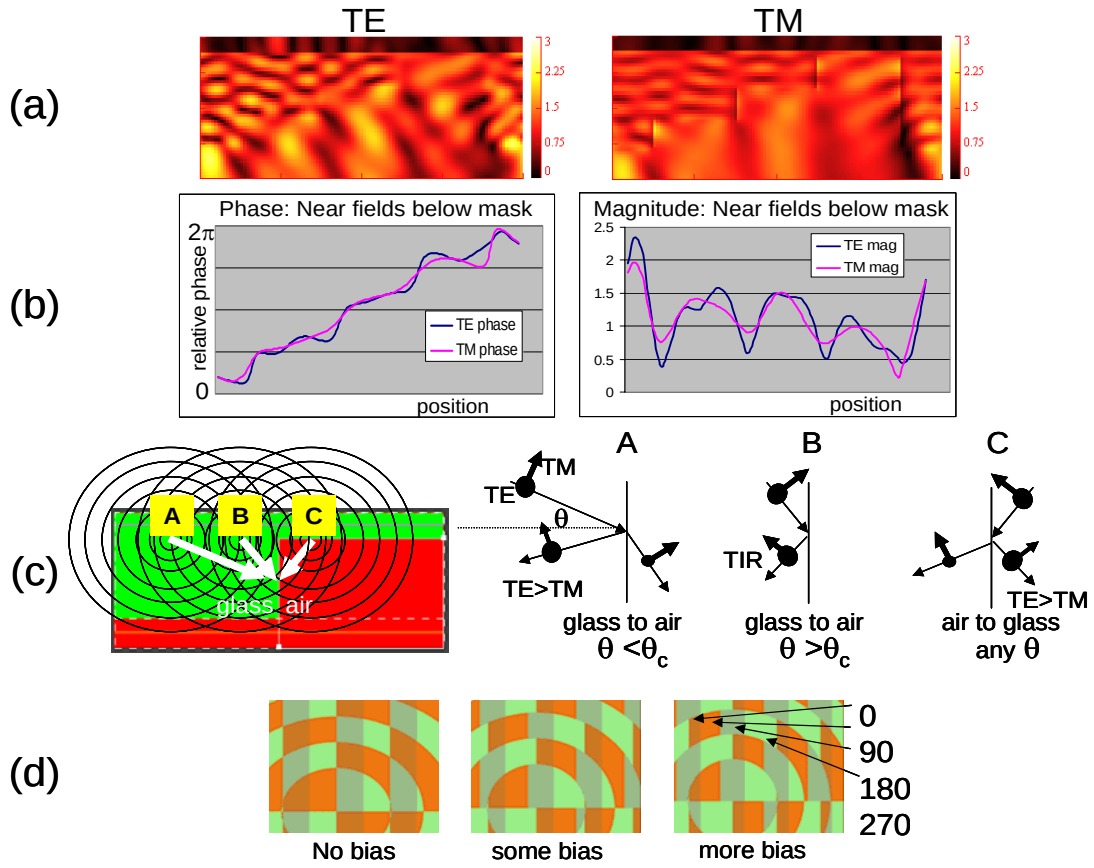

Figure 5-21. Polarization-dependent propagation through 4-phase progression

(a) Slice through 4-phase progression of propagating fields show more reflections and thus more interference effects of TE polarization. (b) Result is less smooth transmitted fields (phase and transmission), thus more high frequency scattering. (c) A comparison of various Huygen's sources explains the effect in terms of Fresnel reflection (d) To minimize the EM effect, three levels of optical proximity correction (feature bias) were applied to reticle C.

To counteract the inevitable EM interaction with the mask topography and thus increase sensitivity, the design can be altered in various ways. First, as is done often in current IC manufacturing with optical proximity correction, feature sizes can be adjusted

such as to even the transmission between regions of different etch depths. Three variations of this feature biasing were integrated into the design of test reticle C, examples of which are displayed in Figure 5-21d. Additionally, the etch depths can be optimized in what can be referred to as three-dimensional OPC. Of course, there is a close interplay between etch depths, feature sizes and the transmitted fields. Generally, a global optimum of the etch depths should be determined first and the feature sizes optimized based on those etch depths, since the entire mask is etched at the same time. The shifted regions of the four-phase progression were roughly optimized to be 97°, 197° and 294° (instead of 90°, 180°, 270°) for an off-axis monitor with $\sigma_c = 0.8$. It is noted that Reticle B was etched to roughly 90°, 175° and 270° and Reticle C was etched to roughly 97°, 217°, and 314° (a 20° error occurred in the 2nd etch process). Simulation shows that generally an average 1° etch error results in a 1% loss of polarization sensitivity.

5.5.1.2. Mask making limitations

Realistic mask making limitations are sure to further decrease the measurement sensitivity since four-phase mask patterns are non-standard and the small sizes push the limits of state-of-the-art photomask fabrication. Various issues associated with mask fabrication are likely to impact sensitivity:

1. Phase assignment within analyzer design affects manufacturability. The absolute phase shift of a particular pattern location is arbitrary. The only important aspect is the period of the four-phase grating, not the placement. Thus, care must be taken to minimize the number of small, sub-resolution slices to be fabricated. The initial RPG design of reticle B is not ideal due to the small 0 and 180 features found in the center of the pattern. Comparing the layout to a SEM of the mask, Figure 5-22a illustrates the difficulty in manufacturing the small phase slices as they do not appear to be on the mask. The center of the TE analyzer, however, appears more similar to the layout. This manufacturability error in the initial TM RPG design is likely responsible for the very large DC offset observed in the TM behavior of Figure 5-17d. Since the center region did not manufacture correctly,

a large 0^{th} diffraction order contributed a noticeable difference in pattern behavior. Although this did not have much effect on the sensitivity, it does highlight the necessity of calibrating the test reticle. This phase assignment problem of the TM analyzer was corrected in the design of Reticle C, shown in Figure 5-22b.

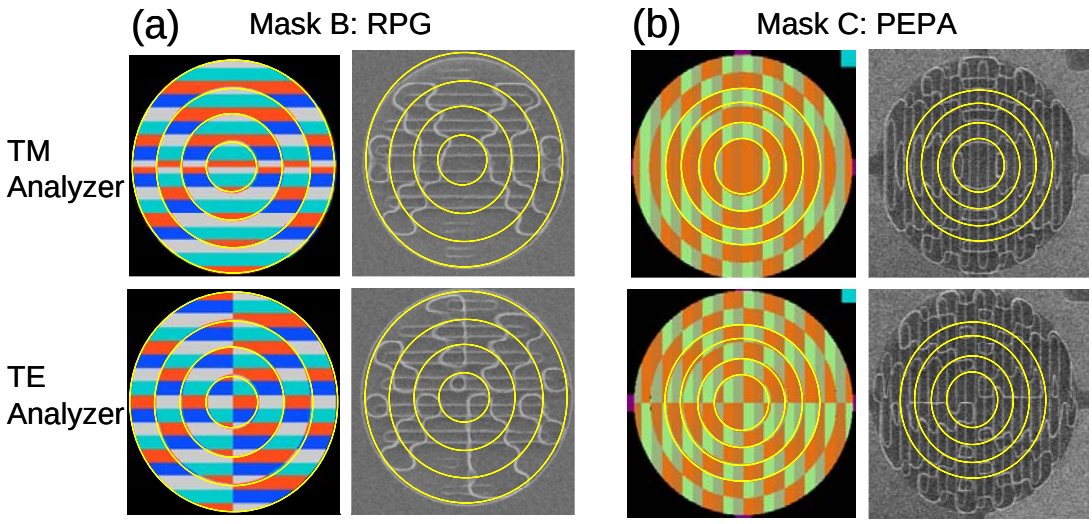

Figure 5-22. Mask making effects and layout improvement

(a) SEMs of reticle B show difficulty in reproducing small phase steps in center of TM analyzer initial design. (b) Reticle C design shows some improvement in layout and manufacturability.

2. Mask fabrication process flow. All three reticles fabricated in this thesis were done so with slightly different strategies. For reticles A and B, the chrome was patterned with electron beam and etched, then each subsequent phase etch was patterned with a laser write tool. Reticle C, however, used electron beam to pattern each phase etch region and used chrome as the etch mask whenever possible. This resulted in slightly better pattern fidelity (Figure 5-22b) and less alignment error between process steps.
3. Sidewall angle, corner rounding, and errors in the feature size and phase etch will all have an impact on the diffraction efficiency of the mask patterns. Actual etch depths of reticles B and C were discussed in the last section. However, measurement of sidewall angle and the true pattern fidelity would require an AFM

with, perhaps, a carbon nanotube tip due to the small trenches being measured. The resultant estimated loss of sensitivity for various cases are listed in Table 5-5.

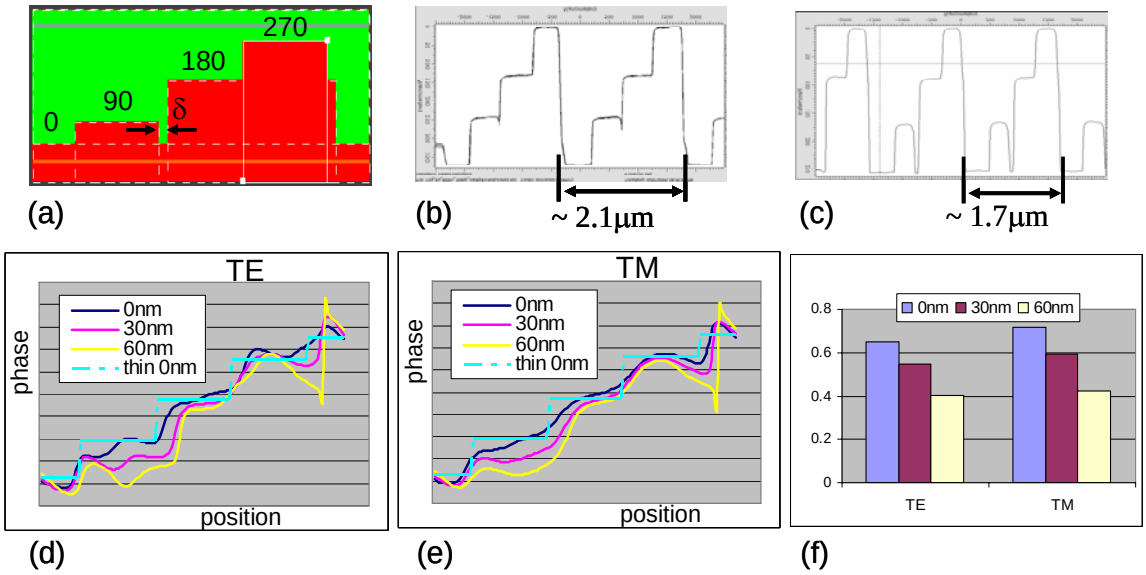

Figure 5.23. Effect of process misalignment

(a) Misalignment between second and third patterning steps of mask fabrication process results in loss of mask pattern fidelity. AFM measurements from test reticles (b) B and (c) C show evidence of the known 30nm and 60nm misalignment (primarily in x direction). TEMPEST simulation shows effect on (d&e) phase of near fields and (f) intensity in the +1 diffracted orders for misalignments (δ) of 0, 30 and 60nm. Impact on imaging is a DC bias and loss of polarization sensitivity.

4. Process misalignment. Inevitably, the two patterning steps required to fabricate the four-phase structure with standard photomask fabrication technologies are likely to be somewhat misaligned. Figure 5-23 investigates the impact of this process misalignment when it is oriented orthogonal to the four-phase grating (and thus will have the greatest impact). A 30nm and 60nm misalignment in the x-direction was independently measured for reticles A and B, respectively. The resulting defect in the mask topography is observed from AFM measurements of linear phase gratings (LPG) on both reticles in Figure 5-23b and c. TEMPEST simulation in the same figure illustrates the impact of this misalignment as a degradation of the near field phase progression and, ultimately, in the loss of intensity in the +1 diffraction order. The 60nm misalignment of reticle B results

in roughly a 40% loss of sensitivity. Overlay error was minimal (<3nm) in reticle C and is thus not expected to impact sensitivity.

5.5.1.3. Effects of the resist stack and immersion

Due to the high angles of incidence present at the image plane, the details of the resist stack can have a profound effect on imaging at high-NA. A few of these considerations and their impact on PSM polarimetry are:

1. High index resists decrease the high-NA vector effect that provides the polarization measurement. A simple application of Snell's law ($n_1\sin(\theta_1) = n_2\sin(\theta_2)$) shows that the off-axis vectors shown in Figure 5-2 are bent towards the normal as light propagates into resist. Essentially all production resists used for IC manufacturing have an index of refraction near 1.7, thus the polarization dependent z-component of electric field will decrease from the aerial image as

$$E_z = \frac{\sin(\theta)}{n_{resist}} E_{TM} \qquad \text{Eq. 5-30.}$$

   Thus, a low-index resist such as PMMA (n_r ~1.3) would help to increase the measurement sensitivity and would in some cases convert the electric field saddle into a peak at the center of the image. However, it would likely require much higher exposure doses than most production resists which have been optimized for exposure sensitivity.

2. Fresnel reflection causes difference in behavior between TE and TM analyzers. At large angles of incidence, the refection and transmission coefficients of light propagating through a material interface become polarization dependent. TM polarization has a higher transmission coefficient, thus will couple more efficiently into the resist. Consequently, it will take less exposure dose to clear a large open field with TM polarization. In other words, the clearfield intensity, the value that measurements are generally normalized to, will be greater for off-axis TM illumination. However, in analyzing a particular polarization component, both TE and TM analyzers scatter the relevant polarization component such that it

becomes the TM component in the pupil, thus creating the z-component signal in resist. Neglecting all other effects, both analyzers will require the same exposure dose to clear the center of the image for equivalent intensity in each polarization component. Finally, since the signal used for measurements in PSM polarimetry is the intensity at the center of the image relative to the clearfield intensity, the TE analyzer will be more sensitive simply due to Fresnel reflection (i.e. it has a lower Clearfield intensity). This effect is clearly evident from Figures 5-17b and 5-18b (severe resist), where simulation involved only photoresist and an underlying BARC (bottom anti-reflective coating) and resulted in a 40% difference in the clearfield intensity between unpolarized and polarized light. However, most resist stacks used with high-NA employ a topside coating and optimize thin film thicknesses to minimize this Fresnel reflection effect. Experimental results from reticles B and C suggested this difference was only about 5%, which is reflected in Figures 5-17c and 5-18c (moderate resist).

3. Immersion lithography, where a high index liquid is placed between the last lens element and the resist stack, will alter the stack's effect on monitoring in various ways. With less drastic index changes the Fresnel effect will decrease. Also, by increasing the critical angle thus enabling the creation of hyper-NA tools, the polarization-dependent signal will increase making PSM polarimetry even more attractive for very high NAs. However, larger NAs will also require the manufacturing of smaller mask features and will increase the EM topography effects.

5.5.1.4. Effects of the PEPA or RPG design

As was observed in Figures 5-16 to 5-18, the PEPA analyzers offer a 2-3x sensitivity improvement over RPGs of comparable size. This is because the RPG analyzers are slightly different from the proximity effect function derived in Section 5.1.1.2 and thus do not take full advantage of the concept of reciprocity. Another synonymous explanation is that the PEPA analyzers more efficiently scatter light into high-NA to create a stronger vector effect signal in the center of the image. This more efficient high-NA scattering is evident from comparing the far field diffraction patterns of

PEPA and RPG ($NA_{scattered}$ = 0.56) analyzers in Figure 5-16a. Furthermore, adding more rings to the PEPA design will increase the signal and sensitivity. Figure 5-25d shows this effect, where enlarging it from 4 to 6 rings increases the signal by roughly 40%.

A more subtle and interesting distinction between the PEPA and RPG becomes apparent in investigating an off-axis RPG analyzer designed to scatter light to higher angles ($NA_{scattered}$ = 0.72), shown in Figure 5-19. Although intuition implies that an RPG that scatters light to higher NA will create more of a high-NA signal. However, this is not the case since it is less similar to the proximity pattern. Even more interesting is the fact that the TM analyzer displays a DC offset, even in the ideal case of a thin mask simulation. Thus, there is some aspect of the design that treats TE and TM light differently.

One explanation for this is that it can be contributed to the fact that there are two effects happening simultaneously. First, the light is being redirected by the four-phase progression (i.e. diffracted into only the +1 and higher orders). Second, the light is being diffracted into high spatial frequencies by the radial grating aspect of the analyzer. When these two effects occur in orthogonal planes, as they are with the TE analyzer, then a clean separation of the effects results. However, when these two effects are in the same plane, as with the TM analyzer, they tend to get blended together. This results in an unwanted DC order passing through the center of the projection lens simply due to the nature of the design. Thus, the entire curve for the TM analyzer is raised by this DC component.

5.5.1.5. Subtle difference between proximity effects of TE and TM polarization

An alternate, and likely equivalent explanation to the one presented in the previous section, brings up an interesting subtle distinction between the proximity effects due to off-axis TE and TM illumination. This alternate explanation is offered by revisiting how the PEPA analyzers were derived in the first place, as was explained in Section 5.1.1.2. This. Figure 5-24 illustrates this derivation in a slightly different way. The proximity effect of z-component light is derived by first convolving the coherent

illumination source with an unaberrated pupil. Taking the inverse Fourier transform of this function results in the point spread function (PSF), which for a circular pupil is in the shape of the Airy function. The two spatial derivatives of this PSF produce the polarization dependent z-component proximity functions in which the PEPAs were derived from. However, in the case of off-axis illumination (Figure 5-24b), the resulting PSF is a complex function consisting of the Airy pattern multiplied by a linear phase progression corresponding to the off-axis frequency. The derivative of a complex function (C) is found by the chain rule

$$\frac{\partial}{\partial x}C = \frac{\partial}{\partial x}[C_M \,\mathbf{exp}(iC_P)] = (\frac{\partial}{\partial x}C_M)\,\mathbf{exp}(iC_P) + iC_M \,\mathbf{exp}(iC_P)(\frac{\partial}{\partial x}C_P) = P_{X1} + P_{X2} \quad \text{Eq. 5-30.}$$

where C_M and C_P are the magnitude and phase of the complex function. This implies that there are actually two proximity functions for each polarization component. These two functions are, for example for the X-polarization, P_{X1} and P_{X2} in Figure 5-24. For the on-axis case, both P_{Y2} and P_{X2} are zero (the values in the figure can be shown to be numerical noise). However, for the off-axis case, P_{TE2} is zero but P_{TM2} becomes appreciable as the angle of incidence is increased.

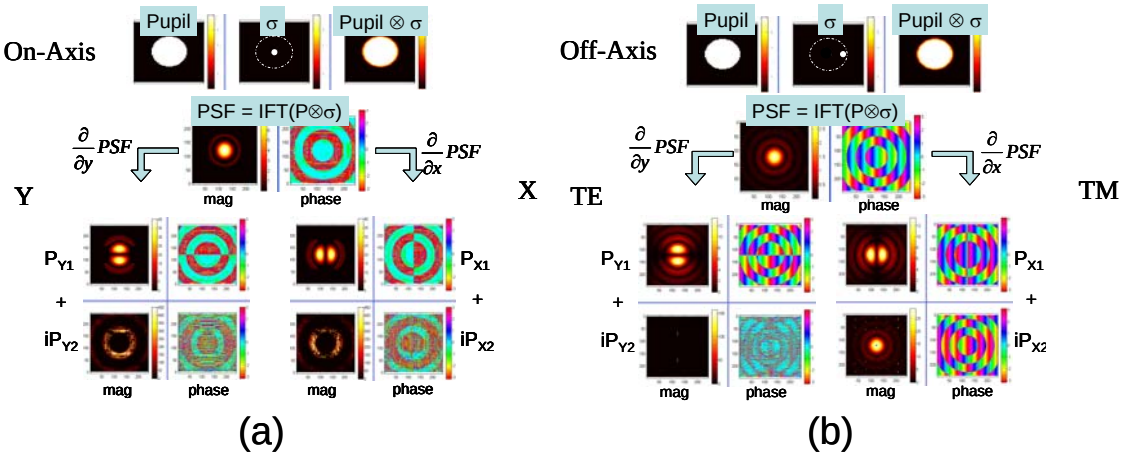

Figure 5-24. Derivation of the z-component proximity effect for on- and off-axis illumination

(a) On-axis derivation results in only one function for each polarization (PY1, PX1). (b) Off-axis derivation results in extra pattern for TM component and the reason for the TM analyzer DC bias observed in Figure 5-19.

In comparing the RPG analyzers to these five proximity functions, the DC bias of the TM analyzer can be explained. First, the TE analyzer has no resemblance (i.e. is completely orthogonal) to all of the functions, except for P_{TE1}. Thus, it will only spill light (which is z-component) into the image center when it is TE polarized. However, the TM RPG has some similarity to three functions: the PSF, P_{TM1} and P_{TM1}. It's similarity to P_{TM1} will spill z-component light (the desired signal) into the center. However, it's similarity to the PSF will spill x- and y-component light into the center, which in Figure 5-24 originate from TM and TE light, respectively. Thus, the DC bias is observed with the TM RPG. Additionally, it's similarity to P_{TM2} will spill light into z-component from TM polarization simply due to the fact that light originated from an off-axis illumination ray. Note that P_{TM2} is the same form as the PSF; only the magnitudes vary depending on the off-axis angle they are derived from. Another example to clarify the point is to consider an open clear field mask. Both the PSF and P_{TM2} have some similarity to a clear field. Thus, TE light is only coupled into a y-component at the wafer. However, TM light is coupled into both x- and z-component light at the wafer. The proximity effect patterns derived in this section are also employed in Chapter 7, where pattern matching is used to identify areas in a design layout that are sensitive to these off-axis vector effects.

5.5.1.6. Pinhole misalignment

Additionally, pinhole alignment on the backside of the reticle is somewhat difficult and is of concern. A misaligned pinhole creates a mismatch between the actual phase progression across the mask and the pre-programmed phase correction of the four-phase grating within each analyzer. Thus, the spill-over to the center of the pattern is no longer completely collinear, resulting in a loss of signal. Unfortunately, the severe 400μm misalignment essentially destroyed the polarization signal from reticle C, although it is expected that a future attempt will achieve alignment of better than 100μm. Figure 5-23a shows the effect of pinhole misalignment when the misalignment is either parallel or perpendicular to the direction of the polarization component being measured. For example, if the misalignment occurs in the x-direction for the y-polarization monitor, a 50% loss of signal occurs for a 200μm misalignment, which corresponds to a 0.2 error in illumination spot (σ_c). The effect is similar for both on- and off-axis analyzers, under

the thin mask approximation. However, the thick mask diffraction efficiency of the 4-phase progression will vary in a slightly non-linear manner for off-axis illumination, depending on the orientation of misalignment. A reasonable target for alignment accuracy is roughly 100μm, where only a 25% loss of signal occurs. Additionally, it is noted that larger PEPAs will be slighly more sensitive to pinhole alignment, due to the greater extent of average phase error across the mask pattern. Thus, a design trade-off may exist between pattern size and expected pinhole alignment accuracy. Again, reticle calibration should account for the changed response of each analyzer due to pinhole misalignment.

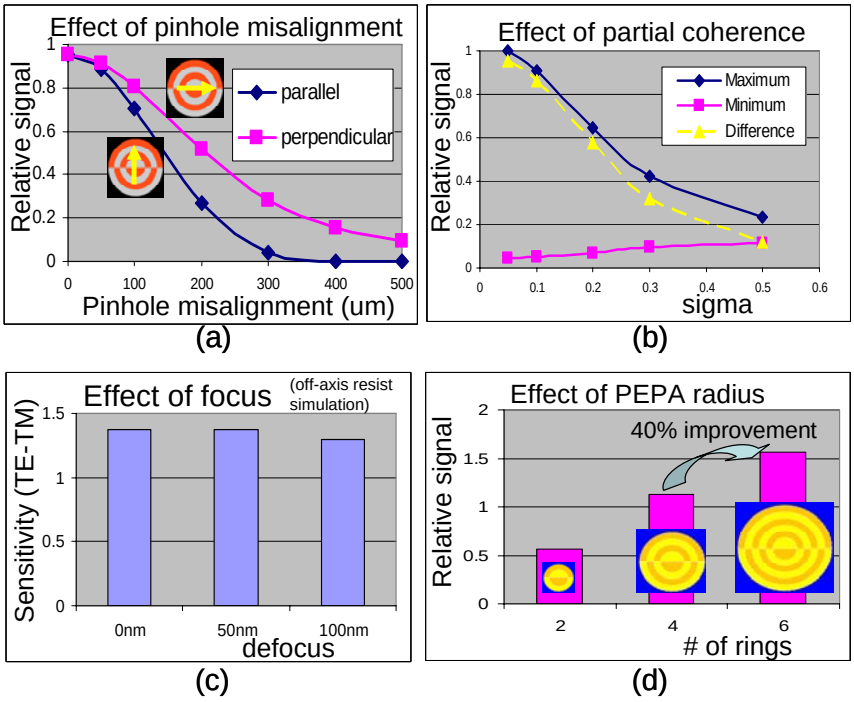

Figure 5-25. Effects of pinhole alignment, partial coherence, focus and PEPA radius

Effects of (a) pinhole misalignment is shown when misalignment is parallel or perpendicular to the measured polarization component. (b) Partial coherence effect (pinhole size, 100um ~ 0.1sigma), (c) focus effect, and (d) effect of PEPA radius.

5.5.1.7. Finite sigma (pinhole size)

Additionally, pinhole size, which determines the partial coherence (sigma), will have an impact on signal strength as shown in Figure 5-23b. A sigma of 0.1 (100μm pinhole radius) was chosen for these experiments where a 10% loss of signal is sacrificed

for the need to expose at reasonable dose ranges. Smaller pinholes could achieve slightly higher signal, but would require considerably more exposure dose, scaling as the square of the pinhole radius.

5.5.2. Sources of measurement error

The ultimate capability of this polarization monitoring technique will depend not only on the achieved measurement sensitivity but also on the ability of the experimental setup to accurately and repeatably extract the correct measurement. Calibration of the reticle accounts for the variation in polarization sensitivity between analyzers due to all of the reasons discussed in the previous section. However, various sources of experimental error will ultimately limit the resolution in which the Stokes parameters can be extracted. These sources of error can be discussed in terms of random and systematic errors.

Since the Stokes parameter measurement is extracted from multiple die from multiple wafers, random errors can result from any variability in the process, such as disparity in the resist process, focus variation, etc. As an example, the variation of the signal due to focus is seen in Figure 5-23d serves to slightly decrease measurement sensitivity, where for a simulated off-axis PEPA analyzer sensitivity decreases by about 1% and 7% of the clear field intensity for 50nm and 100nm of defocus, respectively. The corresponding changes in the maximum signals (i.e. when the polarized light corresponds to the component being measured)is 0.1% and 5% of the clear field intensity. Thus, defocus causes a non-linear effect but is small for reasonable amounts of defocus. Additionally, determining the exact dose that causes the center of the resist image to clear is somewhat subjective and will contribute a random component to the measurement error. However, it is noted that exposure dose variations are likely not an issue since the measurement consists of comparing the signal dose to a nearby clearfield dose. As long as the dose is constant within roughly a 50μm diameter, dose variations among die will not effect the measurement. It is estimated that in the experiments described in Section 5.4, variation in the signal due to random errors was on the order of ±2% of the clearfield. The effect of random errors can be minimized by adding redundancy into the technique by, for example, employing more analyzers for a Stokes measurement.

Systematic errors arise whenever the calibrated W matrix does not accurately reflect the true imperfections of the measurement apparatus. This apparatus includes not only the photomask and resist, but the entire lithography tool. Such systematic differences between the calibration and actual experimental setup may result from lens aberrations (either scalar, polarization-dependent or chromatic), differences in the resist stack used (thickness, type, BARC, ARC, etc), exposure at different focal planes, flare, etc.

The primary systematic error in the experiments conducted with reticle B were likely due to the assumption that patterns in various field locations behave identically and that the W matrix was calculated from multiple field locations. A simple experiment where all field locations were exposed with depolarized light indicated that this assumption was not entirely accurate. Although the results of this test do not specify the polarization behavior of the patterns, up to four percent of the clear field variation in signal was detected, indicating that the patterns are indeed slightly different. This variation is not a fault of the mask maker. Rather these patterns, by leveraging large amounts of proximity effect spill-over to one location, tend to amplify slight variations in the mask fabrication process. A second systematic error, although expected to be small, is the possibility for a slight discrepancy between the Apollo measurement and the actual illumination that the RPGs were exposed with since the measurements were taken on subsequent days and in slightly different field locations. It is estimated that systematic errors were on the order 15% of the clearfield for the reticle B experiments, due primarily to the across field similarity assumption. In future experiments, it will likely be on the order of ±1 or 2% of the clearfield, noting that calibration and experiment will likely be done in different tools.

To help understand the potential impact of these errors on this reticle B experiments, random perturbations were induced into the data and error bars (rather, error circles on the S_1/S_0 and S_2/S_0 plot) were produced via a Monte Carlo approach. Normal distributions for the random and systematic errors were assumed with standard deviations of σ_f and σ_s, respectively. Two combinations of error magnitudes are reported in Figure 5-26 for both the actual experimental data and that of a similar simulated case where the

total polarization sensitivity has been scaled to match the experimental data (recalling that simulation often shows 3-6 times the measurement sensitivity of experiment). Evident from Figure 5-26 is that the impact of errors is much greater in experiment than simulation, which is most likely due to the large systematic cross field similarity assumption. However, given a more complete calibration scheme as employed in the reticle C experiments, this technique should be capable of measuring the Stokes parameters to within about 0.03 to 0.04 for the current reticle C design. However, this does not represent a fundamental limit of this technique. Rather, there are many variables yet to be optimized to increase both measurement sensitivity and decrease experimental error, as have been discussed in this chapter. Table 5.5 compares the estimated measurement sensitivity and resolution in measuring the Stokes parameters for the experiments that have been conducted and that of potential future experiments. The best likely scenario reports a possible Stokes measurement to within about 0.02.

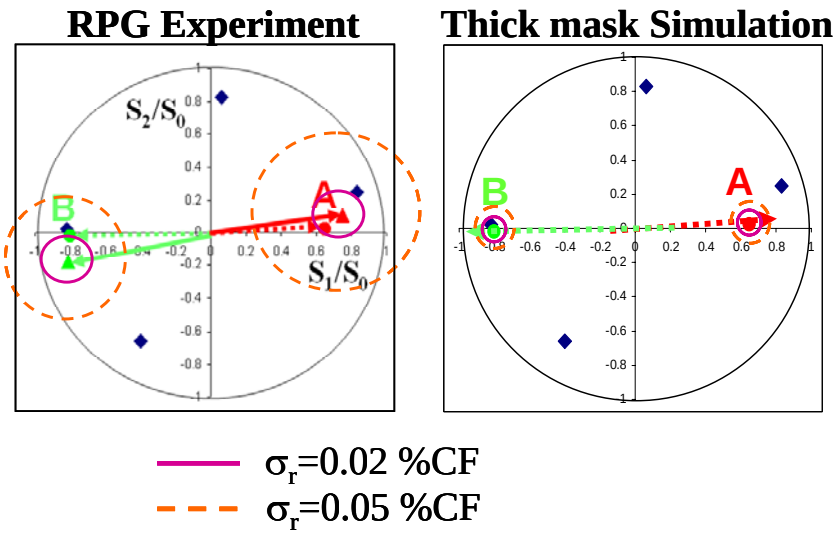

Figure 5-26. Error analysis

Error analysis of random errors (normal distribution with σ_r) on Stokes measurement for reticle B experiment. The systematic error from the across field similarity assumption explains why the experimental data is much more sensitive than a similar simulated case. This assumption is not necessary in the experimental setup of the reticle C.

5.6. Electrical test monitors

Finally, a variation to the test mask design is proposed to enable electrical detection of the signal via a double exposure. A sample mask design for exposure 1 and exposure 2 are shown in Figure 5-27. The first exposure creates an unexposed path in the photoresist between two contact pads, located elsewhere on the design. The second exposure will, depending on the polarization state of the illumination and the exposure dose used, result in either an open circuit or closed circuit after the developed resist pattern is transferred to an underlying metal or poly-silicon layer. This analysis assumes a positive photoresist.

Figure 5-28 illustrates this concept with an aerial image of a Y-polarization analyzer. When the light is polarized in the Y-direction, the bright spot in the center of the image exposes the photoresist. Thus, no metal (or other conducting material such as polysilicon) remains in the center, thus creating an open circuit. However, when light is polarized in the X direction, an electrical path remains between contact pads, thus creating a closed circuit. As before, multiple die are exposed with increasing exposure dose. However, in this case the signal is obtained by contacting the contact pads with electrodes, attempting to run current between them. The exposure dose that causes the transition from a closed circuit to an open circuit is recorded as the ‘signal’. Other than the altered means of extracting the signal, calibration of the analyzers and measurement of the Stokes parameters are the same as described above for the non-electrical monitors. Without the electrical test layout, the signal would be obtained with a SEM either manually or perhaps with an automated image processing algorithm. The electrical test patterns likely offer a much more convenient and practical means of implementation of the PSM polarimeters. In addition to much faster data collection, the electrical test monitors alleviate the subjective act of visually extracting the signal from photoresist images. However, additional complications and sources of variability may arise due to the addition of extra processing steps.

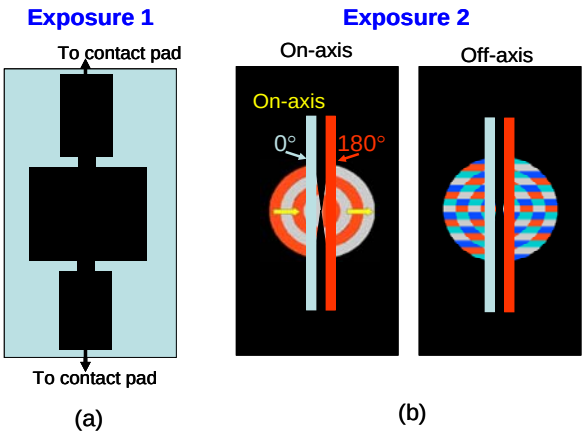

Figure 5-27. Double exposure layout for electrical test analyzers

Sample electrical test mask layout for (a) exposure 1 and (b) exposure 2. Reasonable misalignment between exposures is tolerated in the design.

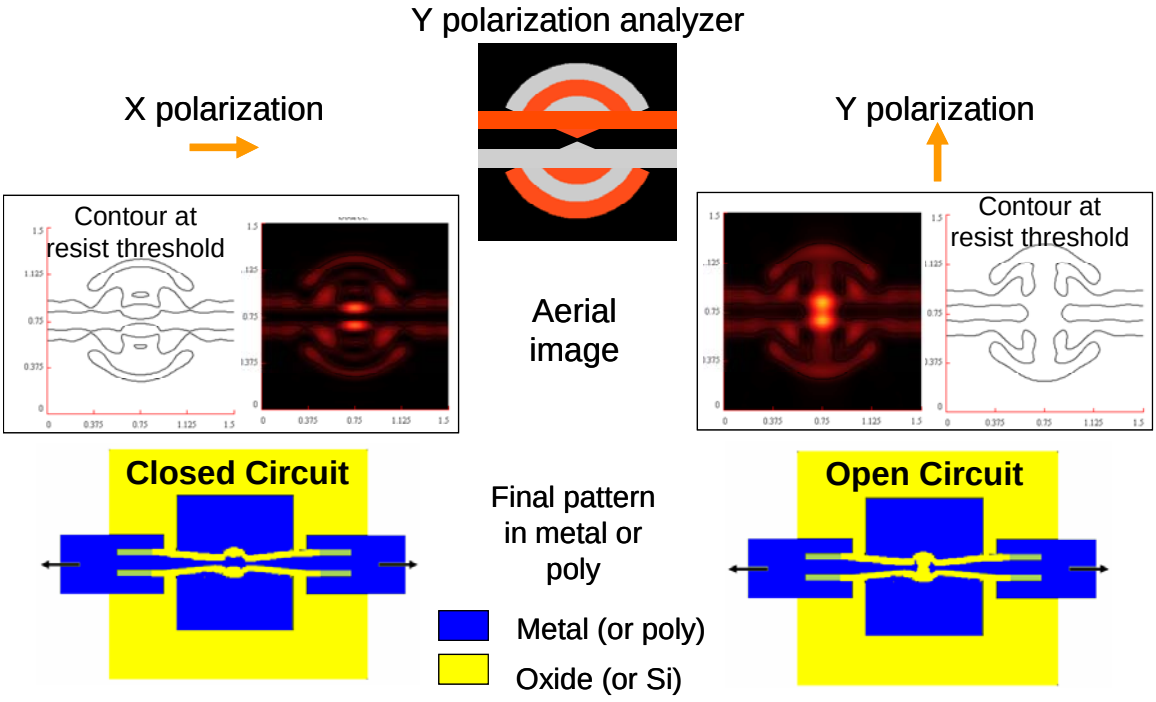

Figure 5-28. Electrical test analyzers

Double exposure enables electrical signal and simplifies data collection, which consists of probing for an open or closed circuit.

5.7. Overall assessment: How practical is PSM Polarimetry?

Section 5.4.2 illustrated how the current design should achieve a measurement sensitivity of about 1 percent of the clear field per percent change in polarization and a Stokes measurement to within about 0.03 or 0.04. However, this estimate does not represent a fundamental limit of this technique and potential improvements to the reticle design, reticle fabrication, and experimental setup have been discussed. For example, sensitivity improvements are possible by including more rings in the PEPA design, decreasing pinhole size, programming redundancy in the design with intentional pinhole and process misalignment, improving 3-D optical proximity correction, using a thin and low index photoresist, improving phase assignement within the PEPA or, potentially, by using a three-phase progression (instead of four-phase) to increase manufacturability. In addition to design improvements, the evolution of mask making capabilities is sure to increase the diffraction efficiency of these monitors. For example, better backside pinhole alignment, improved three-dimensional pattern fidelity, sidewall angle, and layer-to-layer alignment will couple more light into the intended polarization-dependent high-NA signal. Alternately, a direct-write strategy in HSQ, a negative tone resist with glass-like properties, may ultimately be the best method to fabricate the polarization analyzers on a test reticle. Furthermore, improvements in the experimental setup will enable better resolution in extracting the Stokes parameters. Such improvements include taking care to ensure accurate calibration of the W matrix, using finer dose steps, and decreasing variability such as that caused by focus and resist stack variation. Additonally, automating the signal extraction from photoresist images – or using the electrical test version - may eliminate some measurement subjectivity, decrease experimental error and decrease the time needed for measurements.

Finally, to try and answer the question, “how practical is PSM polarimetry?” Table 5-5 summarizes the sensitivity lost due to realistic imaging conditions, the overall measurement sensitivity and the resolution in the Stokes measurement for the experiments conducted for this thesis and for examples of potential future attempts. Although imaging and experimental non-idealities will always exist to some extent, by manipulating the design to maximize sensitivity and by fine tuning the experimental

setup to decrease errors, a reasonable polarization measurement is likely possible. For example, if the pinholes can be accurately aligned (±50μm), then a 10 ring analyzer is feasible using sigma of 0.1 (100μm pinhole radius). Accounting for reasonable sensitivity lost do to other parameters, this is likely to achieve a sensitivity of roughly 2 percent of the clear field per percent change in polarization and a Stokes measurement (S_1/S_0 or S_2/S_0 parameters) to within 0.02, corresponding to a polarization measurement to within 1%. This is certainly sufficient for the first generation or two of lithography tools with polarized illumination, where a target for polarization control is likely within about 0.05.

		10 ring PEPA (best likely possible)		Good 6 ring PEPA		Expected reticle C with fixed pinholes		Actual Reticle C PEPA		Actual Reticle B RPG(64NA)	
		TE	TM	TE	TM	TE	TM	TE	TM	TE	TM
Ideal thin mask, aerial, 6ring	% Loss of sensitivity	100	100	100	100	100	100	100	100	100	100
Design (PEPA vs RPG)		0	0	0	0	0	0	0	0	70	70
Design (#rings)		-35	-35	0	0	0	0	0	0	0	0
resist (index (1.7) and Fresnel)		8	8	20	20	20	20	20	20	20	20
EM effects		20	-5	20	-5	20	-5	20	-5	20	-5
etch error		2	2	3	3	20	20	20	20	3	3
feature size error		1	1	1	1	10	10	10	10	1	1
overlay error		5	5	10	10	5	5	5	5	40	40
other mask degradation		15	15	20	20	20	20	20	20	20	20
Pinhole size		0	0	0	0	0	0	0	0	0	0
Pinhole alignment		5	10	10	10	0	0	90	100	0	0
random error (σ_r)	±CF	0.01		0.015		0.02		0.02		0.02	
systematic error (σ_s)		0.02		0.02		0.01		0.01		0.15	
Relative sensitivity to ideal 6ring		74	92	40	52	35	46	4	0	9	12
Estimated sensitivity (%CF per % pol change)		**1.92**	**2.39**	**1.04**	**1.36**	**0.91**	**1.19**	**0.09**	**0.00**	**0.23**	**0.31**
Stokes resolution (±S1/S0)		**0.02**		**0.03**		**0.04**		**0.62**		**0.23**	

Table 5-5. Sensitivity analysis of PSM polarization analyzers

Sample cases of actual and expected measurement sensitivity and resolution of the Stokes parameter measurement using the radial phase gratings (RPG) from test reticle B and the more sensitive proximity effect polarization analyzers (PEPA) from test reticle C.

5.8. Summary

A technique has been presented to monitor polarization in high-NA and immersion projection printing. A series of phase shifting test mask patterns have been derived from basic principles and, when properly calibrated, are sufficient to monitor polarization of any arbitrary illumination scheme. Various simulation studies and

experiments conducted on two multi-phase test reticles appear to validate the scientific principles of phase shift mask polarimetry and have enabled investigation of various non-idealities.

The first test mask employed radial phase gratings and special illumination frequency selecting apertures to create polarization-dependent signals in photoresist. A measurement sensitivity of about 0.3 percent of the clear field per percent change in polarization state was achieved, agreeing with a technique developed by Nikon to within about 10%. Potential sources of error were identified, concluding that in the first experimental setup, the assumption that patterns behave the same across the imaging field was the main source of error, enabling an S_1/S_0 or S_2/S_0 Stokes measurement to only within 0.23. The second test reticle employed the more sensitive proximity effect polarization analyzers, a backside pinhole layer for illumination frequency selection and a more robust experimental setup. However, despite an initial misalignment complication of the backside layer, the results agree with theory. Theory predicts that, once the pinhole alignment is corrected in the near future, a sensitivity of about 1 percent of the clear field per percent change in polarization state can be achieved, corresponding to a measurement of the Stokes parameters to within 0.03 to 0.04. However, future improvements have been discussed and are likely to double the measurement sensitivity to 2 and decrease the Stokes measurement resolution to within 0.02. This makes PSM polarimetry a viable commercial solution for monitoring linear polarization for at least the first or second generation of lithography tools with polarization control, where the specification for the S_1/S_0 Stokes parameter is likely to be within 0.05.

6 Monitors for Self-diagnostics of Phase Shift Mask Performance

Phase shift masks (PSMs) offer the lithographer an added dimension in image creation, thus enabling the printing of smaller features and increasing CD control and focus latitude. However, these advantages are not without cost, both financially and in manufacturing complexity. Manufacturing imperfections such as uneven etch rates either across the mask or due to varying feature density result in actual phase errors. Also, even when precisely fabricated, the three-dimensional nature of PSMs cause an effective imbalance in both phase and transmission between regions of different phase. Furthermore, both of these effects are usually feature-dependent [17][34][81]. Various existing measurement techniques have emerged to quantify these errors; most based on either a specialized phase interferometer, an atomic force measurement (AFM), image plane analysis, or pupil-plane analysis in a modified AIMS tool [68][15].

This chapter introduces a new *in-situ* image plane technique, the interferometric-probe monitor (IPM), to measure effective phase and transmission errors in the phase-shifted regions of a PSM. A two-phase pattern is designed to coherently spill electric field into the center of the target if either a phase and/or transmission imbalance exists between the phase regions. Due to the orthogonality of phase and transmission errors, a sub-printable interferometric probe of either 0 or 90 degree phase allows amplification and detection of either type of error. The intensity change is a linear function of phase or transmission error and depends only on the size of the pattern and probe used. Errors are quantified by comparing probe response to a nearby identical, but isolated, probe and are measurable on either an AIMS tool or observed in printed photoresist. As an example,

for an alternating 0-180 degree PSM (Alt-PSM), a 90 degree probe amplifies phase error where a 0 degree probe amplifies transmission error. Sensitivity of the monitor is related to the pattern size and can theoretically achieve up to 1% of the clear field per 1° phase error with only a five-ring design (radius = 3.1 λ/NA). Achievable sensitivity clearly outperforms existing measurement techniques for feature sizes with one dimension less than 0.5λ/NA, such as contacts and phase trenches, and does not require through-focus analysis. Phase and transmission errors can be compared among various feature types and sizes and among different locations in the field. Functionality is only slightly affected by lens aberrations and reasonable probe-manufacturing errors. Mask manufacturing is relatively simple and can be placed on a special test mask or interspersed in a production mask layout.

Section 6.1 describes the basic principle of the IPM and derives a mathematical theory from the proximity effect of coherent imaging. Section 6.2 describes example IPM targets used to determine phase and transmission errors for standard ALT-PSMs and PSMs with arbitrary phase. Also, a variation of the IPM used to calibrate edge effects is introduced and a discussion of the potential integration of the IPM concept into EDA is provided. Experimental results are reported in Section 6.3 and a discussion of practical considerations and comparison to existing techniques are provided in Section 6.4. It is concluded in Section 6.5 that this technique is expected to be capable of monitoring phase with a sensitivity of over 1.5% of the clear field per degree phase error with an illuminator with $\sigma = 0.05$. This is most likely feasible in a modified AIMS tool and need not involve a wafer production tool.

6.1. Concept

The finite size of the optics in projection printing tools result in the inability to exactly replicate mask patterns onto the wafer. Rather, interference effects of light captured within the pupil degrade imaging and result in the proximity effect. This is a familiar lithographic phenomenon where the electromagnetic influence of an object point on an image point depends on the wavelength of light, size of the lens, distance between points and state of illumination. For coherent illumination (very small sigma) this

proximity effect is the well-known Airy function, also referred to as the electric-field point spread function (PSF). Thus, any arbitrary clear field location A in the object plane (reticle) will contribute electric field to any other arbitrary location C in the image plane (wafer) dependent on the magnitude and phase of the point spread function centered on point A. By reciprocity, then the influence on point C by any and all mask locations is simply the point spread function centered on point C. Thus, any point equidistant from the center location will have the same influence at that point.

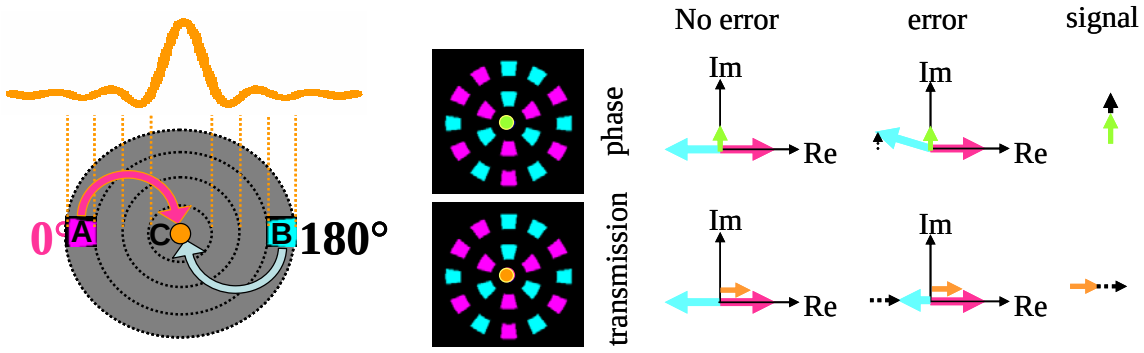

Figure 6-1. Interferometric probe monitor concept

Influence function (PSF) on center location with coherent illumination. The interferometrc-probe monitor for PSM performance (IPM-PSM) measures an imbalance in the proximity effect spill-over of two locations of opposite phase and equidistant from the center. A 90 degree (imaginary) probe in the center enhances the signal for phase error and a 0 degree (real) probe enhances transmission error.

As shown in Figure 6-1, considering only two small open mask locations, A and B, equidistant from point C, the total electric field at C is:

$$E_C = E_{A\Rightarrow C} + E_{B\Rightarrow C} = (Airy_A \times T_A \times e^{i\phi_A} \times dArea_A) + (Airy_B \times T_B \times e^{i\phi_B} \times dArea_B) \quad \text{Eq. 6-1.}$$

where T_A, ϕ_A, T_B, ϕ_B, are the transmission and phase of points A and B, respectively. Since the magnitude and phase of the Airy function are identical at the two locations, a differential geometric factor is defined as follows:

$$dG = Airy_A \times dArea_A = Airy_B \times dArea_B \quad \text{Eq. 6-2.}$$

Thus rewriting the electric field at C:

$$E_C = (T_A e^{i\theta_A} + T_B e^{i\theta_B})dG \qquad \text{Eq. 6-3.}$$

If the phase and transmittance of both locations are identical, the fields due to each will coherently add. Likewise, if location B is 180 degree phase-shifted (i.e. $\phi_A = 0$, $\phi_B = 180°$), the fields will coherently subtract, resulting in no net electric field at C. However, should this phase difference be slightly other than 180 due to a phase error in B (i.e. $\phi_A = 0$, $\phi_B = 185°$, $\Delta\phi_B = 5°$), and assuming T_A and T_B are both 1, the resultant electric field at C can be written as:

$$E_C = (1 - \cos(\Delta\phi_B) + i\sin(\Delta\phi_B))dG \qquad \text{Eq. 6-4.}$$

Taking the complex conjugate, the time-averaged intensity at C is therefore:

$$I_C = [(1 - \cos(\Delta\phi_B)^2 + \sin^2(\Delta\phi_B))dG^2 \qquad \text{Eq. 6-5.}$$

noting that the intensity varies as the square of the phase error at location B.

A linear intensity variation with much improved sensitivity can be obtained with the addition of a sub-resolution, 90° phase interferometric probe located at C. The 90° probe adds an imaginary component to the electric field at C. With the appropriate choice of probe size and geometric factor (dG), this component dominates the intensity, increasing its sensitivity to $\Delta\phi_B$ as follows:

$$E_C(90° probe) = [1 - \cos(\Delta\phi_B) + i\sin(\Delta\phi_B)]dG + i\,\mathrm{Im}(E_P) \qquad \text{Eq. 6-6.}$$

$$I_C(90° probe) = (1 - \cos(\Delta\phi_B))^2 dG^2 + [\sin(\Delta\phi_B)dG + \mathrm{Im}(E_P)]^2 \qquad \text{Eq. 6-7.}$$

Note that for small phase errors ($\Delta\phi_B$), the first term becomes negligible. Likewise, a transmission error between A and B is amplified with the use of a 0° probe, which adds a real electric field component:

$$E_C(0° probe) = \mathrm{Re}(E_P) + [1 - \cos(\Delta\phi_B) + i\sin(\Delta\phi_B)]dG \qquad \text{Eq. 6-8.}$$

$$I_C(0° probe) = [\mathrm{Re}(E_P) + (1 - \cos(\Delta\phi_B))dG]^2 + \sin^2(\Delta\phi_B)dG^2 \qquad \text{Eq. 6-9.}$$

The vector diagrams of the fields spilled into the center of the image in Figure 6-1 show the interferometric behavior of the probe. Since intensity is the square of the electric field, the probe serves to amplify either the real (0°) or the imaginary (90°) spill-over.

6.2. Applications

6.2.1. Application 1: Monitor for standard Alt-PSM phase and transmission

Figure 6-1 shows the influence of two equidistant points on the center of a circular target with coherent illumination. As discussed in the previous section, a 0 or 90 degree probe at location C enables detection of either phase or transmittance error between the two locations. Signal strength is related to the size of the openings. Thus, assuming errors due to processing are similar for all 180° regions, a larger signal is obtained by simply increasing the size of the two openings. IPM functionality is maintained as long as the target design consists of equal openings of 0 and 180° phase at any particular radius. An example set of targets for measuring errors in phase trenches is shown in Figure 6-2a&b. The placement of 0 and 180 regions is completely arbitrary and was chosen only to minimize the impact of lens aberrations.

SPLAT (thin mask) simulation of these targets clearly show how the 90° and 0° probe targets are sensitive to phase and transmittance, respectively, and is shown in Figures 6-2c&d. As the phase of the shifted regions is varied from 180 to 190, the intensity of the 90° target probe increases while the 0° target probe remained constant. Conversely, as the transmittance of the shifted regions is varied from 100% to 80%, only the 0° target probe shows sensitivity. The response for both conditions is linear with error and is consistent with the theory described in Section 6-1. These particular targets show theoretical sensitivities of 0.7% of the clear field intensity per degree of phase error with a 90° probe and 0.6% of the clear field intensity per degree of transmittance error with a 0° probe.

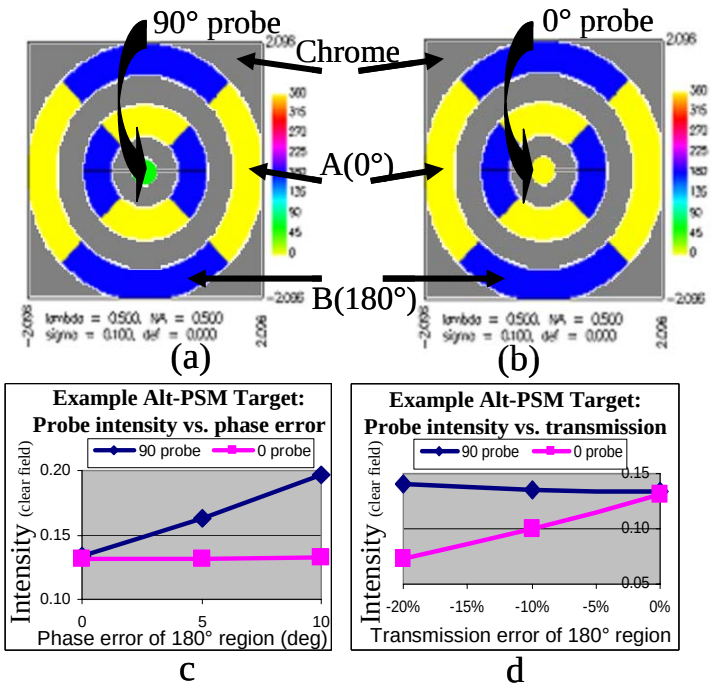

Figure 6-2. Example targets for monitoring phase-trench performance in Alt-PSMs

90° probe (a) is sensitive to phase error (c) while 0° probe (b) is sensitive to transmission error (d).

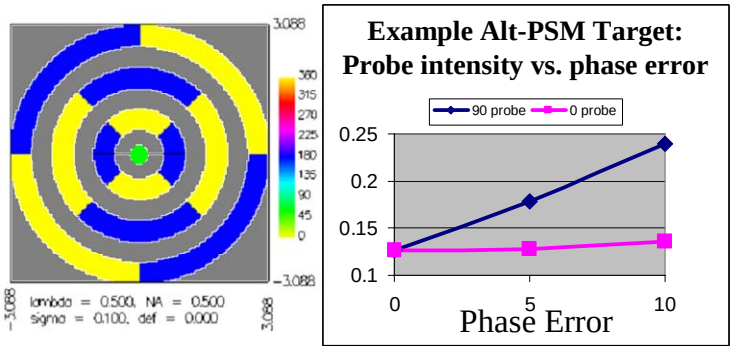

Figure 6-3. A correctly designed target with more open rings shows increased sensitivity

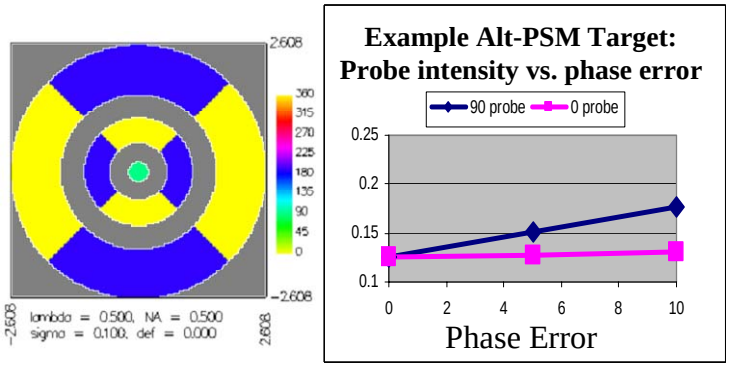

Figure 6-4. Incorrectly designed target

Targets must consist of only openings in alternating rings due to the alternating sign of the Airy pattern. Otherwise, sensitivity is lost as shown here (compared to Figure 6-3).

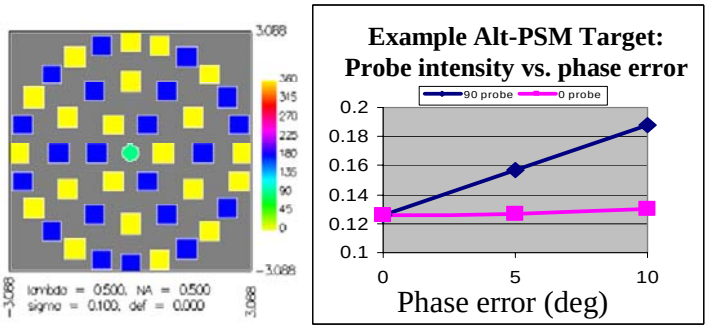

Figure 6-5. Target for contact phase and transmission

The sensitivity of determining effective phase and transmission error in an array of properly designed alternating contacts depends only on the number of contacts used.

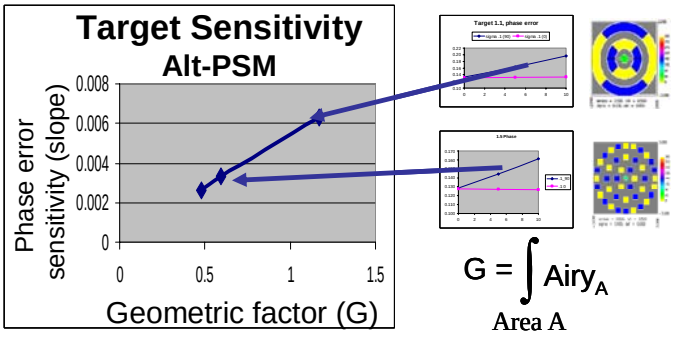

Figure 6-6. Target sensitivity vs. geometric factor

Target sensitivity for phase error depends linearly on geometric factor for a given probe size. Transmission error sensitivity is similar.

Since signal strength is related to the size of the pattern, sensitivity is improved simply by extending the area of the phase regions, thus increasing the geometric factor:

$$G = \int dG = \int Airy_A dArea_A \qquad \text{Eq. 6-10.}$$

With the addition of phase regions in the 5th Airy ring, Figure 6-3 shows improvement in phase sensitivity to over 1% of the clear field intensity per degree of phase error. However, due to the alternating sign of the Airy pattern with successive ring number, targets must consist only of openings in alternating rings, either even or odd. For example, the addition of the fourth ring in Figure 6-4 adds a negative geometric factor, ultimately decreasing the target's sensitivity.

The targets described thus far measure effective phase and transmission in trench features, thus closely approximating the behavior of alternating line and space patterns. However, various feature types are analyzed by simply altering the mask design. For example, Figure 6-5 displays an array of alternating contacts. Again, a 90° or 0° probe will measure the effective phase or transmittance error, respectively, in each 180° contact. The sensitivity is related only to the number of contact openings and the size of the probe. The design only requires that there be equal 0° and 180° openings for any given radius and that only alternating rings are used.

Clearly, target sensitivity is related to pattern size. Figure 6-6 illustrates this relationship by linearly relating phase error sensitivity (slope) to geometric factor (G) for a particular probe size. Here no transmittance error is assumed and for a 0.2 λ/NA radius probe, the phase error slope is .534*G. Thus, to determine phase error for a particular feature, a target consisting of that feature and a 90° probe is designed satisfying the discussed design requirements. The geometric factor is calculated depending on the mask design. The mask is then exposed, comparing target probe intensity to a near-by identical, but isolated, probe. Phase error sensitivity for that pattern is predicted by plotting a line of appropriate slope (determined by the geometric factor and probe size) originating from the isolated probe intensity. Finally, the measured target probe intensity is fit to this prediction to determine phase error.

A similar experimental process using a 0° probe measures transmittance error, assuming no phase error is present. Again, the relationship between error slope and geometric factor is linear and for a .2 λ/NA radius probe, goes as: transmittance error slope = .254*G.

Here it has been assumed that only phase error is present for the 90° probe measurement and only transmittance error is present for the 0° probe measurement. However, only some accuracy is lost should these assumptions be false since transmittance error has only a very small effect on the phase target (90° probe) and vice-versa. The next section discusses a more detailed analysis of the probe response, taking into consideration both errors simultaneously and is valid for PSMs with phases other than 0° and 180°.

6.2.2. Application 2: Monitor phase and transmission of arbitrarily phased regions

Although current mask making technology would principally require analysis of 180° phase shifted regions, this technique is also valid for features of any phase or when both regions are phase-shifted. This more general application of this interferometric-probe technique again involves two similar targets, differing only by the phase of their probes. Referring to the derivation in Section 6.2, the probe intensity relations for both a 0° and 90° probe target for any phase-shift (ϕ_B) and transmittance (T_B) are rewritten as:

$$I_C(90) = G^2(1 + T_B \cos(\phi_B))^2 + [\mathrm{Im}(E_P) + G \times T_B \sin(\phi_B)]^2 \qquad \text{Eq. 6-11.}$$

$$I_C(0) = [\mathrm{Re}(E_P) + G(1 + T_B \cos(\phi_B))]^2 + (G \times T_B \sin(\phi_B))^2 \qquad \text{Eq. 6-12.}$$

Note it has been assigned that $T_A = 1$ and $\phi_A = 0°$, since transmission and phase of the non-shifted regions are defined as the reference for the shifted regions. Since both the geometric factor (G) and the probe contribution to the electric field (E_P) are determined by the design and intensities are measured in experiment, the result is simply two equations with two unknowns. Thus, the phase and transmission of any phase-shifted feature, which conforms to the design specifications described in Section 6.1, is

characterized by exposing two targets and two isolated reference probes through dose. The reference probes quantify the real and imaginary E_P once the square root is taken of the measured intensities. Finally, T_B and ϕ_B are found from the above equations with simple numerical iteration. An example is shown in Figure 6-7, where probe response is shown for a set of targets very similar to those in Figure 6-2, except that the pattern consists of 0° and 90° regions, not 0° and 180°. Both 0° and 90° probes respond differently to errors in phase and transmittance, however the two measurements are enough to determine both errors quantitatively.

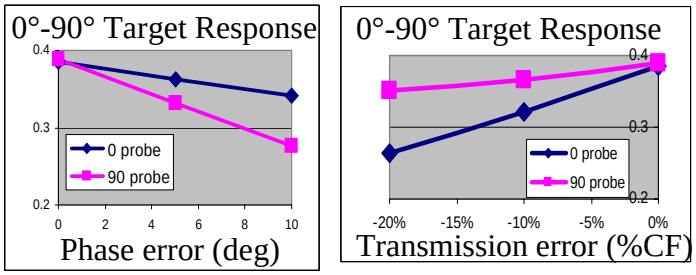

Figure 6-7. Targets for arbitrary phase regions

Targets can be designed to measure imbalance of any phase features. Response of a target similar to Fig 2 (except with 0-90°, not 0-180°) is shown here.

Furthermore, this technique remains applicable even if both regions (1 and 2) are phase-shifted. For example, a common technique used to restore intensity balance in Alt-PSMs is to equalize edge scattering in the 0° and 180° regions by over-etching both equally. [94] In this case a similar analysis is possible, only with the following substitutions: $T_A = 1$, $T_B = T_2 - T_1$ and $\phi_A = 0°$, $\phi_B = \phi_2 - \phi_1$. Thus, T_B and ϕ_B become simply the difference in transmission and phase of the two regions. This difference, not the true phase and transmission, is of primary concern with Alt-PSMs.

6.3.3. Application 3: Edge effects

Thus far the focus of this chapter has been to determine phase and transmission error in PSMs, assuming errors were constant within each individual feature. However, due to the oscillating nature of the Airy pattern, some areas within a feature will have a larger influence than others, an effect that should be considered in analyzing results.

Conversely, this characteristic of the Airy pattern could be used as another lever to calibrate other mask making concerns such as edge effects. Figure 6-8 shows again how central influence depends on radius; ring centers have either a strong positive or negative influence while regions between rings have no influence at all. Thus, to determine the impact of edges, probe responses (both 0° and 90° probes) are compared between two targets similar to those in Figure 6-8, which we name IPM-EDGE. Target 1 consists of identical 0° (A) and 180° (B) regions, each covering two adjacent Airy rings so the geometric factor (G) is nearly zero. Hence, this target is not sensitive to overall phase or transmission error. Target 2 is similar, except that the phase shifted region (B) is constructed so its total geometric factor is the same as region A. However, its perimeter falls somewhere in the middle of rings 1 and 3, not between rings like Target 1. Thus, any difference in the way these two targets respond results directly from edge effects.

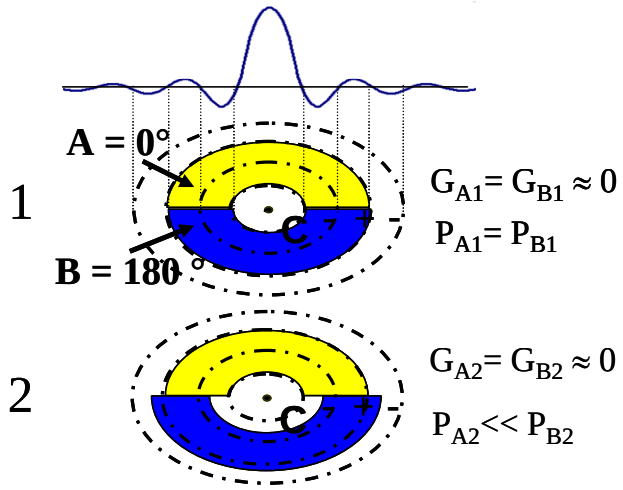

Figure 6-8. Target for edge effects

Probe response comparison measures edge effects due to difference in perimeter factors. Both transmission and phase are measured with 0 and 90 probes.

The total electric field at the center can then be approximated as:

$$E_C = E_{\mathbf{Pr}obe} + (P_B - P_A) T_{perimeter} e^{i\theta_{perimeter}}) \qquad \text{Eq. 6-13.}$$

where P denotes a perimeter factor and is determined from the design as

$$P_A = w \int_{perimeterA} Airy_A dl \qquad \text{Eq. 6-14.}$$

and w is an effective edge width (perhaps 0.01 λ/NA). Since $P_B = P_A$ for Target 1, the response is simply E_{Probe}. This acts as a reference for Target 2 and quantifies E_{probe}. A similar process to that described in Section 6.2.2 is used to extract the effective phase and transmission of the edges ($T_{perimeter}$ and $\phi_{perimeter}$)with Target 2. Two targets with different probes again produce two equations with two unknowns ($T_{perimeter}$ and $\phi_{perimeter}$). The results give the effective phase and transmission of an edge region considered to have width w.

6.3. Experimental verification

Multiple configurations of the IPM, all following the simple design rules outlined in Section 6.1, were fabricated on test reticle A, along with some of the illumination patterns previously discussed in this thesis. One example layout of a three-ring IPM designed to measure the phase error between 0 and 180 degree contacts is shown in Figure 6-9. An isolated probe is located near-by and acts as a reference for the measurement. The top-down SEM of the reticle in Figure 6-9b again shows evidence of the slight misalignment error in writing the second level etch. This clearly results in under-sizing the shifted regions and appears to decrease the expected probe intensity by more than 50%. Furthermore, the small crescent-shaped region of 0 degree phase within the probe may contaminate the probe electric field with a non-90 degree component. This may confuse the distinction between phase and transmission measurement. This phase contamination was due to the misalignment and the difficulty in biasing the resist process because of the chromeless, multi-phase illumination monitors on the same mask. Simply selectively over-sizing the resist openings and thus ensuring chrome was used as the etch mask, as is typically done with alternating phase shifting masks, alleviated this problem for the fabrication of test reticle B. However, the experiments conducted on reticle B were dedicated to the polarization monitoring of Chapter 5.

The experimental procedure consisted of using an AFM to locate the two mask locations with the largest difference in phase depth (see Figure 6-9c for sample vertical cutline through the pattern). Both AIMS tool measurements and patterns printed in resist

were then compared for IPM-PSMs at these two mask locations. A sample resist image is shown in Figure 6-9d with the probe position circled to remind the reader that the only matter of concern is the dose at which the probe begins to print. This dose, when expressed as a percentage of the clear field intensity, is the measurement signal.

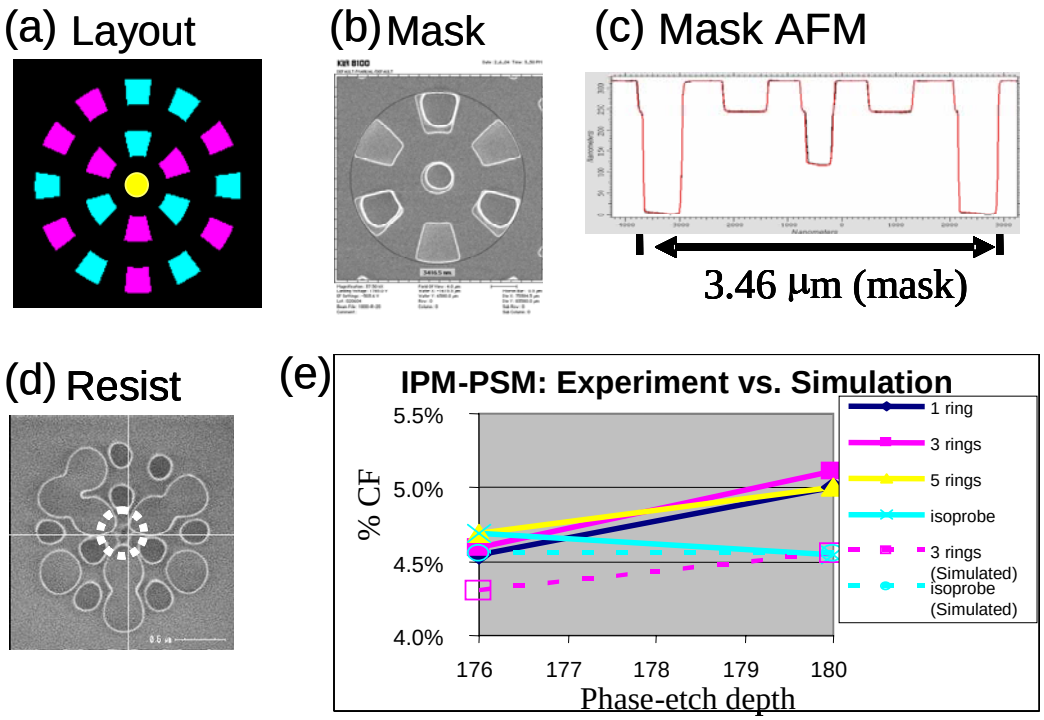

Figure 6-9. IPM experimental results

(a) Layout, (b) SEM and (c) AFM measurements of the mask show the shifted regions were undersized. (d) The measurement consists of monitoring how resist clears at the center of the pattern. (e) General trends agree between experiment and simulation and differences are explained.

Experimental results from two mask locations are compared to simulation in Figure 6-9e. AFM measurements show the difference in theoretical phase shift based on the actual depths of the features to be about four degrees for the two considered mask locations. As expected, the surrounding patterns spill more or less light into the center depending on the local phase depth, whereas the isolated probe remains relatively constant. Although subtle, the slope of the line increases between the one and three-ring patterns. This is expected since more openings in the pattern spill more light into the center, increasing signal strength and sensitivity. Additionally, the slope decreases

between the three and five-ring patterns and is also expected. The smallest illumination condition possible in the tool used was $\sigma = 0.39$. Thus, the IPM-PSM is limited by the mutual coherence radius which, in this case, falls somewhere between the third and fifth ring of the Airy pattern. Unfortunately for $\sigma = 0.39$, the presence of the fifth ring actually decreases measurement sensitivity.

The dashed lines in Figure 6-9e show simulation of a case closely approximating the measured three-ring patterns. The measurement sensitivity, or slope of the line, closely matches the experimental results. However, the isolated probe was expected to cross the pattern probe when the actual depth was 180 degrees. In this case, they cross about about 177 degrees which is likely explained due to the under sizing and contamination of the 90 degree probe.

The three-ring contact pattern signal appears to be about 0.13% of the clear field intensity per degree of phase error. Although small, this measurement is of the true image-plane mask performance which is, for small features, likely not predicted accurately by a mask-plane AFM measurement. Furthermore, this measurement probably has a higher potential sensitivity than that for most other image-plane analysis techniques for certain feature types. For example, in the through-focus technique discussed by Wong [94] (analysis of a 0-180 degree chromeless linespace pattern through focus), the measurement sensitivity decreases when chrome is located between the shifted regions and becomes very feature-size dependent. However, the IPM-PSM relies on the presence of chrome. Thus, for features such as alternating contacts, it may provide the best measurement.

The low apparent signal discussed in this section is primarily limited by two factors: the undersized probe and the limitations of the mutual coherence radius. Table 6-1 shows a comparison of this experiment to a series of thick mask simulated cases with different values of partial coherence. Simulating the same situation as was present in experiment ($\sigma = 0.39$), a sensitivity of 0.24 was predicted. Thus, roughly half of the sensitivity was probably lost due to the probe phase contamination. However, a reasonable illuminator in a current scanner or AIMS tool ($\sigma = 0.20$) would increase this

to 0.60 and perhaps in the future a modification of an AIMS tool with a very small sigma aperture ($\sigma = 0.05$) should increase the mutual coherence radius large enough to achieve over 1% of the clear field per degree phase error with this three ring target. Of course, a larger coherence radius enables more target rings. Additionally, to counteract EM effects, the probes should be slightly larger than was used in this experiment, which could result in a doubling of the signal. Thus, a sensitivity of over 1.5% of the clear field per degree phase error is likely possible.

	Experiment	Simulation		
	σ=0.39	σ=0.39	σ=0.20	σ=0.05
Sensitivity	0.15	0.24	0.6	0.82

Table 6-1. Sensitivity analysis: experiment and simulation

6.4. Analysis of practical considerations and comparison to existing techniques

The effect of various practical imaging considerations such as aberrations, probe fabrication errors and partial coherence are of interest. It is noted that, except for with the probe, electromagnetic effects and mask making limitations are not a concern for these monitors as they have been for the three illumination monitors discussed in Chapters 3-6. In fact, these monitors are intended to measure the combined impact of these two effects since the effective phase of a shifted region will be influenced by both EM effects and imperfections in mask making (sidewall angle, roughness, etc.).

The design's versatility allows the engineer to minimize the impact of aberrations by constructing the surrounding pattern to be nearly orthogonal to all Zernike polynomials of concern. For example, the targets displayed in this paper behave well under the influence of lens aberrations, showing less than 4% variation in probe intensity with 0.01λ (rms) of the most common Zernike terms. Probe transmission uncertainty is built into the analysis technique by the use of a nearby, identical and isolated probe. Slight errors in probe phase have negligible effect due to the nature of the time-averaged intensity, which is evident upon inspection of the intensity equations for both probe

types. However, large errors in probe phase, as was observed with the probe phase contamination in the experiments conducted with test reticle A, can confuse the phase and transmission measurement and decrease sensitivity to both. Furthermore, although completely coherent illumination is ideal, partially coherent illumination (small σ) is sufficient to achieve sensitivity and is easily accounted for in the theory by consideration of the mutual coherence function. Smaller σ, however, enables larger mask patterns and, with a larger geometric factor (G), thus enables greater sensitivity.

Finally, the detection sensitivity possible with this technique out-performs existing techniques for many useful feature types. Direct interferometric methods usually involve an illumination scheme much different than that used in a lithography-printing tool [68]. While they have the ability to very accurately measure actual etch depth, they will not predict effective intensity and phase imbalance caused by the three-dimensional nature of a PSM. Most other existing techniques rely on image-plane analysis, like the method presented here, but fail to meet the sensitivity feasible with the IPM-PSM. These techniques generally compare images of a two-phase pattern exposed through focus and dose to simulation, indirectly measuring phase error. For example, the peak image-plane intensities of two adjacent openings of opposite phase will vary depending on phase and transmission imbalance [94]. Extraction of each error is possible by analyzing the thru-focus behavior, assuming best focal position is known. However, the sensitivity of this approach is highly dependent on feature size, and is optimal for two small, directly adjacent features as seen in Figure 6-10 (L=0.5, S=0). Considering only phase error, the amount the peak intensities differ is greatest for a $0.5\lambda/NA$ opening without chrome. However, when both openings and spacer are $0.5\lambda/NA$ or for a case such as alternating contacts, sensitivity considerably declines. For comparison, the performance of the five-ring IPM-PSM from Figure 6-3 is displayed in Figure 6-8 with a dotted line. Clearly the IPM shows comparable sensitivity to the best-case scenario with the through focus technique. It is noted that much greater sensitivity is readily available by simply using smaller σ and more target rings.

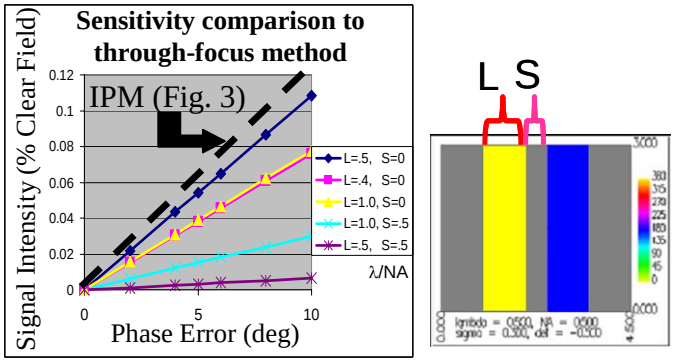

Figure 6-10. Comparison to existing method

Many existing techniques rely on comparison of through-focus behavior to simulation. Sensitivity is feature dependent. Comparison to a small 5 ring IPM (dotted line) is shown. Much greater IPM sensitivity is easily attained with more target rings.

6.5. Summary and overall assessment

A phase-shifting mask pattern has been introduced to evaluate effective phase, transmittance and edge effects of the shifted regions in a PSM. The coherent interaction between an interferometric-probe and a surrounding pattern allows sensitive detection while the orthogonality of phase and transmission errors enables two distinguishable measurements. Monitors can be used on a special test mask or included in the layout of a production mask and can be analyzed with either an AIMS tool or printed resist from a projection printing tool exposure. Actual mask performance is analyzed for a particular feature, to include the effects of real mask making errors as well as effective electromagnetic printing effects. Good sensitivity is available for both phase trenches and contacts and is limited only by the number of features built into the design. Monitors are relatively insensitive to aberrations and reasonable probe-phase manufacturing errors. They show improved performance for many feature types over existing techniques and do not require through-focus analysis. Experimental results suggest that a measurement sensitivity of over 1% of the clear field per degree phase error is possible on a lithographic scanner, where the minimum σ is around 0.2. However, with an aperture stop to achieve $\sigma = 0.05$, 1.5% of the clear field per degree phase error is likely possible. The most likely practical application for this technique would be on an AIMS tool at the mask shop for monitoring the effective phase of contacts or minimum feature alternating

trenches. This type of measurement is not feasible with any other known image-plane technique.

7 Screening IC Layouts for Vulnerabilities to Polarization and High-NA Effects Using Pattern Matching

Polarization has quickly become an important issue in optical lithography for semiconductor manufacturing control [2][83]. The rapid adoption of immersion lithography and hyper-numerical aperture (NA) projection printing systems requires the vector nature of light to not be neglected. While Chapter 5 discussed polarization monitoring and much attention has been paid elsewhere to developing and understanding lithography tools with polarization control [66][19], this chapter is intended to help understand how these effects may impact design layouts.

A pattern matching method for quickly estimating the extent to which high-NA and polarization vector effects reduce image quality in projection printing is derived and evaluated for prototypical layout patterns. The angular rotation of the in-incidence plane TM electric field component produces two unwanted effects. It reduces the collinear addition of electric fields at the location of the peak image intensity and, more importantly, it also introduces an electric field component perpendicular to the image plane that acts like stray light. While these imaging effects can be simulated rigorously, the challenge is to quickly screen an entire layout to identify the small subset of regions that must be analyzed more carefully. The approach developed mathematically and evaluated in this chapter consists of finding a set of local theoretical patterns having the maximum lateral impact at a reference point. As illustrated Figure 7-1, pattern matching is then used to find areas in a layout that resemble these maximum lateral test functions (MLTFs) by scanning them over the entire chip layout. Vulnerability scores, representing linear sensitivity to either high-NA effects or to perturbations of illumination

polarization state, are determined for each location from a weighted combination of multiple match factors (the degree of similarity to each pattern). These effects are important as intensity changes of over 40% and 10% can occur with NA and polarization, respectively, even in simple layouts. This technique can serve as an efficient means to communicate in advance to designers the potential impacts of effects that are difficult to describe, even with the use of advanced design rules. Additionally, this method can assist in developing test masks designed to help learn about a process flow.

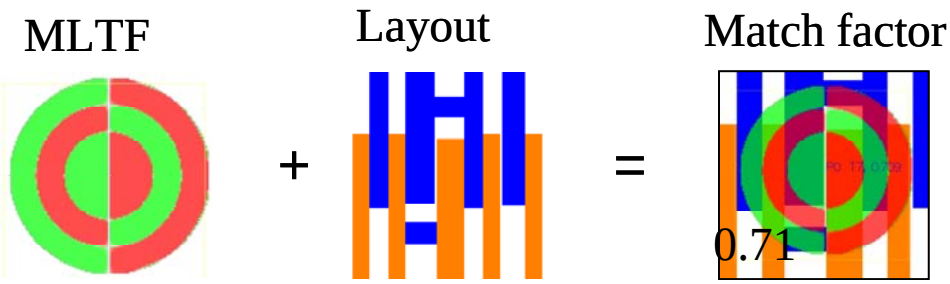

Figure 7-1. Pattern matching concept

Pattern matcher finds areas in a layout that are similar to a defined maximum lateral test function (MLTF).

Section 7.1 introduces the concept of pattern matching and references previous work done in this line of research. The MLTFs used to extend pattern matching to account for high-NA and polarization effects are derived from basic principles in Section 7.2. Section 7.3 then describes the pattern matching scheme used to determine a layout's vulnerability to these effects. Two examples are presented in Section 7.4 for on-axis coherent illumination. Section 7.5 describes how this technique can be extended to account for various other optical effects such as off-axis illumination, pupil scalar wavefront aberrations, or mask making variations. Additionally, a pattern matching strategy is discussed for layouts with optical proximity correction.

7.1. Pattern matching: concept and prior work

The pattern matcher was designed by Gennari to rapidly scan a layout for areas of high similarity to a given pattern [25]. Previous applications of pattern matching have

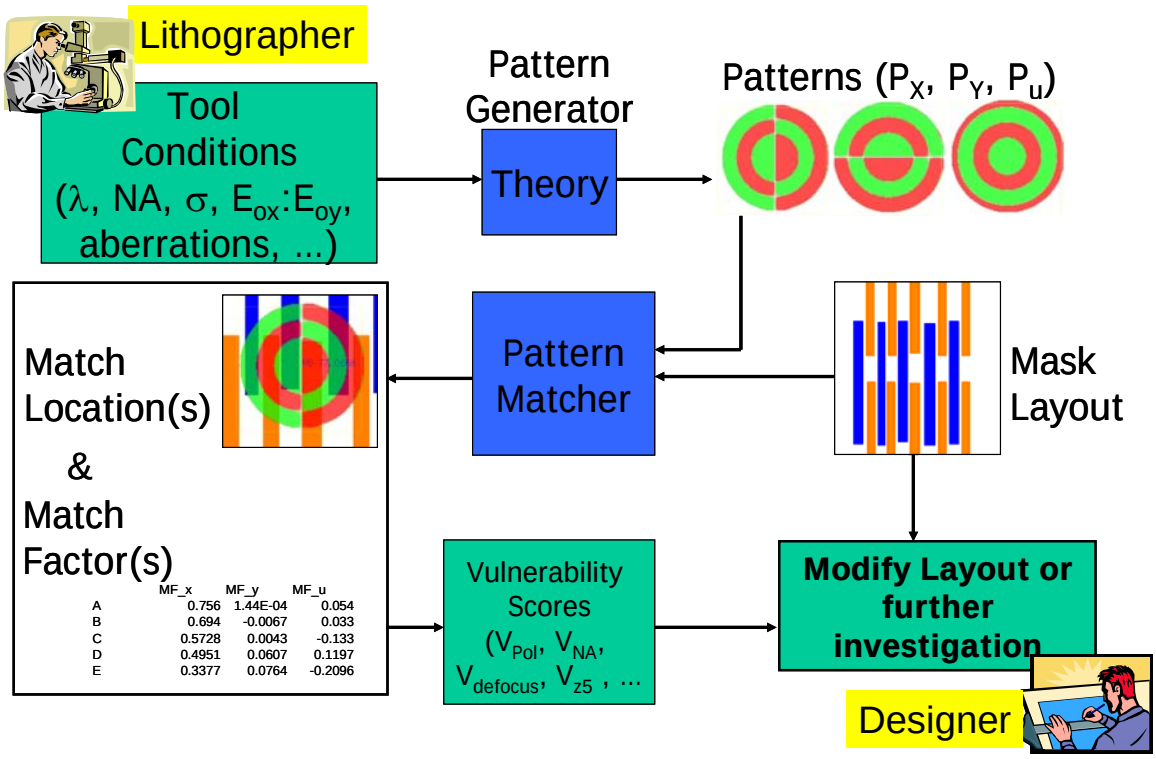

7-2. Pattern matching flow.

included projection lens aberrations, layer-to-layer alignment, defects, reflective notching, and laser assisted thermal processing and have been discussed by Gennari [25], Neurether [65], and Robins [77]. The basic pattern matching algorithms and concept are described further in [25]. The concept of pattern matching and typical flow are shown in Figures 7-1 and 7-2. Input to the pattern matcher consists of a layout in GDS format and a pattern file, which is a sequence of complex numbers describing the magnitude and phase of the pattern with which to match against. The lithographer identifies the relevant tool condition and the patterns are generated, such as those described in Section 7-2. The pattern matcher then scans the layout for areas which have a high match factor with that MLTF. Match factor is essentially the normalized integral of the MLTF multiplied by the layout, a measure of their degree of similarity. The match factors and match locations are output in tabular format. For this project and for subsequent work, the pattern matcher was modified by Holwill to output all of the sections of the layout with high match factors in a format compatible with the Panoramic simulator. Simulation was used to confirm the calculated vulnerability predictions. In addition, Holwill modified the

program to calculate the match factors for multiple MLTFs simultaneously, thus allowing the vulnerability scores to be calculated [32]. The pattern matcher's fast runtime is due to the fast algorithms employed for the matching, including a pre-integration algorithm that removes the need to process each pixel of the layout [24].

7.2. Pattern (MLTF) Derivation from High-NA Vector Effects

It is well documented in lithography that the electric field component oriented radially in the pupil, or the TM component, will suffer a loss of contrast due to high-NA vector effects [2][83][6]. This section will explain the mechanism that causes this and derive a set of patterns that, through proximity effects, maximize this unwanted side effect of high-NA imaging. The derivation is similar to that for the polarization monitors of Chapter 5. However, it is cast in a slightly different manner to emphasize extendibility to off-axis illumination and pupil effects. The following section will then describe how these patterns, or maximum lateral test functions (MLTFs), are used with pattern matching to predict the vulnerability of a layout to high-NA and polarization vector effects.

As seen in Figure 7-3, a large angle of incidence at the wafer plane means that the TM component in the pupil is rotated to be partially normal to the wafer. This introduced z-component of electric field will destructively interfere in locations where the x and y-components constructively interfere. This acts somewhat like stray light and causes the interference pattern to be image-reversed and out-of-phase with the traditional scalar, or low-NA, image. This z-component (E_Z) was shown in Section 2.1.1.2 to follow the relation:

$$E_z(x) = \sin(\phi) E_{TM}(x) = \frac{NA}{n_{resist}} E_{TM}(x) = \frac{k_x}{k_0} E_{TM}(x) = \frac{j}{k_0}\frac{\partial}{\partial x} E_{TM}(x) \qquad \text{Eq. 7-1.}$$

where k_x is the propagation vector along the wafer and ϕ is the angle of incidence. Thus, the z-component of the electric field is proportional to the spatial derivative of the low-NA, or scalar, components.

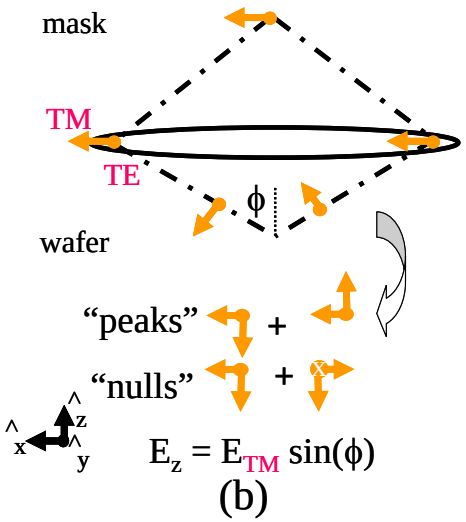

Figure 7-3. Vector effects of high-NA imaging induce a field component normal to the image plane.

Extending this concept to three dimensions and noting that fields in the image plane can be described by two orthogonal polarization components (x and y):

$$E_{Z,PSF}(x,y) = \frac{j}{k_0}\frac{\partial}{\partial x}\mathrm{PSF}(x,y) + j\frac{j}{k_0}\frac{\partial}{\partial y}\mathrm{PSF}(x,y) \qquad \text{Eq. 7-2.}$$

where PSF is the point spread function and describes the electric field profile at the image plane due to a coherent illumination source. In a Koehler illumination scheme for an on-axis coherent source (small sigma), this field profile is simply the Airy pattern or, likewise, the optical proximity function. Here it will be used to derive a proximity effect function for the z-component of light resulting from high-NA imaging. Similarly, the PSF can be described as the inverse Fourier transform of the Pupil convolved with the point source:

$$\mathrm{PSF}(x,y) = IFT(Pupil \otimes source) = C_M \exp(iC_P) \qquad \text{Eq. 7-3.}$$

where C_M and C_P refer to the magnitude and phase of PSF(x,y). Complex formulation will be required when considering the off-axis case later.

Invoking the chain rule,

$$\frac{\partial}{\partial x}\mathrm{PSF}(x,y) == \frac{\partial}{\partial x}[C_M \exp(iC_P)] = (\frac{\partial}{\partial x}C_M)\exp(iC_P) + iC_M \exp(iC_P)(\frac{\partial}{\partial x}C_P) = P_{X1} + iP_{X2}$$

Eq. 7-4.

$$\frac{\partial}{\partial y}\mathrm{PSF}(x,y) == \frac{\partial}{\partial y}[C_M \exp(iC_P)] = (\frac{\partial}{\partial y}C_M)\exp(iC_P) + iC_M \exp(iC_P)(\frac{\partial}{\partial y}C_P) = P_{Y1} + iP_{Y2}$$

Eq. 7-5.

results in four orthogonal complex components (P_{X1}, P_{X2}, P_{Y1}, P_{Y1}) of the function describing the z-component of electric field.

Figure 7-4a depicts a visual representation of the above equations, showing the four components as separate, orthogonal, complex patterns. For this on-axis case, P_{X2} and P_{Y2} are assumed to be numerical noise, since $\frac{\partial}{\partial \boldsymbol{x}}\boldsymbol{C_P}$ and $\frac{\partial}{\partial \boldsymbol{y}}\boldsymbol{C_P}$ is 0 or infinity due to the step-like phase function of the Airy pattern. This is a direct result of the coherent illumination where the source point is on-axis. Thus, P_{X1} and P_{Y1} describe the proximity effect functions at the image plane of z-component light for incident, on-axis, x- and y-polarized light, respectively. In the case of off-axis illumination, P_{X2} and/or P_{Y2} may become significant depending on how the off-axis TE and TM polarizations relate to the x and y coordinate system. See Section 5.5.1.5 for a more in-depth analysis of the resulting subtle differences in the proximity effect of off-axis TE and TM polarized light.

Reciprocity then implies that these patterns, when located in the object plane, are most effected by polarization and high-NA effects (i.e. they are the patterns that, due to proximity effects, 'spill' the most amount of z-component light into the center of the image). These patterns form the basis of the polarization monitoring technique described in Chapter 5. Figure 7-4b shows by simulation (using Panoramic software) how one of these patterns is sensitive to incident polarization state as a considerable jump in intensity at the center of the pattern's image is detected for orthogonal polarization states. For the purposes of this chapter, they form the set of maximum lateral test functions (MLTFs). The next section describes how they are used with pattern matching to determine a layout's vulnerability to high-NA and polarization.

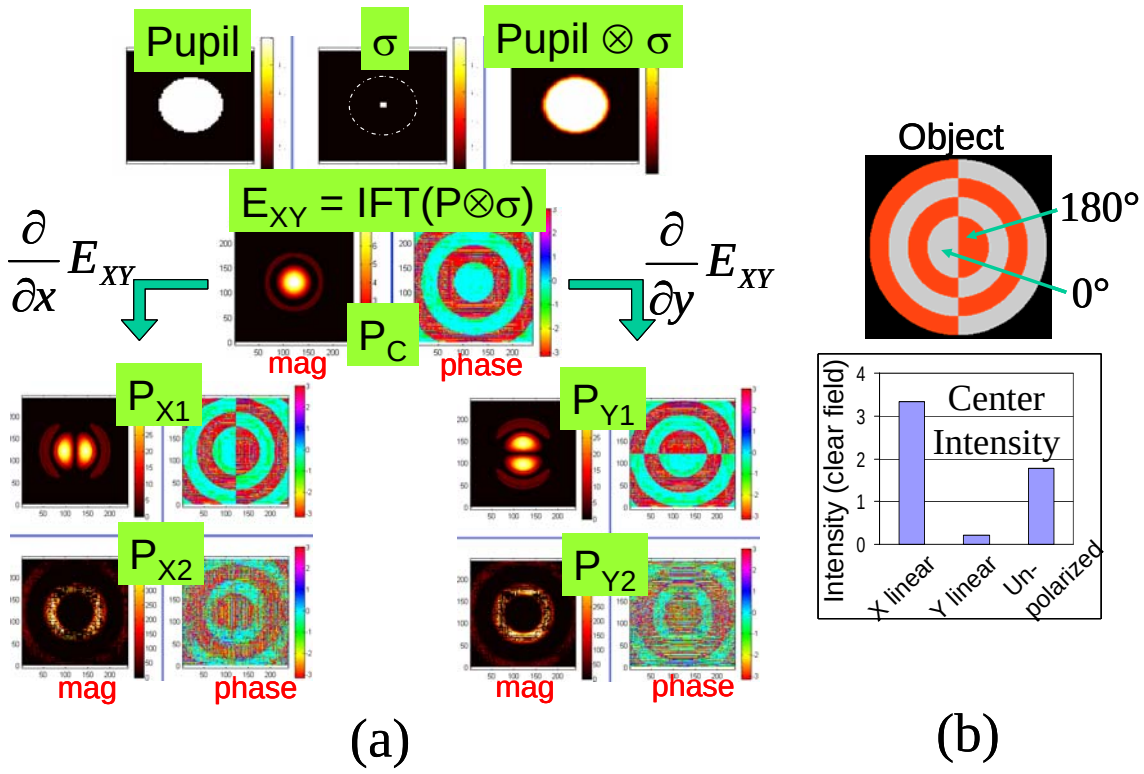

Figure 7-4. On-axis MLTF derivation

(a) Visual representation of equations 7-3 to 7-5 for coherent illumination, resulting in four complex components of high-NA, z-component proximity effect. PX2 and PY2 are assumed numerical noise for explained reasons. (b) Patterns PX1 and PY1 are related to the polarization monitors of Chapter 5 and show very good sensitivity to polarization state.

7.3. Predicting Vulnerability to High-NA and Polarization using Pattern Matching

The patterns, or MLTFs, derived in the previous section coherently spill z-component light into the center of the pattern for a particular polarization component. Thus, an area in an integrated circuit layout that somewhat resembles one of these MLTFs will, for coherent illumination, cause a certain amount of z-component light to be 'spilled' into the center. The amount of this spillover will depend on the degree of similarity, or match factor, between the layout and the MLTF.

In order to determine the vulnerability of a layout to high-NA and polarization, it is first noted that the electric field at any location can be written as the sum of orthogonal polarization components:

$$E_P = E_X \hat{x} + E_Y \hat{y} + (E_{X\to Z} + iE_{Y\to Z})\hat{z} \qquad \text{Eq. 7-6.}$$

where $E_{X\to Z}$ refers to the high-NA conversion of x-polarized incident light into z-component electric field in the image. Due to the linearity invoked by coherent illumination, each field component can be approximated by multiplying three factors: the amount of field incident in the appropriate polarization component (E_{OX}, E_{OY}), the match factor for the appropriate MLTF superimposed over the layout at point P (MF_C, MF_{X1}, MF_{X2}, etc.), and the percentage of electric field spilled into the center for a 100% match ($E_{C,max}$, $E_{X1,max}$, etc. , constants which can be determined via simulation):

$$\begin{aligned} E_P = {} & (E_{OX}\cdot MF_C \cdot E_{C,\mathbf{max}})\hat{x} + (E_{OY}\cdot MF_C \cdot E_{C,\mathbf{max}})\hat{y} \\ & + \mathbf{[\{}E_{OX}(MF_{X1}\cdot E_{X1,\mathbf{max}} + iMF_{X2}\cdot E_{X2,\mathbf{max}}\mathbf{\}} \\ & + \mathbf{\{}E_{OY}(iMF_{Y1}\cdot E_{Y1,\mathbf{max}}\hat{z} + iMF_{Y2}\cdot E_{Y2,\mathbf{max}}\hat{y})\mathbf{\}]}\hat{z} \end{aligned} \qquad \text{Eq. 7-7.}$$

Noting that the two quantities in {} are orthogonal due to the spatial orthogonality of E_{ox} and E_{oy}. Intensity is, therefore, $I_P = E_P \cdot E_P^*$, where * refers to the complex conjugate. Note that the first two terms are simply the scalar image, or convolution of the point spread function with the layout. Also note that MF_{X2} and MF_{Y2} result in fields oriented in $\hat{z}$ and are out of phase with those of P_{X1} and P_{Y2}. These terms only become relevant in the off-axis case, described in Section 7.5.

Vulnerability scores are subsequently calculated by determining the change in intensity at P due to either high-NA effects or perturbation to the illumination polarization. Vulnerability to high-NA is:

$$V_{NA} = I_{P,High-NA} - I_{P,Low-NA} \qquad \text{Eq. 7-8.}$$

which is simply determined by the term enclosed by [ ] in equation 7-7. This can be useful in identifying areas that will be most misrepresented by simulation (or tuning the layout with optical proximity correction) using scalar imaging models. Vulnerability to perturbation in illumination polarization is:

$$V_{Pol} = \frac{\partial I_P}{\partial E_{OX}} \qquad \text{Eq. 7-9.}$$

evaluated where E_{OX}:E_{OY} is the intended polarization ratio and $E_{0X}^2 + E_{0Y}^2 = 1$. This can be useful in identifying areas most sensitive to unintended variations in the source polarization. Examples of each of these are shown in the next section.

To sum, five match factors (3 for the on-axis case) for each location of interest and some pre-determined constants are sufficient to determine vulnerability. Assuming that not every grid point in the layout is of interest, this can be done orders of magnitude faster than simulation. Thus, layout areas can be quickly identified for more scrutiny.

7.4. Simulated Examples

This section will describe two simulated examples showing the validity of vulnerability predictions for high-NA (V_{NA}) and perturbation to illumination polarization state (V_{Pol}). These examples are with on-axis coherent illumination and alternating phase shift masks. However, the next section will show that this technique is extendable to various off-axis illumination schemes with any mask technology. This work has been extended to do so by Holwill [32].

To illustrate the vulnerability to high-NA technique, Figure 7-5a shows a set of alternating PSM and binary layout clips that were fabricated to show a large range of match factors. Additionally, the match factor results and calculated V_{NA} scores for each layout clip are listed. The corresponding plot shows good correlation between the calculated and simulated values of $I_{High\text{-}NA}$ and $I_{Low\text{-}NA}$. Additionally, the V_{NA} score is linearly proportional to intensity change with a slope of about 80% of the clear field per V_{NA} and that the average intensity change due to this effect can be around 40% of the clear field. Thus, this technique proves an efficient method to determine, for example,

areas that will be the most misrepresented by a scalar imaging model. Additionally, areas can be found that are likely to have the greatest difficulty in scaling to use in a higher numerical aperture tool.

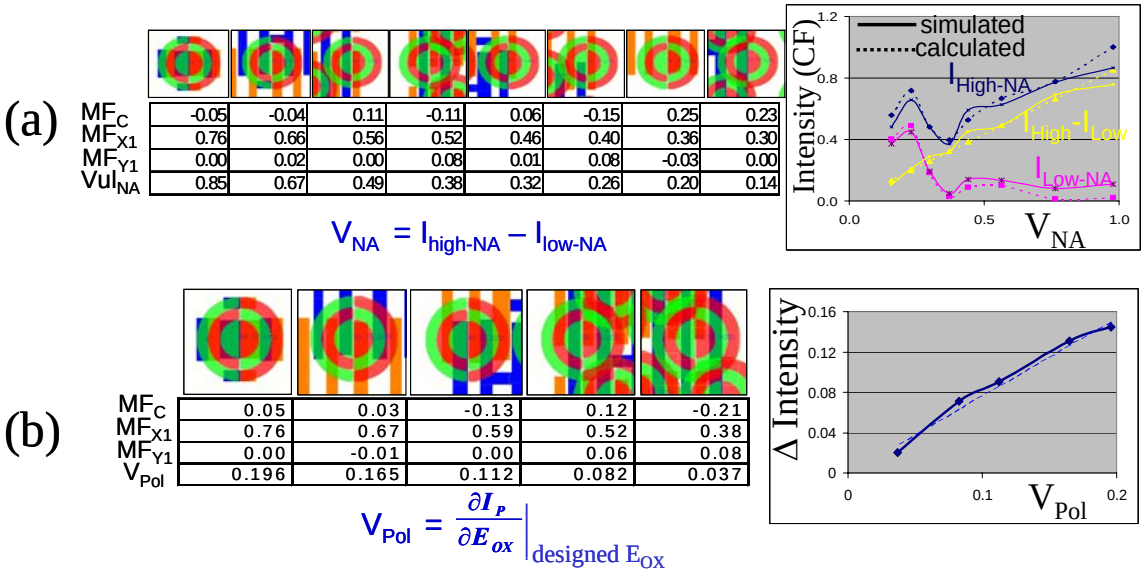

Figure 7-5. Simulated vulnerability score examples

Simulation confirms vulnerability predictions to (a) high-NA and (b) illumination polarization variation. Vulnerability scores are good indicators of intensity change at match location.

The second example, illustrated in Figure 7-5b, uses a slightly different set of fabricated layout clips to show prediction of a layout's vulnerability to perturbation in the illumination polarization state. The corresponding plot shows a potential practical use for this technique. Here it is assumed that these layout clips were intended to be used with 100% y-polarized light. However, the illumination design is not perfect resulting in, for this example, 10% unwanted x-polarized light. A nearly-linear correlation exists (with a slope of about 77% I_{CF}/Vpol) between the V_{Pol} scores and the actual (simulated) change in intensity at those locations for this perturbation to the illumination polarization. This indicates that this technique is a good means to quickly screen layouts for areas that are susceptible to this potential process variation. Simulation, on the other hand, would require simulating the entire layout twice (once for each polarization condition) and comparing the results. This is likely a much more time consuming process. Also note that if a 10% variation is reasonable for control of the illumination polarization state, then

image intensity for some layouts can change up to about 10% of the clear field. For both of these examples, prediction is accurate with simulation by better than 90%.

7.5. Extension to Off-Axis Illumination and Other Optical Effects

The pattern matching framework and mathematical derivation of the MTLFs proposed in this paper are extendable to multiple variations of the illumination and pupil function. The coherent source point used in equation 3 is not required to be on-axis; nor is the pupil function required to be unaberrated. Any off-axis illumination frequency or any scalar wavefront pupil aberration can be easily substituted, resulting in a set of MLTFs unique to a particular imaging condition. This section will show examples of these extensions and discuss other issues for practical implementation of this pattern matching technique.

7.5.1. Off-axis illumination

Figures 7-6a shows a set of patterns derived for a single monopole oriented along the x-axis. Note the phases of the resulting MLTFs are no longer constant-valued step functions. Rather, a linear phase progression exists corresponding to the illumination spatial frequency used. Additionally, P_{X2} begins to contribute to the central intensity. This can be attributed to the fact that the lack of symmetry of a diffraction pattern in the pupil due to an off-axis illumination ray results in diffraction orders that are not completely interfered with. Thus, a point-spread function-like effect inevitably 'spills' z-oriented light into the center simply due to the off-axis nature of the source. Note that this light is incoherent with that from P_{X1}, resulting from the chain rule derivation. Thus, the difference between the high-NA and low-NA intensities is no longer simply the part of equation 7 enclosed in [ ]. Figure 7-7a shows an example of layout that might have a relatively large matchfactor for one of these patterns. Note how the layout pitch corresponds to the period of the linear phase progression. This implies that the z-component spillover due to high-NA from the surrounding features to the center point (match location) will be in phase. Thus, there will be a relatively large change in the intensity at the match location. This concept has been verified for off-axis illumination by Holwill [32] in a manner similar to the on-axis cases of Figure 7-5.

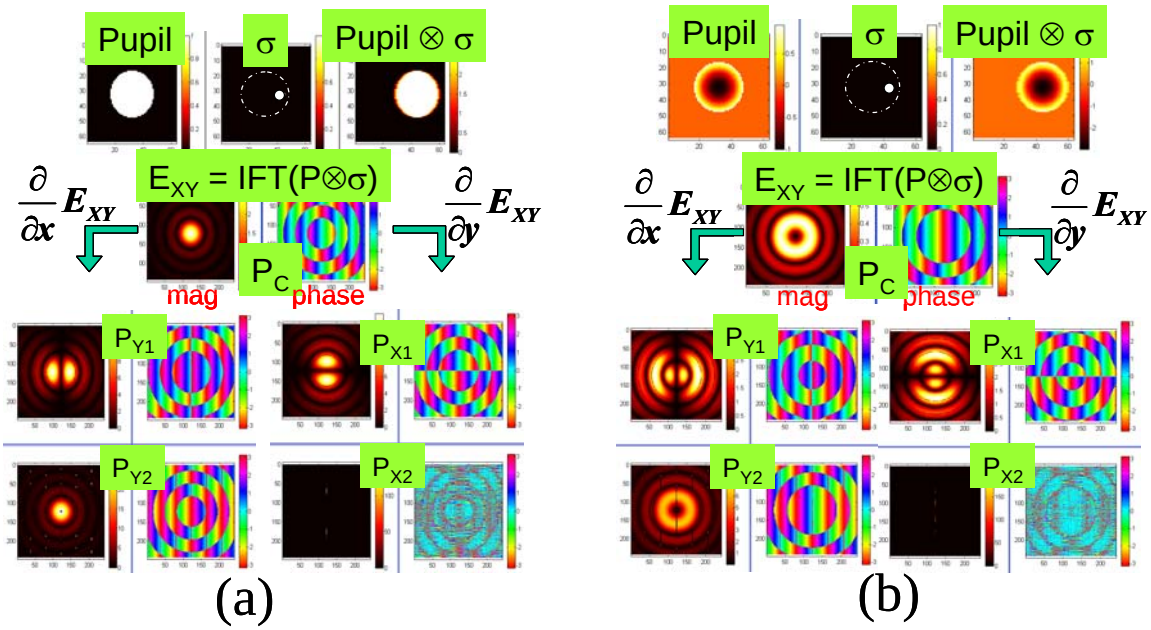

Figure 7-6. Off-axis MLTF derivation

Derivation of MLTFs for (a) off-axis illumination and (b) off-axis illumination with defocus aberration. MLTFs can derived for various optical conditions.

The examples in this paper have focused on coherent illumination, where the patterns are derived for a single illumination frequency. However, pattern matching for other illumination schemes are feasible, although runtimes are likely to increase. For example, dipole illumination can be represented by two sets of patterns from opposing source locations. Since illumination source points are designed to be temporally incoherent, total intensity at the wafer will simply be an averaging of the intensities from each source point. In the case of dipoles, symmetry may allow faster runtimes by allowing one dipole to be neglected. Generally, this technique is suited for illumination schemes accurately represented by a few single illumination frequencies.

7.5.2. Pupil scalar aberrations

Figure 7-6b shows the addition of an aberrated pupil, in this case the defocus aberration, with off-axis illumination. Thus, using the resulting set of MLTFs, vulnerability scores can be determined for V_{NA} or V_{Pol} for this tool condition. Or, by using similar mathematics and comparing the aberrated to the unaberrated case, one can determine the vulnerability to defocus ($V_{defocus}$) or to any other type of aberration.

Aberrations are typically represented by combinations of Zernike polynomial terms. These aberration patterns are similar in nature to those discussed in reference [78], with the addition of the allowed off-axis illumination and method of calculating vulnerability scores.

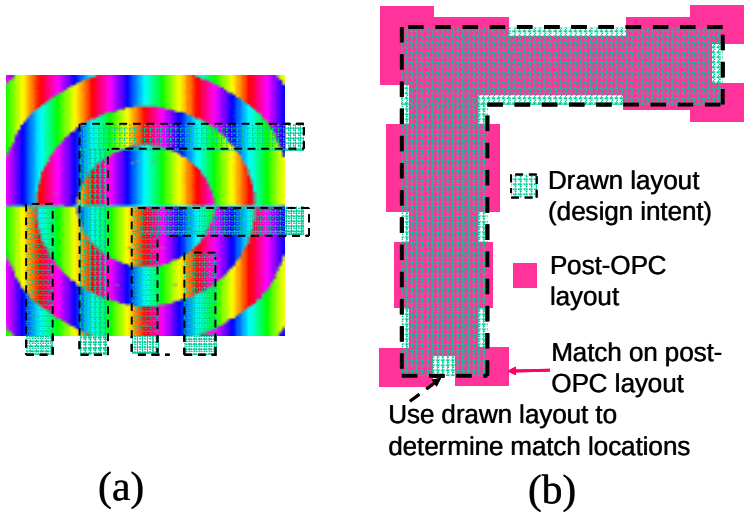

Figure 7-7. Off-axis and OPC example

(a) Example of layout with high match factor for off-axis case. Note how feature pitch corresponds to period of phase progression. (b) Matching strategy for post-OPC layouts.

7.5.3. Pattern matching scheme for optical proximity correction

The pattern matcher operates by determining the match factors for a set of locations depending on a user-defined matching scheme. This allows a trade-off between run time and accuracy. Typically, matching is done for all corners and selected edge points. However, optical proximity correction (OPC), a commonly used technique to make a layout more manufacturable, can dramatically increase the number of corners and potentially increase runtime. Thus, the matching scheme depicted in Figure 7-7b is proposed. Here, it is assumed that the post-OPC layout succeeds in creating an image intensity profile that crosses the resist threshold according to the pre-OPC (design intent) layout. Assuming that perturbations to intensity only matter along feature edges, matching would be done using the post-OPC layout. However, the match locations would be determined using the pre-OPC design (i.e. the dotted line in Figure 7-7b). This

should increase both accuracy and runtime. See reference [25] for further discussion of factors affecting runtime.

7.5.4. Mask manufacturing errors

The logic used in creating the interferometric probe monitors (IPM) for PSM performance of Chapter 6 has implications for EDA integration and design for manufacturability. The research was initially intended to create a target design to be used as a pattern matching lateral test function to find areas in a layout that would be most sensitive to errors in the effective phase of shifted regions in a PSM. However, since infinite possible IPM configurations exist, no single pattern could serve as a lateral test function to identify mask locations most susceptible to phase and transmission errors. However, an algorithm based on the IPM technique could potentially be built in to the pattern matching software. For example, the influence of phase-error residual effects from the surrounding layout, weighted appropriately by the Airy pattern, could be calculated for a particular mask location. Depending on the phase of the intended feature at that location, either the real or imaginary part of this residual effect would be of concern. The magnitude of these effects and how they interact with the existing feature would be compared to a threshold, thus identifying potential sites susceptible to the effects of phase error.

7.6. Summary and overall assessment

A technique to quickly screen integrated circuit design layouts for regions most vulnerable to high-NA and polarization vector effects has been presented. These effects are important, even in simple layouts, and can cause intensity changes of about 40% or 10%, respectively. A set of maximum lateral test functions (MLTFs) are first derived from basic principles. These are theoretically the most sensitive patterns to high-NA and polarization effects. A pattern matching scheme is then implemented to find areas in the layout that somewhat resemble these MLTFs. A large degree of similarity, or match factor, implies vulnerability to these effects. A quantitative vulnerability score is determined by a weighted combination of three to five match factors. The vulnerability scores are linearly proportional to intensity change with a slope of about 80% of the clear field per vulnerability score. Predictions are generally accurate with simulation to better

than 90%, suggesting this is a good technique to quickly screen layouts for areas in need of more attention. Examples have been shown for on-axis coherent illumination with an unaberrated pupil. However, extension of this technique to various off-axis illumination schemes, aberrated pupils, and multiple mask strategies has been discussed.

Finally, it is noted that this technique can be somewhat similar to a simulator using the sum of coherent systems (SOCS) approximation [13]. SOCS essentially decomposes an optical system into an orthogonal, and thus incoherent, set of appropriately weighted eigenfunctions. This technique is similar in nature, however the aim is to use the minimum number of functions (MLTFs) to extract vulnerability to a particular effect. In practice, these two techniques would complement each other, for each might have a use at different stages in the design cycle. For example the pattern matching approach might be an efficient means to communicate to designers in advance the potential impacts of effects that are difficult to describe, even when using advanced design rules.

8 Polarization aberrations: A comparison of various representations and PSM birefringence monitor

Various representations of polarization aberrations are described and compared in this chapter for optical lithography. Polarization aberrations, which are potentially important with hyper numerical aperture tools, are a complicated phenomena that refer to induced polarization dependent wavefront distortions as light propagates through an imaging system. Pupil representations based on the following concepts are discussed: the physical polarization properties, the Mueller matrix, the Jones matrix, and the Jones matrix decomposed into a Pauli spin matrix basis. Although each has its own advantages and disadvantages, it is concluded that the Jones matrix representation decomposed into a Pauli spin matrix basis offers the most useful format for the lithographer due to its compact notation, physically intuitive interpretation, ability to be implemented into standard imaging equations, and its usefulness as an input into a lithographic simulator. Depending on the assumptions that can be made, the pupil specification consists of three to eight independent functions, where a normalization constant is calculated to ensure a physically realizable pupil. An example is shown to illustrate the usefulness of this strategy. Also, a simple metric for lens polarization quality based on this representation is proposed. Finally, a phase shift mask monitoring technique is introduced to characterize projection lens birefringence.

8.1. Introduction

The adoption of immersion and ultra-high numerical aperture (NA) projection printing systems in semiconductor manufacturing demands that the state of polarization be closely monitored and understood throughout multiple components of the optical

system. Much attention has been paid recently to the state of polarization of the illumination source and the polarizing effects of the photomask [83][6][18]. However, polarization issues may also arise from within the projection lens pupil (and, potentially, the immersion liquid or solid) in the form of polarization aberrations.

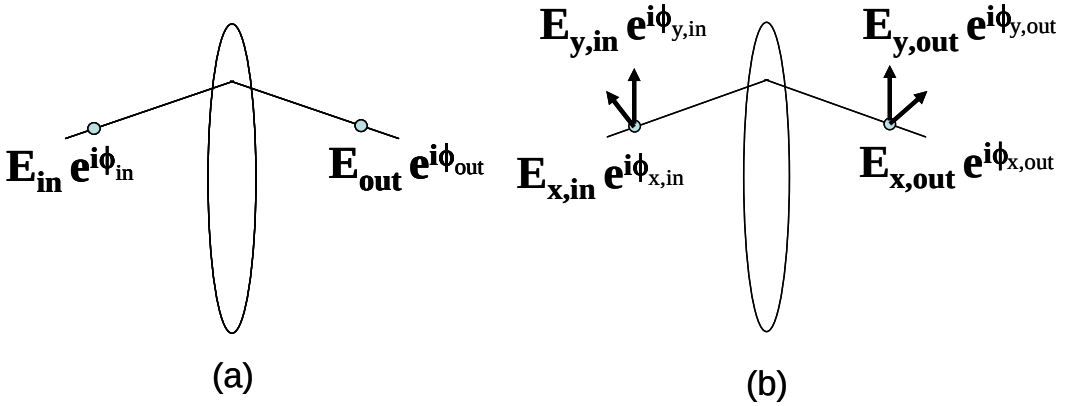

Figure 8-1. Scalar vs. polarization aberrations

(a) Traditional aberration theory assigns one number to each pupil position for the optical path difference. (b) Polarization dependent wavefront distortions can cause an intricate and often non-intuative coupling between complex field components, creating the need for a more complicated characterization of the pupil.

Scalar wavefront aberrations, the induced variation of phase across the pupil, are relatively well understood, controlled and corrected for in today's industry. This analysis generally associates a single number with each pupil location that relates the exiting phase (ϕ_{out}) with the incident phase (ϕ_{in}) of a given ray, as seen in Figure 8-1a. The relative phase change across the pupil is described by the optical path difference ($\Phi(\rho,\theta)$), which is seen in the scalar diffraction imaging equation for coherent illumination as:

$$E_{Wafer}(x', y', a) = \frac{1}{\pi} \int_0^{2\pi} \int_0^1 E_{Diff}(\rho, \theta, a) e^{ik[\rho \cos(\theta) x' + \rho \sin(\theta) y']} e^{ik\Phi(\rho,\theta)} \rho d\rho d\theta \qquad \text{Eq. 8-1.}$$

where $E_{Diff}(\rho, \theta, a)$ represents the scalar field in the pupil diffracted from the photomask for a given illumination source point (a). The image intensity is then determined as the incoherent sum over all illumination source points:

$$I_{Wafer}(x',y') = \int_{source} \left| E_{wafer}(x',y',a) \right|^2 da \qquad \text{Eq. 8-2.}$$

The optical path difference aberration function is typically decomposed into Zernike polynomials $(Z_j(\rho,\theta))$,

$$\Phi(\rho,\theta) = \sum_j a_j Z_j(\rho,\theta) \qquad \text{Eq. 8-3.}$$

weighted by coefficients (a_j) [7]. The Zernike polynomials form an orthonormal set over a circular pupil and offer a useful means to analyze the impact of scalar lens aberrations. Thus, they have served as the 'language' used in the industry to describe scalar aberrations.

However, subtle phenomena causing polarization dependent wavefront distortions can gain importance when imaging at high numerical aperture. These distortions, termed polarization aberrations, describe not only the variations of amplitude and phase across the pupil, but also the intricate coupling between complex electric field components, depicted in Figure 8-1b. Since light is a transverse electromagnetic wave, it is thus a vector wave that can be described by two orthogonal vector components, both orthogonal to the wave's direction of propagation. Polarization refers to the properties of light (either amplitude or relative phase) associated with these two vector components. Polarization aberrations generally serve to induce a change in the nature of the polarization of light as it propagates through a lens system. The impact of polarization aberrations on imaging results from a complex interplay between the fields scattered into the pupil and the specific nature of the polarization aberrations present in the projection lens system. Generally, polarization aberrations can be described as creating a double image (one for each orthogonal polarization state) which can lead to various undesirable effects such as image placement errors, loss of depth of focus, degraded dose latitude, non-telecentric imaging and/or across field CD errors. For a discussion of the impact of polarization aberrations on imaging, the reader is referred to references [88][82][79]. It is noted that intrinsic lens birefringence, a typical cause of polarization aberration, was a primary reason for the semiconductor industry's abandonment of 157nm lithography a few years ago.

Thus, the potential for polarization aberrations dictates that each pupil location can no longer be characterized by a single scalar quantity. Rather, the true vector nature of light must be considered and the intricate (and often non-intuative) coupling between the complex electric field components must be accounted for. This analysis results in a pupil that, depending on the mathematical basis chosen and the assumptions made, can be described by three to sixteen different functions.

This chapter will describe and compare various representations of polarization aberrations. The goal of this work is to determine a suitable representation to serve as a common 'language' for discussing polarization aberrations and as an easy-to-use input into future lithography simulators. Also, a simple metric for characterizing lens polarization quality will be discussed. Section 8.2 of this paper will describe the physical mechanisms and material properties that can cause polarization aberrations. Sections 8.3 through 5 will describe the Mueller matrix pupil representation, the Jones-pupil representation, and the Pauli-pupil. The situations where each of these representations apply and the assumptions necessary for their validity will be discussed. Each method will be evaluated in terms of its accuracy, the practicality of the assumptions required, the degrees of freedom (and thus the complexity) required to describe the pupil, the feasibility of physical measurement, and its advantages and disadvantages for practical use as an input for a simulation tool. Although each may prove most useful for a particular application, it is concluded that the Pauli-spin formalism generally provides the most convenient means to characterize polarization aberrations for optical lithography. Section 8.6 will discuss the usefulness of the Pauli-pupil to optical lithography, to include a suggested simulation flow and polarization metric. Additionally a simulated example illustrates the usefulness of the Pauli-pupil approach by showing the relative impact that various polarization effects may have on imaging.

8.2. Physical mechanisms causing polarization aberrations

Polarization elements serve to divide incoming radiation into two parts and transmit those parts with differing amplitude and/or phase. Changes in amplitude are termed diattenuation and changes in phase are referred to as retardance. The two parts are found as the eigenvectors of the polarizing element and are sometimes referred to as

the ‘eigenpolarizations.’ The orientation of these eigenpolarizations and the manner in which electric fields oriented in their direction are transmitted depend both on material properties and on the characteristics of interfaces between media. Assuming no scalar effects, the primary eigenpolarization corresponds to the incident electric field component that is passed through the element unperturbed. The state of all other incident fields will be altered to some degree.

The primary material property of interest is the dielectric tensor (**ε**), which describes the relationship between the electric field (**E**) and dielectric displacement (**D**) within a material:

$$\begin{bmatrix} \mathbf{E}_x \\ \mathbf{E}_y \\ \mathbf{E}_z \end{bmatrix} = \boldsymbol{\varepsilon} \begin{bmatrix} \mathbf{D}_x \\ \mathbf{D}_y \\ \mathbf{D}_z \end{bmatrix} = \begin{bmatrix} \varepsilon_{xx} & \varepsilon_{xy} & \varepsilon_{xz} \\ \varepsilon_{yx} & \varepsilon_{yy} & \varepsilon_{yz} \\ \varepsilon_{zx} & \varepsilon_{zy} & \varepsilon_{zz} \end{bmatrix} \begin{bmatrix} \mathbf{D}_x \\ \mathbf{D}_y \\ \mathbf{D}_z \end{bmatrix} \qquad \text{Eq. 8-4.}$$

If the dielectric tensor can be expressed as a constant, than the material is isotropic and no polarization activity occurs. Any other condition is referred to as anisotropic, leading to polarization behavior that depends on the properties of the dielectric tensor. For example, a Hermitian dielectric tensor produces orthogonal eigenpolarizations (thus a homogeneous media) where the eigenvalues determine differing transmission and/or phase velocities along each eigenpolarization direction. A non-Hermitian tensor creates a more complicated situation that can cause various combinations of diattenuation, retardance, and potentially non-orthogonal eigenpolarizations. A material with polarization dependent absorption is referred to as dichroic and one with polarization dependent phase behavior is referred to as having birefringence. Note that the dielectric tensor is truly a function of time and position (or frequency and momentum) [21].

Additionally, propagation through optical interfaces and thin films can cause polarization dependent behavior that will depend on angle of incidence. Since the multiple rays traveling though an optical system have multiple incidence angles, each will experience different amounts of reflection and transmission at each surface. Thus, the curved optical interfaces of most lens elements can become spatially varying weak linear polarizers and retarders.

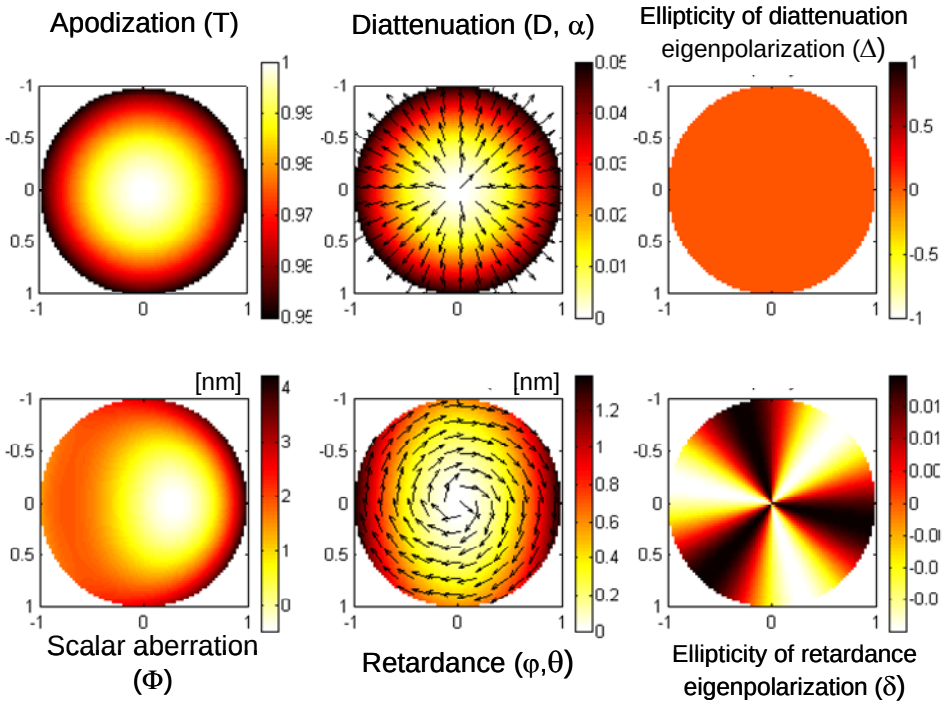

Figure 8-2. Physical properties pupil representation

Polarization aberrations represented by the physical properties that cause both scalar and polarization effects.

Although polarization aberrations can cause light propagating along a ray path to diverge (i.e. ray splitting though double refraction caused by birefringence), researchers at IBM and Carl Zeiss have shown that, given small levels of error, the cumulative effect of the lens system can be described by a single pupil-function [11]. Each location in this function describes the net polarization characteristics of a single ray path through the optical system. Thus, a typical lens element can be characterized by the physical properties shown in Figure 8-2, which consist of eight degrees of freedom for each pupil location. The top three functions describe transmission effects: apodization (T, equal attenuation of both eigenpolarizations), diattenuation (consisting of a magnitude (D) and eigenpolarization orientation (α) to a chosen coordinate system) and ellipticity of the diattenuation eigenpolarization (Δ, resulting from complex eigenvectors which implies a phase relationship between the eigenpolarizations). The bottom three functions describe phase effects: the traditional scalar phase optical path difference (Φ, equal wavefront distortion for both eigenpolarizations), retardance (consisting of a magnitude (φ) and

eigenpolarization orientation (θ)), and ellipticity of the retardance eigenpolarization (δ). Note that this representation does not account for any depolarization effects, which is the coupling of polarized light into unpolarized light. Depolarization will be discussed further in Section 8.3 with the Mueller-matrix pupil representation.

The values of the physical mechanisms in Figure 8-2 have been chosen at random and remain the same for each representation described in this paper. They are: scalar transmission (quadratic with a maximum of 5% attenuation), diattenuation (maximum 5% oriented radially), ellipticity of the diattenuation eigenpolarizations (eigenpolarizations are purely linear in this example), scalar phase aberration (5nm peak defocus, 5nm piston, 2.5nm peak coma-x), retardance (quadradic with 1nm maximum retardance mixed with 0.4nm astigmatism, fast axis oriented tangentially), and ellipticity of the retardance eigenpolarizations (trefoil behavior with maximum ellipticity of 0.02). Reference [88] shows a similar format for different aberration quantities.

Although the representation shown in Figure 8-2 is physically intuitive, it is generally inconvenient for dealing with partially coherent imaging since it is incompatible with the vector imaging equations. Additionally, it is not necessarily a convenient input format for a simulation tool, as each component is not easily decomposed into an orthonormal basis, such as the Zernike polynomials. The remainder of this chapter will describe alternate ways to represent the same physical mechanisms of polarization aberrations.

8.3. Various representations

8.3.1. The Mueller Pupil

Polarization can be described using several calculi, with the Mueller calculus and the Jones calculus being the two most common. The representation described in this section is based on the Mueller calculus, which considers time-averaged intensities. In the Mueller calculus, any polarization state is characterized by a Stokes Vector (**S**), defined as

$$\mathrm{S} = \begin{bmatrix} s_0 \\ s_1 \\ s_2 \\ s_3 \end{bmatrix} = \begin{bmatrix} P_H + P_V \\ P_H - P_V \\ P_{45} - P_{135} \\ P_R - P_L \end{bmatrix} \qquad \text{Eq. 8-5.}$$

where P_H, P_V, P_{45}, P_{135}, P_R, P_L, refer to the time averaged flux of light polarized with a certain orientation (horizontal linear, vertical linear, 45° linear, 135° linear, right circular, or left circular). In other words, P_H is the intensity measured by a slow detector after the light passes through a perfect horizontal polarizer. Thus s_0 indicates the total flux, while s_1, s_2 and s_3 are measures of the preference between orthogonal polarization components. From the Stokes vector, various attributes can be obtained such as degree of polarization

$$DOP = \frac{\sqrt{s_1^2 + s_2^2 + s_3^2}}{s_0} \qquad \text{Eq. 8-6.}$$

and others (degree of linear or circular polarization, ellipticity, orientation of the major axis, etc.). A good overview of various polarization metrics is provided by Chipman [11]. A degree of polarization less than one indicates partially polarized light, which is a combination of polarized and unpolarized light where unpolarized light has no preferential polarization direction when averaged over time.

The Mueller matrix (**M**) describes how an incident Stokes vector ($\mathbf{S}_{\text{in}}$) is coupled into an exiting Stokes vector ($\mathbf{S}_{\text{out}}$) for a particular sample or lens element. This coupling is unique for a given wavelength, incident angle and position on the lens. The coordinate system can be arbitrarily chosen, such as in Figure 8-3a.

$$\mathbf{S}_{out} = \mathbf{M}\mathbf{S}_{in} = \begin{bmatrix} m_{00} & m_{01} & m_{02} & m_{03} \\ m_{10} & m_{11} & m_{12} & m_{13} \\ m_{20} & m_{21} & m_{22} & m_{23} \\ m_{30} & m_{31} & m_{32} & m_{33} \end{bmatrix} \begin{bmatrix} s_0 \\ s_1 \\ s_2 \\ s_3 \end{bmatrix}_{in} \qquad \text{Eq. 8-7.}$$

A useful means to visualize polarization in the Mueller calculus is with the Poincare sphere [16], shown in Figure 8-3b. Any purely polarized Stokes vector can be represented by a unit vector on the Poincare sphere, where longitude indicates orientation and latitude indicates degree of circular polarization. Any point along the equator

represents a pure linearly polarized state. The Cartesian coordinates of the Poincare sphere correspond to s_1, s_2 and s_3, as shown in Figure 8-3b. The Mueller matrix describes how any incident Stokes vector is rotated within the Poincare sphere to produce an exiting Stokes vector. Unpolarized light has no preferential orientation on the sphere. Partially polarized light can be represented by a vector in the sphere with length less than unity, corresponding to the degree of polarization as described in equation 8-6 (possible values range from 0 to 1).

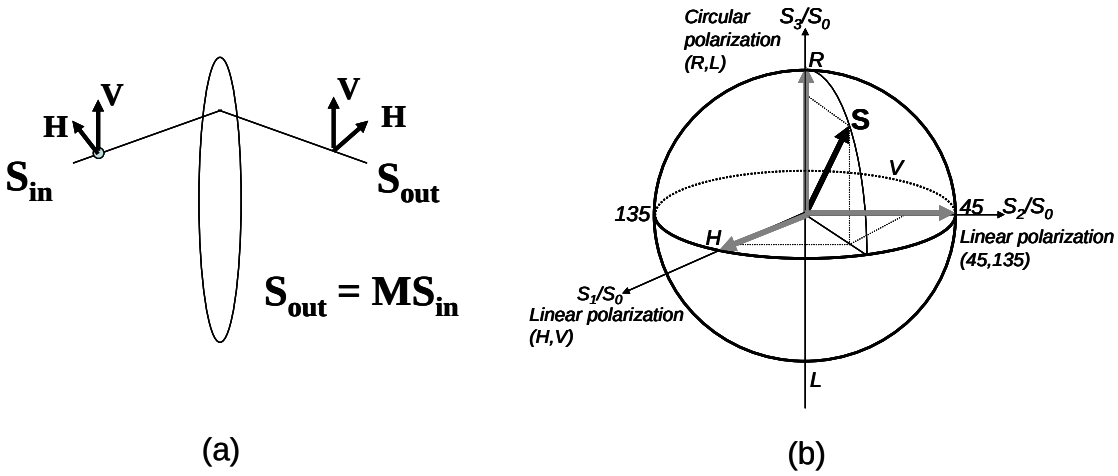

Figure 8-3. The Mueller matrix and Poincare sphere

(a) The Mueller matrix describes the transformation between input and output Stokes vectors, which describe polarization state. (b) The Poincare sphere is a useful tool to represent the Mueller calculus.

The description of polarization aberrations for the pupil from Figure 8-2 can be re-casted into the Mueller-matrix pupil representation shown in Figure 8-4. This method offers both several advantages and disadvantages.

A primary advantage of the Mueller-pupil representation is that it is capable of describing all possible polarization effects, to include depolarization and non-reciprocity [16]. Depolarization is the coupling of polarized light into unpolarized light, a phenomena that is closely related to scattering and is typically caused by rapidly varying diattenuation or retardance in time, space or wavelength. For example, optical flare, which presents a concern in lithography, can likely be described as a depolarization effect. Whereas eight degrees of freedom were required to describe the physical

mechanisms that alter polarization state; the additional eight degrees of freedom offered by the Mueller matrix enable description of depolarization, where the amount of depolarization may depend on input polarization state. As proposed in reference [16], depolarization can be represented by a warping of the Poincare sphere. Additionally, the Mueller-pupil is capable of describing the effect of inhomogeneous materials which may lead to non-reciprocity, where time-reversed symmetry is lost. The other primary advantage for applications such as lens metrology is that the Mueller calculus is well suited for describing irradiance measuring instruments. Thus, absolute phase information is irrelevant and slow detectors may be used since only time-averaged intensities matter.

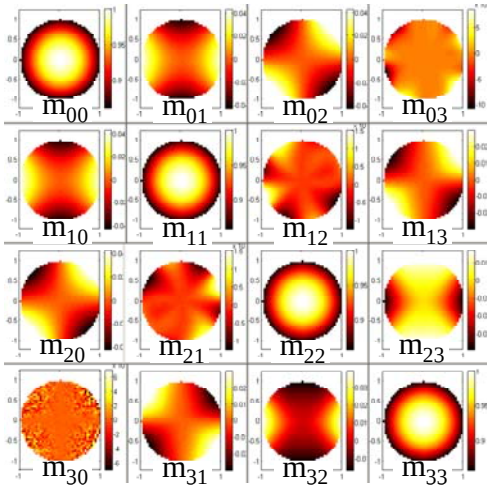

Figure 8-4. The Mueller-pupil.

However, the primary disadvantage of the Mueller-pupil for optical lithography is that absolute phase information is lost. Thus, it does not easily manipulate instantaneous fields and is generally inconvenient for analyzing imaging, where interference effects require the accurate accountability of phases. Furthermore, the Mueller-pupil is rather cumbersome and difficult to interpret. In a homogeneous material with negligible depolarization, the Mueller matrices are not a compact representation since they over-specify the pupil. Additionally, the polarization properties (diattenuation, retardance, and depolarization) of the pupil are not easily extracted from the Mueller-pupil. However, a trained eye can learn to interpret them as certain terms indicate the presence of particular effects, which are listed in Table 8-1. Finally, the Mueller-pupil does not offer a

convenient format for input to a simulation tool. In addition to the cumbersome number of degrees of freedom, all 16 pupil functions are closely coupled. Thus, it would be relatively easy to create a physically unrealizable pupil by randomly varying any of the input parameters. An example of a physically unrealizable Mueller matrix is one that induces a degree of polarization greater than one.

Mueller element	Indicates the presence of:
m_{01}, m_{10}	X-Y Linear diattenuation
m_{02}, m_{20}	45-135 Linear diattenuation
m_{03}, m_{30}	Circular diattenuation
m_{12}, m_{21}	H-V Linear retardance
m_{13}, m_{31}	45-135 Linear retardance
m_{23}, m_{32}	Circular retardance

Table 8-1. The off-diagonal elements of the Mueller-pupil indicate the presence of various types of polarization behavior

8.3.2. The Jones Pupil

The Jones-pupil representation described in this section is based on the Jones calculus, an alternate means of describing polarization [38]. The primary difference between the Jones calculus and the Mueller calculus is that the former deals with instantaneous complex fields whereas the later considers only time averaged intensities. In the Jones calculus, the polarization of the radiated field is described by the Jones vector:

$$\boldsymbol{E} = \begin{bmatrix} \boldsymbol{E}_x e^{i(\varpi t - kz + \varphi_x)} \\ \boldsymbol{E}_y e^{i(\varpi t - kz + \varphi_y)} \end{bmatrix}, \text{ or more compactly, } \quad \boldsymbol{E} = \begin{bmatrix} \boldsymbol{E}_x e^{i\varphi_x} \\ \boldsymbol{E}_y e^{i\varphi_y} \end{bmatrix} \qquad \text{Eq. 8-8.}$$

where the x and y directions can be arbitrarily chosen to be any orthogonal components (because light is a transverse electromagnetic wave), both perpendicular to z, the

direction of propagation. Thus, each component is specified by a magnitude and a relative phase.

The transformation between an input Jones vector and an exiting Jones vector for a particular sample, lens element, or ray path through an optical system is described by the Jones matrix:

$$\begin{bmatrix} \boldsymbol{E}_{x,out}\boldsymbol{e}^{i\varphi_{x,out}} \\ \boldsymbol{E}_{y,out}\boldsymbol{e}^{i\varphi_{y,out}} \end{bmatrix} = \begin{bmatrix} \boldsymbol{J}_{xx} & \boldsymbol{J}_{xy} \\ \boldsymbol{J}_{yx} & \boldsymbol{J}_{yy} \end{bmatrix} \begin{bmatrix} \boldsymbol{E}_{x,in}\boldsymbol{e}^{i\varphi_{x,in}} \\ \boldsymbol{E}_{y,in}\boldsymbol{e}^{i\varphi_{y,in}} \end{bmatrix} \qquad \text{Eq. 8-9.}$$

where J_{ij} are complex and describe the coupling between the input (j) polarization and output (i) polarization components. This convenient form allows 8-1 to be rewritten in vector form as:

$$\mathbf{E}_{wafer}(x',y',a,Pol) = \begin{bmatrix} E_x \\ E_y \\ E_z \end{bmatrix}_{Wafer} = \frac{1}{\pi}\int_0^{2\pi}\int_0^1 \begin{bmatrix} F_{xx} & F_{xy} \\ F_{yx} & F_{yy} \\ F_{zx} & F_{zy} \end{bmatrix} \begin{bmatrix} J_{xx} & J_{xy} \\ J_{yx} & J_{yy} \end{bmatrix} \begin{bmatrix} E_x \\ E_y \end{bmatrix}(a,Pol)_{Diff} e^{ik[\rho\cos(\theta)x'+\rho\sin(\theta)y']}\rho d\rho d\theta$$

Eq. 8-10.

where all three matrices within the integral can be functions of field position (x',y') and pupil position (ρ,θ). The diffracted fields $\begin{bmatrix} E_x \\ E_y \end{bmatrix}$ are also dependent on the location (a) and polarization (pol) of the illumination source point. The first matrix within the integral ($\mathbf{F}_{ij}$) relates the coupling between pupil and wafer polarization components due to a combination of high-NA vector effects and thin film effects of the resist stack. This matrix combines the thin film matrix and the polarization matrix, as defined by Flagello [19], which can both be thought of as polarization-specific transfer functions that effectively modify the frequency content within the lens. In other words, they represent the pupil-independent polarization aberrations inherent to high-NA imaging in photoresist. The second term within the integral is the Jones Matrix which has been written to absorb the scalar aberration term $\boldsymbol{e}^{ik\Phi(\rho,\theta)}$. Similar to equation 8-2, the total image intensity is then:

$$I_{wafer}(x',y') = \int_{source}\int_{pol} \left|\mathbf{E}_{wafer}(x',y',a,pol)\right|^2 dpol\, da \qquad \text{Eq. 8-11.}$$

where the integral over the source reflects the incoherent summation of intensity due to orthogonal polarization components.

The Jones matrices can be defined in terms of the physical properties discussed in Section 8.2. Polar decomposition theory, which employs a singular value decomposition of the complex Jones matrix, shows that any Jones matrix can be expressed as the order-independent product of a homogenous partial polarizer ($\mathbf{J}_D$) , a homogeneous pure retarder ($\mathbf{J}_R$) and a scalar component ($\mathbf{J}_S$) [88]. Homogeneous in this context refers to an element with orthogonal eigenpolarizations. Thus:

$$\begin{bmatrix} J_{xx} & J_{xy} \\ J_{yx} & J_{yy} \end{bmatrix} = \mathbf{J}_{Tot} = \mathbf{J}_S \cdot \mathbf{J}_D \cdot \mathbf{J}_R \qquad \text{Eq. 8-12.}$$

where the three Jones matrix components can be defined in terms of the physical properties discussed earlier [37]:

$$\mathbf{J}_S = T\,\mathbf{exp}(i\Phi) \qquad \text{Eq. 8-13.}$$

$$\mathbf{J}_D = \begin{bmatrix} P_1\,\mathbf{cos}^2\,\alpha + P_2\,\mathbf{sin}^2\,\alpha & (P_1 - P_2)\,\mathbf{sin}\,\alpha\,\mathbf{cos}\,\alpha \cdot e^{-i\Delta} \\ (P_1 - P_2)\,\mathbf{sin}\,\alpha\,\mathbf{cos}\,\alpha \cdot e^{i\Delta} & P_1\,\mathbf{sin}^2\,\alpha + P_2\,\mathbf{cos}^2\,\alpha \end{bmatrix} \qquad \text{Eq. 8-14.}$$

$$\mathbf{J}_R = \begin{bmatrix} e^{i\varphi/2}\,\mathbf{cos}^2\,\theta + e^{-i\varphi/2}\,\mathbf{sin}^2\,\theta & (e^{i\varphi/2} - e^{-i\varphi/2})\,\mathbf{sin}\,\theta\,\mathbf{cos}\,\theta \cdot e^{-i\delta} \\ (e^{i\varphi/2} - e^{-i\varphi/2})\,\mathbf{sin}\,\theta\,\mathbf{cos}\,\theta \cdot e^{i\delta} & e^{i\varphi/2}\,\mathbf{sin}^2\,\theta + e^{-i\varphi/2}\,\mathbf{cos}^2\,\theta \end{bmatrix} \qquad \text{Eq. 8-15.}$$

All variables were defined in Section 8.2 except P_1 and P_2, which are the principle coefficients of the amplitude transmission for the two orthogonal diattenuation eigenpolarizations of $\mathbf{J}_D$. P_1 has been set to 1 since the scalar effects are accounted for in T and P_2 is related to diattenuation magnitude (D) as $P_2 = \sqrt{(P_1 - D)/(P_1 + D)}$. It is noted that each parameter is generally a function of both field and pupil position.

Using the Jones calculus, the aberrated pupil of Figures 8-2 and 8-4 can be re-represented as Jones-pupils. Figure 8-5 presents each component's magnitude and phase while Figure 8-6 shows their real and imaginary components. Since the Jones matrices

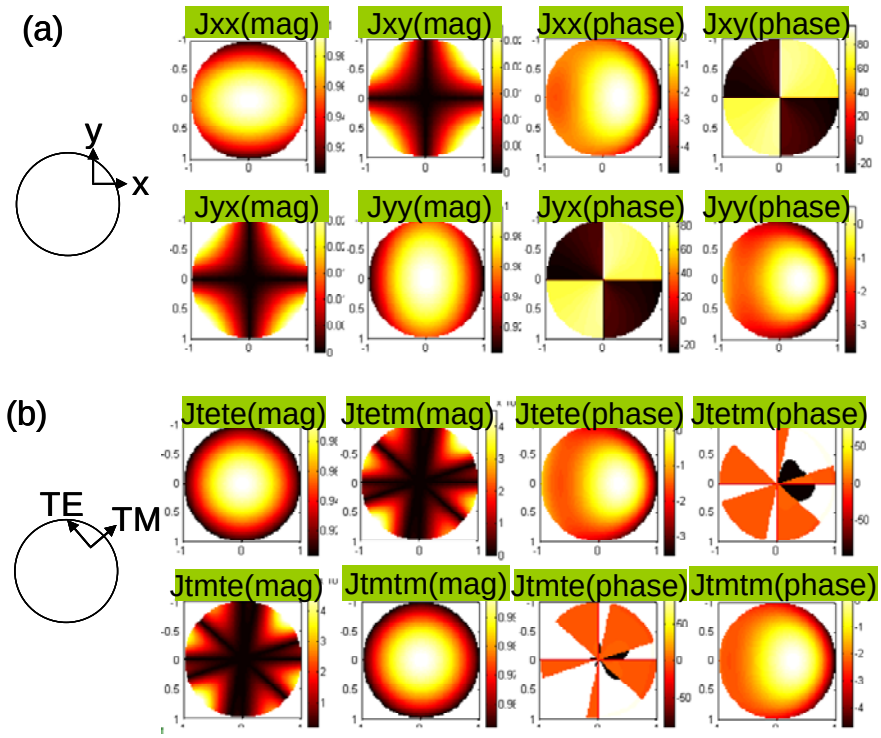

Figure 8-5. The Jones-pupil

The Jones-pupil representation of polarization aberrations in (a) mask coordinate or (b) pupil coordinate systems.

are dependent on coordinate system, they can be expressed either in mask coordinates (x-y, Figure 8-5a) or in pupil coordinates (TE-TM, Figure 8-5b). Additionally, if expressed in real and imaginary form, each component can be decomposed into Zernike polynomials (Figure 8-6). Further discussion of this and the relationship of the Jones-Zernike coefficients to imaging are provided by Totzeck [88]. Alternately, since polarization effects are likely to be most severe at the outer portions of the pupil, one could decompose them into annular-Zernikes or perhaps weight the Zernike polynomials with a radially dependent component (r^2 or $\cos(\phi)$, where ϕ is the angle of incidence associated with a given pupil radius).

Thus, for the purposes of partially coherent imaging, the Jones calculus and Jones-pupils are much more convenient than their Mueller counterparts, assuming any depolarization can be neglected. However, care must be taken to accurately account for

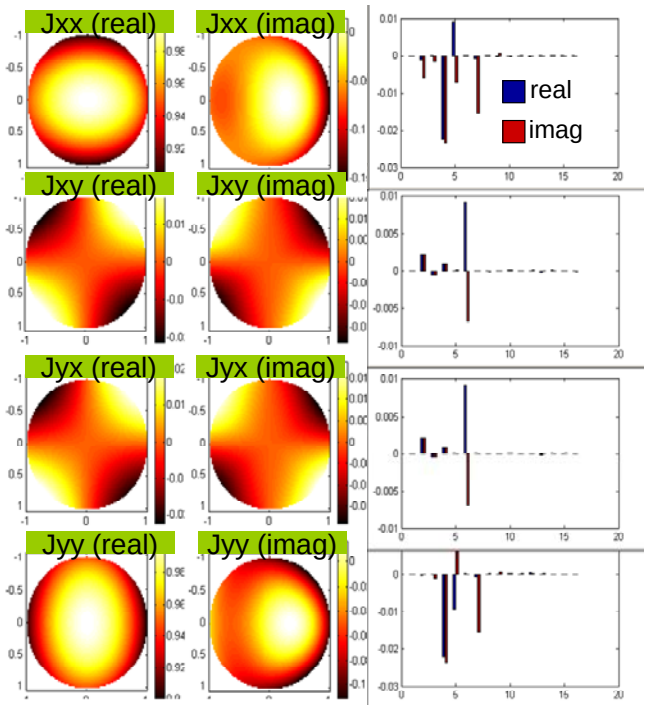

Figure 8-6. Jones-Zernike decomposition

Decomposition of the real and imaginary parts of the Jones-pupil in Zernike polynomials.

partially polarized light because the Jones matrices are only designed to act on pure polarization states. The image intensity due to the unpolarized portion can usually be found as an average of those due to orthogonal incident components. One potential disadvantage that the Jones-pupil has compared to the Mueller-pupil is that it typically requires an interferometric method to measure, whereas the Mueller-pupil can be measured with slow detectors and a set of calibrated polarization instruments [11].

Although the Jones calculus and Jones matrices are most appropriate for partially coherent imaging, the Jones-pupils are not necessarily the most useful representation of polarization aberrations for all applications. The next section will recast the Jones-pupils in an alternate basis, that of the Pauli-spin matrices, and then compare the usefulness of both representations. It will be shown that the Pauli-spin matrix basis proves a much more convenient 'language' to discuss polarization aberrations and as a more useful format for input into a simulation tool.

8.3.3. The Pauli Pupil

It is known in linear algebra that any complex NxN matrix can be expressed as a linear sum of N^2 trace-orthogonal, Hermitian basis matrices [4]. For a 2x2 matrix, the appropriate basis set often consists of the identity matrix (σ_0) and the Pauli spin matrices (σ_1, σ_2, σ_3):

$$\sigma_0 = \begin{bmatrix} 1 & 0 \\ 0 & 1 \end{bmatrix} \quad \sigma_1 = \begin{bmatrix} 1 & 0 \\ 0 & -1 \end{bmatrix} \quad \sigma_2 = \begin{bmatrix} 0 & 1 \\ 1 & 0 \end{bmatrix} \quad \sigma_3 = \begin{bmatrix} 0 & -\boldsymbol{i} \\ \boldsymbol{i} & 0 \end{bmatrix} \qquad \text{Eq. 8-16.}$$

Thus, as suggested by Jones in 1948 [39] and further developed by Chipman [12], the Jones matrices can be written in an alternate form as:

$$J_{Tot} = a_0\sigma_0 + a_1\sigma_1 + a_2\sigma_2 + a_3\sigma_3 \qquad \text{Eq. 8-17.}$$

$$= a_0 \cdot \left(\sigma_0 + \frac{a_1}{a_0}\sigma_1 + \frac{a_2}{a_0}\sigma_2 + \frac{a_3}{a_0}\sigma_3 \right) \qquad \text{Eq. 8-18.}$$

where the complex coefficients of the Pauli expansion are related to the Jones matrix elements as:

$$\boldsymbol{a}_0 = \frac{\boldsymbol{J}_{xx} + \boldsymbol{J}_{yy}}{2} \qquad \boldsymbol{a}_1 = \frac{\boldsymbol{J}_{xx} - \boldsymbol{J}_{yy}}{2} \qquad \boldsymbol{a}_2 = \frac{\boldsymbol{J}_{xy} + \boldsymbol{J}_{yx}}{2} \qquad a_3 = \frac{J_{xy} - J_{yx}}{-2i} \qquad \text{Eq. 8-19.}$$

The advantage of decomposing the Jones matrix into the Pauli spin matrix basis becomes clear with the description of how each Pauli coefficient represents a particular type of polarization behavior [51]. These descriptions are listed in Table 8-2.

The aberrated pupil of Figures 8-2, 8-4, 8-5 and 8-6 can then be decomposed into the Pauli spin matrix basis and recast into the so-called Pauli-pupil shown in Figure 8-7. The coordinate axes for Figure 8-7a are chosen in the mask coordinate system (X-Y), whereas the coordinate axes for Figure 8-7b are chosen in the pupil coordinate system (TM-TE). Thus, a brief glance at this representation reveals the types of polarization behavior that comprise the aberrated pupil for the field location of interest. The real and imaginary representation of the Pauli coefficients can be further decomposed into Zernike

Pauli-pupil coefficient	**Physical meaning**
Magnitude (a_0)	Average transmission for orthogonal polarization components (traditional apodization function) + normalization constants (one for diattenuation, one for retardance)
Phase (a_0)	Average optical path difference for orthogonal polarization components (traditional scalar aberration function)
Real(a_1/a_0)	Linear diattenuation along the coordinate axes
Imaginary(a_1/a_0)	Linear retardance along the coordinate axes
Real(a_2/a_0)	Linear diattenuation along the bisectors (45° and 135°) to the coordinate axes
Imaginary(a_2/a_0)	Linear retardance along the bisectors (45° and 135°) to the coordinate axes
Real(a_3/a_0)	Circular diattenuation
Imaginary(a_3/a_0)	Circular retardance

Table 8-2. Physical meanings of the Pauli-pupil coefficients

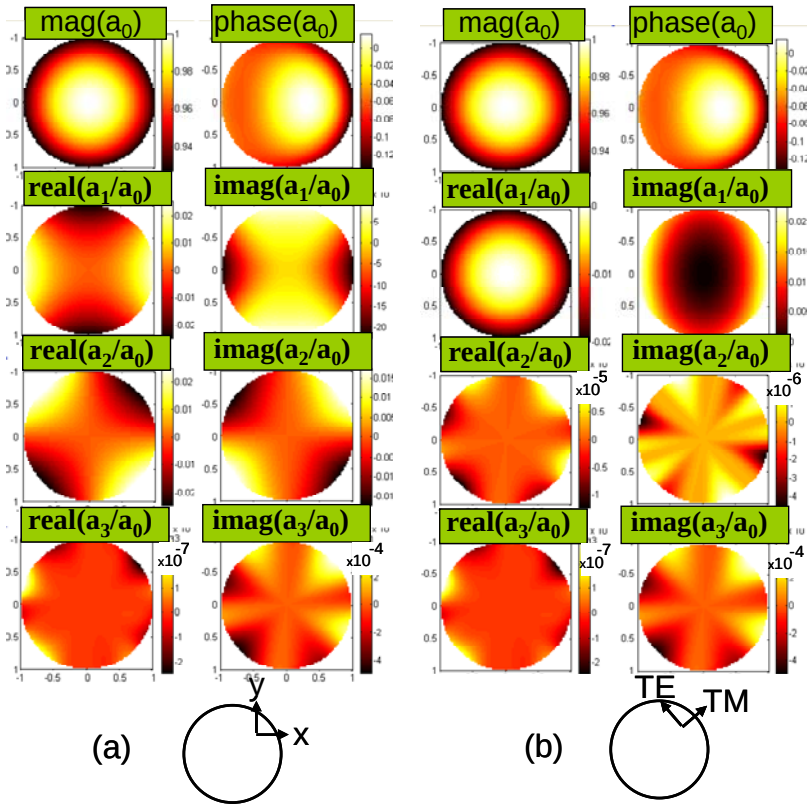

Figure 8-7. The Pauli-pupil

The Pauli-pupil representation in (a) mask coordinate or (b) pupil coordinate systems offers a compact and physically intuitive explanation of polarization aberrations.

polynomials, allowing the entire aberrated pupil to be described by a series of Zernike coefficients.

Prior to discussing the usefulness of the Pauli-pupil to optical lithography, it is important to identify two subtleties in dealing with the Jones and Pauli matrices. First, all of the analysis in this paper refers to what can be called the 'instrumental' Jones matrices. Here, the entire projection lens system is considered as a single entity. Each location in the Pauli-pupil represents the Jones matrix describing a single ray path through the entire optical column. This Jones matrix is unique for a particular field and pupil position. If, however, the optical column is considered as a system of multiple elements, then the total Jones matrix for a ray path can be determined as follows:

$$\boldsymbol{J}_{Total} = \boldsymbol{J}_N \cdot \boldsymbol{J}_{N-1} \cdots \boldsymbol{J}_1 \qquad \text{Eq. 8-20.}$$

where J_1 and J_N describe the first and last elements, respectively [38]. The order dependence results from the concept of causality, which demands that the polarization state at any particular time and place can only depend on simultaneous or past events. If desired, each element's Jones matrix can be decomposed into Pauli-spin coefficients, identifying the diattenuation and retardance properties of each element. Furthermore, just as the instrumental Jones matrices can be divided into individual elements, each element can be further divided into a sequence of infinitesimally small slices [39]. These small slices are often referred to as the differential or exponential Jones matrices and have a fundamental equivalence to the material's dichroic and birefringent properties described by the dielectric tensor.

The second subtlety results from the mixed presence of large amounts of diattenuation and retardance. Employing polar decomposition, where $\boldsymbol{J}_{Tot} = \boldsymbol{J}_S \cdot \boldsymbol{J}_D \cdot \boldsymbol{J}_R$, and decomposing each Jones element into a Pauli-spin basis:

$$\boldsymbol{J}_{Total} = \boldsymbol{J}_S \cdot \left(\boldsymbol{d}_0\sigma_0 + \boldsymbol{d}_1\sigma_1 + \boldsymbol{d}_2\sigma_2 + \boldsymbol{d}_3\sigma_3\right) \cdot \left(\boldsymbol{r}_0\sigma_0 + \boldsymbol{r}_1\sigma_1 + \boldsymbol{r}_2\sigma_2 + \boldsymbol{r}_3\sigma_3\right) \qquad \text{Eq. 8-21.}$$

$$= \boldsymbol{J}_S \boldsymbol{d}_0 \boldsymbol{r}_0 \cdot \left(\sigma_0 + \left|\frac{\boldsymbol{d}_1}{\boldsymbol{d}_0}\right|\sigma_1 + \left|\frac{\boldsymbol{d}_2}{\boldsymbol{d}_0}\right|\sigma_2 + \left|\frac{\boldsymbol{d}_3}{\boldsymbol{d}_0}\right|\sigma_3\right) \cdot \left(\sigma_0 + \boldsymbol{i}\left|\frac{\boldsymbol{r}_1}{\boldsymbol{r}_0}\right|\sigma_1 + \boldsymbol{i}\left|\frac{\boldsymbol{r}_2}{\boldsymbol{r}_0}\right|\sigma_2 + \boldsymbol{i}\left|\frac{\boldsymbol{r}_3}{\boldsymbol{r}_0}\right|\sigma_3\right) \qquad \text{Eq. 8-22.}$$

It is noted that the coefficients of a partial polarizer (d_1, d_2, d_3) are purely real and those of a retarder (r_1, r_2, r_3) are purely imaginary. The magnitudes of the normalized coefficients are used in equation 8-21 to emphasize this point. Both d_0 and r_0 are real quantities.

Comparing equation 8-22 to 8-18, it can be shown that:

$$a_0 \cong J_S \cdot d_0 \cdot r_0 \ , \quad a_1 \cong |d_1| + i|r_1| \ , \quad a_2 \cong |d_2| + i|r_2| \ , \quad a_3 \cong |d_3| + i|r_3| \qquad \text{Eq. 8-23.}$$

for an element with either mostly diattenuation, mostly retardance, or small values of mixed diattenuation and retardance. When large amounts of diattenuation and retardance exist simultaneously in a single Jones matrix these approximations break down. In this case, the definitions of diattenuation and retardance are somewhat arbitrary and appear to be a matter of preference. Diattenuation and retardance of a mixed element can be defined in one of two ways. As discussed earlier, polar decomposition can be used to describe a mixed element as the product of a pure retarder and a pure diattenuator. In this case, diattenuation is defined by equation 8-14 and retardance is defined by equation 8-15. Alternately, one can define diattenuation and retardance by the real and imaginary components, respectively, of the coefficients of the Pauli-spin matrix expansion of the total Jones matrix (a_1, a_2, a_3). Neither definition is necessarily more fundamental.

For simplicity, small levels of mixed diattenuation and retardance are assumed for the remainder of this paper. Although this is a very good approximation for the high-quality systems expected in optical lithography, this is not a strict requirement for using the Pauli-pupil representation. If small values of aberrations can not be assumed, the Pauli-pupil remains advantageous, requiring only that the alternate definition of of diattenuation and retardance (described in the last paragraph) is employed.

8.4. The Pauli-pupil in optical lithography

The Pauli-pupil representation, decomposed into Zernike polynomials, is proposed as the ‘language’ to describe polarization aberrations for optical lithography. The Pauli-pupil is advantageous compared to other representations due to its physically

intuitive interpretation, its compact notation, and its usefulness as an input into a lithography simulator.

As described in the previous section, the polarization properties of the projection optics are immediately evident from the Pauli-pupil representation. The real and imaginary portions of the Pauli coefficients represent diattenuation and retardance along orthogonal axes, as listed in Table 8-2. Traditional scalar aberrations are accounted for solely by the phase of a_0. Finally, the real part of a_0 is comprised of three parts: a term accounting for scalar attenuation (equal attenuation of both polarization components) and two normalization constants for both diattenuation and retardance. These normalization constants are essential to ensure a physically realizable pupil is described by the representation.

Thus, depending on the assumptions that can be made, the pupil can be specified by three to eight functions. Assuming no scalar attenuation and that the eigenpolarizations are always linear (both decent assumptions for state of the art tools), the pupil can be specified by only five input functions: a_0(phase), a_1(real and imaginary), and a_2 (real and imaginary); and a_0(magnitude) is calculated to ensure a realizable pupil. An additional assumption that all eigenpolarizations are oriented either radially or tangentially (not a bad first order assumption for some lenses), only three functions are necessary: a_0(phase) and a_1(real and imaginary) when the pupil coordinate system (TM-TE) is used (as in Figure 8-7b).

Although it provides a more compact notation, neglecting the a_3 coefficient is not required for the Pauli-pupil representation. Depending on the level and types of aberrations in the system and the user's accuracy requirements, a_3 may become worth investigating. In this case, one input function may be added for circular retardance (a_3(imaginary)) and one for circular diattenuation (a_3(real)). The representation remains physically intuitive, although it is not as compact.

Whereas the eight functions of the Jones-pupil are closely coupled to each other, the three or eight functions of the Pauli-pupil are mathematically independent. In other

words, modifying one component will not result in a physically unrealizable pupil, as long as the a_0 term is adjusted accordingly. Thus, diattenuation and retardance can be varied independently in a meaningful way, a task not easily accomplished with the Jones-pupil representation. Additionally, the Pauli-pupil coefficients can be decomposed into Zernike polynomials, resulting in a compact pupil specification of only a series of Zernike coefficients. For either the Jones or Pauli representation, it is likely that the first 12 or 16 Zernike coefficients are sufficient to describe low levels of aberration.

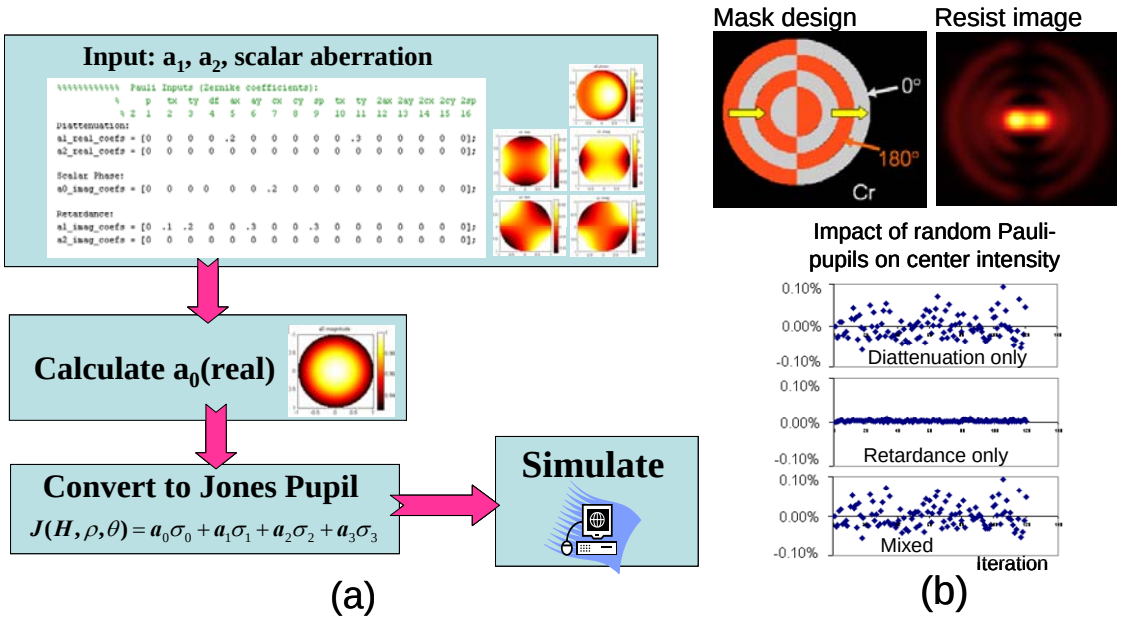

Figure 8-8. Simulation flow and example

(a) Proposed simulation flow based on the Pauli-pupil. (b) Monte Carlo simulation example showing how the image central intensity of a phase shift mask polarization monitor is affected by randomly generated Pauli-pupils.

To illustrate the usefulness of the Pauli-pupil representation as an input into a lithography simulator, the simulation flow in Figure 8-8a is proposed. The user is free to specify Zernike coefficients for the three to eight Pauli-pupil input functions. The program then calculates the a_0 term, converts to Jones pupils (in whatever form is most convenient for the imaging equations being used) and simulates. With this scheme, the user can begin to understand the impact of each coefficient without the worry of creating an unreal situation. Note that the scalar aspects of the aberrated pupil can either be

considered separately or absorbed into the Pauli- or the Jones-pupil. However, care must be taken to ensure that it is either one or the other; they should not be counted twice.

To illustrate the usefulness of this methodology, the simulation flow of Figure 8-8a was implemented using Panoramic simulation software with a recently developed Matlab interface. A Monte Carlo simulation was constructed, where randomly generated a_1 and a_2 Pauli-pupil coefficients were generated in Matlab. The a_0 coefficient was then calculated and the Pauli-pupils were converted into Jones-pupils. A loop was constructed that called the Panoramic aerial image simulator to calculate the image with each Pauli-pupil. For this example, the intensity at a specific location was recorded, although critical dimension, depth of focus, or any other lithographic metric could also be used.

This simulation methodology was used to determine the relative impact that polarization aberrations might have on the polarization monitoring technique developed in Chapter 5. The phase shift mask polarization monitor produces an image in resist as shown in Figure 8-8b, where the intensity at the center of the image is dependent on the state of the illumination polarization. To determine the sensitivity of these monitors to relatively large amounts of polarization aberrations, this pattern was simulated in the Monte Carlo scheme described above. The first 16 Zernike coefficients of the a_1 and a_2 functions were randomly generated with values between ± 0.1. The changes in measured intensities when compared to simulation with an unaberrated pupil are plotted in Figure 8-8b, showing the impact of only diattenuation, only retardance and mixed diattenuation and retardance. It is clear that these monitors are much more sensitive to diattenuation than to retardance. While these histograms are not necessarily realistic for state of the art lithographic systems, they do show the usefulness of using the Pauli-pupil as an input. This strategy can be used to determine tool specifications given certain imaging requirements, or to determine expected imaging variation given realistic levels of potential aberration.

Additionally, a simple metric of lens polarization quality is proposed based on the Pauli spin matrix representation of a Jones pupil. When details of polarization activity are not required, the a_0(magnitude) term provides a simple, but useful, means to

characterize lens quality when the scalar component is filtered out. In the absence of complete Jones Pupil data, this information (along with the traditional scalar aberration function) could be provided by tool manufacturers as a rough measure of lens polarization quality. Of course, if and when metrology is developed for the end user to characterize the polarization aberrations in a particular tool, any of these representations can be converted to another, depending on which is most useful for the purpose at hand.

8.5. Phase shift mask birefringence monitor

A new type of birefringence monitor based on phase shift masks is proposed in this section. Birefringence is important in steppers at 193nm due to its inherent existence in crystal structures. Special care is made to reduce effects by clocking the lenses, but it is important to measure residual birefringence at levels between 0 and 15nm which amount to 0 and .078 peak waves at the edge of the pupil. Birefringence could be measured on an optical bench by having polarizers that are orthogonal in the entrance and exit pupils of the lens. The small amount of rotation due to birefringence will create a fairly small transmission in the presence of birefringence. The detection of the small amount of birefringence could be greatly enhanced by providing a reference wave with which the birefringent component could be interferometrically interacted.

These elements of a birefringence test measurement system can be built into a photomask and a detector that is polarized on the wafer. The system might consist of that shown in Figure 8-9, where the two orthogonal polarizers are located on the backside of the photomask and above the wafer, respectively. A mask pattern is created to produce a reference wave that primarily passes through the lens center and a signal wave that passes through an off-axis pupil position. Although several embodiments are feasible, the example in Figure 8-9 uses a sub resolution chromeless grating oriented at 45 degrees to the two orthogonal polarizers. This creates an interferometric reference for proximity effect spill-over from the signal rays that pass through the surrounding open field. An added advantage of the chromeless grating is that both the absolute phase and phase delay between orthogonal polarization components can be programmed by varying the etch depth of the grating, as shown in Figure 8-10. The second polarizer at the image plane

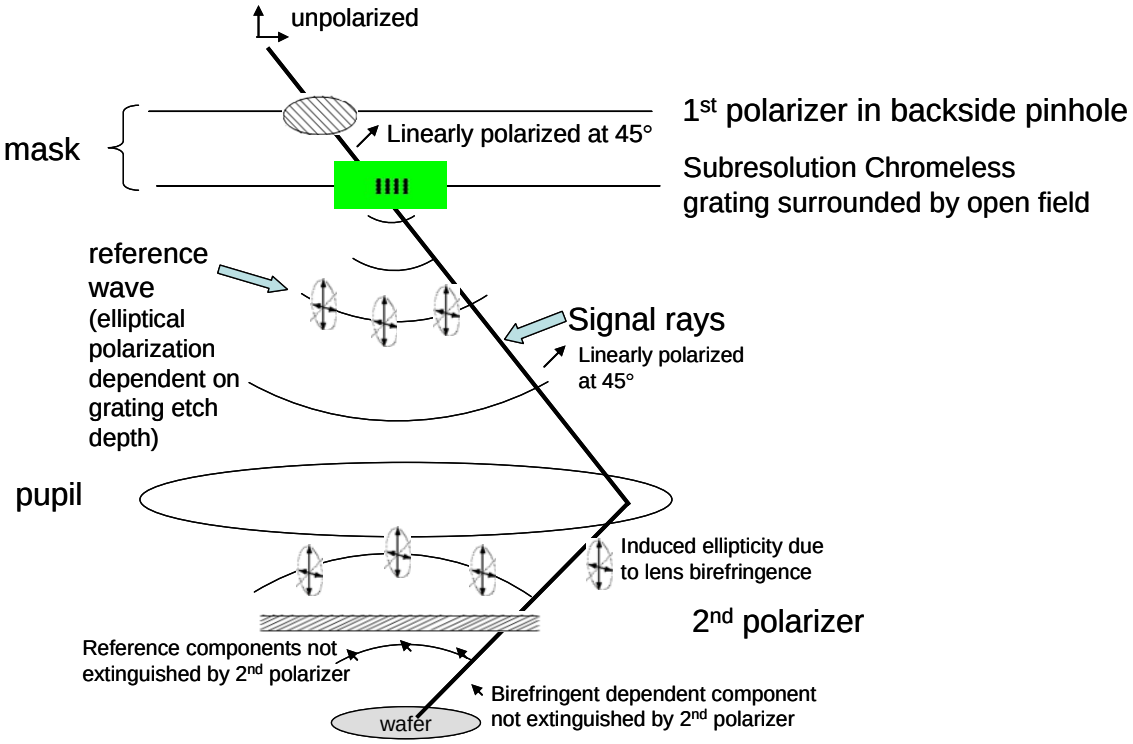

Figure 8-9. PSM birefringence monitor

Birefringence monitoring system consists of a polarizing pinhole in a layer on the backside of the mask, a chromeless subresolution grating and a 2nd polarizer placed above the image plane.

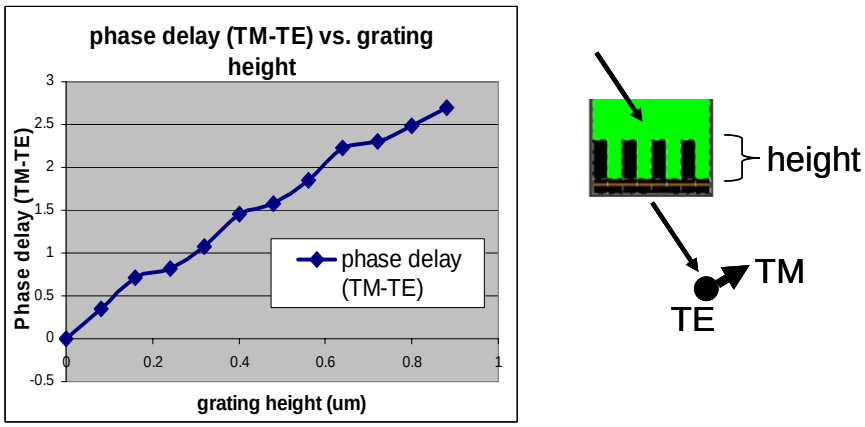

Figure 8-10. Tuning the probe polarization state by varying the height of the chromeless grating

Effective index of refraction is higher for TM polarization than TE polarization

could be provided by a wire-grid polarizer built into an integrated aerial image sensor (polarizer and CCD combination), such as those proposed and built by Xue [99] or Kunz [44].

As an example, Figure 8-11a shows the resulting aerial images in the presence of birefringence for the situation described in Figure 8-9 and the birefringence pupil map shown in Figure 8-11b. With no birefringence, the image is simply a dip in intensity at the probe location. In the presence of birefringence this dip turns into a peak and changes in intensity much greater than the surrounding background intensity. Sampling of the birefringence along various eigenpolarizations is possible simply by using multiple combinations of chromeless gratings and backside pinhole gratings.

Calibration of the test reticle will be essential, as neither the chromeless gratings or polarizers will be ideal polarization elements. Finally, by sampling birefringence along various orientations, the retardance aspect of the Pauli-pupil (imaginary portions of the coefficients) can be constructed.

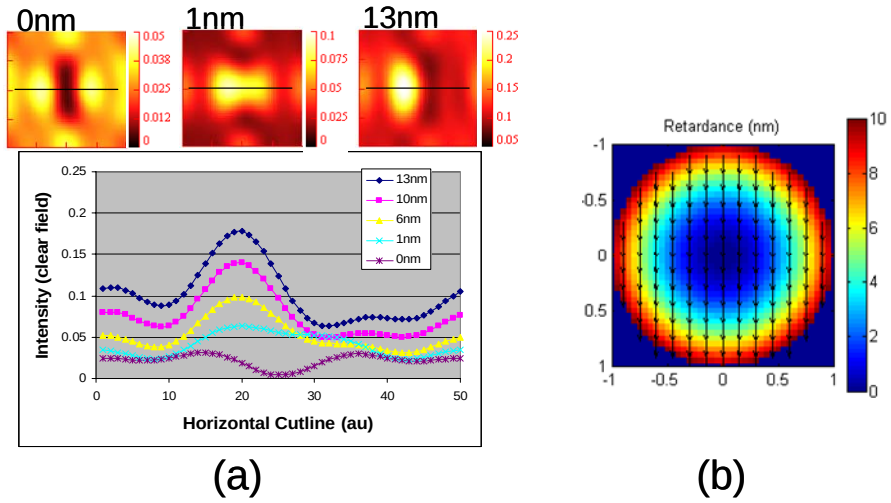

Figure 8-11. Simulated example of birefringence monitor

(a) Aerial image horizontal cutlines for varying amounts of birefringence show interferometric sensitivity. (b) Birefringence pupil map shown for 10nm peak value where arrows denote fast axis

8.6. Conclusion

Various representations describing polarization aberrations have been investigated and compared. The advantages and disadvantages of each embodiment for optical lithography have been discussed and are summarized in Table 8-3. It is concluded that the Jones matrices represented in the Pauli-spin basis are most useful and are thus proposed as the 'language' to discuss polarization aberrations in optical lithography. This representation, termed the Pauli-pupil, offers the user a compact and physically intuitive description of polarization activity while maintaining a format that is easily integrated into standard imaging equations. An input format for a simulation tool is proposed based on the Pauli-pupil that consists of three to eight input functions, depending on the assumptions that can be made. A normalization term is calculated to ensure a physically realizable pupil. Additionally, a simplified metrology metric for lens polarization quality has been discussed and a technique to monitor lens birefringence with phase shift masks has been proposed.

	Advantages	Disadvantages
Mueller-pupil	• accounts for all polarization effects, including depolarization (flare) and non-reciprocity • measurable with slow detectors	• absolute phase is lost • difficult to interpret • 16 coupled functions (often over specifies pupil)
Jones-pupil	• maintains absolute phase • fits vector imaging equations	• 8 coupled functions • requires interferometric methods to measure • no depolarization
Pauli-pupil	• physically intuitive • compact notation (3-8 functions, depending on valid assumptions) • useful input in lithography simulator • easily converted to Jones for use in imaging equations	• requires interferometric methods to measure • no depolarization

Table 8-3. Summary of compared pupil representations

9 Conclusions

The primary contributions of this thesis have been the invention, theoretical development, experimental verification, and investigation of the limiting factors of five novel classes of phase shift test patterns for *in-situ* characterization of various lithographic effects. These patterns were derived as mathematical functions from basic principles that when realized in the object plane of an imaging system, each serve to engineer a wavefront that interacts with one particular optical effect. This provides a measurable image-plane signal that, for optical lithography, is typically recorded in photoresist. Recent advances in photomask fabrication technology have enabled the realization of these complex-valued functions on actual photomasks. The fabrication of four-phase steps in the quartz substrate provides an adequate approximation to a full 2π linear phase progression, enabling such things as the selective diffraction of individual off-axis illumination angular frequencies. Generally, these patterns have been derived to maximize proximity effect spill-over to a central image location, thus are theoretically the most sensitive patterns to the desired optical effects.

The main four phase shift monitors developed in this thesis and conclusions as to their sensitivities, limiting factors and potential improvements are summarized below in Table 9-1. Although all are novel theoretical concepts, the polarization monitors and the interferometric-probe monitors for phase shifting mask performance are likely sensitive and robust enough to find commercial use in industry. Furthermore, there appears to be a pressing need in the industry for a polarization monitoring technique such as PSM Polarimetry. The last line of Table 9-1 comments on the overall assessment of the various applications for each monitor.

	LPG	LPR	PSM Polarimetry	IPM-PSM
Effect measured	illumination angular uniformity and distribution (effective source)	illumination angular uniformity and distribution (effective source)	polarization quality of illuminator (Stokes parameters)	effective phase and transmission of shifted regions of Alt-PSM (due to EM or mask making)
Effect leveraged	selective diffraction from 4-phase progression; pupil as aperture to clip source-image	illumination frequency-dependent proximity effect spillover to central image location	proximity effect of typically unwanted z-component of electric field due to high-NA vector effects	uneven proximity effect spillover to image center for phase or transmission errors; interferometric interaction with probe
Physical image-plane measurement	large area dose to clear of +1 order DC component captured within pupil	dose to clear of image center	dose to clear of image center	dose to clear of central interferometric probe relative to nearby isolated probe
Minimum mask feature size	pitch/4 = 1/8 λ/NA (for maximum pupil shift of Δr=2)	pitch/4 = 1/4 λ/NA (for monitoring largest angle off-axis source location)	pitch/4 = 1/4 λ/NA (for monitoring largest angle off-axis source location)	~ 1/2 λ/NA
Phase etch requirements	4 phase (3 likely possible)	4 phase	4 phase	3 phase (effective phase) 2 phase (effective transmission)
Applications	dipole or quadrupole intensity balance; full source-image measurement	dipole or quadrupole intensity balance; full source-image measurement; temporal coherence monitor	full or partial Stokes parameter measurement, linear or circular polarization	effective phase or transmission (90 or 0 degree probe) of contacts or small ALT-PSM features, edge effects
Primary limitation (cause => effect)	mask making (misalignment => orientation dependence & difficulty with Δr>1.25)	mask making (misalignment & fidelity => orientation dependence & lost signal)	mask making (60-80% signal loss) also 400um pinhole alignment => 80-100% signal loss)	tool constraings (minimum sigma on standard stepper => 70% signal lost with σ = 0.39
Calibration required?	Yes	Yes	Yes	No
Potential improvements	3-D OPC, direct write LPG in HSQ, use backside pinhole and/or pupil aperture, mask making improvements	3-D OPC, direct write LPG in HSQ, use backside pinhole and/or pupil aperture, mask making improvements	better pinhole alignment, more pattern rings, 3-D OPC, smaller pinhole, redundancy, low-index resist,	σ=0.05 aperture in AIMS tool, ensure chrome used as etch stop
Theoretical sensitivity	limited by number of LPGs used in design	300% clear field signal for dipoles (6 ring patterns)	1.25 (4 ring RPG) or 3.5 (4 ring PEPA) %CF/%Δpol [~Stokes w/in 0.01]	~2 %CF/°phase error (5ring, σ=0.05)
Sensitivity achieved for thesis	intensity balance w/in 5%	8% of the clear field signal for dipoles (2 ring patterns)	0.3 (4 ring RPG) %CF/%Δpol [~Stokes w/in 0.20]	~0.15 %CF/°phase error (3ring contacts, σ=0.39)
Projected future signal strength or sensitivity	intensity balance w/in 2-3%	44% of the clear field signal, thus balance w/in 2% for intensity balance of dipoles (6 ring pattern)	1 (6 ring PEPA) or 2 (10 ring PEPA) %CF/%Δpol [~Stokes w/in 0.02 - 0.04]	~1.0 %CF/°phase error (5ring contacts, σ=0.2 scanner) or 1.5 (σ=0.05 AIMS)
Overall assessment (red,yellow,green)	dipole/quad intensity balance: Y full source-image measurement: R	dipole/quad intensity balance: Y full source-image measurement: R	linear polarization (S1,S2): G circular polarization (S3): Y	phase error: G trans error: Y edge effects: R

Table 9-1. Overall assessment of the phase shift monitors developed in this thesis.

Three non-standard, industrial-quality photomasks have been designed and fabricated for this thesis. Experiments done on a variety of lithography tools have not only validated their scientific principles, but have revealed a number of subtle – and not so subtle – practical limitations due to realistic imaging conditions. The primary limitation for most of these monitors has been a direct result of pushing the mask making process to its current limits. Although these test reticles were fabricated with standard photomask manufacturing equipment, the processes used were non-standard. Thus, the development of these reticles provided a learning experience for not only the author, but for the mask maker as well. There is every reason to believe that significant improvements to the 4-phase reticle fabrication process are possible. Alternately, a direct-write strategy in a material such as HSQ, a negative tone photoresist with optical properties comparable to quartz, may provide the most effective means to faithfully fabricate the complex valued functions that form the basis of these PSM monitors. Additionally, the backside layer misalignment that plagued the last test mask will likely see considerable improvement in future attempts. This research has provided a proof-of-principle for these techniques and it is expected that further advances are possible given time, money and engineering effort. Regardless, it is often possible to filter out these mask making imperfections from the measurement data by properly calibrating the test reticle – or to build redundancy and/or safeguards into the design to counteract mask making effects, as was described in detail for the polarization monitors of Chapter 5. For example, even though mask making limitations decreased the signal by roughly 70%, PSM polarimetry is still likely to monitor polarization to within 2%.

The second limitation, in most cases, was the unavoidable electromagnetic interaction as light propagates through the three-dimensional mask topography, even when perfect mask geometries are constructed. The extent that this EM effect impacts imaging and the performance of these monitors is a complex interplay of mask feature size, phase depth and sidewall angle, and the angle of incidence and polarization of the illumination. Although theoretical analysis and simulation provide means to understand this effect, it functions as nuisance to the practical operation of these monitors and can

decrease signal strength by roughly 20%. Again, various smart design practices and/or proper mask calibration is often sufficient to minimize or even negate this effect.

Additional factors that have been investigated in this thesis that have varying degrees of influence on monitor behavior are illumination partial coherence, high-NA vector effects, projection or condenser lens aberrations, specifics of the photoresist stack, focus variation, dose imbalance, and others. These effects can typically be categorized as either random or systematic experimental error and an understanding of them enables fine-tuning of either the mask design or the experimental set-up to maximize sensitivity to the desired effect. For example, the backside pinhole array on test reticle C provided a means to negate deterioration of the signal due to partial coherence effects by isolating one illumination angular frequency for the measurement. At a minimum, this understanding helps to determine the accuracy or reliability of measurement data, such as by estimating error bars as was done for the polarization (Stokes parameters) measurement of Chapter 5.

Secondary contributions of this thesis were found in Chapters 7 and 8. In Chapter 7, some of the knowledge of polarization-dependent proximity effects that was gained in the development of the polarization monitors of Chapter 5 was related to actual IC designs. The application of pattern matching software was extended to very quickly identify areas in a circuit design layout that may be particularly vulnerable to polarization and high-NA vector effects. A large degree of similarity, or match factor, between a layout location and one of the polarization proximity effect patterns implies vulnerability, which is quantitatively assessed with a vulnerability score. The vulnerability scores are linearly proportional to intensity change with a slope of about 80% of the clear field per vulnerability score. Predictions are generally accurate with simulation to better than 90%, suggesting this is a good technique to quickly screen layouts for areas in need of more attention. Examples have been shown in this thesis for on-axis coherent illumination, but have recently been extended by Holwill [32] to account for off-axis illumination schemes.

Additionally, polarization aberrations, the subtle polarization-dependent wavefront distortions that may occur as light propagates through projection optics, were investigated as they may become important with hyper-NA imaging systems. Various mathematical representations of the aberrated pupil were considered and compared. It was concluded that the Jones-matrices decomposed into a Pauli-spin matrix basis (the Pauli-pupil) offers the most convenient format to optical lithography due to its compact notation, physically intuitive interpretation, ability to be implemented into standard imaging equations, and its usefulness as an input into a lithographic simulator. Additionally, a technique to monitor lens birefringence with phase shift masks has been briefly introduced.

To close, the PSM monitors derived and developed in this thesis offer the lithographer, at a minimum, an additional set of tools to enable optical projection printing to remain cost effective for the production of integrated circuits with feature sizes less than $1/6^{th}$ the wavelength of light being used. This thesis has focused on their applications to optical lithography. However, their principles apply to any image-forming optical system. Thus, it is hoped that they may find applications in other adjacent fields of optics or acoustics.

Bibliography

[1] E. Abbe, "Beitrage zur theorie des mikroskops und der mikroskopischen wahrnehmung," Archiv. Microskopische Anat., vol. 9, pp. 413-468, 1873.

[2] K. Adam and W. Maurer, “Polarization effects in immersion lithography,” *Proceedings of the SPIE*, vol. 5377, pp. 329-343, 2004.

[3] K. Adam, *Domain Decomposition Methods for the Electromagnetic Simulation of Scattering from Three-Dimensional Structures with Applications in Lithography*, Ph.D. Thesis, University of California, Berkeley, 2001.

[4] R. Barakat, “Exponential versions of the Jones and Mueller-Jones polarization matrices,” *J. Opt. Soc. Am. A.* 13(158), 1996.

[5] Y. Borodovsky, “Impact of local partial coherence variations on exposure tool performance”, *Proceedings of the SPIE,* vol. 2440, pp. 750-770, 1996.

[6] T. Brunner, N. Seong, W. Hinsberg, J. Hoffnagle, F. Houle, and M. Sanchez, “High-NA lithographic imagery at Brewster’s angle,” *Proceedings of the SPIE* 4691, 1-10 (2002).

[7] T. Brunner, “Impact of lens aberrations on optical lithography,” *IBM J. Res. Develop.*, vol 41, pp. 57-67, Jan/Mar (1997).

[8] T. Brunner, D. Corliss, S. Butt, T. Wiltshire, C.P. Ausschnitt, and M. Smith, "Laser bandwidth and other sources of focus blur in lithography," *Proceedings of the SPIE*, vol. 6154, 6154OV, Mar., 2006.

[9] W. Cheng, J. Farnsworth, T. Bloomstein, and A. Grenville, "Vectorial effects in subwavelength mask imaging," *Proceedings of the SPIE*, vol. 5992, 2005.

[10] Y. F. Cheng, Y. L. Chou, C. L. Lin, and P. Huang, "Study of effects of sidewall angle on process window using 193nm CPL masks in a 300mm wafer manufacturing environment," *Proceedings of the SPIE,* vol. 5992, 59922R, Nov., 2005.

[11] R. Chipman, *Polarimetry*. in: Handbook of Optics (ed. M. Bass), Vol. 2, 2nd edn, McGraw-Hill, New York, Chapter 22, 1995.

[12] R. Chipman, *Polarization Aberrations*, Ph.D. dissertation, University of Arizona, 1987.

[13] N. Cobb, A. Zakhor, E. Miloslavsky, "Mathematical and CAD framework for proximity correction," *Proceedings of the SPIE*, vol. 2726, pp. 208-222, 1996.

[14] M. Creighton, "Influence of illumination non-uniformity on pattern fidelity," *Proceedings of the SPIE*, vol. 5754, pp. 1519-1528, 2005.

[15] G. Dao, G. Liu, A. Snyder, and J. Farnsworth, "New Approach to Phase Metrology for Manufacturing of 248nm Lithography Based Embedded Attenuated Phase-shifting Mask", *Proceedings of the SPIE*, vol. 2793, pp. 359-370, 1996.

[16] B. DeBoo, J. Sasian, and R. Chipman, "Degree of polarization surface maps for analysis of depolarization," *Optics Express*, Vol. 12, No. 20, 4941-4958, 2004.

[17] N. Eib, O. Kobozeva, C. Neville, and E. Croffie, "Error budget for a 193nm complementary phase-shift mask," *Proceedings of the SPIE*, vol. 4692, pp. 379-389.

[18] Estroff, Y. Fan, A. Bourov, B. Smith, P. Foubert, L. Leunissen, V. Philipsen, and Y. Aksenov, "Mask-induced polarization effects at high-NA," *Proceedings of the SPIE*, vol. 5754, pp. 555-566, 2004.

[19] D. Flagello, B. Geh, S. Hansen, and M. Totzeck, "Polarization effects associated with hyper-numerical-aperture (>1) lithography," *Journal of Microlithography, Microfabrication, and Microsystems*, vol. 4(3), 031104, Jul-Sep, 2005.

[20] D. Flagello, *High Numerical Aperture Imaging in Homogeneous Thin Films*, Ph.D. Thesis, University of Arizona, 1993.

[21] M. Fox, *Optical properties of solids*, Oxford University Press, 2002.

[22] M. Fritze, B. Tyrrell, S. Cann, C. Carney, B. Blachowicz, D. Brzozowy, T. Kocab, S. Bowdoin, P. Rhyins, C. Progler, and P. Martin, "Minimization of image placement errors in chromeless phase-shift mask lithography," *Proceedings of the SPIE*, vol. 4691, pp. 426-436.

[23] 5. T. Fujii, N. Kita, and Y. Mizuno, "On Board Polarization Measuring Instrument for High NA Excimer Scanner," *Proceedings of the SPIE*, vol. 5752, pp. 846-852, 2005.

[24] F. Gennari, G. Robins, A.R. Neureuther, "Validation of the Aberration Pattern Matching OPC Strategy", *Proceedings of the SPIE*, vol. 4692B-54, 2002.

[25] F. Gennari, *Linking TCAD and EDA Through Pattern Matching*, Ph.D. Dissertation, University of California at Berkeley, 2004.

[26] D. Gil, R. Menon, and H. Smith, "Fabrication of high-numerical-aperture phase zone plates with a single lithography exposure and no etching," *J. Vac. Sci. Technol B* 21(6), pp. 2956-2960, Nov/Dec, 2003.

[27] J. W. Goodman, *Introduction to Fourier Optics*, 2nd edition, McGraw-Hill, Chapter 6, 1996.

[28] D. Goodman and A. Rosenbluth, "Condenser aberrations in Kohler illumination", *Proceedings of the SPIE*, vol. 922, pp. 108-134, 1988.

[29] J. W. Goodman, *Statistical Optics*, John Wiley & Sons, 1985.

[30] Grodnesky, E. Morita, K. Suwa and S. Hirukawa, “Characterization of Spatial Coherence Uniformity in Exposure Tools”, *Proceedings of the SPIE*, vol. 3334, pp 289-296, 1998.

[31] P. Gupta, A. Kahng, C. Park, K. Samadi, and X. Xu, "Wafer topography-aware optical proximity correction for better DOF margin and CD control," *Proceedings of the SPIE*, vol. 5853, pp. 844-854, 2005.

[32] Holwill, G. McIntyre, W. Poppe, and A. Neureuther, “Layout ‘Hot Spots’ for Advancing Optical Technologies,” *Proceedings of the SPIE*, vol. 6154, 2005.

[33] H. Hopkins, "On the diffraction theory of optical images," *Proc. Roy. Soc*. A, vol. 217, p.408, 1953.

[34] S. Hotta, T. Pistor, K. Adams, and A. Neureuther, “Effects of Shifter Edge Topography on Through Focus Performance”, *Proceedings of the SPIE*, vol. 4186, pp. 827-837, 2001.

[35] S. Hsu, D. V. D. Broeke, J. Chen, X. Shi, M. Hsu, T. Laidig, W. Conley, L. Litt, and W. Wu, "RET integration of CPL technology for random logic," *Proceedings of the SPIE*, vol. 5377, pp. 510-526, 2004.

[36] Huggins, T. Tsuyoshi, M. Ong, R. Rafac, C. Treadway, D. Choudhary, T. Kudo, S. Hurukawa, S. Renwick, and N. Farrar, " Effects of laser bandwidth on OPE in a modern lithography tool," *Proceedings of the SPIE*, vol. 6154, 6154OZ, Mar., 2006.

[37] S. Jiao, and L. Wang, “Jones-matrix imaging of biological tissues with quadruple-channel optical coherence tomography,” *J. Biomedical Optics*, vol. 7, No. 3, 350-358, 2002.

[38] R.C. Jones, “A new calculus for the treatment of optical systems: 1. Description and Discussion of the Calculus,” *J. Opt. Soc. Am*. 31(488), 1941.

[39] R.C. Jones, “A new calculus for the treatment of optical systems: VII. Properties of the N-Matrices,*” J. Opt. Soc. Am*. 38(671), 1948.

[40] A.C. Kak and M. Slaney, *Principles of Computerized Tomographic Imaging*, IEEE Press, 1988.

[41] J.P. Kirk and C.J. Progler, “Pupil Illumination: in situ measurement of partial coherence”, *Proceedings of the SPIE*, vol. 3334, pp. 281-288, 1998.

[42] J. Kirk and S. Schank, “Detection of focus and spherical aberration by use of a phase grating,”, *Proceedings of the SPIE*, vol. 4346, pp.1355-1361, 2001.

[43] Kohler, US Patent 1143287, 1915.

[44] R. Kunz, D. Rathman, S. Spector, M. Rose, and M. Yeung, “A high-frame-rate DUV-optimized CCD for simultaneous measurements of illumination intensity, polarization amplitude, and polarization direction for very high NA imaging systems,” *Proceedings of the SPIE*, vol. 5754, pp. 107-118, 2004.

[45] B. Lafontaine, M. Dusa, A. Acheta, C. Chen, A. Bourov, H. Levinson, L. Litt, M. Mulder, R. Seltman, J. v. Praagh, "Flare and its impact on low-k1 KrF and ArF lithography," *Proceedings of the SPIE*, vol. 4691, pp. 44-56.

[46] D. Levenson, S. Tan, G. Dai, Y. Morikawa, N. Hayashi, and T. Ebihara, "The vortex via process: analysis and mask fabrication for contact CDs < 80nm," *Proceedings of the SPIE*, vol. 5040, p. 344-370, 2003.

[47] D. Levenson, N. Viswanathan, and R. Simpson, "Improving resolution in photolithography with a phase-shifting mask," *IEEE Trans. Electron Devices*, vol. 29, p. 1812, 1982.

[48] Litel web page: http://www.litel.net, Technical presentation of source metrology instrument (7248B-PSN-1003).

[49] S. Lu and R. Chipman, "Mueller matrices and the degree of polarization," *Optics Communications*, vol. 146, p. 11-14, 1998.

[50] T. Matsuyama and T. Nakashima, "Study of high NA imaging with polarized illumination," *Proceedings of the SPIE*, vol. 5754, p. 1078-1089, 2005.

[51] J. McGuire and R. Chipman, "Diffraction image formation in optical systems with polarization aberrations. II: Amplitude response matrices for rotationally symmetric systems," *J. Opt. Soc. Am. A*. 8(6), 833-840, June, 1991.

[52] G. McIntyre, G. Robins, and A. Neureuther, "Phase shifting mask as a precision instrument for characterizing image-forming optical systems," *Proceedings of the SPIE*, vol. 5878, 587808, 2005.

[53] G. McIntyre and A. Neureuther, "Initial experimental verification: characterizing tool illumination and PSM performance with phase-shifting masks," *Proceedings of the SPIE*, vol. 5377, pp. 185-194, 2004.

[54] G. McIntyre and A. Neureuther, "Characterizing illumination angular uniformity with phase shifting masks," *Proceedings of the SPIE*, vol. 5040, pp. 162-170, 2003.

[55] G. McIntyre and A. Neureuther, "Linear phase ring illumination monitor," *J. Vac. Sci. Technol. B.*, vol. 21(6), pp. 2800-2805, Dec. 2003.

[56] G. McIntyre and A. Neureuther, "Monitoring Polarization and High NA with Phase Shifting Masks: Radial Phase Grating," *J. Vac. Sci. Technol. B*, vol. 23(1), pp. 302-306, Jan, 2004.

[57] G. McIntyre and A. Neureuther, "PSM Polarimetry: Monitoring polarization at 193nm high-NA and immersion with phase shifting masks," *Journal of Microlithography, Microfabrication, and Microsystems*, vol. 4(3), 031102, Jul-Sep, 2005.

[58] G. McIntyre, A. Neureuther, V. Vellenki, and P. Reynolds, "Experimental verification of PSM Polarimetry: Monitoring polarization at 193nm high-NA with phase shift masks," *Proceedings of the SPIE*, vol. 6154, 6154OD, 2006.

[59] G. McIntyre and A. Neureuther, “Interferometric-probe monitors for self-diagnostics of phase-shifting mask performance.” *Proceedings of the SPIE*, vol. 5130, pp. 1324-1330, 2003.

[60] G. McIntyre, J. Holwill, A. Neureuther, L. Capodieci, Y. Zou, H. Levinson, and J. Kye, “Screening layouts for high-NA polarization effects using pattern matching,” *J. Vac Sci. Technol. B*, vol. 23(6), pp. 2646-2652, Nov. 2005.

[61] G. McIntyre, J. Kye, H. Levinson, and A. Neureuther, “Polarization Aberrations in ultra high numerical aperture projection printing: A comparison of various representations,” *Journal of Microlithography, Microfabrication, and Microsystems*, accepted for publication, Apr., 2006.

[62] G. McIntyre, *Linear Phase Ring Illumination Monitor*, M.S. Thesis, University of California, Berkeley, 2003.

[63] L. Melvin, B. Painter, and L. Barnes, "Applying assist features to improve two dimensional feature process robustness," *Proceedings of the SPIE*, vol. 5992, 59921N, 2005.

[64] P. Naulleau, E. Anderson, E. Gullikson, J. Bokor, *Optical Communications* 200, 2001, 27-34.

[65] Neureuther and F. Gennari, “No-Fault Assurance: Linking Fast Process CAD and EDA,” *Proceedings of the SPIE*, vol. 4889, 2002.

[66] H, Nishinaga, N. Tokuda, S. Owa, S. Hirukawa, O. Tanitsu, T. Kudo, and H. Tanaka, "Development of polarized-light illuminator and its impact," *Proceedings of the SPIE*, vol. 5754, pp. 669-680, 2004.

[67] H. Nishinaga, N. Tokuda, S. Owa, S. Hirukawa, O. Tanitsu, T. Kudo, and H. Tanaka, "Development of polarized-light illuminator and its impact," *Proceedings of the SPIE*, vol. 5754, pp. 669-680, 2004.

[68] S. Peng and M. Hibbs, “Direct Interferometric Phase Measurement Using an Aerial Image Measurement System”, *Proceedings of the SPIE*, vol. 3677, pp. 734-739, 1999.

[69] V. Philipsen, J. Bekaert, et al, “Mask topography effect in chromeless phase lithography,” *Proceedings of the SPIE*, vol. 5567, 2004.

[70] Phillips, S. Slonaker, C. Treadway, and G. Darby, "Influence of illumination tilt on imaging," *Proceedings of the SPIE*, vol. 5754, pp. 1562-1573.

[71] C. Pierrat and A. Wong, "MEF revisitied: low k1 effects versus mask topography effects," *Proceedings of the SPIE*, vol. 5040, pp. 193-202, 2003.

[72] T. Pistor, A. Neureuther, and R. Socha, "Modeling oblique incidence effects in photomasks," *Proceedings of the SPIE*, vol. 4000, pp. 228-237, 2000.

[73] C. Progler, "The life of ray," presented at the 2nd International Symposium on Immersion Lithography, Brugges, Belgium, Sep., 2004.

[74] C.J. Progler, H. Du, and G. Wells, “Potential causes of across field CD variation”, *Proceedings of the SPIE*, vol. 3051, pp. 660-671.

[75] G. Pugh, B. DeWitt, C. Sager, and P. Reynolds, “Detailed Study of a Phase-Shift Focus Monitor”, *Proceedings of the SPIE*, vol. 2440, 1995.

[76] G. Robins, K. Adam, and A. Neureuther, "Measuring optical image aberrations with pattern and probe based targets," *J. Vac. Sci. Technol B* 20(1), pp. 338-343, Jan/Feb, 2002.

[77] F. Gennari, G. Robins, and A. Neureuther, "Validation of the aberration-pattern-matching OPC strategy," *Proceedings of the SPIE*, Vol. 4692, pp. 444-453, 2002.

[78] G. Robins, *Interferrometric pattern and probe based aberration monitors*, Ph.D. Disseration, Department of Electrical Engineering and Computer Science, University of California, Berkeley, CA, May 2005.

[79] Rosenbluth, G. Gallatin, K. Lai, N. Seong, and R. Singh, “Topics in polarization ray tracing for image projectors,” *Proceedings of the SPIE*, vol. 5875, 17-33 (2005).

[80] K. Sato, S. Tanaka, T. Fujisawa, S. Inoue, “Measurement of effective source shift using a grating-pinhole mask”, *Proceedings of the SPIE*, vol. 3679, pp. 99-107, 1999.

[81] R. Schenker, H. Kirchauer, A. Stivers, and E. Tejnil, “Alt-PSM for 0.10um and 0.13um Poly Patterning”, *Proceedings of the SPIE*, vol. 4000, pp. 112-120, 2000.

[82] Seong, K. Lai, A. Rosenbluth, G. Gallatin, “Assessing the impact of intrinsic birefringence on 157nm lithography,” *Proceedings of the SPIE*, vol. 5377, 99-103 (2004).

[83] B. Smith and J. Cashmore, “Challenges in high NA, polarization, and photoresists,” *Proceedings of the SPIE*, vol. 4691, pp. 11-24, 2002.

[84] H. Smith, "A proposal for maskless, zone-plate-array nanolithography," *J. Vac. Sci Technol B* 14(6), pp. 4318-4322, Nov/Dec, 1996.

[85] T. Pistor, *Expanding the simulation capability of TEMPEST*, M.S. Thesis, University of California, Berkeley, 1997.

[86] L. Thompson, G. Wilson, and M. Bowden, *Introduction to Microlithography*, American Chemical Society Professional Reference Book, Second Edition, p. 26, 1994.

[87] K. Toh, G. Dao, R. Sing, and H. Gaw, "Optical lithography with chromeless phase-shifted masks," *Proceedings of the SPIE*, vol. 1463, pp. 74-86, 1991.

[88] M. Totzeck, P. Graupner, T. Heil, A. Gohnermeier, O. Dittman, D. Krahmer, V. Kamenov, J. Ruoff, and D. Flagello, “How to describe polarization influence on imaging,” *Proceedings of the SPIE*, vol. 5754, 23-37 (2005).

[89] M. van de Kerkhof, W. de Boeij, M. Demarteau, B. Geh, L. Leunissen, P. Martin, and M. Cangemi, "Mask substrate birefringence requirements for hyper-NA lithography," *Proceedings of the SPIE*, vol. 6154, 615444, Mar., 2006.

[90] Watson, R. Cirelli, M. Mkrtchyan, and R. Travers, “Characterizing Partial Coherence Uniformity in a Deep Ultraviolet Step and Repeat Tool”, *J. Vac. Sci. Technol. B* 15(6), pp. 2399-2403, Nov/Dec 1997.

[91] M. Weik, The ENIAC Story, Ordnance Ballistic Research Laboratories, Aberdeen Proving Ground, MD, 1961.

[92] A. Wong, *Resolution Enhancement Techniques*, SPIE Press, 2001.

[93] *ibid*., p. 62.

[94] *ibid*., Chapter 5.

[95] A. Wong, *Rigorous three-dimensional time-domain finite-difference electromagnetic simulation*, Ph.D. thesis, Chapter 7, Department of Electrical Engineering and Computer Science, University of California, Berkeley, CA, Sep. 1994.

[96] www.benchmarktech.com (Benchmark Technologies, Inc.)

[97] www.litel.net (Litel Instruments)

[98] www.panoramictech.com (Panoramic Technologies)

[99] J. Xue and C. Spanos, "Design of an Integrated Aerial Image Sensor," *Proceedings of the SPIE*, vol. 5752, pp. 392, 2005.

[100] Zibold, E. Poortinga, H. Doornmalen, R. Schmid, T. Scherubl, and W. Harnisch, " Advances with the new AIMS fab 193 2nd generation: a system for the 65 nm node including immersion," *Proceedings of the SPIE*, vol. 5853, p 371-379, 2005.